Spring 4-14-2014

Optimization of layered battery cathode materials synthesized via spray pyrolysis

Miklos Lengyel
Washington University in St. Louis

WASHINGTON UNIVERSITY IN ST. LOUIS

School of Engineering and Applied Science

Department of Energy, Environmental and Chemical Engineering

Dissertation Examination Committee:

Richard L. Axelbaum, Chair

Pratim Biswas

William E. Buhro

Cynthia Lo

Venkat Subramanian

Xiaofeng Zhang

Optimization of Layered Battery Cathode Materials Synthesized via Spray Pyrolysis

by

Miklós Lengyel

A dissertation presented to the
Graduate School of Arts and Sciences
of Washington University in St. Louis
in partial fulfillment of the
requirements for the degree
of Doctor of Philosophy

May 2014

St. Louis, Missouri

Table of Contents

List of Figures

List of Tables

Acknowledgments

I would like to express my gratitude to everyone who helped me throughout these years and made this thesis possible. I am especially grateful for the guidance, wisdom and patient instruction of my advisor, Dr. Richard Axelbaum, who not only helped me develop as a critical thinking and nurture my passion for research, but at the same time made certain that I become an excellent engineer, and that I mature as a leader capable of managing students and peers as well and setting an example, which has already motivated others to pursue similar routes. Without his guidance, support and insights this work would not have been possible.

I would like to thank my committee members Dr. Ilias Belharouak, Dr. Pratim Biswas, Dr. Sophia Hayes, Dr. Cynthia Lo and Dr. Venkat Subramanian for their review of my proposal and this dissertation, as well as providing valuable comments and suggestions. Attending their lectures and discussions with them has always been enjoyable, inspiring and helpful. My sincere thanks are given to Dr. Xiaofeng Zhang and Dr. Ilias Belharouak at Argonne National Laboratory, who systematically trained me on Li-ion battery fabrication and testing with patience, and helped guide our understanding of lithium ion battery research. I would especially like to thank Dr. Xiaofeng Zhang for mentoring me while he was at Washington University and for the helpful discussions ever since. I would like to thank Mr. Dror Elhassid, Mr. Gal Atlas, Mr. Will Moller and Mr. Ted Briscoe for their work, friendship and helpful discussions over the years. I would like to thank Ms. Hope Bretscher, Mr. Peter Luo, Ms. Deanna Lanigan, Mr. Jonathan Martin and Mr. Matthew Tracy for their help as a student researcher over the summers.

I would like to thank Dr. Tyrone Daulton at the Center for Materials Innovation, Ms. Kate Nelson, Mr. Howard Wynder, Mr. Nathan Reed, Dr. Wei-Ning Wang at the Nano Research Facility, Dr. Paul Carpenter at Earth and Planetary Sciences and Patty Wurm at the EECE department for their training, assistance and approval of my operation on the dedicated instruments and facilities.

I am grateful to all the members and alumni of the Laboratory for Advanced Combustion & Energy Research and my colleagues at the EECE department. A special thanks to Ben Kumfer, Melissa Holtmeyer, Sumitava De, Yi Fei, Fei Xia, Xiaofei Wang, Vivek Shah, Alireza Faghaninia, Vrajesh Mehta, Venkat Ramadesigan, Kuan-Yu Shen and all my other friends in the EECE Department. Their outstanding work ethics motivated me to move forward in all my endeavors. I would like to thank Melissa Holtmeyer for mentoring me as a safety coordinator and for keeping the lab a safe place to work. I would like to thank all the department staff for their administrative assistance.

This work was funded by the National Science Foundation, the Center for Materials Innovation at Washington University in St. Louis and X-Tend Energy, LLC, all whose support is gratefully acknowledged.

My very special thanks to my parents, my grandparents, my brother and my friends from Hungary (Mr. Csaba Tóth, Ms. Anita Mák, Mr. György Köcse, Mr. Dániel Szlivka, Mr. László Hégely) whom I owe everything I am today. Without their support and friendship this work would not have been possible. I would especially like to thank my wife, Júlia Szilágyi, who has been here for me throughout all these years, whether I was happy or sad, for her enduring patience, understanding and love throughout these years, which helped me get through this and many other challenges. She makes my life happy and full of joy.

Miklós Lengyel

Washington University in St. Louis
May 2014

Dedicated to my parents, Mária Babay and János Lengyel

My brother Tibor Lengyel

And my wife, Júlia Szilágyi

ABSTRACT OF THE DISSERTATION

Optimization of Layered Cathode Materials Synthesized via Spray Pyrolysis

by

Miklós Lengyel

Doctor of Philosophy in Energy, Environmental and Chemical Engineering

Washington University in St. Louis, 2014

Professor Richard L. Axelbaum, Chair

Rapid advancements of techniques for the synthesis of Li-ion battery materials are critically needed to address the requirement of a clean and efficient transportation sector. The current research serves this goal by developing an approach to producing layered cathode materials with superior electrochemical performance for electric vehicles (EVs). Current widespread application of EVs is primarily limited by their short range and their high price, which is primarily driven by the cost of the battery pack. The cost of the battery pack is driven by the cost of the cathode material that empowers it.

Novel, high throughput and inexpensive synthesis methods delivering nanostructured materials are a key to meeting these requirements. The synthesis techniques need to be scalable, robust, and reproducible while producing high-density materials for lithium ion batteries. To this end we advance spray pyrolysis for the synthesis of the layered NMC composite materials, which are showing high promise as a cathode material. Spray pyrolysis produces high purity materials, and the limited number of process parameters allows for low cost and excellent control over product properties and outstanding batch-to-batch reproducibility.

Layered Li-excess composite materials show nearly twice the capacity of commercial $LiCoO_2$ cells. The materials are inexpensive, have improved safety characteristics and long cycle life. Yet, as recently demonstrated, the materials suffer from an inherent layered-spinel phase change. This leads to a voltage fade over extended cycling, and this shortcoming needs to be addressed before commercial implementation is feasible.

In this work spherical-shape layered $xLi_2MnO_3 \cdot (1-x)LiNi_{1/3}Mn_{1/3}Co_{1/3}O_2$ composites were synthesized. The relationship between composition and material stability under different synthesis conditions (350 °C – 800°C reactor temperatures, 0.5 – 2.5 M concentration, 6.6 – 10.4 lpm flow rates) were explored. We found that from among the compositions corresponding to x = 0.3, 0.5 and 0.7, the composition for x = 0.3, or $Li_{1.14}Mn_{0.46}Ni_{0.2}Co_{0.2}O_2$, provides improved stability and the least amount of voltage fade while displaying capacities around 190 $mAhg^{-1}$ after 100 cycles at C/10 rate at room temperature. At the same time, for x = 0.5, or $Li_{1.2}Mn_{0.54}Ni_{0.13}Co_{0.13}O_2$, the material delivers 205-210 $mAhg^{-1}$ discharge capacities at C/3 rate at room temperature after 100 cycles, but displays more voltage fade over cycling.

This work demonstrated that the major process parameters (flow rate, reactor synthesis temperature and concentration) can be accurately controlled and the synthesis method is robust. The reproducibility of the process was evaluated using charge and discharge tests and the standard deviation for cycling tests was 4 $mAhg^{-1}$ at C/3 rate based on 4 batches produced under identical conditions on different dates. This indicates excellent batch-to-batch reproducibility.

Post-synthesis annealing temperature optimization was performed for cobalt doped samples at 850 °C and 900 °C and we found that annealing for 900 °C for 2 hours improves the cycling

stability of the samples. We evaluated the effect of lithium content between 3.3 wt% excess and 3.3 wt% deficiency and annealed the materials for 2, 5 and 20 hours at 900 °C. This helped develop a fundamental understanding between surface area and internal structural changes related to the Li_2MnO_3 structural component of the materials. Spray pyrolysis uniquely allows for the accurate control of stoichiometry and composition to trace contaminant level at these concentrations.

Furthermore, through a collaborative research between Argonne National Laboratory, X-Tend Energy, LLC and Washington University in St. Louis a novel, highly scalable patent-pending slurry spray pyrolysis process was developed, which allows the production of battery materials with excellent electrochemical performance and provides a general platform for oxide materials at greater than 50 gh^{-1} scale. This unique process is the only known solution to the hollow sphere issue that has challenged spray pyrolysis synthesis for decades, namely producing particles greater than 2 μm size with a solid (non-hollow) but porous interior morphology. Tap densities greater than 1.0 gcm^{-3} are achieved at greater than 50 gh^{-1} scale as compared to 0.4-0.6 gcm^{-3} at 2 gh^{-1} scale. $Li_{1.2}Mn_{0.54}Ni_{0.13}Co_{0.13}O_2$ produced by this novel process delivered ~205 $mAhg^{-1}$ discharge capacity after 100 cycles at C/3 rate at room temperature, reproducing the electrochemical performance of the laboratory scale synthesis process and meeting or exceeding the performing of materials produced by co-precipitation.

Voltage fade was addressed in the latter part of the work by varying the compositional ratio and using trace elemental doping. Results demonstrated for the first time that by selectively doping the $xLi_2MnO_3 \cdot (1-x)LiNi_{1/3}Mn_{1/3}Co_{1/3}O_2$ materials voltage fade can be reduced, as indicated by dQ/dV curves.

The spray pyrolysis process for $xLi_2MnO_3 \cdot (1-x)LiNi_{1/3}Mn_{1/3}Co_{1/3}O_2$ materials, in particular for layered $Li_{1.2}Mn_{0.54}Ni_{0.13}Co_{0.13}O_2$ displayed the highest capacity (c.a. 205-210 $mAhg^{-1}$ after 100 cycles at C/3 rate at room temperature) among all cathode materials synthesized via spray pyrolysis to date.

Preface

Energy supply has become critical to maintain sustainable global development in the 21st century. With the rapidly growing economies and populations there is an increasing global demand for energy, especially crude oil. According to the Energy Information Administration (EIA), the U.S. consumed approximately 18.6 million barrels of oil per day in 2012, 40% of which was imported primarily from the Western Hemisphere (Canada). The consumption of petroleum in transportations leads to the emission of greenhouse gases, which have adverse effects on global climate. Electric vehicles have the potential to reduce the petroleum consumption by introducing vehicles that have zero tailpipe emission when combined with carbon neutral energy generation. Lithium-ion batteries are also projected to play a role in grid scale stationary storage, enabling the effective use of renewable energies.

In recent years, the primary focus of Li-ion battery research has been to develop new materials and new chemistries, which deliver higher energy density, high power and long cycle life for Plug-In Hybrid Electric Vehicle (PHEV) and Electric Vehicle (EV) applications. Due to the advancement of battery technologies, EVs are now a commercial reality. Several new models were launched over the past 3 years using lithium ion battery packs. Tesla Motors manufactures EVs, such as the Roadster and Model S, that offer a competitive mileage range to gasoline-powered vehicles at a sticker price of about 100,000 USD. These vehicles primarily use lithium transitional metal oxide material (e.g. NCA) for their batteries. The current demand for these vehicles is so high that Tesla Motors recently announced that besides partnering with additional

battery manufacturers to diversify their battery supplier portfolio, they will establish their own battery production facility. Rimac Automobili created an EV sports car using $LiFePO_4$ based chemistries for their battery packs, with a price tag between 800,000 – 1,000,000 USD. Nissan Motors manufactures the Leaf, having a 70 mile/charge range, but they have announced improvements to their transitional metal oxide batteries to extend the range of the vehicle. PHEVs are becoming commercially available as well with the Chevrolet Volt and the Toyota Prius Plug-in Hybrid, for example. Current widespread application of PHEVs and EVs is either limited by their range or by their price, which is primarily driven by the cost of the battery pack. A leading driver of the high cost is the cost of the cathode material. In general, current batteries use inexpensive graphite anodes. Besides these issues the lifetime of the battery pack of an EV is expected to be 8 years compared to the average 15-year life expectancy for a gasoline powered engine. Currently no materials exist that satisfies all three criteria of energy density, cost and lifetime. Novel, high throughput and inexpensive synthesis methods that can deliver state-of-the-art nanostructured materials are a key to meeting these criteria.

This research applies spray pyrolysis to produce high-quality layered cathode materials to meet the above-mentioned goals and improve the performance of the layered chemistry.

"I wonder often whether any other generation has seen such astounding revolutions of data and values as those through which we have lived. Scarcely anything material or established which I was brought up to believe was permanent and vital, has lasted. Everything I was sure or taught to be sure was impossible, has happened."

- *Winston Churchill: My Early Life: A Roving Commission*

(1874-1965)

Chapter 1

Introduction

1.1 Demand for Li-ion Batteries

Due to their high theoretical and practical energy density, lithium-ion batteries are attractive power sources for portable consumer electronic applications, Plug-in Hybrid Electric Vehicles (PHEVs) and Electric Vehicles (EVs). Since the demonstration of a reversible cathodic electrochemistry in layered $LiCoO_2$ by Goodenough *et al.* and its introduction in a commercial cell by Sony in the early 1990's, the Li-ion battery industry rapidly expanded both in research and market because of the high volumetric and gravimetric energy density delivered by these cells compared to other battery technologies, as shown in Figure 1 [1, 2]. Li-ion batteries are considered the most attractive choice of electronic energy storage for portable electronics, transportation and grid scale energy storage devices, as demonstrated by the vast number of papers published in the field [3, 4, 5, 6, 7, 8, 9, 10, 11, 12, 13, 14, 15, 16].

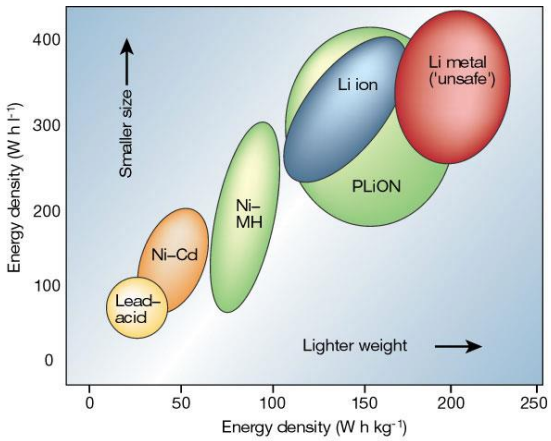

Figure 1 - Comparison of energy density of different battery technologies [12].

For grid scale energy storage different technologies, such as molten salt batteries (e.g. sodium-beta alumina), pumped hydro and Compressed Air Energy Storage (CAER) technologies are being developed to compete with industrial scale lithium ion battery storage plants [5, 17, 18]. Recently, the idea of recycling depleted EV batteries in grid scale applications has surfaced to find a potential use for the expensive battery packs, but these are preliminary discussions. An alternative technology for grid scale storage is presented by redox flow batteries [19]. These technologies are currently under development and may hold the potential of revolutionizing renewable energy storage and load leveling at grid scale.

Currently, the main driving force for the rapid development of Li-ion battery technologies is the need for batteries for PHEVs and EVs. PHEVs allow for mileage in a fully electric mode and have a gasoline engine to mitigate the range criteria. For example Toyota's Prius Plug-in Hybrid has a small, 12 mile range in a fully electric mode, while the Chevy Volt offers 35 miles on a single charge. Such a battery needs to supply high energy with weight and volume constraints for long-range driving, and it needs to be functional after 5,000 deep cycles (≥ 50% state of charge, SOC) for EVs and 300,000 cycles for PHEVs. EVs do not include a gasoline engine. Therefore either they need to be recharged once the battery is depleted or as an alternative solution the battery pack needs to be "swapped" to extend the range. Beyond the range and the cycleability criteria the batteries need to meet strict safety standards (including environmental safety concerns), need to be inexpensive to allow widespread commercial application and need to be lightweight. Figure 2 summarizes the major development goals for PHEVs and EVs.

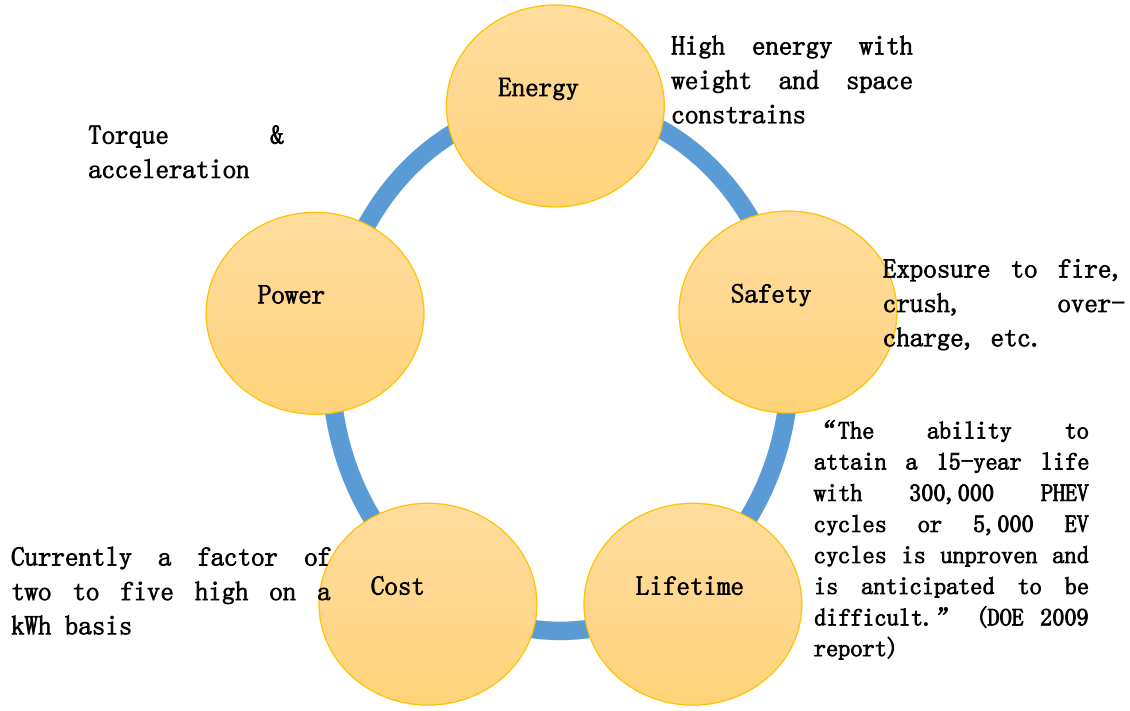

Figure 2 – Summary of the primary development goals for PHEVs and EVs.

Recently, several EVs were successfully introduced to the market. The Nissan Leaf offers a 75 mile range per charge starting at 30,000 USD, which is a competitive range typically in urban environments. The Tesla Model S and Roadster can be purchased with an 85 kWh battery pack that offers a 265 mile driving range starting at 100,000 USD, which is the only known fully electric vehicle with such a range. Clearly these costs cannot compete with other inexpensive gasoline powered vehicles and further advancement of the battery technologies primarily on the manufacturing side are needed to allow widespread commercial implementation.

1.2 Lithium-ion Battery Basics

Lithium ion batteries are comprised of an anode and a cathode, separated by a porous separator membrane (see Figure 3). In a lithium battery, Li ions migrate repeatedly between the anode and

cathode. During charge for the intercalation compounds, which are currently the most widely used chemistries, the lithium ions migrate from the cathode and deposit on the anode, while electrons migrate in an external circuit. The entire process is reversed during discharge. During charge, energy is consumed from an external power supply and this is almost completely utilized during discharge (except for, for example, parasitic losses and thermal effects, which decrease efficiency). In commercial batteries the anode materials are almost exclusively carbon (graphite) based materials. While other materials, such as lithium titanate ($Li_4Ti_5O_{12}$), metallic lithium, silicon anodes and graphene have been widely researched, none of these competing technologies has reached maturity yet [20, 21, 22, 23, 24, 25, 26, 27]. Cathode materials are typically transition metal oxides, such as layered $Li[M]O_2$ (M = Co, Ni, Mn), spinel $Li[M']_2O_4$, olivine-type $Li[M'']PO_4$ (M'' = Fe, Mn) and their derivatives [28, 29].

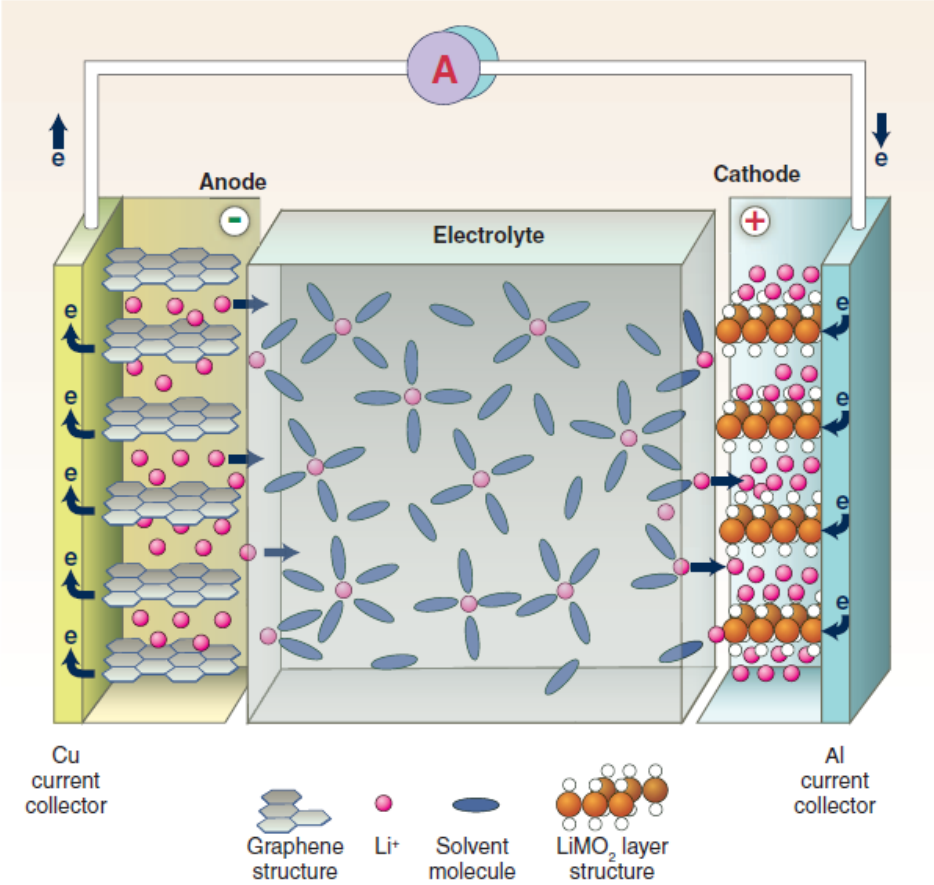

Figure 3 - A schematic representation of a lithium ion battery [5].

The intercalation/de-intercalation reaction is the most important reaction mechanism for Li-ion rechargeable batteries, and involves the insertion of Li ions into interstitial sites in the crystal without changing the basic crystal structure. Intercalation chemistry for Li-ion battery systems was first proposed by M.S. Whittingham [30]. The intercalation reaction ideally is a reversible process, where Li ions can be repeatedly extracted and reinserted into the host materials without any structural degradation. The insertion reaction normally occurs when the host has an open framework or a layered-type crystal structure. Typically Li resides in the interstitial sites while the host framework primarily consists of transitional metal ions.

1.3 Anode Materials for Li-ion Batteries

Lithium metal anodes are typically used for the initial development of both lithium ion battery anodes and cathodes as an "infinite" source of lithium compared to the other electrode's capacity. Often anode host structures are synthesized without the lithium and then lithium is subsequently inserted during the initial discharge. Commercial application of lithium metal anodes is limited primarily because of safety limitations associated with dendrite formation and its reactivity with organic electrolytes. Lithium air batteries (as discussed below) try to develop integrated solutions for lithium anodes as well, however to date the necessary breakthroughs have not been obtained [31, 32, 33].

Carbon, specifically graphite, has been extensively studied as an anode material due to its extremely low cost, excellent safety characteristics and availability. The practical capacity of the graphite electrode is about 372 $mAhg^{-1}$ and allows the intercalation of one Li ion per six carbons (LiC_6). Graphite's electrochemistry is also based on the intercalation mechanism. Similar to more advanced cathode materials, graphite also forms a surface electrolyte interface (SEI) during cycling, which adds to the capacity fade mechanism of the cell. The capacity fade mechanisms have been extensively studied and the understanding of these nanoscale phenomenon considerably improved over recent years [34, 35, 36, 37, 38, 39, 40, 41]. A variety of carbon-base materials anode materials, such as carbon fibers, carbon nanotubes, mesocarbon microbeads (MCMB) and graphene nanosheets were also studied to improve the Li to carbon ratio and improve the capacity of the anode material [22, 23, 42, 43, 44, 45, 46, 47, 48]. Another attractive anode material is elemental silicon, which offers a tenfold increase in capacity (~4,200 $mAhg^{-1}$) compared to carbon based anodes [20, 22, 26, 49, 50, 51]. Si can intercalate 4.4 Li ions per Si atom [50]. Due to the

resulting negative charge repulsion the material undergoes extreme expansion (300-400 %) during a single charge, which causes severe cracking that leads to delamination of the electrode over cycling [52]. Current research focuses on nanostructured morphologies to improve cycleability of the material [49, 50, 53]. A novel, scalable approach was recently developed by Nexeon Co. in the UK for the production of columnar silicon anodes and is being commercialized showing high potential for this material.

1.4 Cathode Materials in Li-ion Batteries

Olivine-type lithium iron phosphate ($LiFePO_4$) is considered to be one of the safest cathode materials for large-scale applications. Olivine-phase $LiFePO_4$ was first discovered by Padhi, et al. in 1997, synthesized by a solid-state reaction [54]. The material is very stable, however as the material is essentially an insulator, significant challenges were present related to its application. $LiFePO_4$ has a medium theoretical capacity of 170 $mAhg^{-1}$, which can be activated when synthesized by various techniques with a nanostructured, carbon-coated morphology. The material has a flat voltage plateau at 3.5 V versus Li/Li^+. Once a novel method of production was developed by Chiang et al at MIT, the material was successfully commercialized via A123 materials and received significant funding as an early target material for automotive applications [55, 56, 57, 58, 59, 60, 61]. Alternative synthesis technologies (including spray pyrolysis and hydrothermal synthesis) that involve intimate mixing with carbon to improve the conductivity were successfully developed and as demonstrated by Rimac Automobili, may find application in the EV industry. Primary development of these materials focuses on grid scale applications due to its mediocre capacity.

$LiCoO_2$, the most well-known layered cathode material was originally developed by Goodenough et al. in the 1980s [1]. $LiCoO_2$ is iso-structural to α-$NaFeO_2$ ($R\bar{3}m$ symmetry) with oxygen atoms in a cubic-close-packed (*ccp*) arrangement (Figure 4). In the ideal layered materials, Li and Co atoms occupy the octahedral and interstitial sites [62, 63]. During charging after 50% of the Li is extracted from the cathode Co^{+4} atoms form, which may react violently with the organic electrolyte and lead to thermal runaway as observed by various battery abuse tests (ARC, punctuation tests) [64]. This limits the practical capacity of layered $LiCoO_2$ to ~ 140 $mAhg^{-1}$ compared to the theoretical 280 $mAhg^{-1}$. Various studies focused on stabilizing this material by doping with Ni and Mn, however without changing the chemistry substantially no significant improvements were achieved. This limits $LiCoO_2$ to portable electronic application and does not permit PHEV /EV implementation.

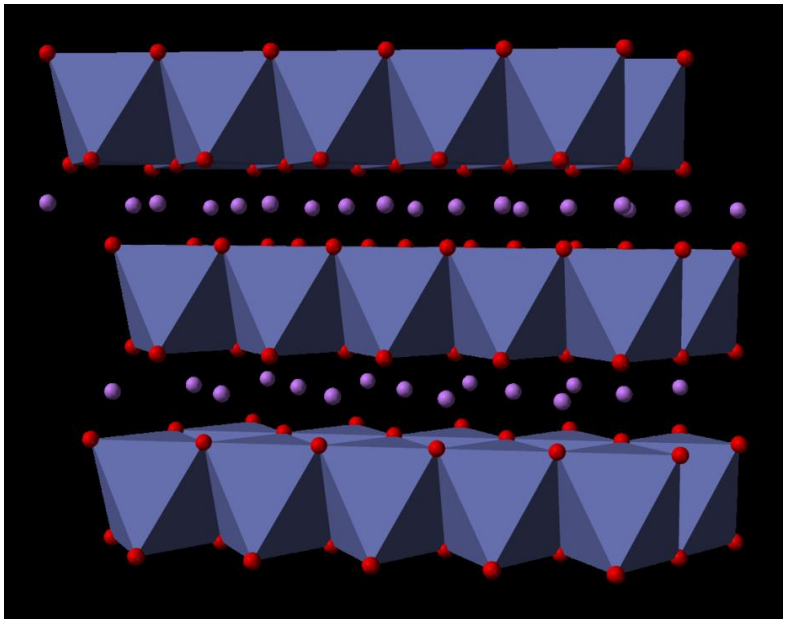

Figure 4 – Ideal structure of lithium cobalt oxide. The purple dots represent lithium ions in the interstitial sites, while the octahedra represent the cobalt atoms (from http://en.wikipedia.org/wiki/File:Lithium-cobalt-oxide-3D-polyhedra.png)

$LiMnO_2$ is thermodynamically stable compound, however upon cycling it converts to a spinel material, which has poor cycling performance primarily due to the disproportionation and subsequent dissolution of Mn^{+3} [62, 63]. $LiMnO_2$ and similar oxides represent a widely researched class of cathode materials with similar derivatives, such as $LiNi_{0.5}Mn_{1.5}O_4$ being candidate materials for high voltage spinel materials [65, 66, 67, 68, 69, 70, 71, 72, 73]. One of the key challenges is identifying a stable electrolyte that will not decompose and allow the utilization of the 5 V voltage plateau of these materials. Li_2MnO_3 is an alternative layered-type material with rock-salt structure and has a theoretical capacity of ~ 458 $mAhg^{-1}$ [74, 75, 76, 77]. The material cannot easily be activated (electrochemical or chemical methods may be necessary) and upon cycling fades rapidly as demonstrated by recent studies performed at Sanyo [78, 79, 80]. By "combining" Li_2MnO_3 with $LiMO_2$ (where M=Mn, Ni, Co, etc.) structural components "composite" materials may be

formed delivering capacities in excess of 200 $mAhg^{-1}$ [80, 81, 82, 83]. Figure 5 shows a schematic diagram of the integrated structural components as proposed in reference [84].

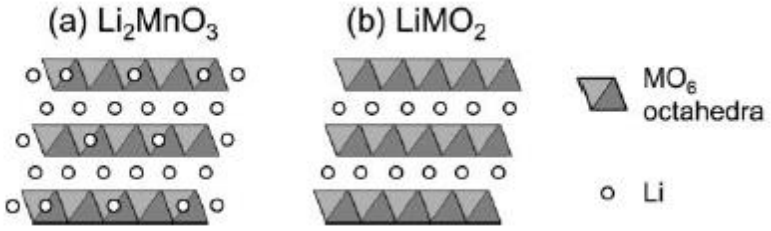

Figure 5 Layered structures of (a) Li_2MnO_3, (b) $LiMO_2$ (M= Mn, Ni, Co) from [84].

Originally, when the materials were designed the Li_2MnO_3 was primarily considered to be electrochemically inactive and to play a stabilizing role in the structure. Several excellent papers were published and a co-precipitation and a solid state synthesis route was pioneered out of Argonne National Laboratory by Thackeray, Dahn, Manthiram and others [84, 85, 86, 87, 88, 89, 90]. These studies revealed that by charging the material to greater than 4.6 V vs. Li the Li_2MnO_3 component becomes electrochemically active thus delivering capacities in excess of 250 $mAhg^{-1}$ reproducibly. To date the exact details of the activation process are not known, although extensive studies indicated that it is coupled to a virtual loss of "Li_2O" from the structure [91, 92, 93, 94, 95]. Recent modelling and simulation work further developed the understanding of the activation process and structural ordering in the materials [96, 97, 98, 99]. The materials have often been referred to both being layered-layered composites and layered-spinel composites. During this thesis the composites will be termed layered-layered composites, although it is understood that the structure is more complex.

When synthesized by co-precipitation the materials demonstrate excellent electrochemical properties, although the reproducibility of the process is questionable, particularly at large scale.

To improve the electrochemical properties and capacity retention nanostructured and core-shell structured materials were tested, but overall none of these improved the capacity retention significantly [100, 101, 102, 103, 104, 105, 106, 107, 108]. Surface treatment primarily with $LiNiPO_4$ and F-based materials achieved partial success in improving the electrochemical performance but these processes are often complicated, add complexity to the synthesis and are not always scalable e.g. if aluminum coating is applied by PVD methods [85, 96, 109, 110, 111, 112].

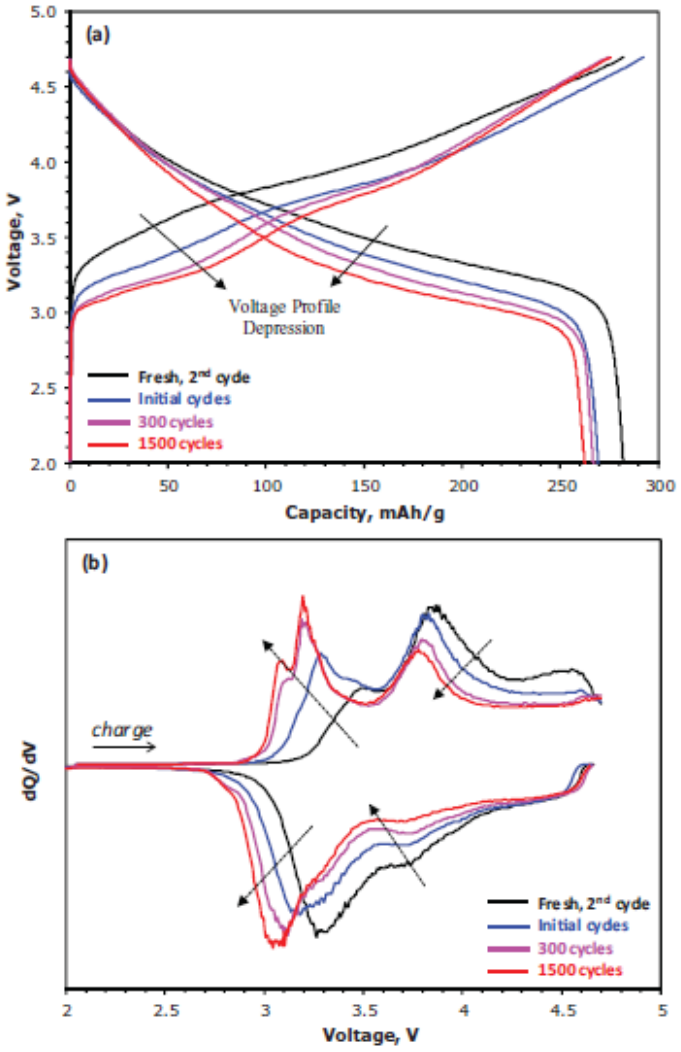

Figure 6 – Voltage fade of $Li_{1.2}Co_{0.1}Mn_{0.55}Ni_{0.15}O_2$ over 1500 cycles at room temperature [113].

Over cycling the materials display a voltage fade over that is caused by an internal layered-spinel phase change (see Fig. 6) and has been studied extensively recently [113, 114, 115, 116, 117, 118]. As of this writing the voltage fade is speculated to be a layered-spinel transition occurring due to the complicated structure of the materials and causes an overall loss of power, which needs to be addressed before commercial implementation of these materials is possible. To date the only know solution is that demonstrated by Tarascon et al. and lies with the development of similar chemistries [119]. Recently, our group achieved partial success for the chemistries as discussed in Chapter 6 [120]. Therefore, demonstrating a scalable, reproducible synthesis method and improving the stability of these materials is of great importance and will be the primary focus in the following chapters.

1.5 Batteries beyond conventional lithium ion chemistries

This section will briefly discuss a few chemistries, which offer advantages vs. conventional lithium ion batteries either in terms of safety or energy density.

Intercalation chemistries can be obtained by other small elements similar in size to lithium, which can occupy interstitial sites in the host's lattice without altering it significantly. Magnesium represents such an example and magnesium batteries are intensely researched by Aurbach et al [121, 122, 123]. Advantages of a magnesium based battery include the safety, stability over cycling as no SEI layer forms from the electrolyte due to the lower working potential due to the reduced reactivity and oxidizing nature of magnesium. The low operation voltage yields lower energy density and the diffusion coefficient of magnesium in the primarily Mo based structures is low. Finding a scalable synthesis method poses another challenge due to the metastable phases, which are currently used in the prototype materials.

Lithium sulfur batteries were proposed several decades ago due to the extremely high potential energy density (1675 $mAhg^{-1}$) that can be obtained with combining sulfur and lithium [124]. Several challenges exist for this battery configuration. First, elemental sulfur is an insulator and with no mechanism to prevent it, agglomeration of sulfur and surface precipitation lead to rapid capacity fade due to deactivation of the active material. The insulating nature of sulfur causes low rate capability. A shuttling mechanism that allows sulfur to pass through the separator membrane from the cathode to the anode side also leads to the loss of active material on the anode.

Recently, with advanced synthesis techniques allowing more elaborate carbon structure formation tunnel and graphene type structures were developed by Cairns et al., Nazar et al. and Scrosati and coworkers [125, 126, 127, 128, 129, 130]. These advanced graphite host structures provide an inexpensive host, encapsulate the sulfur and the charge / discharge product and reduce the shuttling mechanism. Due to these recent advancements 1500 cycles were successfully demonstrated and these materials are becoming more attractive candidates for commercialization, with companies such as Oxis Energy (UK) and Sion Power (Tucson, AZ) evaluating commercial implementation.

Lithium-air batteries (including other metal air, such as Zn-air batteries) received extensive interest over the past several years due to the high capacity that could be obtained by reacting lithium with oxygen. A lithium-air cell offers significant weight advantages with no active cathode material stored and the highest energy density that could easily compete with gasoline based vehicles. Depending on the calculation the materials may offer capacities in excess of 4000 $mAhg^{-1}$. Fundamental challenges still exist and will need to be addressed before

commercial implementation is possible and a brief overview of these challenges is provided based upon several reviews [25, 31, 32, 131, 132, 133, 134].

The first major challenge is that to date it has not been demonstrated unambiguously, that Li can reversibly combine with oxygen and form either Li_2O or Li_2O_2. The proposed lithium air cells either use aqueous electrolytes or organic electrolytes and a metallic lithium anode, which already represents significant challenges related to the safety of the cell. In case of aqueous electrolytes an additional protective membrane is required, while organic electrolytes typically easily decompose under such an oxidizing environment and most of the reviews cite this as the main reaction instead of the desired recombination of lithium with oxygen. No active cathodic catalyst has been developed and advanced synthesis techniques controlling the pore size and surface area are necessary to advance the technology. If the reaction would be supplied by air instead of oxygen, the air needs to be prepurified, while adding an oxygen tank would significantly complicate the setup and increase costs. It is understood that significant research needs to be done for all the battery parts (cathode, anode, separator, electrolyte) before such a cell can reach maturity.

1.6 Overview of Synthesis Processes for Cathode Materials

This section will briefly discuss the numerous synthesis methods that are currently being studied for the production of battery materials. Solid-state reactions are widely used due to their simplicity and ease of scale-up. Layered $LiCoO_2$, spinel-$LiMn_2O_4$ and olivine-type $LiFePO_4$ were initially synthesized via solid-state reaction [1, 68, 135]. Solid-state reaction has been widely applied for the synthesis of lithium transition metal oxides and other battery materials [136, 137, 138, 139, 140, 141, 142]. Ball-milling is an alternative version of solid-state reactions [112, 143]. While the

simplicity is clearly an advantage, the long processing times, the difficulty of controlling morphology and impurity phases pose significant challenges to delivering robustness and reproducible, high quality products. Freeze-drying represents another derivation of solid state synthesis posing similar challenges [144].

Wet-chemistry processes, including the state-of-the art co-precipitation process for the production of layered cathode materials, require solvents and additives to produce the cathodes. A variety of materials can be produced via wet-chemistry processes including layered $LiMO_2$ (M=Li, Co, Mn, Ni etc), spinel $LiMn_2O_4$, olivine $LiFePO_4$ and silicates. Wet chemistry processes allow us to produce various morphologies due to the different complexing agents used (see Fig. 7) [83, 145, 146, 147, 148, 149, 150].

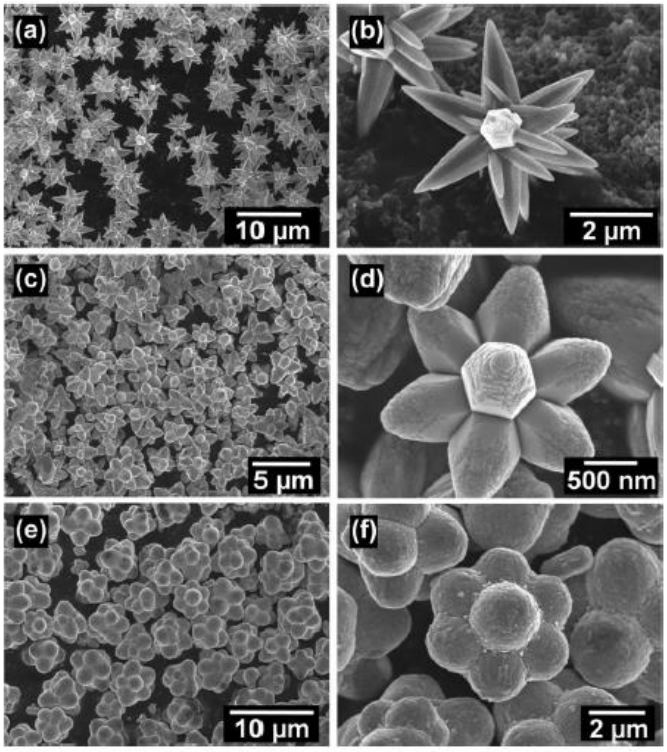

Figure 7 - Effect of triethyl citrate concentration from aqueous solution precipiation [150].

Sol-gel methods are very similar, the major difference being that a sol is formed, which turns into a gel and then is heated to high temperatures (> 300 °C) to form the product. The organic gelation agents and surfactants increase the manufacturing cost significantly, which limits the commercial potential of the process [151].

Recently the Dahn research group developed a combinatorial chemistry approach for the production of battery materials [152]. This high throughput screening method is more typically applied in the pharmaceutical industry for drug discovery, however as demonstrated by Wildcat Technologies in San Diego, CA, it may lead to novel battery materials as well.

A molten salt synthesis method represents a transition between wet chemistry processes and solid-state processes. The method was successfully applied for producing layered cathode materials, although it is expected that the high temperature process would significantly increase manufacturing costs [153].

Recently, a co-precipitation process originally developed by Argonne National Laboratory for the synthesis of layered cathode materials was licensed by Envia Systems, Toda America and General Motors for producing layered cathode materials [88, 105, 149, 154, 155]. The materials demonstrated excellent electrochemical performance if the desired phase is formed, however the process has known issues with reproducibility due to the lack of accurate control of system variables (pH, precipitating agents, etc.). This may lead to different colors due to phase separation, *i.e.*, Li_2MnO_3 phase, which are detrimental to the electrochemical performance. The process requires high temperature heat treatment to perform post-synthesis lithiation combined with annealing and several purification steps are necessary to reduce the contaminations of the product.

Wet-chemistry and solid state processes often consist of multi-steps requiring precise control over precursor chemistry, reaction temperature and pH as well as long-annealing times are required at high temperatures. While some of these parameters can be tolerated and eliminated over scale up, a simple aerosol based process may offer a solution to most of these challenges.

Aerosol based synthesis methods became popular for the production of electrochemically active materials. The term aerosol generally means small particulates suspended in gas phase. Particles can be spherical, fiber-like, or irregular shaped and can have dense or hollow interior. Compared to other processes aerosol-based processes provide a scalable approach to produce nanostructured powders with narrow size distribution reproducibly in an inexpensive method.

Aerosol methods involve gas-to-particle reactions and liquid-droplet-to-particle reactions for powder synthesis. Gas-to-particle processes are more prevalent for single component oxides typically used in chemical vapor deposition (CVD) and physical vapor deposition (PVD) processes. This research will focus on the liquid droplet-to-particle synthetic route for the production of layered transitional metal oxides using the spray pyrolysis process originally developed by Zhang [156]. Spray drying and flame spray pyrolysis are also often discussed in the literature for producing electrochemically active materials [157, 158, 159, 160, 161, 162, 163, 164, 165, 166, 167, 168].

During spray pyrolysis the short residence time in the reactor allows large throughput; the process is scalable; no further post-synthesis purification steps are required; batch-to-batch reproducibility is excellent and the contamination profile of the product meets or exceeds the purity of the precursor. The mesoporous morphology of the product allows complete activation

of the material. These properties coupled to the excellent electrochemical performance show great potential for future implementation.

Spray pyrolysis reactions proceed through the following basic steps: (1) droplet formation; (2) transport of the droplets into a high-temperature environment; (3) evaporation of the solvent; (4) thermal decomposition to form products (schematic provided in Figure 8). These steps involve a wide range of physical and chemical processes (evaporation, sintering, diffusion, decomposition, combustion, *etc.*).

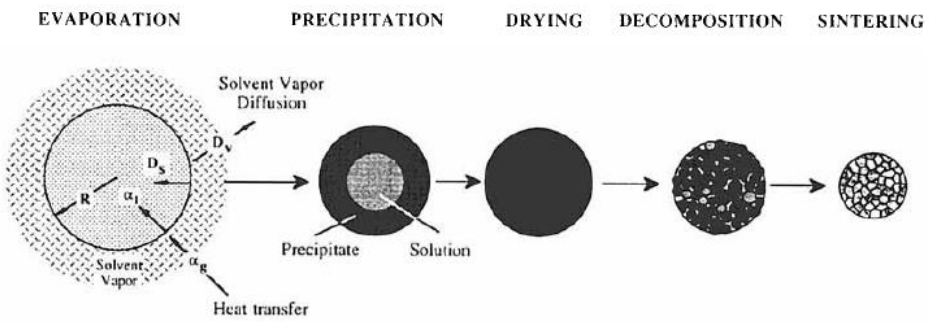

Figure 8 – Stages of spray pyrolysis [169]

Spray pyrolysis has its technical challenges: phase segregation and morphology control. Morphology control primarily consists of the ability to influence the interior hollowness of the product powder during particle formation [169, 170, 171]. This affects macroscopic properties, such as the tapped density of the material, which affects the energy density.

During the initial formation of the particles the precursor droplets may undergo rapid drying, which can lead to surface precipitation instead of volume precipitation, resulting in a hollow interior [169, 172, 173]. Similarly, due to rapid gas evolution following the decomposition of the precipitated salts an impermeable melt may form, and thus the particles can be "inflated", which can also lead to a hollow interior [169, 172]. High temperature densification can be used to reduce the

hollowness of the product powders to some extent, although this will lead to increased sintering of the primary particles and will not prevent hollow sphere formation for particles greater than 2 μm [174].

Several experimental and modeling studies were established primarily for single component oxides to overcome hollow sphere formation. For single component oxides Jain *et al.* found that melt formation during precipitation may be a critical criteria to judge the ability of solid or hollow interior formation [170]. By changing the concentration of the precursor solution partial success was obtained for barium titanate particles [175, 176]. Hydrolysis assisted spray pyrolysis was also partially successful for CeO_2 powders, but adding a precipitating aid may initiate phase segregation in multi-component oxide materials [177]. Solid silver particles were successfully produced by complexing Ag atoms with NH_3 [178]. These studies demonstrate that in order to overcome and prevent hollow shell formation the fundamental solution phase cluster formation needs to be affected in the precursor solution. Grinding the as-synthesized particles and combining spray pyrolysis and spray drying allowed Taniguchi and coworkers to demonstrate partial success in obtaining particles with a solid interior morphology as well [179].

Phase segregation can occur during the formation of the particles, when due to the different chemical nature of the components, they precipitate at different times during the solvent evaporation phase of particle formation [169, 172, 180]. To date no report indicates that the electrochemical performance of cathode materials synthesized by spray pyrolysis would be compromised by phase segregation.

Spray pyrolysis methods have been reported to produce layered $LiCoO_2$ [181, 182], $LiNiO_2$ [183], spinel $LiMn_2O_4$ [168, 184, 185, 186, 187, 188, 189, 190], $LiNi_{0.5}Mn_{1.5}O_4$ [167, 191, 192, 193, 194, 195], olivine $LiFePO_4$ powders [196, 197, 198, 199], layered composite materials [156, 200, 201, 202] and other electrochemically active materials, such as semiconductors [170, 171, 172]. The advanced, nanostructured morphology of materials prepared by spray pyrolysis allowed the materials to display equal or improved performance compared to materials synthesized by other methods due to the high purity of the products [203, 204].

1.7 Objectives and Dissertation Outline

The objective of this dissertation is to advance the spray pyrolysis method for layered composite materials and to further develop our understanding of the process and the materials, and to improve capacity fade properties, cycle life and capacity retention. In addition, a goal of this work is to identify a path to overcome the voltage fade associated with these materials. Parallel to these efforts the scale up of the process will be studied with the goal of increasing the production rate to greater than 10 gh^{-1} as well as to overcome hollow sphere formation and increase the tap density of the materials.

With these objectives, the dissertation will have five chapters. Chapter 2 will discuss the methodology and experimental apparatus in detail. Chapter 3 will focus on compositional variations of $xLi_2MnO_3(1-x)LiNi_{1/3}Mn_{1/3}Co_{1/3}O_2$. Using the optimal composition identified, Chapter 4 will discuss the effects of synthesis properties on the electrochemical performance of layered materials. Chapter 5 will address the effects of surface area, lithium content and annealing conditions. Chapter 6 will show results related to the voltage fade and doping. Chapter

7 will discuss the results related to scale up of the process and overcoming hollow sphere formation.

Chapter 2

Research Methodology

2.1 Powder Synthesis – Spray Pyrolysis

Throughout the thesis spray pyrolysis or slurry spray pyrolysis will be used for the production of lithium ion battery cathode materials. During spray pyrolysis the particles' size distribution and morphology are defined by the atomization method. Prior work indicates that the chemistry of precursor salts, additives and the synthesis conditions can have some effects on the secondary particle size of the product [169, 170, 171, 172, 173, 176, 178, 180, 205]. The hollowness of the powder above 2 μm size can sometimes be mitigated, but previously no work discussed an ultimate solution to the problem. Typical atomization techniques use atomizers, nebulizers and various spray nozzles (high pressure nozzles, rotary atomizers, two-fluid nozzles). When the droplets enter the furnace the solvent rapidly evaporates, the salts precipitate and form a solid or hollow shell like structure. Before entering the hot furnace reactor, the precursor droplets enter a low-temperature evaporator, which allows the slow evaporation of water. This effect is more prominent for smaller droplets, which are typically generated by atomizers, such as a BGI Collison jet atomizer. For larger droplets synthesized by an ultrasonic nebulizer the drying temperature's effect did not have a beneficial contribution to reduce the interior hollowness.

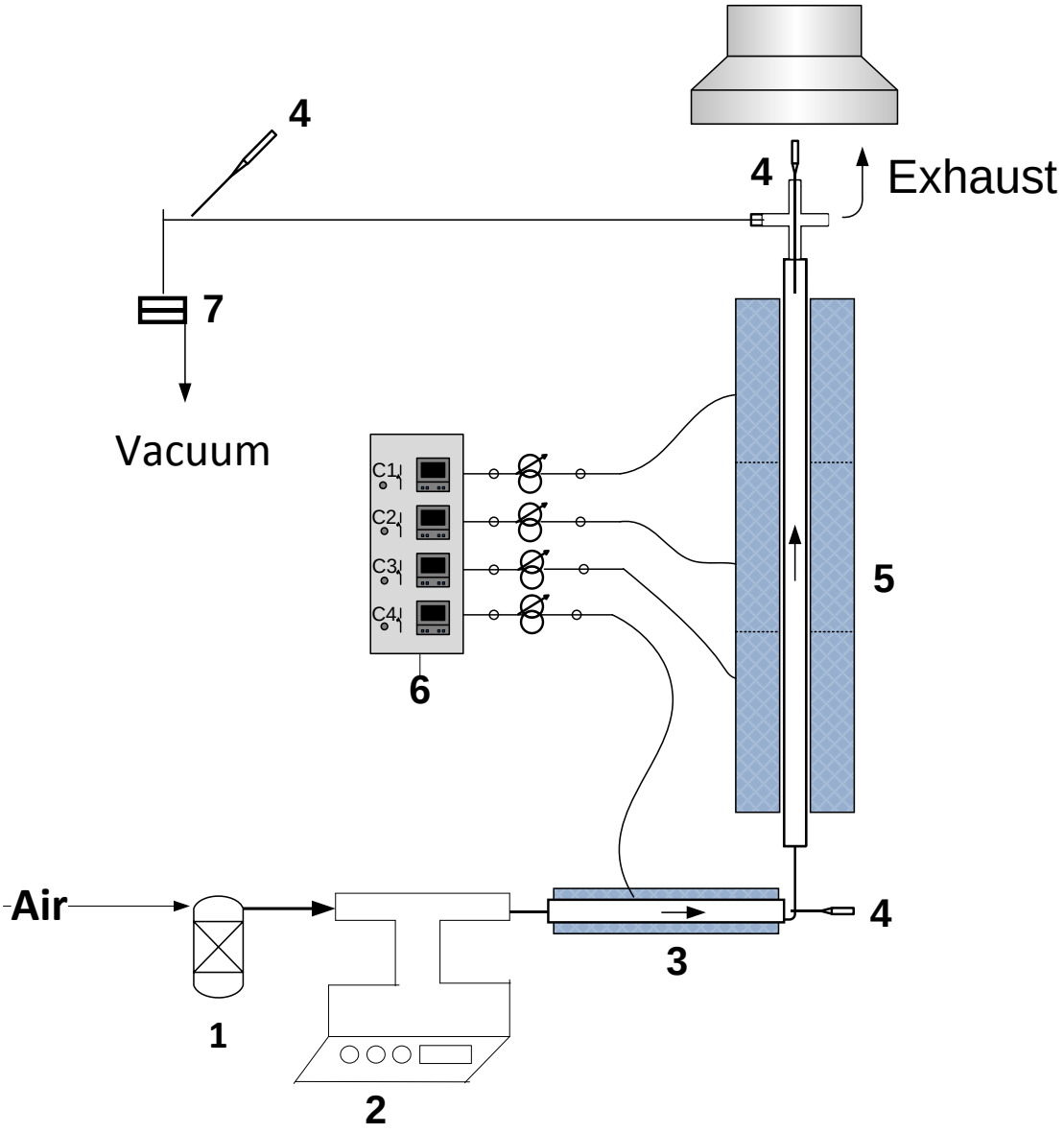

Figure 9 - Schematic diagram of the tubular furnace reactor setup: (1) Bubbler; (2) Ultrasonic nebulizer; (3) 22 inch long preheater; (4) Thermocouple; (5) Ceramic tube; (6) Temperature controller; (7) Porous membrane filter.

The aerosol flow reactor (AFR – Fig. 9) consists of a preheater that is maintained at a constant 200 °C wall temperature and a ceramic flow reactor maintained typically at 575 °C wall temperature unless otherwise indicated. Typical residence time in the system was 6 seconds, which corresponds to 6.6 lpm flow rate. The ultrasonic nebulizer (Sonaer Inc.) requires a special swirling air motion at the inlet to entrain the generated droplets in the flow. Below this flow rate most of the generated droplets fall back to the nebulizing chamber and particle production is minimal.

Modelling of the elemental steps of particle formation is beyond the goals of the current thesis. The drying rates for a typical droplet were estimated according to results reported in *Aerosol Technology* for droplets and a comprehensive modelling study [206, 207]. Based upon these sources the droplet evaporation rates and times in the hot furnace reactor are in the order of $10^9 gs^{-1}$ and 10 ms, respectively. These short time frames indicate that the initial droplet formation will primarily determine the shell formation tendency of the droplets.

The droplet size of the ultrasonic nebulizer is primarily determined by the Lang-equation [174, 208]:

$$d_d = 0.34\left(\frac{8\pi\gamma}{\rho f^2}\right)^{1/3}$$

where γ and ρ presents the density and f the frequency of the ultrasonic crystal. This equation can be used to estimate the final particle size, for example using the procedure reported in [209]:

$$d_p = d_d\left(\frac{c_{pr}M_p}{\rho_p M_{pr}}\right)^{1/3}$$

Where c_{pr} is the concentration of the solute in a precursor, M_p and M_{pr} are the molecular masses of the precursor and the final products and ρ_p is the density of the product.

Figure 9 shows that the aerosolized precursors first enter the preheater followed by the hot furnace reactor, where the precursors decompose to form the as-synthesized powders. The gas temperature at the exit of the hot furnace reactor is also monitored and is typically maintained between 490-510 °C. The powder is collected downstream of the reactor using porous, polycarbonate membrane filters and vacuum. To control the moisture level of the air entering the system near the exhaust additional compressed and pre-dried air is supplied. The precursor solution is prepared by dissolving typically the appropriate amounts of Li, Ni, Mn and Co nitrates in ultrapure (18.6 MΩ) water and stirring the solution at room temperature until complete dissolution is achieved.

2.2 Annealing heat-treatment

In order to obtain the desired, highly crystalline materials an annealing heat treatment was necessary. In Chapter 4 the effects of reactor synthesis temperature are discussed in details. When the synthesis temperatures were below 575 °C the powders were hygroscopic due to the presence of unreacted lithium nitrate in the powder. Above 575 °C the nitrates fully decompose although the primary particle sizes are small. Therefore the as-synthesized materials are typically subject to a short annealing heat-treatment at temperatures between 800-900 °C for 2 hours to improve the crystallinity of the samples in a box furnace (Thermal Product Solution). A typical annealing heat treatment will proceed as follows: 1 hour 20 minutes of ramp up to 900 °C (~ 10 °Cmin^{-1} heating rate), 2 hours hold at 900 °C followed by 4 hours and 20 minutes of cooling (~ 3 °Cmin^{-1} cooling rate). The cooling typically proceeds slower at the low temperatures due to natural convection.

Alternative solutions to increasing the primary particle size have also been reported for lithium ion battery cathode materials. By extending the hold time in the aerosol phase as in case of applying a fluidized bed reactor the primary particle coarsening can be improved, such that no or reduced annealing heat treatment is necessary to obtain good electrochemical performance [210, 211].

2.3 Particle Size Measurements

The particle size distribution is an important characteristic of powder products. In situ aerosol measurements are indicative of final product properties and were measured with an electric low-pressure impactor (ELPI - DEKATI). Preliminary studies were performed using a Welas 2100 aerosol particle sizer (APS Palas Instruments) and an Optical Particle Sizer (TSI – OPS 3330). After synthesis the particle size distributions can be characterized with other instruments. A Dynamic Light Scattering instrument (Malvern Instruments) was tested to measure particle size distribution after annealing. It was discovered that the instrument's setup and the lack of additional detectors in the unit was not capable of accurately measuring the particle size distribution, due to the polydisperse nature of the product. Measurements using a miniMOUDI cascade impactor provided us with an offline method to measure particle size distribution. Alternatively, scanning electron microscopy (SEM) measurements gave us an indication of the particle size distribution. These images indicate that the secondary particle size varied between 0.2 ~ 10 μm. These data were supplemented by tap density measurements (Quantachrome tap density analyzer) to characterize bulk density of the product.

2.4 Crystallographic Analysis - Powder Diffraction

X-ray powder diffraction is a common physical measurement to investigate and characterize the structure of the crystalline powders. In this research, X-ray powder diffraction was performed using a Rigaku Geigerflex D-MAX/A Diffractometer using Cu-Kα radiation. The instrument is equipped with a vertical goniometer and a scintillation counter. The following settings were used for data collection: power is 1.5 kW with 35 kV voltage and 35 mA current. Data was collected using MDI's Datascan software and processed using Jade 9 software. Typical scan step size is 0.04 ° (2θ) with 1 s dwell time for equilibration.

Cell refinement was performed using MDI's Jade software to identify the crystal phase and refine the cell parameters with whole pattern fitting (WPF) using the formula card of $LiNi_{1/3}Mn_{1/3}Co_{1/3}O_2$ as the reference structure. Alternatively Rietveld-refinement was applied to further characterize the results using the EXPGUI software package. To extract preliminary instrument parameters NIST's silicon standard was measured at the experimental conditions mentioned above.

2.5 Morphological Studies

Particle morphology was primarily examined with a scanning electron microscope (FEI Nova Nano SEM) that has Energy Dispersive X-Ray Spectroscopy (EDAX) capabilities. Typical working distance is 5 mm and the operating voltage is 10-15 kV for best results.

In the current research a Tunneling Electron Microscope (TEM Tecnai^{TM} G^2 Spirit) will be applied to examine primary particle characteristics and interior morphology.

2.5 Other Characterization Techniques

Specific surface area of the powders was measured by Brunauer-Emmett-Teller surface analyzer (BET, Quantachrome Autosorb-1 Series, Nova) using N_2 as the adsorbent. Thermogravimetric analysis (TGA – TA instruments) was used to characterize the decomposition properties of the precursor solutions. Inductively coupled plasma mass spectrometry and optical emission spectroscopy (ICP-MS / ICP-OES – Perkin Elmer) were used to verify the composition and the contamination profile of the precursor solutions and the annealed powders.

2.6 Battery Performance Evaluation

A Li-ion battery consists of an anode and a cathode separated by a conductive membrane separator. All the components in a Li-ion cell were soaked in electrolyte containing Li salts. In the current research, the powders were tested as cathode active materials in 2032-type coin cells vs. a lithium anode. To prepare the cathode laminate, a mixture of the annealed powder, polyvinylidene-fluoride (PVdF – KF Polymer, Japan), Super-P or Super C45 conductive carbon black (Timcal) were suspended in N-methyl-2-pyrrolidene (NMP – Sigma Aldrich) and then homogenized to form a slurry. A typical cathode film contained 80 wt % active material, 10 wt % carbon black and 10 wt % PVdF. The cathode slurry was coated on an Al foil using the doctor blade technique to form a thin, cathode film. By varying the thickness of the film various loading densities between 0.5 – 6 $mgcm^{-2}$ can be obtained. On average a loading density of 3-4 $mgcm^{-2}$ is a typical value for the tested cathode discs. Two further processing methods were tested. Initially, after casting the cathode films were dried overnight in mild vacuum, then

vacuum dried at 130 °C overnight and then cathode discs are punched. Later, this process was modified. First, following the casting a 40 °C temperature is applied with light vacuum drying for 1 hour, which is followed by a high temperature drying at 130 °C for greater than 2 hours in light vacuum. Equivalent performance was verified by comparing electrochemical performance of 5 films. No adhesion studies were performed and from an electrochemical perspective the cathode discs did not demonstrate better electrochemical performance when calendered. Therefore, typically non-calendered electrodes, or only mildly calendered (95 % of the original thickness) were tested. The films were used to prepare 13 mm diameter cathode discs and then tested in 2032 type coin cells.

The 2032 coin-type test batteries were assembled in a glove box filled with ultra high purity argon. The cells consist of the following components, in the order listed: cathode housing, cathode disc, electrolyte, separator, lithium anode, spacer, spring and anode housing with a gasket. A thin Li foil is typically used as an anode and a polypropylene membrane (Celgard 2500) is used as the separator. The electrolyte was either 1M $LiPF_6$ in ethylene carbonate/diethyl carbonate/dimethyl carbonate solution (EC:DEC:DMC = 1:1:1 by volume – MTI Corp.) or 1.2 M $LiPF_6$ in ethylene carbonate/ ethyl-methyl carbonate (EC:EMC = 3:7 by weight – Tomiyama High Purity Chemicals) for samples provided by Argonne National Laboratory. The electrochemical performance of the cells was tested using either MTI battery analyzers (MTI BST8-WA) or using a Gamry reference 600 potentiostat or an Arbin Instruments tester at various charge/discharge rates. Typically the following cycle and rate capability test protocols were applied for the battery testing, as detailed in Tables 1 and 2. The applied protocol will be

mentioned in the respective chapters. Battery testing was carried out at room temperature (22 °C) unless otherwise specified. Some batteries were tested at 55 °C in an environmental chamber.

	Cycle test protocol 1 (1C = 280 $mAhg^{-1}$)	Cycle test protocol 2 (1C=200 $mAhg^{-1}$)
Activation	1 cycle 2.0-4.8 V at C/10	1 cycle 2.0-4.8 V at C/10
Subsequent cycles	99 cycles 2.0-4.8 V at C/10	3 cycles 2.0-4.6 V at C/10 96 cycles 2.0-4.6 V at C/3

Table 1 Cycling test protocols used in this research.

	Rate capability test protocol 1 (1C=280$mAhg^{-1}$)	Rate capability test protocol 2 (1C=200$mAhg^{-1}$)
Activation	5 cycle 2.0-4.9 V at C/10 (28 mAg^{-1})	1 cycle 2.0-4.8 V at C/10 (20 mAg^{-1})
Subsequent cycles	5 cycles 2.0-4.9 V at C/5 (56 mAg^{-1}) 5 cycles 2.0-4.9 V at C/2 (140 mAg^{-1})	4 cycles 2.0-4.6 V at C/10 (20 mAg^{-1}) 10 cycles 2.0-4.6 V at C/5 (40 mAg^{-1})

5 cycles 2.0-4.9 V at C3/4 (210 mAg^{-1})	20 cycles 2.0-4.6 V at C/2 (100 mAg^{-1})
5 cycles 2.0-4.9 V at 1C (280 mAg^{-1})	40 cycles 2.0-4.6 V at 1C (200 mAg^{-1})
75 cycles 2.0-4.9 V at C/10 (28 mAg^{-1})	25 cycles 2.0-4.6 V at C/10 (20 mAg^{-1})

Table 2 Rate test protocols used in this research.

Part of the battery tests were validated at Argonne National Laboratory (ANL) throughout this research. The battery test results obtained at Washington University show consistency to the data acquired at ANL. Cycle and rate test protocol 1 were adopted from a previous collaboration with Dr. Vincent Battaglia at Lawrence Berkeley National Laboratory (LBNL), while protocol 2 was adopted from ANL. The application of protocol 2 showed certain advantages. By increasing the rate of cycle tests from C/10 to C/3 rate the electrochemical test better represents an intermediate usage, similar to what could be expected on a highway if applied in an EV and also significantly reduces battery testing time from 3 months to approximately 1 month. The rate test in protocol 2 has similar advantages. Also by cycling the material at elevated rates for more cycles one can evaluate if additional capacity fade effects can potentially arise in the material.

Cell testing and characterization typically required 1-3 months. Thus, new chemistries can be evaluated on a 3-month interval including material synthesis and characterization. Throughout this research we will build upon the knowledge obtained by Zhang during his research at

Washington University to further improve the layered chemistry and optimize its electrochemical performance [156].

The current research will focus on understanding the synthesis parameters that govern the physical and electrochemical properties of the material. To this end the flow rate, the precursor concentration and the aerosol flow reactor's temperature will be studied, as these key parameters define the physical properties and crystallography of the product synthesized in an aerosol based process. Lower synthesis temperatures or insufficient residence time at a given temperature leads to necking between the particles, which will lower the bulk (tap) density of the material. Complete decomposition at a temperature will lead to isolated spheres and thus increase the tap density of the material. Rapid precipitation throughout the drying phase can lead to hollow spheres and large primary particles, which are typically undesired for a good cycle and rate capability. The primary particle size needs to be accurately controlled during the aerosol synthesis and the annealing to lead to an optimal primary particle size that delivers good capacities with a desirably low surface area to avoid side reactions has. Additionally, as it will be demonstrated in the current work, spray pyrolysis uniquely allows the control of the composition to the trace level. As it is discussed in later chapters this permits accurate control of the material's composition, which is unlikely to be reproduced by any other synthesis technique, thus allowing further stabilization of the layered or any similar chemistry.

The author of this thesis was responsible for the first-hand performance of the vast majority of the synthesis work and electrochemical testing experiments described in this thesis. Experimental

assistance from Gal Atlas, Dror Elhassid and Kuan-Yu Shen as well as from undergraduate students spending summer internships contributing to the research with minor tasks is gratefully acknowledged per the co-authorship of the respective papers. The thesis and the resulting papers were written by the author with helpful revisions provided by Dr. Richard Axelbaum and Dr. Xiaofeng Zhang. Helpful discussions by Dr. Ilias Belharouak provided additional insights to the battery field.

Chapter 3

Composition Optimization of Layered Lithium Nickel Manganese Cobalt Oxide Materials Synthesized Via Ultrasonic Spray Pyrolysis

3.1 Introduction

Due to their high theoretical and practical energy density, lithium-ion batteries are attractive power sources for consumer electronic applications, Plug-in Hybrid Electric Vehicles (PHEVs) and Electric Vehicles (EVs). To allow for practical implementation, the cathode materials need to display high capacity (capacities greater than 200 $mAhg^{-1}$), good rate capability and capacity retention over cycling, and excellent safety characteristics. EV and PHEV applications require inexpensive cathode materials synthesized by scalable, rapid and reproducible methods. The Mn and Ni based layered materials are relatively inexpensive and display improved safety characteristics compared to their Co-based counterparts. Significant research has been performed to improve the capacity and the safety of these cathode materials by adopting a layered-layered composite structure [13, 84, 86, 106, 112, 212, 213]. The composite materials are considered to be an integrated mixture of Li_2MnO_3 and $LiMO_2$ (where M=Mn, Ni, Co), forming a rock-salt-type α-$NaFeO_2$ structure. The Li_2MnO_3 component was originally integrated into the material to improve the cycling stability of the $LiMO_2$ component [86, 214]. Later it was discovered that the

Li_2MnO_3 component can be electrochemically activated by charging to 4.6 V vs. Li/Li^+ yielding a high total theoretical capacity (240-280 $mAhg^{-1}$ between 2.0-4.8 V) thus making the material an attractive candidate for PHEV applications [88, 215]. Due to their high capacities (>200 $mAhg^{-1}$), good cycling stability and inexpensive raw materials, much work has been done to analyze the lithium-rich layered-layered materials and understand the activation of Li_2MnO_3 [90, 92, 93, 94, 216]. During the initial charging, the Li_2MnO_3 component of the material undergoes activation, coupled to oxygen release, which causes a net loss of "Li_2O" from the structure. The resulting structural component only allows the reinsertion of a single lithium ion per transition metal, thereby causing a large, irreversible first cycle capacity loss [85, 217].

Several synthesis techniques have been evaluated for layered composite materials, including sol-gel methods, solid state processes, co-precipitation synthesis, combustion synthesis and ball milling [102, 103]. While the methods are promising they have challenges associated with purity, uniformity and reproducibility for commercial scale production.

Aerosol based synthesis methods offer a promising alternative. Compared to co-precipitation, spray pyrolysis delivers high-purity nanostructured materials in a rapid, simple and scalable process. The nanostructured morphology allows for fast lithium-ion diffusion and increases the rate capability of the composite materials [11, 101, 218, 219]. While controlling the primary particle size accurately is beneficial for improving the rate capability, it is important to maintain secondary particle sizes above 1 μm, to minimize particle agglomeration that arises from van der Waals interactions [220]. Together, this allows for high power densities and high volumetric energy densities [221]. Aerosol processes typically allow accurate control of both the primary and secondary particle size with the application of appropriate aerosolizing equipment and annealing

conditions [174, 222]. Spray pyrolysis has another significant advantage: since the formation of particles occurs from the pyrolysis of individual precursor droplets, the chemical composition can be controlled accurately, which results in excellent particle-to-particle and batch-to-batch reproducibility [172, 180].

Aerosol based synthesis methods have been widely reported for producing lithium ion battery anode and cathode materials. A few examples include layered $LiNi_{1/3}Mn_{1/3}Co_{1/3}O_2$, spinel $LiMn_2O_4$, $LiFePO_4$, $LiAl_{0.05}Mn_{1.95}O_4$ and similar materials, such as Co_3O_4 [58, 61, 179, 223, 224, 225, 226, 227]. Waser et al reported a flame-assisted synthesis for producing $LiFePO_4$ materials [228]. Recently, Kang and coworkers obtained promising results using aerosol-based synthesis methods for producing a number of nanostructured layered cathode materials and similar chemistries including composites of Li_2MnO_3 and $LiMO_2$, $Li_4Ti_5O_{12}$, Co_3O_4 [115, 200, 201, 229, 230, 231, 232, 233, 234, 235, 236, 237, 238]. A recent study by Oljaca *et al.* from Cabot Corp. compared the electrochemical performance of $LiNi_{1/3}Mn_{1/3}Co_{1/3}O_2$ synthesized via spray pyrolysis and co-precipitation demonstrating advantages for materials synthesized via spray pyrolysis [203].

Earlier a spray pyrolysis synthesis method was developed by this group for producing high-energy, layered cathode materials of $Li_{(1+y)}Ni_{0.25}Mn_{0.75}O_{(2.25+y/2)}$ materials with excellent electrochemical performance [239, 240, 241, 242]. To improve the capacity retention and rate capability of these materials the effect of cobalt doping was evaluated on $Li_{1.2}Mn_{0.54}Ni_{0.13}Co_{0.13}O_2$ synthesized both with a Collison-type jet atomizer and a 2.4 MHz ultrasonic nebulizer [243]. Cobalt addition improved the capacity retention and the cycling performance of the materials as the cobalt-containing material had a discharge capacity of 238 $mAhg^{-1}$ at cycle 50, when cycled between 2.0-4.8 V vs. Li at C/10 rate (where 1C= 280 $mAhg^{-1}$) while the cobalt-free material

displayed 220 $mAhg^{-1}$ discharge capacity at cycle 50 when cycled between 2.0-4.8 V vs. Li at C/10 rate (where 1C= 230 $mAhg^{-1}$). Increasing the secondary particle size of the powders from below 1 μm to a mean particle size of 1.7 μm improved the stability and capacity retention of the product [243].

The purpose of the current study is to evaluate the effect of the composition of layered lithium nickel manganese cobalt oxides when produced by ultrasonic spray pyrolysis. Three chemistries ($Li_{1.14}Mn_{0.46}Ni_{0.2}Co_{0.2}O_2$, $Li_{1.2}Mn_{0.54}Ni_{0.13}Co_{0.13}O_2$ and $Li_{1.26}Mn_{0.6}Ni_{0.07}Co_{0.07}O_2$) are studied and their electrochemical properties evaluated.

3.2. Experimental

The spray pyrolysis process incorporates a tubular aerosol flow reactor to produce Li-rich composite materials. The precursor solutions were prepared by dissolving $LiNO_3$, $Mn(NO_3)_2{\cdot}4H_2O$, $Ni(NO_3)_2{\cdot}6H_2O$ and $Co(NO_3)_2{\cdot}6H_2O$ (Alfa Aesar) in the desired ratios in deionized water. The precursor solution was aerosolized using a 2.4 MHz ultrasonic nebulizer (Sonaer Inc.). The dry particles had a mean particle size of 1.7 μm as measured using an electrical low-pressure impactor (ELPI Dekati) [243]. Water-saturated compressed air was used as the carrier gas at a constant flow rate of 6.6 liters per minute (lpm). The aerosol gas stream was carried into a 22 inch long preheater, which was kept at 200 °C (wall temperature), followed by a vertical furnace reactor that was kept at 450 °C. The residence time in the system was 6 seconds. The decomposed powders were collected downstream of the reactor using porous polycarbonate membrane filters (Whatman, GE). Details of the method and the system are reported elsewhere [239, 243]. The as-synthesized powders were annealed for 2 hours either at 850 °C or 900 °C.

The annealed powders were characterized by X-ray powder diffraction (XRD) using a Rigaku Diffractometer (Geigerflex D-MAX/A) at a scan rate of 0.04 $°s^{-1}$. The primary particle size was estimated from SEM-images. Structural refinement was accomplished using the whole pattern fitting (WPF) method with Jade software. The formula card of $LiNi_{1/3}Mn_{1/3}Co_{1/3}O_2$ was used as the reference structure for the refinement. Rietveld-refinement was performed using the EXPGUI software package.

The particle morphology was examined with an FEI Nova 2300 Field Emission scanning electron microscope. The elemental analysis of the precursor solutions and the annealed powders was obtained by inductively-coupled-plasma mass spectrometry (Perkin Elmer Elan DRC II ICP-MS). In order to analyze the oxide samples by ICP-MS, the samples were dissolved in a mixture of concentrated HNO_3 and 30% high-purity H_2O_2. Brunauer-Emmett-Teller (BET) surface area measurements were conducted to characterize the specific surface area of the samples (Autosorb-1, Quantachrome Instruments).

Cathode film fabrication was performed according to the procedure reported earlier [239]. The cathode slurry was prepared using polyvinylidene fluoride (PVdF) binder solution (Kureha Corp. Japan) and Super-P conductive carbon black (Timcal) suspended in 1-methyl-2-pyrrolidinone (NMP). 2500 Celgard membranes (Celgard LLC) were used to separate the cathode discs and the pure lithium anode. Two electrolytes were studied: 1 M $LiPF_6$ in ethylene carbonate/diethyl carbonate/dimethyl carbonate solution (EC:DEC:DMC = 1:1:1 by volume) (MTI Corp.) and 1.2 M $LiPF_6$ in ethylene carbonate/ethyl-methyl-carbonate solution (EC:EMC = 3:7 by weight) (Tomiyama High Purity Chemicals).

The powders were tested in 2032-type coin cells (Hohsen Corporation) assembled in an argon-filled glove box. Cycling tests were performed between 2.0-4.8 V at C/10 rate (28 mAg^{-1}) unless otherwise indicated. Rate capability tests were performed between 2.0-4.9 V at C/10, C/5, C/2, C3/4, 1C and C/10 rates. Both cycling and rate capability tests were conducted using an MTI-BST8-WA-type battery tester. All electrochemical tests were performed at room temperature, 22 °C.

3.3 Physical and crystal properties

Table 3 shows that the measured stoichiometry of the precursor solution and the annealed powders, as determined by ICP-MS, match the target values closely. No detectable evaporative loss of lithium occurred during the annealing heat treatment.

Target Stoichiometry	Precursor stoichiometry as measured by ICP-MS	Annealed powder stoichiometry as measured by ICP-MS
$Li_{1.130}Mn_{0.464}Ni_{0.203}Co_{0.203}O_2$	$Li_{1.148}Mn_{0.451}Ni_{0.210}Co_{0.209}O_2$	$Li_{1.141}Mn_{0.457}Ni_{0.207}Co_{0.206}O_2$
$Li_{1.200}Mn_{0.533}Ni_{0.133}Co_{0.133}O_2$	$Li_{1.223}Mn_{0.531}Ni_{0.134}Co_{0.135}O_2$	$Li_{1.160}Mn_{0.532}Ni_{0.133}Co_{0.135}O_2$
$Li_{1.259}Mn_{0.593}Ni_{0.074}Co_{0.074}O_2$	$Li_{1.288}Mn_{0.588}Ni_{0.076}Co_{0.077}O_2$	$Li_{1.310}Mn_{0.589}Ni_{0.076}Co_{0.076}O_2$

Table 3 ICP-MS analysis of the precursor solutions for $Li_{1.14}Mn_{0.46}Ni_{0.2}Co_{0.2}O_2$, $Li_{1.2}Mn_{0.54}Ni_{0.13}Co_{0.13}O_2$, $Li_{1.26}Mn_{0.6}Ni_{0.07}Co_{0.07}O_2$ and their respective annealed powders.

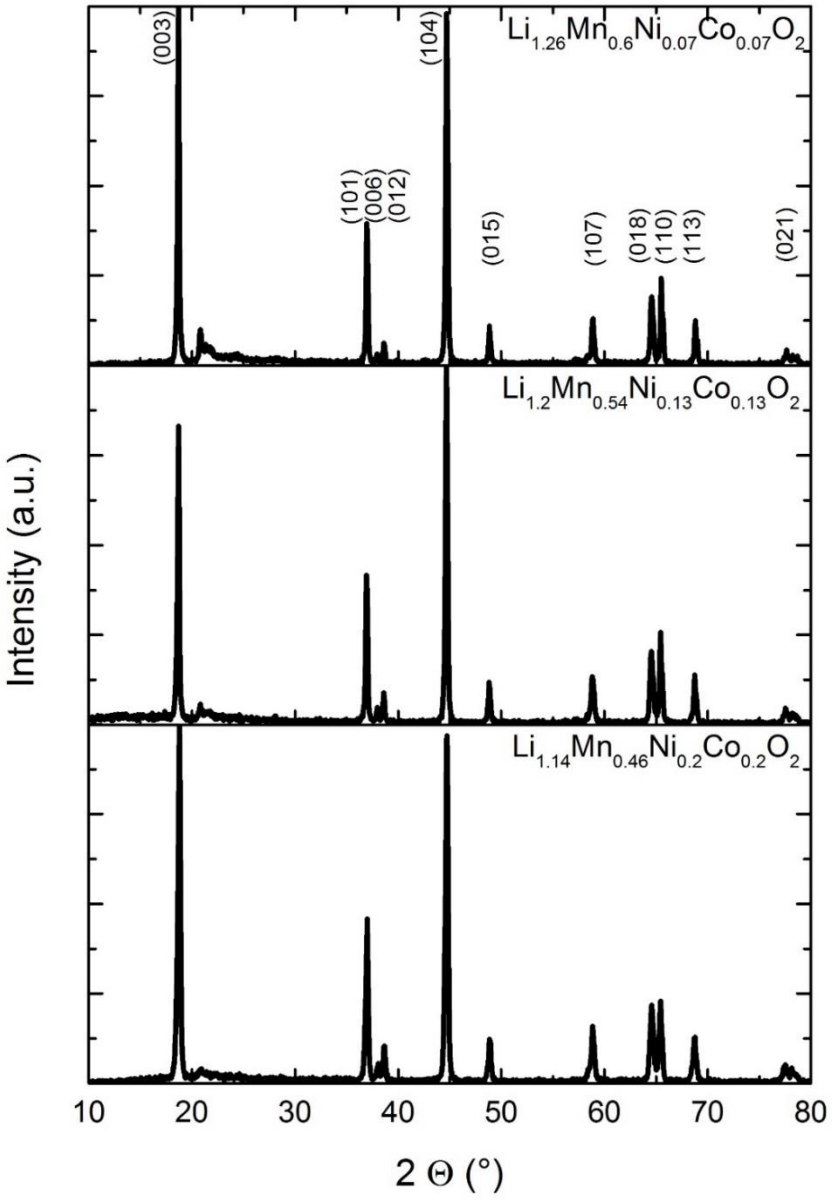

Figure 10 XRD patterns of $Li_{1.14}Mn_{0.46}Ni_{0.2}Co_{0.2}O_2$, $Li_{1.2}Mn_{0.54}Ni_{0.13}Co_{0.13}O_2$ and $Li_{1.26}Mn_{0.6}Ni_{0.07}Co_{0.07}O_2$. The arrows indicate the broad peak between 20- 25° 2Θ due to the ordering between the structural components.

Figure 10 compares the XRD patterns of $Li_{1.14}Mn_{0.46}Ni_{0.2}Co_{0.2}O_2$, $Li_{1.2}Mn_{0.54}Ni_{0.13}Co_{0.13}O_2$ and $Li_{1.26}Mn_{0.6}Ni_{0.07}Co_{0.07}O_2$ after annealing at 900 °C for 2 hours. No impurity phases can be

observed in the patterns and the results are comparable to those obtained when the materials were prepared by co-precipitation or molten salt synthesis [102, 103, 153, 244]. The XRD patterns for $Li_{1.14}Mn_{0.46}Ni_{0.2}Co_{0.2}O_2$, $Li_{1.2}Mn_{0.54}Ni_{0.13}Co_{0.13}O_2$ and $Li_{1.26}Mn_{0.6}Ni_{0.07}Co_{0.07}O_2$ display a broad peak between 20-25° 2 θ, due to the existence of integrated Li_2MnO_3-type domains in the structure [239]. The peak becomes more intense with increased Li_2MnO_3 content in the materials, as indicated by the arrows. The clear splitting of the (006), (012) and (018), (110) peaks is indicative of the layered structure of the materials [113]. The XRD patterns of the powders annealed at 850 °C show nearly identical features and therefore are not displayed.

Rietveld refinement was performed on $Li_{1.14}Mn_{0.46}Ni_{0.2}Co_{0.2}O_2$, $Li_{1.2}Mn_{0.54}Ni_{0.13}Co_{0.13}O_2$ and $Li_{1.26}Mn_{0.6}Ni_{0.07}Co_{0.07}O_2$. The structures were modeled as a mixture of Li_2MnO_3 and $LiNi_{1/3}Mn_{1/3}Co_{1/3}O_2$, in 3:7, 5:5 and 7:3 molar ratios, respectively [245, 246, 247] and the reliability factors validate the assumed structural model. Table 4 shows the atomic positions and unit cell parameters following the structural refinement. Comparing the three materials annealed at 850 °C and 900 °C, the $Li_{1.2}Mn_{0.54}Ni_{0.13}Co_{0.13}O_2$ material shows almost identical atomic positions and cell parameters at both temperatures, whereas minor differences can be observed at the two temperatures for both $Li_{1.14}Mn_{0.46}Ni_{0.2}Co_{0.2}O_2$ and $Li_{1.26}Mn_{0.6}Ni_{0.07}Co_{0.07}O_2$. The unit cell parameters do not change significantly, which makes them consistent with the composite structure assumption.

$Li_{1.14}Mn_{0.46}Ni_{0.2}Co_{0.2}O_2$

Phase I: Li_2MnO_3 (*C2/m*)					
Element	Site		Fractional coordinate (850 °C/900 °C)		Occup. (850 °C/900 °C)
Li1	2b	0/ 0	0.5/ 0.5	0/ 0	0.8540/ 0.8540
Mn1	2b	0/ 0	0.5/ 0.5	0/ 0	0.1460/ 0.1460
Li2	2c	0/ 0	0/ 0	0.5/ 0.5	1.0/ 1.0
Li3	4h	0/ 0	0.6700/ 0.6641	0.5/ 0.5	0.9860/ 0.9860
Mn2	4h	0/ 0	0.8595/ 0.4466	0.5/ 0.5	0.0140/ 0.140
Li4	4g	0	0.6648/ 0.1687	0/ 0	0.0870/ 0.0870
Mn3	4g	0	0.1867/ 0.1642	0/ 0	0.9130/ 0.9130
O1	4i	0.1495/ 0.3112	0/ 0	0.1939/ 0.2229	1/ 1
O2	8j	0.1732/ 0.3036	0.3321/ 03298	0.2424/ 0.2433	1/ 1
a (850 °C/900 °C)	4.957 Å/ 4.922 Å				
b (850 °C/900 °C)	8.519 Å/ 8.626 Å				
c (850 °C/900 °C)	5.014 Å/ 5.071 Å				
β (850 °C/900 °C)	108.90°/ 109.43°				
Phase II: $LiNi_{1/3}Mn_{1/3}Co_{1/3}O_3$ ($R\bar{3}m$)					
Element	Site		Fractional coordinate		Occup.
Li1	3b	0/ 0	0/ 0	0/ 0	0.9700/ 0.9700
Ni1	3b	0/ 0	0/ 0	0/ 0	0.0300/ 0.0300
Li2	3a	0/ 0	0/ 0	0.5/ 0.5	0.0300/ 0.0300
Ni2	3a	0/ 0	0/ 0	0.5/ 0.5	0.3050/ 0.3050
Mn1	3a	0/ 0	0/ 0	0.5/ 0.5	0.3350/ 0.3350
Co1	3a	0/ 0	0/ 0	0.5/ 0.5	0.3300/ 0.3300
O1	6c	0/ 0	0/ 0	0.2408/ 0.2432	1.0/ 1.0
a (850 °C/900 °C)	2.852 Å/ 2.856 Å				
c (850 °C/900 °C)	14.223 Å/ 14.236 Å				
wRp (850 °C/900 °C)	0.1902/ 0.2091		*Rp* (850 °C/900 °C)	0.1346/ 0.1535	
Chi^2 (850 °C/900 °C)	1.552/ 1.617		Phase ratio	3:7	

$Li_{1.2}Mn_{0.54}Ni_{0.13}Co_{0.13}O_2$

Phase I: Li_2MnO_3 (*C2/m*)					
Element	Site		Fractional coordinate (850 °C/900 °C)	Occup. (850 °C/900 °C)	
Li1	2b	0/ 0	0.5/ 0.5	0/ 0	0.8540/ 0.8540
Mn1	2b	0/ 0	0.5/ 0.5	0/ 0	0.1460/ 0.1460
Li2	2c	0/ 0	0/ 0	0.5/ 0.5	1.0/ 1.0
Li3	4h	0/ 0	0.7191/ 0.6810	0.5/ 0.5	0.9860/ 0.9860
Mn2	4h	0/ 0	0.6810/ 0.8310	0.5/ 0.5	0.0140/ 0.140
Li4	4g	0	0.1687/ 0.1687	0/ 0	0.0870/ 0.0870
Mn3	4g	0	0.1767/ 0.1708	0/ 0	0.9130/ 0.9130
O1	4i	0.2731/ 0.2663	0/ 0	0.1939/ 0.2105	1/ 1
O2	8j	0.2719/ 0.2690	0.3342/ 03298	0.2439/ 0.2370	1/ 1
a (850 °C/900 °C)	4.949 Å/ 4.947 Å				
b (850 °C/900 °C)	8.526 Å/ 8.529 Å				
c (850 °C/900 °C)	5.010 Å/ 5.009 Å				
β (850 °C/900 °C)	108.91°/ 108.94°				
Phase II: $LiNi_{1/3}Mn_{1/3}Co_{1/3}O_3$ ($R\bar{3}m$)					
Element	Site		Fractional coordinate	Occup.	
Li1	3b	0/ 0	0/ 0	0/ 0	0.9700/ 0.9700
Ni1	3b	0/ 0	0/ 0	0/ 0	0.0300/ 0.0300
Li2	3a	0/ 0	0/ 0	0.5/ 0.5	0.0300/ 0.0300
Ni2	3a	0/ 0	0/ 0	0.5/ 0.5	0.3050/ 0.3050
Mn1	3a	0/ 0	0/ 0	0.5/ 0.5	0.3350/ 0.3350
Co1	3a	0/ 0	0/ 0	0.5/ 0.5	0.3300/ 0.3300
O1	6c	0/ 0	0/ 0	0.2427/ 0.2415	1.0/ 1.0
a (850 °C/900 °C)	2.851 Å/ 2.850 Å				
c (850 °C/900 °C)	14.218 Å/ 14.216Å				
wRp (850 °C/900 °C)	0.2040/ 0.2152		*Rp* (850 °C/900 °C)	0.1393/ 0.1482	
Chi^2 (850 °C/900 °C)	1.602/ 1.833		Phase ratio	5:5	

$Li_{1.26}Mn_{0.6}Ni_{0.07}Co_{0.07}O_2$

Phase I: Li_2MnO_3 (*C2/m*)					
Element	Site		Fractional coordinate (850 °C/900 °C)		Occup. (850 °C/900 °C)
Li1	2b	0/ 0	0.5/ 0.5	0/ 0	0.8540/ 0.8540
Mn1	2b	0/ 0	0.5/ 0.5	0/ 0	0.1460/ 0.1460
Li2	2c	0/ 0	0/ 0	0.5/ 0.5	1.0/ 1.0
Li3	4h	0/ 0	0.7385/ 0.6810	0.5/ 0.5	0.9860/ 0.9860
Mn2	4h	0/ 0	0.7863/ 0.1520	0.5/ 0.5	0.0140/ 0.140
Li4	4g	0	0.1687/ 0.1687	0/ 0	0.0870/ 0.0870
Mn3	4g	0	0.1749/ 0.1831	0/ 0	0.9130/ 0.9130
O1	4i	0.2182/ 0.2663	0/ 0	0.2216/ 0.2105	1/ 1
O2	8j	0.2422/ 0.2363	0.3209/ 03211	0.2481/ 0.2479	1/ 1
a (850 °C/900 °C)	4.950 Å/ 4.945 Å				
b (850 °C/900 °C)	8.493 Å/ 8.506 Å				
c (850 °C/900 °C)	5.007 Å/ 5.016 Å				
β (850 °C/900 °C)	108.84°/ 108.87°				
Phase II: $LiNi_{1/3}Mn_{1/3}Co_{1/3}O_3$ ($R\bar{3}m$)					
Element	Site		Fractional coordinate		Occup.
Li1	3b	0/ 0	0/ 0	0/ 0	0.9700/ 0.9700
Ni1	3b	0/ 0	0/ 0	0/ 0	0.0300/ 0.0300
Li2	3a	0/ 0	0/ 0	0.5/ 0.5	0.0300/ 0.0300
Ni2	3a	0/ 0	0/ 0	0.5/ 0.5	0.3050/ 0.3050
Mn1	3a	0/ 0	0/ 0	0.5/ 0.5	0.3350/ 0.3350
Co1	3a	0/ 0	0/ 0	0.5/ 0.5	0.3300/ 0.3300
O1	6c	0/ 0	0/ 0	0.2430/ 0.2428	1.0/ 1.0
a (850 °C/900 °C)	2.845 Å/ 2.846 Å				
c (850 °C/900 °C)	14.215 Å/ 14.221Å				
wRp (850 °C/900 °C)	0.2197/ 0.2377		*Rp* (850 °C/900 °C)	0.1558/ 0.1693	
Chi^2 (850 °C/900 °C)	1.761/ 1.919		Phase ratio	7:3	

Table 4 Result of the two-phase Rietveld-refinement assuming a phase ratio of 3:7, 5:5 and 7:3 between Li_2MnO_3 and $LiNi_{1/3}Mn_{1/3}Co_{1/3}O_2$ for $Li_{1.14}Mn_{0.46}Ni_{0.2}Co_{0.2}O_2$, $Li_{1.2}Mn_{0.54}Ni_{0.13}Co_{0.13}O_2$, $Li_{1.26}Mn_{0.6}Ni_{0.07}Co_{0.07}O_2$, respectively.

Figure 11 shows the SEM micrographs of the powders after annealing at 900 °C for 2 hours. The secondary particles are spherical in shape and consist of nano-sized primary grains, forming a porous morphology. The primary particle size varies between 120-300 nm after annealing at 900 °C for 2 hours. The mean secondary particle size of the powder is approximately 1.7 μm, as measured by ELPI [239, 243]. The secondary particle size is largely defined by the particle

generation method. Compared to materials synthesized with the Collison-nebulizer the ultrasonic powder generation allowed an increase in both the production rate and the particle size [242]. SEM micrographs of the powders after annealing at 850 °C show similar features and therefore are not displayed.

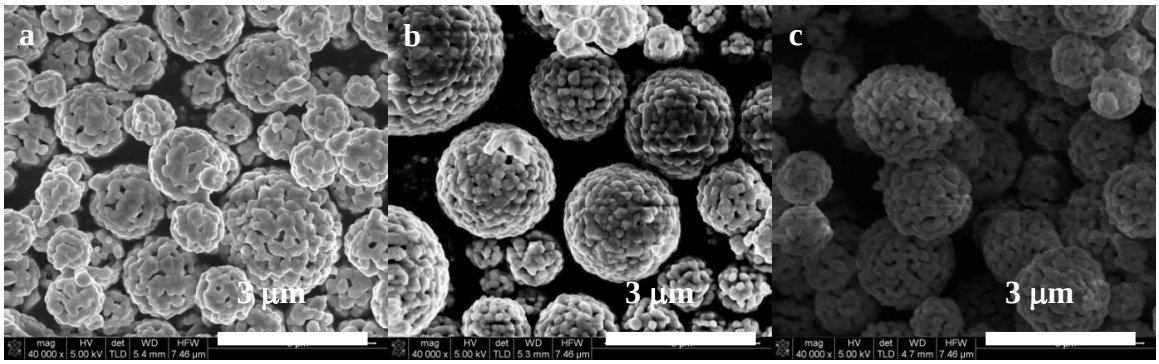

Figure 11 SEM micrographs of powders after annealing at 900 °C for 2 hours: (a) $Li_{1.14}Mn_{0.46}Ni_{0.2}Co_{0.2}O_2$; (b) $Li_{1.2}Mn_{0.54}Ni_{0.13}Co_{0.13}O_2$; and (c) $Li_{1.26}Mn_{0.6}Ni_{0.07}Co_{0.07}O_2$.

Table 5 shows the average primary particle size of the annealed powders estimated by the SEM-images. The primary particle sizes were estimated by measuring the longest axis of 100 primary particles and averaging them [248]. Increasing the annealing temperature from 850 °C to 900 °C promotes crystal growth and coarsening, and consistently increases the primary grain size of the powders as observed in the SEM images. The primary particle size of $Li_{1.2}Mn_{0.54}Ni_{0.13}Co_{0.13}O_2$ is smaller than that of $Li_{1.14}Mn_{0.46}Ni_{0.2}Co_{0.2}O_2$ or $Li_{1.26}Mn_{0.6}Ni_{0.07}Co_{0.07}O_2$. A possible explanation is as follows: $Li_{1.14}Mn_{0.46}Ni_{0.2}Co_{0.2}O_2$, has a larger content of $LiMn_{1/3}Ni_{1/3}Co_{1/3}O_2$, which as a single component crystallizes in a trigonal $R\bar{3}m$ structure; therefore the preferential growth of layered $LiMn_{1/3}Ni_{1/3}Co_{1/3}O_2$ increases the primary particle size. Similarly, $Li_{1.26}Mn_{0.6}Ni_{0.07}Co_{0.07}O_2$ contains more layered Li_2MnO_3, which as a single material crystallizes in a *C2/m* structure, and thus the preferential growth leads to an increase in the primary particle

size. There is no preferential phase growth in $Li_{1.2}Mn_{0.54}Ni_{0.13}Co_{0.13}O_2$ (x = 0.5), and this minimizes the primary particle size. A similar behavior was reported earlier for Pb-based perovskite structures [249].

	Primary particle size (nm)	
Annealing temperature	850 °C	900 °C
$Li_{1.14}Mn_{0.46}Ni_{0.2}Co_{0.2}O_2$	150	190
$Li_{1.2}Mn_{0.54}Ni_{0.13}Co_{0.13}O_2$	130	165
$Li_{1.26}Mn_{0.6}Ni_{0.07}Co_{0.07}O_2$	160	175

Table 5 Estimated primary particle sizes based on SEM-images.

The BET surface area measurements, shown in Table 6, confirm that the surface area of the powders is consistently reduced when the annealing temperature is increased from 850 °C to 900 °C, with the most significant coarsening occurring for $Li_{1.2}Mn_{0.54}Ni_{0.13}Co_{0.13}O_2$. Table 6 also shows that the increased lithium and manganese content of $Li_{1.2}Mn_{0.54}Ni_{0.13}Co_{0.13}O_2$ and $Li_{1.26}Mn_{0.6}Ni_{0.07}Co_{0.07}O_2$ promotes the coarsening compared to that observed for $Li_{1.14}Mn_{0.46}Ni_{0.2}Co_{0.2}O_2$. This is consistent with earlier reports for similar chemistries [239, 242]. Although all materials have relatively high surface area and display phase-pure layered structures at both annealing temperatures, it is expected that structural rearrangement and the reduction in surface area at higher temperature will improve the capacity retention of these materials.

Composition	BET 850 °C (m^2g^{-1})	BET 900 °C (m^2g^{-1})	% reduction
$Li_{1.14}Mn_{0.46}Ni_{0.2}Co_{0.2}O_2$	7.33	6.45	12
$Li_{1.2}Mn_{0.54}Ni_{0.13}Co_{0.13}O_2$	9.35	6.40	32
$Li_{1.26}Mn_{0.6}Ni_{0.07}Co_{0.07}O_2$	12.23	6.45	47

Table 6 BET surface area of $Li_{1.14}Mn_{0.46}Ni_{0.2}Co_{0.2}O_2$, $Li_{1.2}Mn_{0.54}Ni_{0.13}Co_{0.13}O_2$ and $Li_{1.26}Mn_{0.6}Ni_{0.07}Co_{0.07}O_2$ annealed at 850 °C and 900 °C for 2 hours.

3.4 Electrochemical testing results

Earlier we reported the synthesis of $Li_{1.2}Mn_{0.54}Ni_{0.13}Co_{0.13}O_2$ via spray pyrolysis and compared materials performance when synthesized with a Collison-nebulizer and ultrasonic nebulizer [243]. For this material, optimal electrochemical properties were obtained at an annealing temperature of 900 °C for 2 hours. The secondary particle size was increased when the materials were synthesized with an ultrasonic nebulizer, which was found to improve the capacity retention of the materials. Since $Li_{1.14}Mn_{0.46}Ni_{0.2}Co_{0.2}O_2$, $Li_{1.2}Mn_{0.54}Ni_{0.13}Co_{0.13}O_2$ and $Li_{1.26}Mn_{0.6}Ni_{0.07}Co_{0.07}O_2$ have different compositions and coarsen differently, the effect of annealing temperature was studied and the materials were annealed for either 850 °C or 900 °C for 2 hours. The electrochemical properties of the six cathode materials were tested in 2032 type coin cells vs. Li anodes.

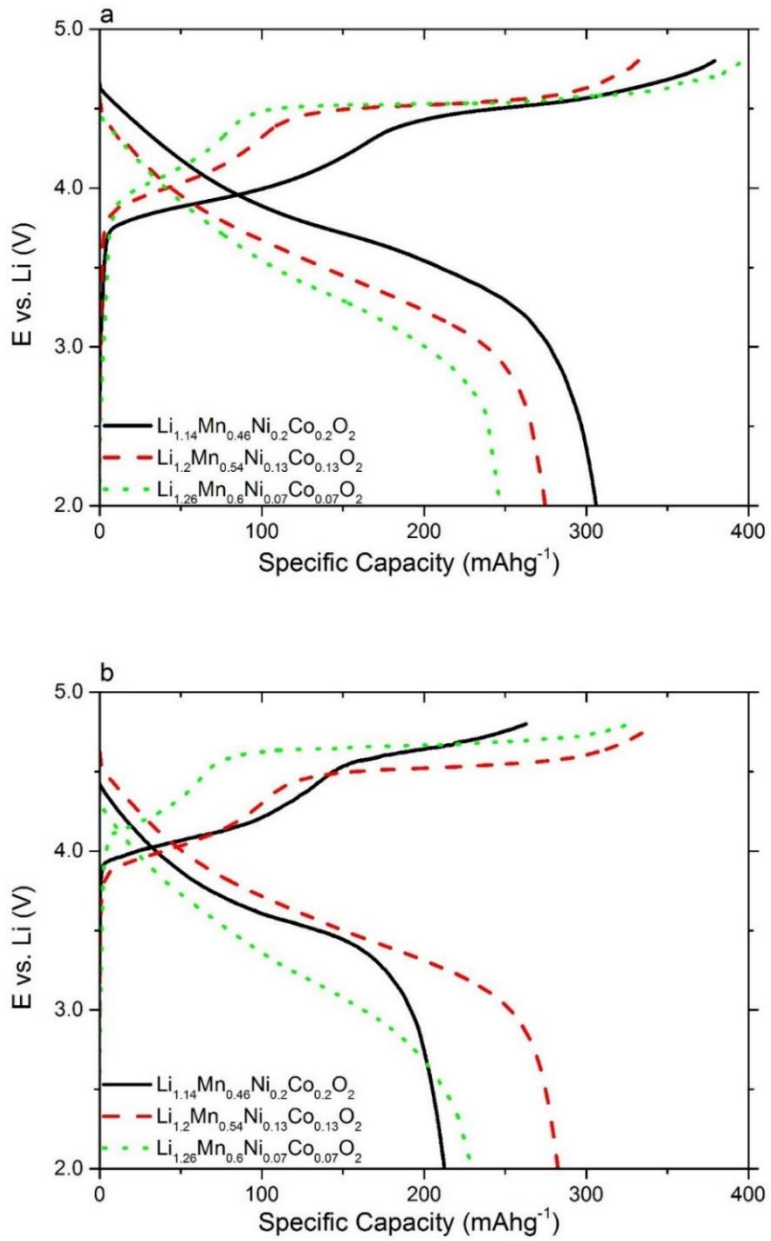

Figure 12 Initial charge and discharge profiles at a constant current density of 28 mAg-1 between 2.0 and 4.8 V: $Li_{1.14}Mn_{0.46}Ni_{0.2}Co_{0.2}O_2$, $Li_{1.2}Mn_{0.54}Ni_{0.13}Co_{0.13}O_2$ and $Li_{1.26}Mn_{0.6}Ni_{0.07}Co_{0.07}O_2$ after annealing at (a) 850 °C and (b) 900 °C.

Figure 12 shows the initial charge and discharge profiles of the six materials, when charged at a constant current density of 28 mAg^{-1} between 2.0 - 4.8 V (1C = 280 mAg^{-1}). A constant-current, constant-voltage cycling protocol was applied for the cells [113, 243]. All of the materials display a two-staged charge profile: the first plateau between 3.5 V and 4.4 V is associated with the Ni^{2+}/Ni^{4+} and the Co^{3+}/Co^{4+} redox couples, while the second plateau above is associated with the activation of the Li_2MnO_3-domains in the material [94]. The $Li_{1.14}Mn_{0.46}Ni_{0.2}Co_{0.2}O_2$, $Li_{1.2}Mn_{0.54}Ni_{0.13}Co_{0.13}O_2$ and $Li_{1.26}Mn_{0.6}Ni_{0.07}Co_{0.07}O_2$ materials annealed at 850 °C display initial charge capacities in reasonable agreement with their theoretical capacities (Table 7).

Material Composition	Theoretical initial charge capacity ($mAhg^{-1}$)	Initial charge capacity at 850 °C ($mAhg^{-1}$)	Initial charge capacity at 900 °C ($mAhg^{-1}$)
$Li_{1.14}Mn_{0.46}Ni_{0.2}Co_{0.2}O_2$	331	379	262
$Li_{1.2}Mn_{0.54}Ni_{0.13}Co_{0.13}O_2$	367	339	341
$Li_{1.26}Mn_{0.6}Ni_{0.07}Co_{0.07}O_2$	404	395	326

Table 7 - Theoretical and measured initial charge capacities of materials after annealing at 850 °C and 900 °C for 2 hours.

The initial charge capacity of $Li_{1.2}Mn_{0.54}Ni_{0.13}Co_{0.13}O_2$ is 339 $mAhg^{-1}$ and 341 $mAhg^{-1}$ after annealing at 850 °C and 900 °C, respectively. As noted from Table 5, the primary particle size of $Li_{1.2}Mn_{0.54}Ni_{0.13}Co_{0.13}O_2$ remains smaller than that of the other chemistries. The smaller primary particles may be responsible for allowing complete activation of the Li_2MnO_3 and $LiMn_{1/3}Ni_{1/3}Co_{1/3}O_2$ components of the materials at both 850 °C and 900 °C [250]. $Li_{1.14}Mn_{0.46}Ni_{0.2}Co_{0.2}O_2$ and $Li_{1.26}Mn_{0.6}Ni_{0.07}Co_{0.07}O_2$ display lower initial charge capacities after

annealing at 900 °C, which may be caused by the larger primary particle size [250, 251]. Figure 12b also shows that the second plateau during the first charge curve for these two chemistries becomes shorter, which indicates that increasing the primary particle size of Li_2MnO_3 beyond a certain size no longer allows complete activation, presumably due to the lower lithium ion diffusion coefficient of this component [76]. Ultimately this leads to a loss of capacity and a reduced rate capability at room temperature. However, based on results from co-precipitation the higher annealing temperature is expected to yield improved cycling stability [250, 251, 252, 253].

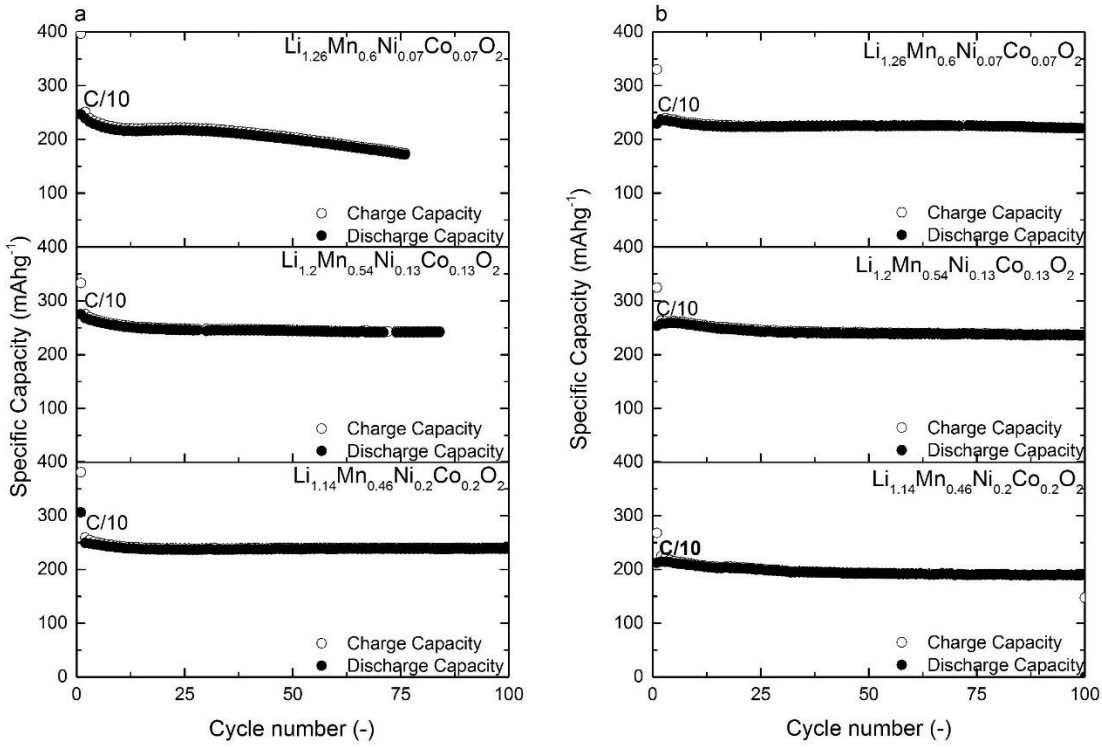

Figure 13 Cycling performance of $Li_{1.14}Mn_{0.46}Ni_{0.2}Co_{0.2}O_2$, $Li_{1.2}Mn_{0.54}Ni_{0.13}Co_{0.13}O_2$ and $Li_{1.26}Mn_{0.6}Ni_{0.07}Co_{0.07}O_2$ annealed at (a) 850 °C for 2 hours and (b) 900 °C for 2 hours.

The cycling performance of the materials was tested between 2.0-4.8 V at a C/10 rate, corresponding to a constant current density of 28 mAg^{-1}. Figures 13a and b compare the cycling performance of the materials annealed at 850 °C and 900 °C for 2 hours. The high-purity synthesis method combined with optimal annealing conditions leads to significant improvements in terms of capacity retention compared to results obtained for these chemistries when synthesized by other methods [102, 201, 244]. Cobalt doping allowed us to increase the annealing temperature, which in turn improves the capacity retention of the materials. Overall, the powders that were annealed at 900 °C display a better capacity retention compared to powders annealed at 850 °C, they are also better than those reported by Son *et al.* for similar compositions and

annealed at 800 °C for 5 hours [201, 238]. This is further supported by the observed efficiencies in Fig. 14.

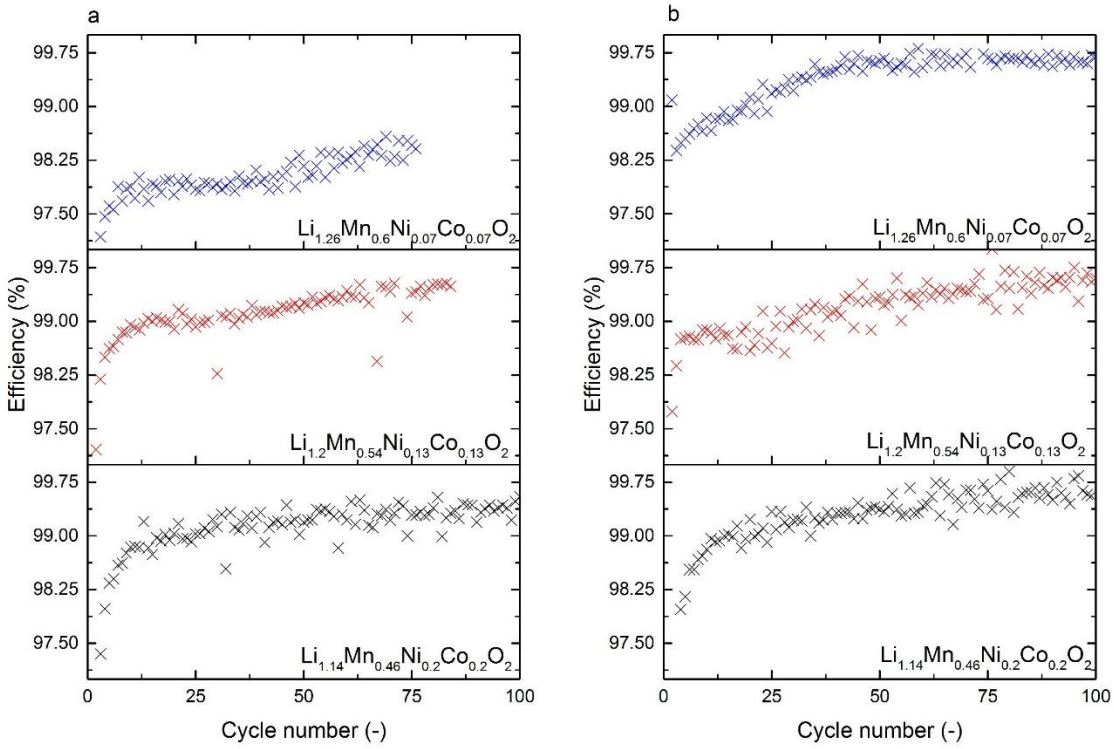

Figure 14 Coulombic efficiency of $Li_{1.14}Mn_{0.46}Ni_{0.2}Co_{0.2}O_2$, $Li_{1.2}Mn_{0.54}Ni_{0.13}Co_{0.13}O_2$ and $Li_{1.26}Mn_{0.6}Ni_{0.07}Co_{0.07}O_2$ annealed at (a) 850 °C for 2 hours and (b) 900 °C for 2 hours.

The higher annealing temperature has the greatest impact on the performance of the $Li_{1.26}Mn_{0.6}Ni_{0.07}Co_{0.07}O_2$ chemistry. Whereas rapid fading is observed in cells made from this material when annealed at 850 °C, with only 80.8% of the initial discharge capacity retained at cycle 50, the material annealed at 900 °C displays 95.4% capacity retention at cycle 50. This is speculated to be partially caused by the reduced activation of the Li_2MnO_3 component. The increased amount of residual lithium remaining in the interstitial sites of the sample promotes cycling stability and leads to less structural change. Similarly, $Li_{1.14}Mn_{0.46}Ni_{0.2}Co_{0.2}O_2$ shows

less capacity fade and higher efficiencies at 900 °C. However, when annealed at 850 °C, $Li_{1.14}Mn_{0.46}Ni_{0.2}Co_{0.2}O_2$ displays higher capacity, yielding 239 $mAhg^{-1}$ at cycle 50 as compared to 193 $mAhg^{-1}$ at 900 °C. No phase separation is observed in the XRD pattern of the $Li_{1.14}Mn_{0.46}Ni_{0.2}Co_{0.2}O_2$ material. Annealing at 900 °C renders part of the Li_2MnO_3 component difficult to be activated, which causes a drop in capacity [251, 252]. At both annealing temperatures the $Li_{1.2}Mn_{0.54}Ni_{0.13}Co_{0.13}O_2$ chemistry displays the highest reversible charge and discharge capacities, with a discharge capacity of 236 $mAhg^{-1}$ at cycle 100 for the sample annealed at 900 °C. According to the cycle and rate tests the electrochemical performance of $Li_{1.14}Mn_{0.46}Ni_{0.2}Co_{0.2}O_2$ and $Li_{1.26}Mn_{0.6}Ni_{0.07}Co_{0.07}O_2$ changes with increased annealing temperature whereas it is almost identical at both temperatures for $Li_{1.2}Mn_{0.54}Ni_{0.13}Co_{0.13}O_2$, which agrees well with the results of the Rietveld-refinement.

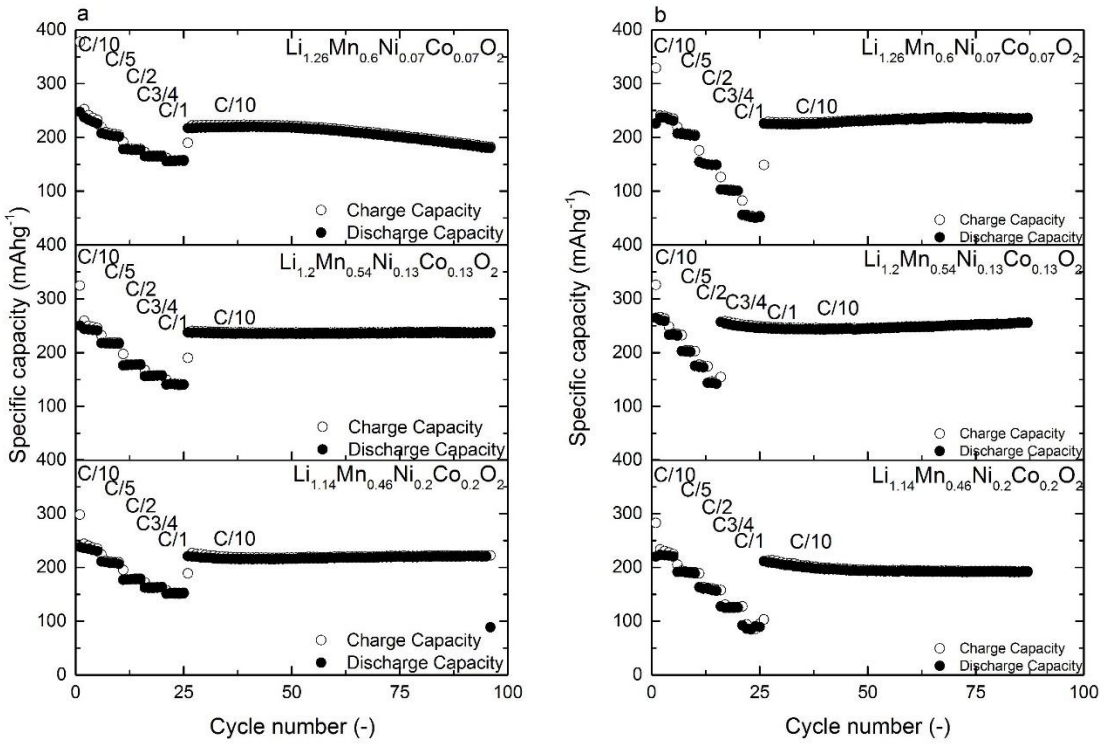

Figure 15 Rate performance of $Li_{1.14}Mn_{0.46}Ni_{0.2}Co_{0.2}O_2$, $Li_{1.2}Mn_{0.54}Ni_{0.13}Co_{0.13}O_2$ and $Li_{1.26}Mn_{0.6}Ni_{0.07}Co_{0.07}O_2$ annealed at (a) 850 °C for 2 hours and (b) 900 °C for 2 hours.

Rate performance tests were conducted between 2.0 – 4.9 V at C/10, C/5, C/2, C3/4, 1C for 5 cycles each and C/10 rate for 70 cycles. These rates correspond to current densities of 28 mAg^{-1}, 56 mAg^{-1}, 140 mAg^{-1}, 210 mAg^{-1} and 280 mAg^{-1}. The results of the rate capability tests of the materials annealed at 850 °C and 900 °C are compared in Figs. 15a and b. The figures show similar trends to those observed in the cycling tests. Although the capacity retention of all the materials improves when annealed at 900 °C, the rate performances of both the $Li_{1.14}Mn_{0.46}Ni_{0.2}Co_{0.2}O_2$ and the $Li_{1.26}Mn_{0.6}Ni_{0.07}Co_{0.07}O_2$ are inferior at this temperature due to the significant coarsening of Li_2MnO_3. $Li_{1.2}Mn_{0.54}Ni_{0.13}Co_{0.13}O_2$ annealed at 900 °C delivers 146 $mAhg^{-1}$ at a current density of 280 mAg^{-1}, which shows a slight improvement from 140 $mAhg^{-1}$

delivered by the material annealed at 850 °C. The enhanced rate capability compared to other chemistries can be the result of the smaller primary particle size, which yields better integration between the two structural components. The increasing capacity of $Li_{1.2}Mn_{0.54}Ni_{0.13}Co_{0.13}O_2$ and $Li_{1.26}Mn_{0.6}Ni_{0.07}Co_{0.07}O_2$ over cycling may be the result of side reactions or a structural transformation due to the high cutoff voltage [34, 254, 255, 256, 257]. The powders produced by spray pyrolysis yield comparable or slightly improved rate capability results compared to pristine material synthesized via co-precipitation [100, 258].

In Fig. 16 the dQ/dV curves for $Li_{1.14}Mn_{0.46}Ni_{0.2}Co_{0.2}O_2$, $Li_{1.2}Mn_{0.54}Ni_{0.13}Co_{0.13}O_2$ and $Li_{1.26}Mn_{0.6}Ni_{0.07}Co_{0.07}O_2$ are compared for materials annealed at 850 °C and 900 °C for 2 hours. All of the materials display a sharp peak above 4.5 V during the first cycle, which is in good agreement with the activation of the Li_2MnO_3 component of the materials. Comparing the curves for cycle 1 and 50, all of the chemistries develop additional charge peaks between 3.1-4.0 V, similar to other reports [113, 115, 201, 242, 244]. The discharge curves for cycle 50 display an additional peak between 2.8-3.2 V. The peak is slightly reduced for $Li_{1.14}Mn_{0.46}Ni_{0.2}Co_{0.2}O_2$ when annealed at 900 °C. The intensity of the additional peaks emerging during the charge curves increases at cycle 50, with an increase in *x* of the composition. Comparing Figures 16a and d, and 16c and f both show that $Li_{1.14}Mn_{0.46}Ni_{0.2}Co_{0.2}O_2$ and $Li_{1.26}Mn_{0.6}Ni_{0.07}Co_{0.07}O_2$ indicate less structural fade in charge and discharge curves after 50 cycles during the high temperature annealing. While the increased amount of residual lithium may in part be responsible for the improved stability, this will ultimately lead to lower charge and discharge capacities.

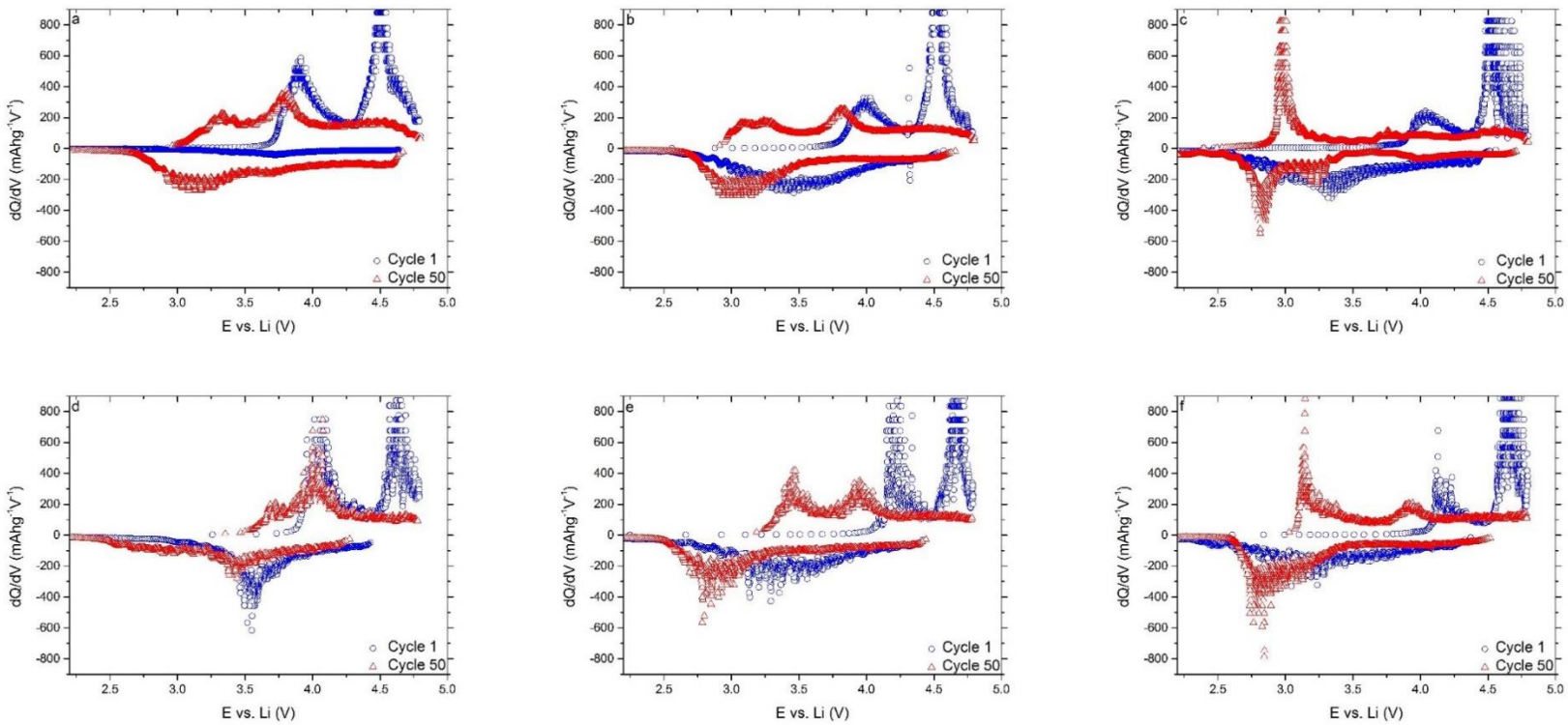

Figure 16 - dQ/dV curves of cycle 1 and cycle 50 for˙(a) $Li_{1.14}Mn_{0.46}Ni_{0.2}Co_{0.2}O_2$, (b) $Li_{1.2}Mn_{0.54}Ni_{0.13}Co_{0.13}O_2$ and (c) $Li_{1.26}Mn_{0.6}Ni_{0.07}Co_{0.07}O_2$ annealed at 850 °C for 2 hours; and (d) $Li_{1.14}Mn_{0.46}Ni_{0.2}Co_{0.2}O_2$, (e) $Li_{1.2}Mn_{0.54}Ni_{0.13}Co_{0.13}O_2$ and (f) $Li_{1.26}Mn_{0.6}Ni_{0.07}Co_{0.07}O_2$ annealed at 900 °C for 2 hours. Cells were cycled with protocol 1.

3.5 Voltage Fade

Aging in lithium ion batteries is typically observed through capacity fade over cycling. Most commercial battery materials display a stable charge-discharge profile and no major changes are observed in the shape of the curves over time [35, 259]. On the other hand, lithium-rich, layered transitional metal oxides are known to display a voltage fade over cycling [116, 242, 244, 257, 260]. The decreasing voltage causes an overall loss of energy of the battery and is a challenge to the battery management systems. While a complete understanding of voltage fade is lacking at present, recent studies agree that it is a result of a complex, structural change including segregation and selective migration of the transitional metals (e.g. Ni) occurring in the material [115, 116, 261, 262].

	Protocol 1 (1C = 280 $mAhg^{-1}$)	Protocol 2 (1C=200 $mAhg^{-1}$)
Activation	1 cycle 2.0-4.8 V at C/10	1 cycle 2.0-4.8 V at C/10
Subsequent cycles	99 cycles 2.0-4.8 V at C/10	3 cycles 2.0-4.6 V at C/10 96 cycles 2.0-4.6 V at C/3

Table 8 Cycling protocols used for studying the voltage fade.

To characterize the nature of the voltage fade during cycling, two electrolytes and two cycling protocols were compared for the $Li_{1.2}Mn_{0.54}Ni_{0.13}Co_{0.13}O_2$ material annealed at 900 °C for 2 hours (protocols 1 and 2 in Table 8). The two different electrolytes were compared because several studies have noted that phase transition begins at the surface, involving transitional metal migration, which may be affected by the chemical composition of the electrolyte and the associated SEI layer forming on the surface [114, 256, 263]. Recent studies that have focused on understanding voltage fade have indicated that high voltage may reduce the stability and accelerate phase transition for these materials [116, 117]. In Fig. 17 the voltage profile evolution for

the 4 cells is compared for cycles 1, 20, 60 and 100. Two cells were fabricated with the EC:DEC:DMC electrolyte (a and c) and two with the EC:EMC electrolyte (b and d). One cell was tested with protocol 1 and the other using protocol 2. All cells display voltage fade as a result of structural change over cycling, especially when protocol 1 is used, a result that is similar to that with other synthesis methods [244]. The discharge potentials of the cells are increasing, and the charge and discharge profiles are changing continuously. The application of protocol 1 leads to spinel-like voltage characteristics, which is highlighted by the circles [244]. When protocol 2 is applied (and thus the upper cutoff voltage is decreased to 4.6 V) the spinel-like voltage fade is less significant. Thus, a reduction of the upper cut-off charge voltage reduces the observed voltage fade of the material [113, 244]. By applying protocol 2, the Li_2MnO_3 component of the material is not fully activated and apparently residues are stabilizing the structure. The Li_2MnO_3 is slowly activated over cycling and this postpones the layered-spinel transition. Nevertheless, a decrease in the charge voltage reduces the cell capacity, as seen in Figure 17.

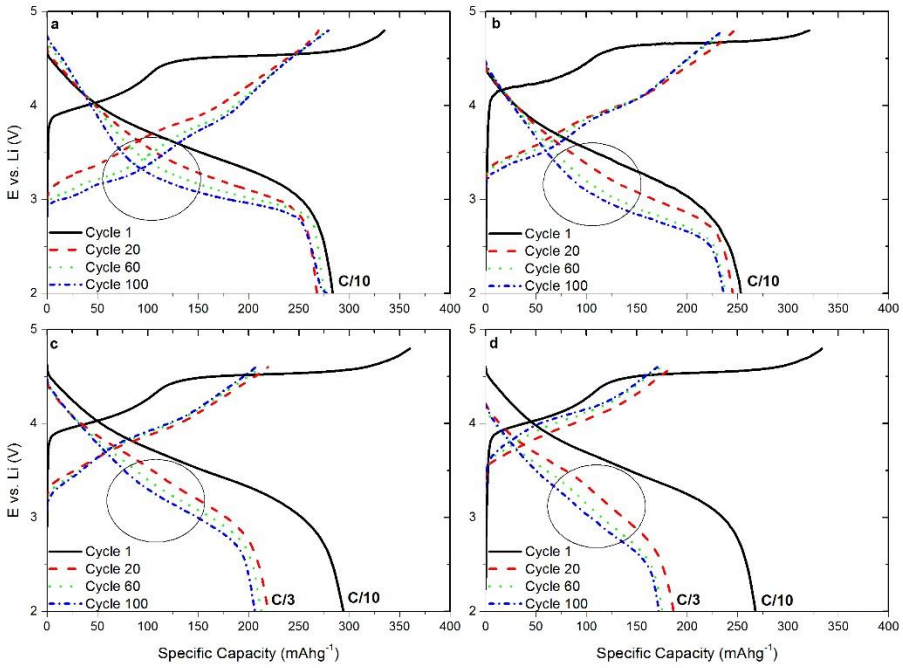

Figure 17 - Comparison of the voltage fade of $Li_{1.2}Mn_{0.54}Ni_{0.13}Co_{0.13}O_2$ with (a) 1M $LiPF_6$ in EC:DEC:DMC 1:1:1 cycled with protocol 1; (b) 1.2 M $LiPF_6$ in EC:EMC 3:7 cycled with protocol 1 (c) 1 M $LiPF_6$ in EC:DEC:DMC 1:1:1 cycled with protocol 2; (d) 1.2 M $LiPF_6$ in EC:EMC 3:7 cycled with protocol 2.

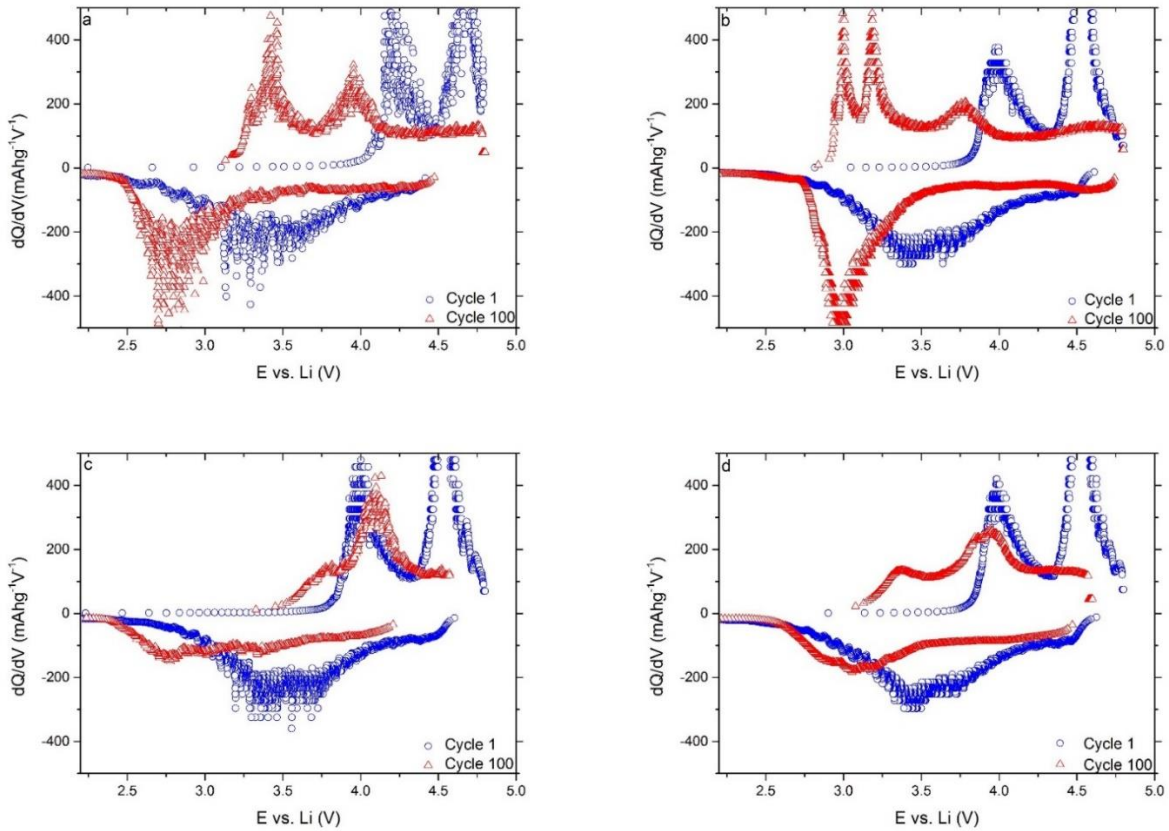

Figure 18 - dQ/dV curves of cycle 1 and cycle 100 for $Li_{1.2}Mn_{0.54}Ni_{0.13}Co_{0.13}O_2$ with (a) 1M $LiPF_6$ in EC:DEC:DMC 1:1:1 cycled with protocol 1; (b) 1.2 M $LiPF_6$ in EC:EMC 3:7 cycled with protocol 1 (c) 1 M $LiPF_6$ in EC:DEC:DMC 1:1:1 cycled with protocol 2; (d) 1.2 M $LiPF_6$ in EC:EMC 3:7 cycled with protocol 2.

Figure 18 compares the dQ/dV curves for cycle 1 and 100 for the two different electrolytes and protocols. The initial charge curves display two peaks during activation and are similar in shape and location in the discharge curves irrespective of electrolyte. When comparing protocols 1 and 2, it is clear that lowering the upper cutoff voltage induces less structural transformation in the materials. Both protocols display a difference in the locations of the peaks emerging at cycle 100 during charging between the two electrolytes.

There are two possible sources of the evolution of voltage profile: interfacial phenomenon and bulk structure evolution. The former is a change in the SEI layer at the electrode interface over cycling, which increases the polarization of the cell. Increasing the upper cutoff voltage to 4.8 V increases electrolyte decomposition for both electrolytes [264, 265, 266]. Electrolyte decomposition will lead to a constant change in the SEI layer and can also be responsible for excess and increasing capacities observed when using protocol 1 for battery testing.

The bulk structure evolution of the material, or more precisely layered-spinel phase transition over cycling, alters the overall shape of the profiles, which is highly dependent on the test protocols. Several studies have identified the possibility of a layered-spinel phase transition over cycling [116, 256, 260, 267, 268, 269]. Such a transformation can explain the rapid voltage profile evolution observed in these materials. The results imply that the Li_2MnO_3 may be a key component affecting the voltage fade.

3.6 Conclusions

$Li_{1.14}Mn_{0.46}Ni_{0.2}Co_{0.2}O_2$, $Li_{1.2}Mn_{0.54}Ni_{0.13}Co_{0.13}O_2$ and $Li_{1.26}Mn_{0.6}Ni_{0.07}Co_{0.07}O_2$ were synthesized via spray pyrolysis to identify a chemistry with optimal electrochemical properties and to compare the performance of the materials to other synthesis methods. Cycling performance and

rate capability studies identified $Li_{1.2}Mn_{0.54}Ni_{0.13}Co_{0.13}O_2$ annealed at 900 °C for 2 hours as having exceptionally high capacity, displaying 236 $mAhg^{-1}$ after 100 cycles. The primary particle size has a significant effect on the electrochemical behavior of the materials. In order to evaluate the effect of primary particle size on stability and electrochemical performance, two annealing temperatures were studied. Smaller primary particles at the same annealing temperature promote electrochemical activation of both the Li_2MnO_3 and the $LiMn_{1/3}Ni_{1/3}Co_{1/3}O_2$ components. Increased stability is obtained when the materials are annealed at 900 °C.

Voltage fade is observed upon cycling for all chemistries. The dQ/dV curves obtained for the different materials indicate that $Li_{1.14}Mn_{0.46}Ni_{0.2}Co_{0.2}O_2$ shows the least amount of voltage fade for the three chemistries studied. This suggests that the amount of Li_2MnO_3 in the material can be correlated to the voltage fade. Increasing amounts of Li_2MnO_3 seems to induce more structural change. The high cycle capacity and excellent activation at both temperature seems to identify $Li_{1.2}Mn_{0.54}Ni_{0.13}Co_{0.13}O_2$ as the optimal chemistry while $Li_{1.14}Mn_{0.46}Ni_{0.2}Co_{0.2}O_2$, with a lower Li_2MnO_3 content, indicates better stability and less fade.

Regardless of the voltage fade observed, powders synthesized via spray pyrolysis have very high capacities and good cycling stability. Uniformity in chemical composition, nanostructure and consistency can be valuable in understanding and studying the chemistry and electrochemistry of these and similar types of materials.

Two cycling protocols were tested to study voltage fade. Increasing the upper cutoff voltage to 4.8 V causes the cycling profile to develop spinel-like characteristics more rapidly. When the upper cutoff voltage is reduced to 4.6 V, the voltage fade seems to be less pronounced, which indicates that besides additional electrolyte decomposition occurring at 4.8 V, the structural transformation is accelerated.

Chapter 4

Effects of synthesis conditions on the physical and electrochemical properties of $Li_{1.2}Mn_{0.54}Ni_{0.13}Co_{0.13}O_2$ prepared by spray pyrolysis

4.1 Introduction

Layered composites of Li_2MnO_3 and $LiMO_2$ (where M = Mn, Ni, Co, etc.) have received significant attention, delivering reversible discharge capacities in excess of 200 $mAhg^{-1}$ [84, 87, 88, 89]. To enable commercial implementation of these materials in plug-in hybrid electric vehicles (PHEVs) and electric vehicles (EVs), a robust synthesis method is required. Conventional synthesis methods include co-precipitation processes, solid-state processes and sol-gel processes [100, 112, 270]. Recently, modified versions of these synthesis techniques were successfully developed, such as polymer assisted synthesis routes, solid state combustion synthesis and freeze drying for producing battery materials [102, 144, 271]. Most of these processes present significant challenges that can hinder large-scale implementation, such as long reaction times, compositional variations in the product, impurities and batch-to-batch inconsistencies. Solid-state synthesis methods are limited by the solid-state diffusivities and therefore can lead to impurity phases or differences in stoichiometry within the powder, which can compromise the electrochemical performance of the product [272, 273, 274, 275]. Sol-gel methods can yield high-quality products, but in general precursors can be expensive and can leave residues in the material [275, 276, 277].

Co-precipitation is considered to be the state-of-the-art for the synthesis of layered composite materials capable of producing advanced cathode morphologies, such as core-shell type materials with improved stability [107]. Nonetheless, co-precipitation has its technological challenges. Co-precipitation can yield non-uniform composition due to differences in solubility of the various precursors, leading to impurity phases [155, 231, 277, 278, 279, 280]. While non-uniformities can be reduced via heat treatment, the hold times are long (>10-20 hours) and temperatures are high (800-1000 °C) [230, 281]. Furthermore, the precipitating agents require several purification steps to be removed and their residues can negatively affect electrochemical performance [231]. These difficulties can also lead to challenges in terms of batch-to-batch reproducibility during large-scale production [231, 277].

Spray pyrolysis is a versatile synthesis technique for the production of multi-component metal oxides (e.g.: $YBa_2Cu_3O_7$, $0.3Li_2MnO_3 \cdot 0.7LiNi_{0.5}Mn_{0.5}O_2$), including layered lithium-ion battery cathode materials [169, 223, 282, 283]. The technical advantages of the process include short residence time (few seconds) in the reactor that allows large throughput; no further post-synthesis purification steps are required; batch-to-batch reproducibility is excellent and the contamination profile of the product meets or exceeds the purity of the precursor [171, 284, 285, 286]. Furthermore, spray pyrolysis typically utilizes inexpensive precursor solutions and simple equipment [171]. Finally, the mesoporous morphology of the product allows for complete activation of the material [219, 287, 288]. These properties, coupled with excellent electrochemical performance, suggest great potential for commercial implementation.

In spray pyrolysis first a precursor solution is prepared by dissolving the appropriate amounts of metal salts, corresponding to the desired stoichiometry [169, 171]. The precursor solution is aerosolized to form droplets and particles are subsequently formed in a flow reactor due to the

evaporation of the solvent, followed by precipitation and thermal decomposition of the precursor salts [239, 243, 289].

The authors have previously reported the synthesis of cobalt-doped materials and $Li_{1.2}Mn_{0.54}Ni_{0.13}Co_{0.13}O_2$ materials were found to display excellent electrochemical performance [243, 289]. Therefore, this chemistry was selected for further optimization. The goal of the present study is to evaluate the effect of synthesis conditions on the electrochemical performance of $Li_{1.2}Mn_{0.54}Ni_{0.13}Co_{0.13}O_2$ in order to demonstrate the robustness of the process. Synthesis conditions were varied (reactor and pre-heater wall temperature, aerosol flow rate, precursor concentration) and their effects on the electrochemical performance and bulk properties of the material were evaluated.

4.2 Experimental

Figure 19 shows a schematic diagram of the modified aerosol flow reactor used for the production of the materials.

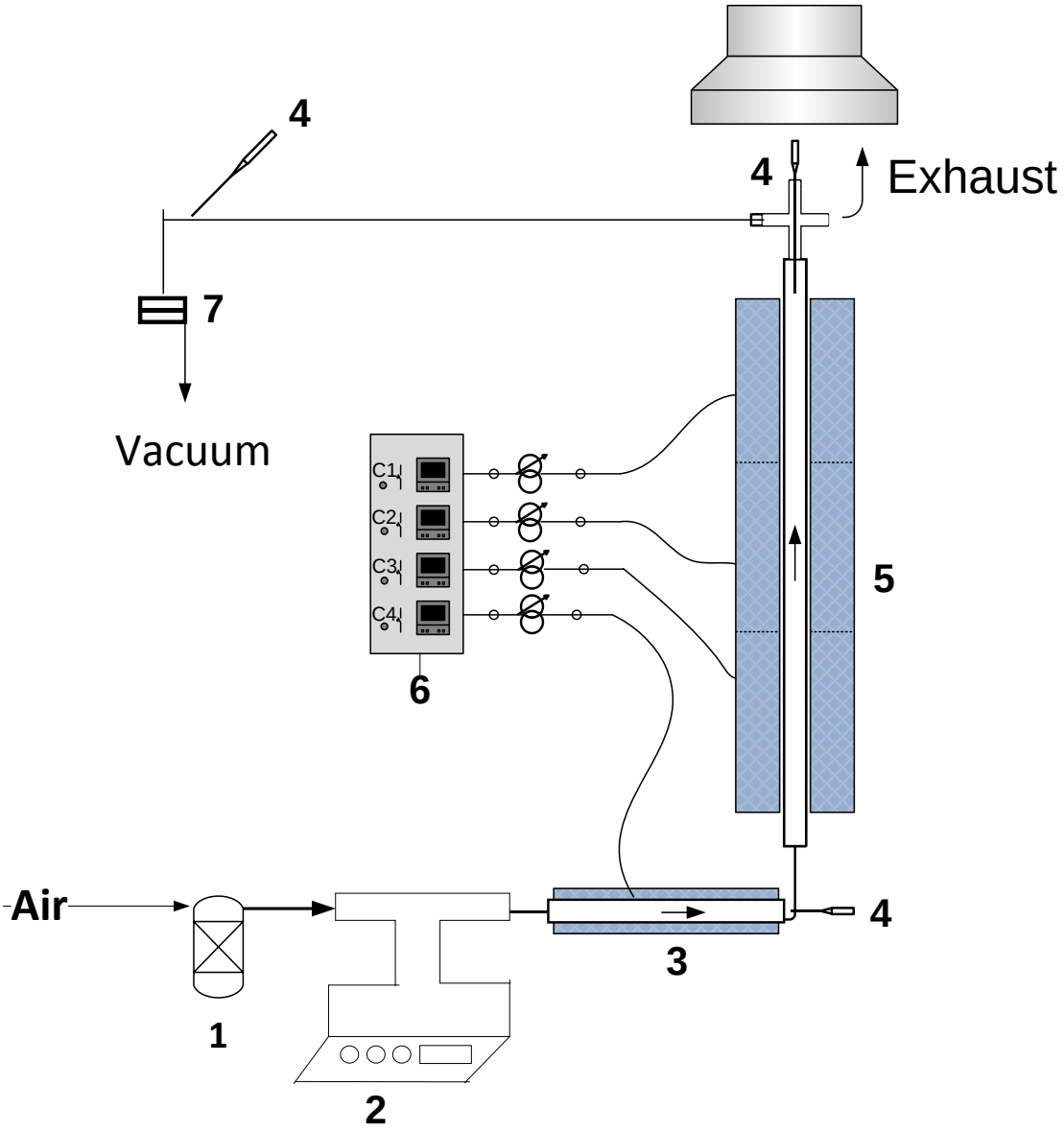

Figure 19 - Schematic diagram of the tubular furnace reactor setup: (1) Bubbler; (2) Ultrasonic nebulizer; (3) 22 inch long preheater; (4) Thermocouple; (5) Ceramic tube; (6) Temperature controller; (7) Porous membrane filter.

The precursor solution was prepared by dissolving $LiNO_3$, $Mn(NO_3)_2 \cdot 4H_2O$, $Ni(NO_3)_2 \cdot 6H_2O$ and $Co(NO_3)_2 \cdot 6H_2O$ (Alfa Aesar) in deionized water at the ratio corresponding to $Li_{1.2}Mn_{0.54}Ni_{0.13}Co_{0.13}O_2$. The total dissolved salt concentration was typically 2.5 $molL^{-1}$(M).

The precursor solution was aerosolized using a 2.4 MHz ultrasonic nebulizer (Sonaer Inc.). Water-saturated air was used as the carrier gas at a constant flow rate of 6.6 liters per minute (lpm). Residence time in the system was typically 6 seconds. The aerosol gas stream was carried into a 22 inch long preheater, which was kept at 200 °C, followed by a 3-zone vertical furnace reactor, which had a uniform wall temperature of either 350 °C, 450 °C, 550 °C, 575 °C or 650 °C. One additional high temperature test was conducted where the preheater was kept at 250 °C and the wall temperature was set to 800 °C. The as-synthesized powders were collected downstream of the reactor on a porous polycarbonate membrane filter (Whatman, GE). The effects of residence time and concentration were studied with fixed preheater wall temperature of 200 °C and reactor wall temperature of 575 °C.

The aerosol particle size distribution was measured using an electrical low-pressure impactor (ELPI Dekati). The as-synthesized powders were subject to annealing heat treatment for 2 hours at 900 °C in a box furnace (Thermal Product Solutions). Thermal decomposition of the precursors was analyzed using a thermogravimetric analyzer (TGA Q5000, TA Instruments).

The annealed powders were characterized by XRD using a Rigaku Diffractometer (Geigerflex D-MAX/A) at a scan rate of 0.04 $°s^{-1}$ between 10° and 80° 2θ. Structural refinement was performed using the whole pattern fitting (WPF) method in the Jade software. The formula card of $LiNi_{1/3}Mn_{1/3}Co_{1/3}O_2$ was used as the reference structure for structural refinement. Rietveld-refinement was performed using the EXPGUI software package.

Particle morphology was examined with an FEI Nova 2300 Field Emission scanning electron microscope (SEM). The primary particle size was estimated from SEM images. EDX spectroscopy was used to determine elemental uniformity in the product. Inductively-coupled-

plasma mass spectrometry (ICP-MS Perkin Elmer Elan DRC II ICP-MS) was used to determine the composition of the precursor solutions and the annealed powders.

The interior morphology of the product was analyzed by embedding the particles in a Ted Pella epoxy-based resin. Sections 120 nm thick were cut from the dry resin using a Leica Ultramicrotome and the sections were examined by SEM. Tapped powder density was measured using a Quantachrome Autotap tapped density analyzer.

Cathode film fabrication was performed according to the procedure reported earlier [239]. The cathode slurry was prepared using a polyvinylidene fluoride (PVdF) binder solution (Kureha Corp. Japan) and Super-P conductive carbon black (Timcal) suspended in 1-Methyl-2-pyrrolidinone (NMP). Electrochemical performance of the powders was evaluated in 2032-type coin cells (Hohsen Corporation) assembled in an argon-filled glove box. Half-cells were assembled for electrochemical tests using pure lithium anodes and 2500 Celgard membranes (Celgard, LLC). The electrolyte solution was 1.2 M $LiPF_6$ in an ethylene carbonate/ethyl-methyl-carbonate solution (EC:EMC = 3:7 by weight) (Tomiyama High Purity Chemicals).

Cycling tests and rate capability tests were performed according to the procedures listed in Table 9. Both cycling and rate capability tests were performed using an MTI-BST8-WA battery tester at room temperature, 22 °C.

	Cycling test protocol (1C=200 $mAhg^{-1}$)	Rate capability test protocol (1C=200$mAhg^{-1}$)
Activation	1 cycle 2.0-4.8 V at C/10 (20 mAg^{-1})	1 cycle 2.0-4.8 V at C/10 (20 mAg^{-1})
Subsequent cycles	3 cycles 2.0-4.6 V at C/10 (20 mAg^{-1}) 96 cycles 2.0-4.6 V at C/3 (66.67 mAg^{-1})	4 cycles 2.0-4.6 V at C/10 (20 mAg^{-1}) 10 cycles 2.0-4.6 V at C/5 (40 mAg^{-1}) 20 cycles 2.0-4.6 V at C/2 (100 mAg^{-1}) 40 cycles 2.0-4.6 V at 1C (200 mAg^{-1}) 25 cycles 2.0-4.6 V at C/10 (20 mAg^{-1})

Table 9 - Testing protocol for rate capability and cycling tests.

4.3 Results and Discussion

4.3.1 Precursor characterization

In a spray pyrolysis process the aerosolized droplets are exposed to significant heating rates. In order to better understand the decomposition reactions occurring in our system, TGA analysis was performed on the precursor solution for $Li_{1.2}Mn_{0.54}Ni_{0.13}Co_{0.13}O_2$ at three different ramp rates: 0.5 °C min^{-1}, 5 °C min^{-1} and 100 °C min^{-1}. As indicated by the solid line in Fig. 20 a,

which is for a ramp rate of 0.5 °C min^{-1} rate, the water (including the crystalline water of the transitional metals) evaporates and then the sample starts to decompose by 70-75 °C. At 5 °C min^{-1} and 100 °C min^{-1} the high heating rate does not permit slow evaporation and drying, thus solvent boiling and material decomposition occur almost simultaneously. At 0.5 °C min^{-1}, 5 °C min^{-1} rate and 100 °C min^{-1} the thermal decomposition is complete by 400 °C, 475 °C and 525 °C, respectively, indicating a similar behavior to our earlier results [156, 240]. Although pure $LiNO_3$ decomposes around 750 °C, the mixture is completely decomposed by 525 °C at all three ramp rates. As earlier studies have indicated, this result suggests that the decomposition temperature profiles can be affected by the presence of water and transitional metals [290, 291, 292]. These studies demonstrated that without further analysis of the individual decomposition events, unambiguous assignment of the peaks in the decomposition profile cannot be made. This is due to the various decomposition reactions involved, as a result of the variable oxidation states of the Ni, Mn and Co ions.

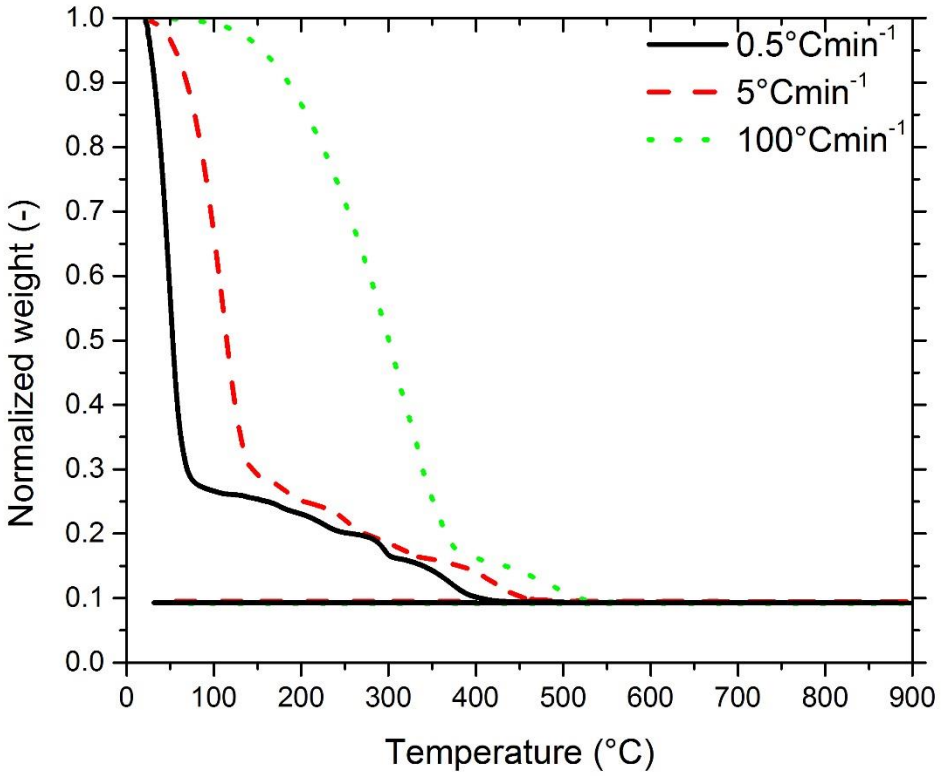

Figure 20 TGA analysis of decomposition of $Li_{1.2}Mn_{0.54}Ni_{0.13}Co_{0.13}O_2$ at 0.5 °Cmin^{-1}, 5 °Cmin^{-1} and 100 °Cmin^{-1}.

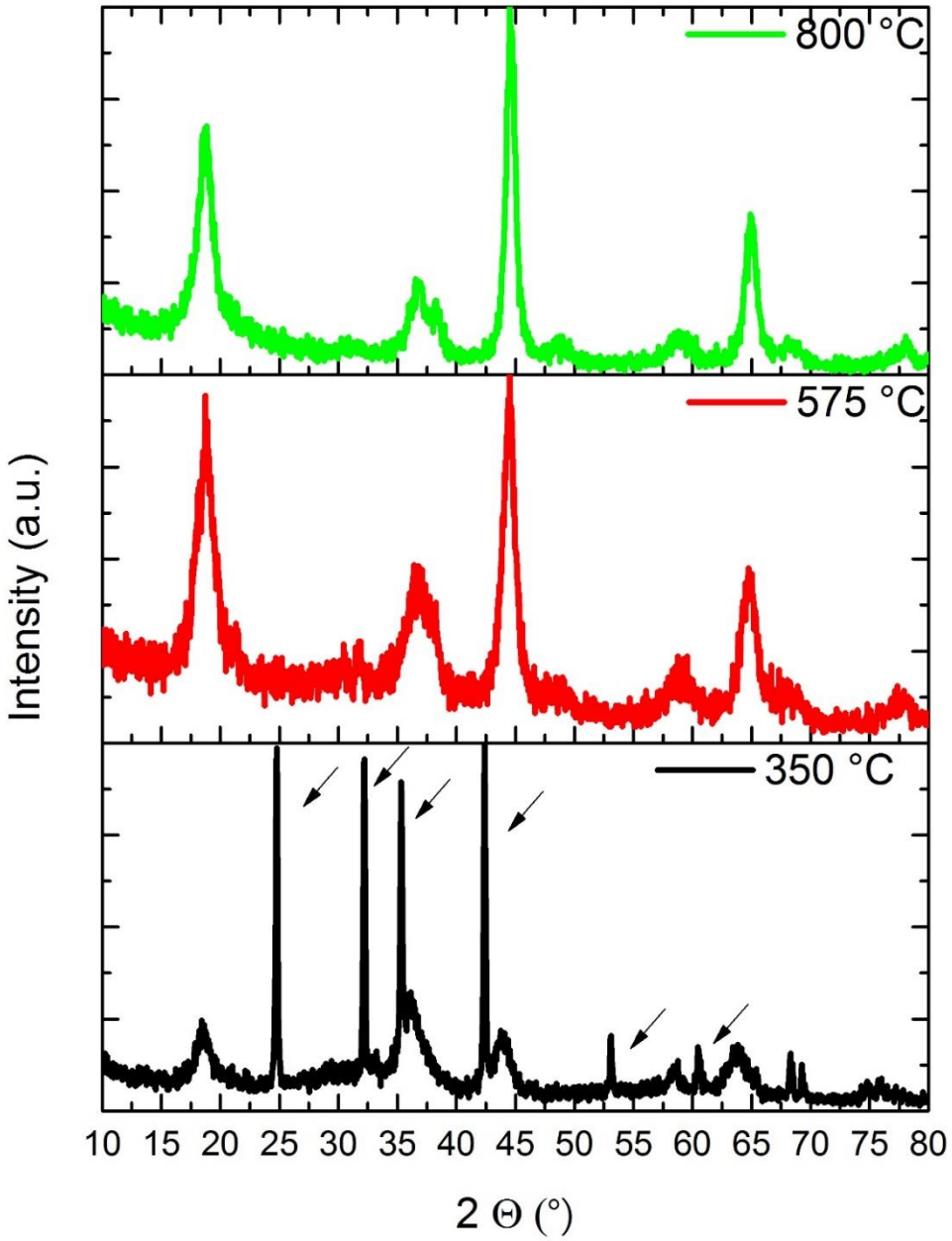

Figure 21 XRD patterns of the as-synthesized powders synthesized at 350 °C, 575 °C and 800 °C. The arrows indicate the peaks corresponding to $LiNO_3$ residues in the sample.

4.3.2 Reactor temperature effects

Several studies have focused on identifying the effects of reactor temperature on the electrochemical properties of various materials synthesized via spray pyrolysis [174, 222, 293]. For a given precursor solution concentration, increasing the synthesis temperature is expected to increase the primary particle size of the materials while having only a minor effect on secondary particle size. Primary particle size can be increased further via post-synthesis annealing, which can lead to longer lithium ion diffusion pathways. Figure 21 shows the XRD patterns of the as-synthesized powders prepared at reactor temperatures of 350 °C, 575 °C and 800 °C. At a synthesis temperature of 350 °C unreacted lithium nitrate residues were found, as indicated by the arrows in Fig. 21. As expected, these powders were hygroscopic. These results are consistent with results of the TGA study.

The as-synthesized particles had a mean particle size of 1.7 μm [243, 289]. Increasing the reactor temperature improves the crystallinity of the powder by promoting growth of the primary particles, as indicated by the increase in the intensity of the peaks with temperature. Similar results for reactor temperature were reported by Kang and Wang for phosphors [174, 222]. Based on the XRD patterns of the as-synthesized materials, the following production temperatures were selected for electrochemical testing: 350 °C, 450 °C, 575 °C, 650 °C and 800 °C. All materials were calcined at 900 °C for 2 hours before electrochemical testing. Thus, the residual $LiNO_3$ in the as-synthesized samples does not appear in the final product.

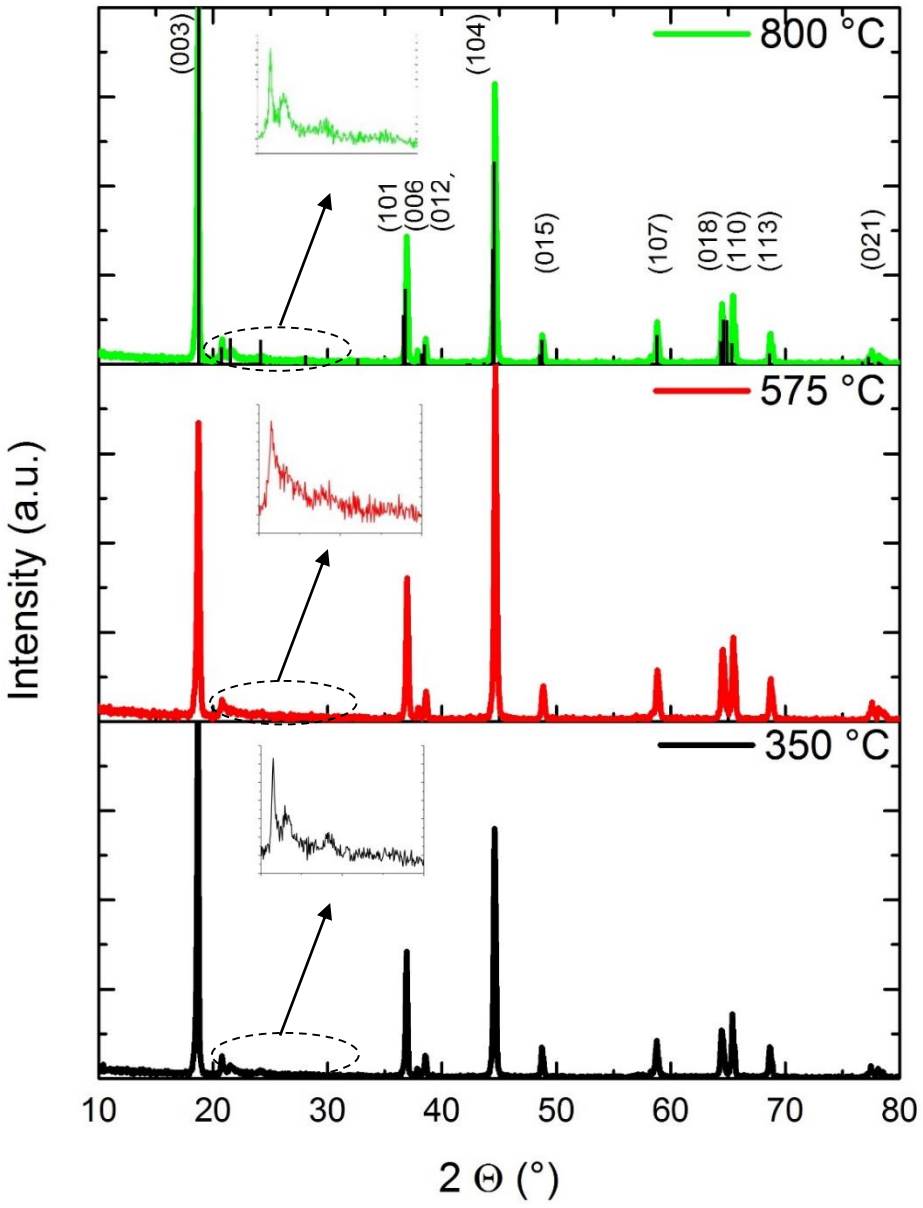

Figure 22 XRD patterns of the annealed powders synthesized at 350 °C, 575 °C and 800 °C. The insets show the superlattice-reflections occurring between 20-25° 2Θ. The standard pdf card is added to the 800 °C pattern using PDF # 04-014-4549.

Figure 22 shows the XRD patterns of powders synthesized at 350 °C, 575 °C and 800 °C after annealing at 900 °C for 2 hours. The products are phase pure materials and the spectra are in

excellent agreement with those for $Li_{1.2}Mn_{0.54}Ni_{0.13}Co_{0.13}O_2$ reported in the literature [89, 102, 113]. All the materials display the broad-peak between 20-25° 2θ corresponding to the ordering between the Li_2MnO_3 and the $LiMO_2$ structural components. Rietveld refinement was performed on $Li_{1.2}Mn_{0.54}Ni_{0.13}Co_{0.13}O_2$ synthesized at 350 °C, 575 °C and 800 °C. The structures were modeled as a mixture of Li_2MnO_3 and $LiNi_{1/3}Mn_{1/3}Co_{1/3}O_2$ at a 5:5 ratio [245, 246, 247]. Table 10 shows the atomic positions, unit cell parameters and reliability factors, which validate the structural model of the refinement. The different synthesis temperatures cause some variation in the atomic position.

Phase I: Li_2MnO_3 (*C2/m*)					
Element	Site	Fractional coordinate		Occup.	
Li1	2b	0/ 0/ 0	0.5/ 0.5/ 0.5	0/ 0/ 0	0.8540/ 0.8540/ 0.8540
Mn1	2b	0/ 0/ 0	0.5/ 0.5/ 0.5	0/ 0/ 0	0.1460/ 0.1460/ 0.1460
Li2	2c	0/ 0/ 0	0/ 0/ 0	0.5/ 0.5/ 0.5	1.0/ 1.0/ 1.0
Li3	4h	0/ 0/ 0	0.6976/ 0.7780	0.6810/0.5/ 0.5/ 0.5	0.9860/ 0.9860/ 0.9860
Mn2	4h	0/ 0/ 0	0.7283/ 0.6529	0.8310/0.5/ 0.5/ 0.5	0.0140/ 0.0140/ 0.0140
Li4	4g	0/ 0/ 0	0.1729/ 0.1687	0.1687/0/ 0/ 0	0.0870/ 0.0870/ 0.0870
Mn3	4g	0/ 0/ 0	0.1705/ 0.1735	0.1708/0/ 0/ 0	0.9130/ 0.9130/ 0.9130
O1	4i	0.2988/ 0.1908	0.2663/0/ 0/ 0	0.1939/ 0.2086	0.2105/1/ 1/ 1
O2	8j	0.3040/ 0.1968	0.2690/0.3252/ 0.3312	03298/0.2236/ 0.2281	0.2370/1/ 1/ 1
a	4.963 Å/ 4.947 Å/ 4.940 Å				
b	8.530 Å/ 8.529 Å/ 8.521 Å				
c	5.025 Å/ 5.009 Å/ 5.021 Å				
β	109.17°/ 109.05°	108.94°/			
Phase II: $LiNi_{1/3}Mn_{1/3}Co_{1/3}O_3$ ($R\bar{3}m$)					
Element	Site	Fractional coordinate		Occup.	
Li1	3b	0/ 0/ 0	0/ 0/ 0	0/ 0/ 0	0.9700/ 0.9700/ 0.9700
Ni1	3b	0/ 0/ 0	0/ 0/ 0	0/ 0/ 0	0.0300/ 0.0300/ 0.0300
Li2	3a	0/ 0/ 0	0/ 0/ 0	0.5/ 0.5/ 0.5	0.0300/ 0.0300/ 0.0300
Ni2	3a	0/ 0/ 0	0/ 0/ 0	0.5/ 0.5/ 0.5	0.3050/ 0.3050/ 0.3050
Mn1	3a	0/ 0/ 0	0/ 0/ 0	0.5/ 0.5/ 0.5	0.3350/ 0.3350/ 0.3350
Co1	3a	0/ 0/ 0	0/ 0/ 0	0.5/ 0.5/ 0.5	0.3300/ 0.3300/ 0.3300
O1	6c	0/ 0/ 0	0/ 0/ 0	0.2419/ 0.2407	0.2415/1.0/ 1.0/ 1.0
a	2.851 Å/ 2.850 Å/ 2.848 Å				
c	14.233 Å/ 14.216 Å/ 14.221 Å				
wRp	0.2131/0.2152/0.2220		Rp	0.1475/0.1482/0.1557	
Chi^2	1.726/ 1.833/ 1.862		Phase ratio	5:5	

Table 10 Result of the two phase Rietveld-refinement assuming a phase ratio of 5:5, between Li_2MnO_3 and $LiNi_{1/3}Mn_{1/3}Co_{1/3}O_2$ for $Li_{1.2}Mn_{0.54}Ni_{0.13}Co_{0.13}O_2$ synthesized at 350 °C, 575 °C and 800 °C.

The SEM-images of Fig. 23 (among other synthesis temperatures omitted for clarity) were used to evaluate the primary particle size of the annealed powders synthesized at different reactor temperatures. The primary particles show crystallinity and the crystal orientation within the

secondary particles is random. The particles are nearly equiaxed, allowing the average primary particle size to be estimated according to the procedure of Buesser and Pratsinis [248]. The primary particle size was determined by averaging the results of 100 primary particle measurements. The primary particle sizes were found to be 335±10 nm, 235±10 nm, 230±10 nm, 320±10 nm and 320±10 nm for powders synthesized at 350 °C, 450 °C, 575 °C, 650 °C and 800 °C, respectively, and annealed at 900 °C for 2 hours. At a 350 °C reactor temperature the decomposition is incomplete, as shown in Fig. 21, and this apparently increases the average primary particle size. As discussed below, this may in part be the result of the ill-defined primary particles, which is caused by the incomplete decomposition.

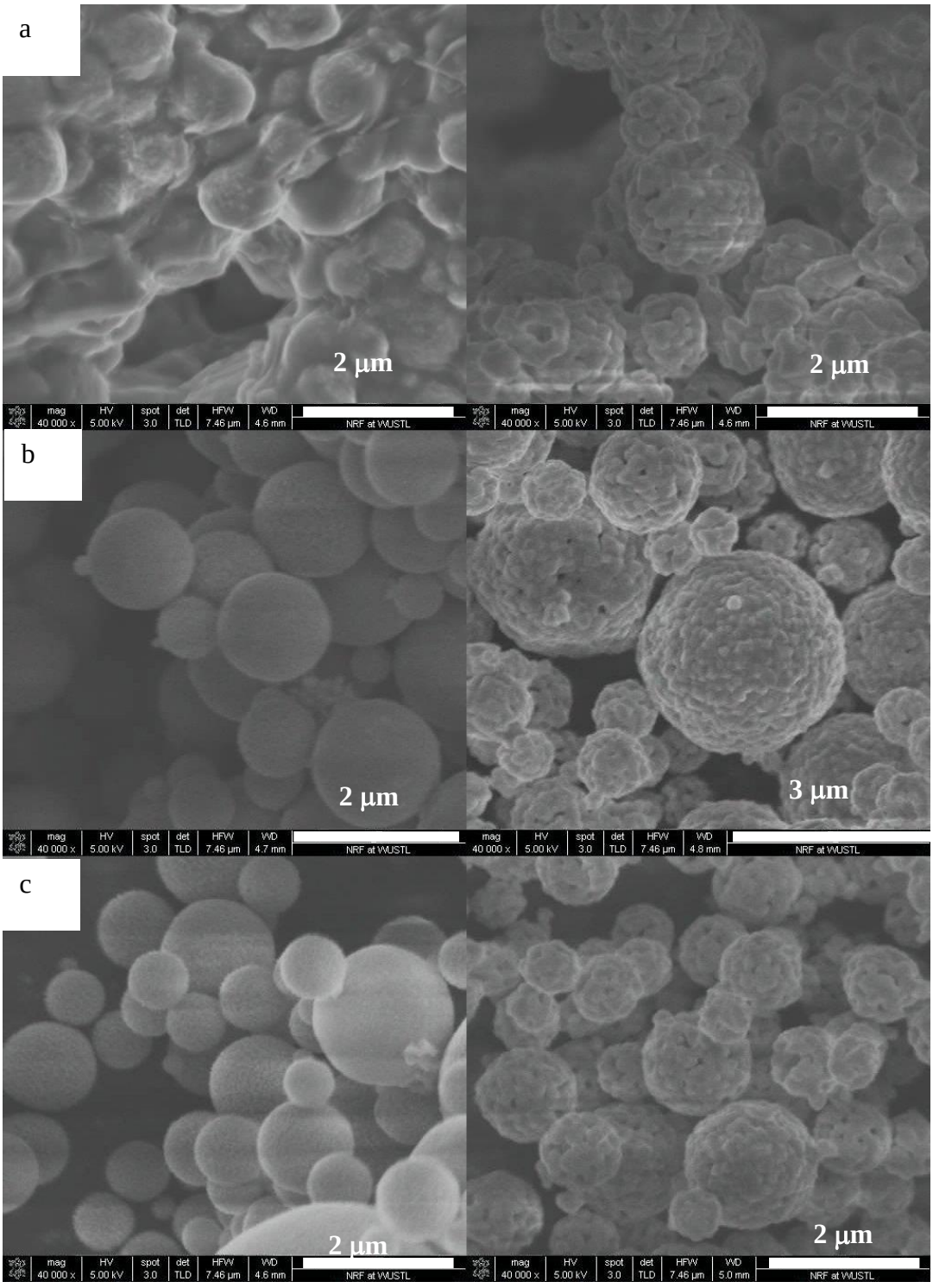

Figure 23 - SEM photographs of powder synthesized at (a) 350 °C; (b) 575 °C; (c) 800 °C. The first column shows pictures of the as-synthesized material, and the second column shows pictures after annealing at 900 °C for 2 hours.

Figure 23 shows the morphology of the annealed powders produced at 350 °C, 575 °C and 800 °C as observed by SEM. The powder synthesized at 350 °C displays an ill-defined cluster of material (Fig. 23a). Spherical particles are apparent, but the particles display necked structures. The as-produced powder is extremely hygroscopic due to the large amount of $LiNO_3$ still remaining in the sample. It is speculated that this morphology is a result of partial redissolution of the unreacted nitrates remaining in the sample. After annealing, a spherical shape is more prevalent, but the particles continue to show necks. When the synthesis temperature increases above 575 °C, necking is no longer observed (Fig. 23b). Smaller particles appear to be porous and spherical. Larger particles, typically above 1.5-2 μm, have dents and are irregularly shaped, indicating that the particles have a hollow interior. Powders synthesized at 650 °C and 800 °C display similar morphologies to powders synthesized at 575 °C (Figs. 23c). The larger primary particles obtained for the as-synthesized powders at reactor temperatures of 650 °C and 800 °C, as indicated by the XRD results in Fig. 21, show that reactor temperature is important in defining the ultimate particle size [174]. The tap densities of the powders synthesized at various temperatures are listed in Table 12. . The largest tap density of 0.86 gcm^{-3} can be observed at the temperature when the powder fully decomposes. Below 575 °C, smaller tap densities are likely to be caused by the observed necking, whereas above 575 °C the tap density does not change beyond measurement error. These tap density results are comparable to other lithium-ion battery cathode powders prepared via spray pyrolysis [179]. Further improvements of the tap density are necessary to meet energy density requirements of electric vehicles. Results of recent improvements, where the tap density is increased to > 1 gcm^{-3}, will be discussed in an upcoming paper.

Synthesis temperature (°C)	Tapped density (gcm^{-3})
450	0.60
550	0.64
575	0.86
650	0.78
700	0.77

Table 11 - Tap density of the powders synthesized at various reactor temperatures after annealing at 900 °C for 2 hours.

A microtome study was performed on the powder synthesized at 575 °C to characterize the interior morphology, which was observed by SEM (Fig. 24). The particles are composed from 100-400 nm size primary particles.

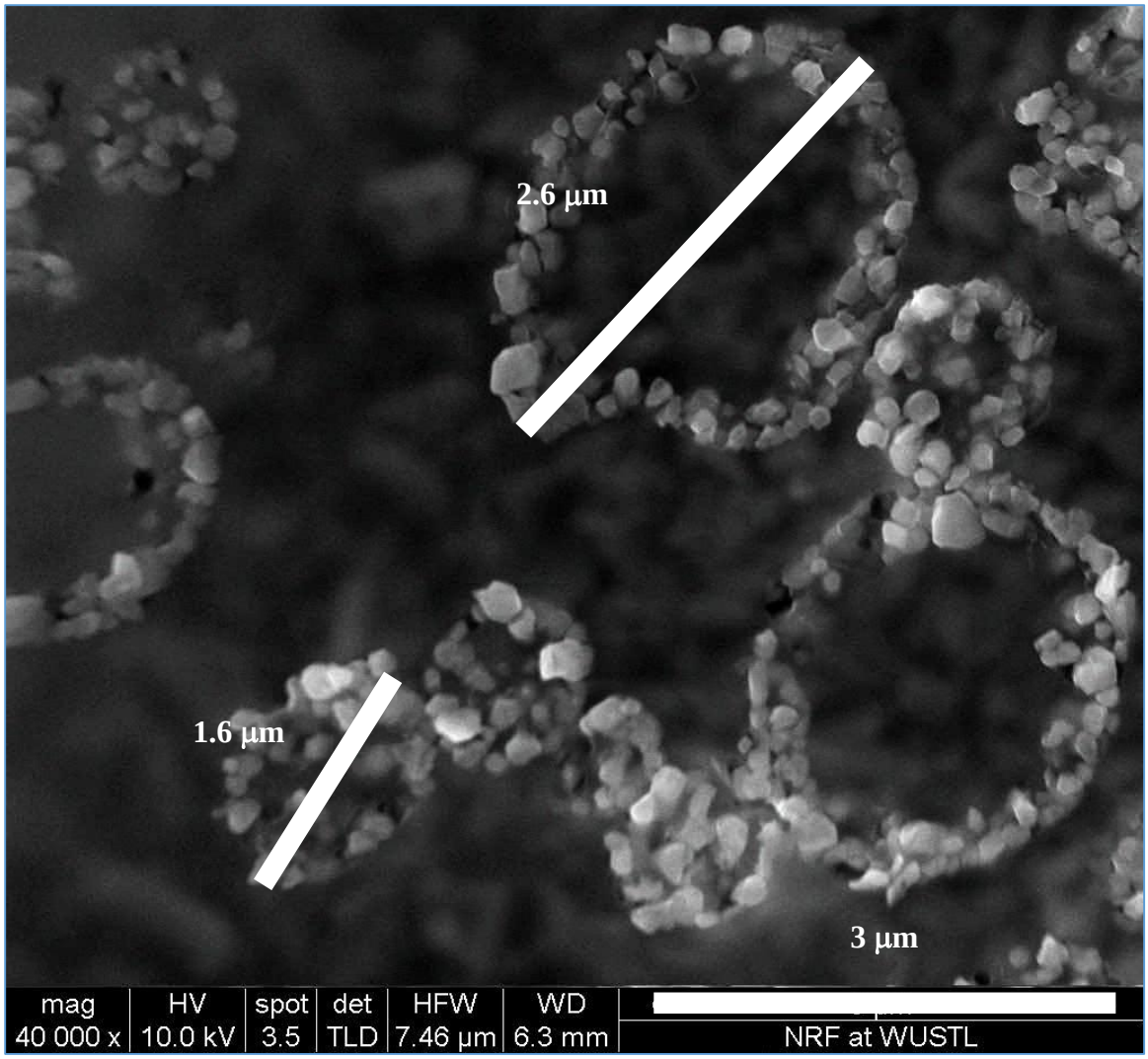

Figure 24 - SEM image showing the interior morphology of the powder.

When the secondary particles are above 1.8-2.0 μm the particles begin to display a hollow interior. As discussed by Messing and Jain, hollow sphere formation is a complex phenomenon affected by many parameters [169, 170]. Once the precursor solution is aerosolized to form droplets, particles form due to the evaporation of the solvent and the subsequent precipitation of the precursor salts [169]. During the rapid drying period if the surface concentration reaches supersaturation before the core reaches saturation, the likelihood to form hollow spheres

increases. Yet, hollow spheres were experimentally observed even for solutions with saturated concentrations throughout the particles [169].

Jain *et al.* found that hollow sphere formation strongly correlates with the tendency of the precursor salt to melt before the decomposition reaction occurs [170]. For example they observed that nitrates of Mn, Ni or Co melt before decomposition and that this property correlates with a tendency to form hollow spheres. This can be further complicated if the gases that evolve during decomposition are not able to leave the surface of the particle, i.e., the permeability of the surface during decomposition is low for the evolving gases. This can yield an inflated particle with a hollow interior. Further study is necessary to understand and overcome hollow sphere formation, but this goes beyond the goals of the current study.

ICP-MS measurements indicate good agreement between the composition of the materials and the desired chemistry, similar to our earlier report [289]. EDX spectroscopy was performed on the powder synthesized at 575 °C to evaluate the elemental distribution of Mn, Ni, Co and O inside the powder (Fig. 25). The distribution of the elements is uniform throughout the powder. No impurity peaks can be detected by EDX spectroscopy and therefore the XRD pattern of the sample is not displayed.

Mn Ni Co O_2

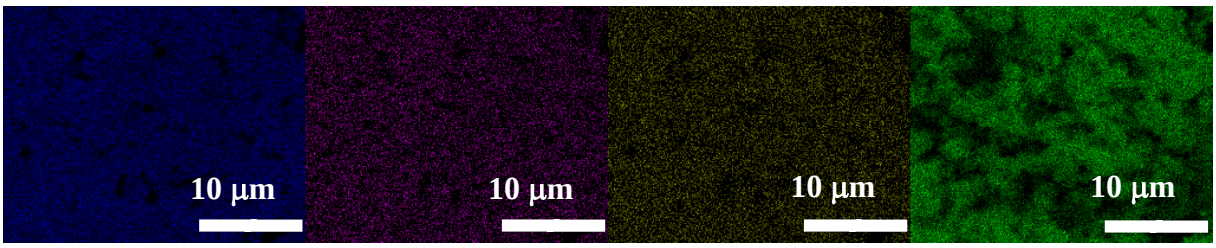

Figure 25 Elemental distribution of Mn, Ni, Co and O_2 in the powder synthesized at 575 °C at 6.6 lpm flow rate as observed by EDX spectroscopy at 10000 times magnification.

In summary, the reactor synthesis temperature does not indicate any difference in the XRD-patterns of the powders, and Rietveld-refinement shows minor deviations in the atomic positions. Unreacted $LiNO_3$, which is present in samples synthesized at 350 °C fully decomposes during the annealing heat treatment. Changes in the synthesis temperature provide us with a method to control primary particle size and the tap density of the powder, but do not present us with a method to reduce the interior hollowness of the structures. Hollow spheres appear to be the main reason behind the low tap density of these materials.

4.3.3. Precursor Concentration Effects

Studies indicate that the concentration of the precursor solution correlates with the secondary particle size of the product [170, 225, 294]. At a fixed reactor temperature a reduction in concentration reduces the secondary particle size [174]. Several studies demonstrated that by reducing the precursor solution concentration to << 0.5 M the secondary particle size can be controlled accurately for single and simple multi-component oxides, allowing for partial control of hollow sphere formation [169, 170, 172, 173, 174, 176, 205]. While these low-concentration studies may help in understanding the fundamental mechanisms of particle formation they do not present a viable option for commercial scale production. Increasing the precursor concentration can also lead to an increase in the number of nucleation sites, which can in turn reduce the primary particle size of the product and this may improve the electrochemical performance of the material [294, 295]. To identify the effect of concentration on the electrochemical performance, three precursor concentrations were studied: 0.5 M, 1 M and 2.5 M. The 0.5 M and 1 M solutions were prepared by diluting the 2.5 M solution to preserve the stoichiometry of the original precursor.

The morphologies of these powders are identical to those in Fig. 23 and therefore are not displayed. The primary particle size of the powder made from the 1 M precursor solution is

240±10 nm, which is very similar to that of the powders synthesized from the 2.5 M precursor. Further dilution of the precursor solution to 0.5 M precursor results in an increase in primary particle size to 350±10 nm. According to Fig. 26 the average secondary particle size of the material synthesized with the 1 M precursor is larger than that for the material synthesized from the 2.5 M precursor. Apparently, the reduced viscosity of the 1 M precursor solution allows larger droplets to form without affecting the nucleation characteristics, as was found in [172, 174, 205]. According to these studies the nucleation properties and the droplet size of sprays typically only change when the concentration is decreased below 1 M. The current results display similar trends with the primary particle sizes being 350±10 nm, 240±10 nm and 230±10 nm for the 0.5 M, 1 M and 2.5 M precursor solution, respectively. These results are consistent with homogeneous nucleation theory wherein a more dilute solution will yield less nucleation sites, and the fewer sites will lead to a larger primary particle size [89, 174, 296].

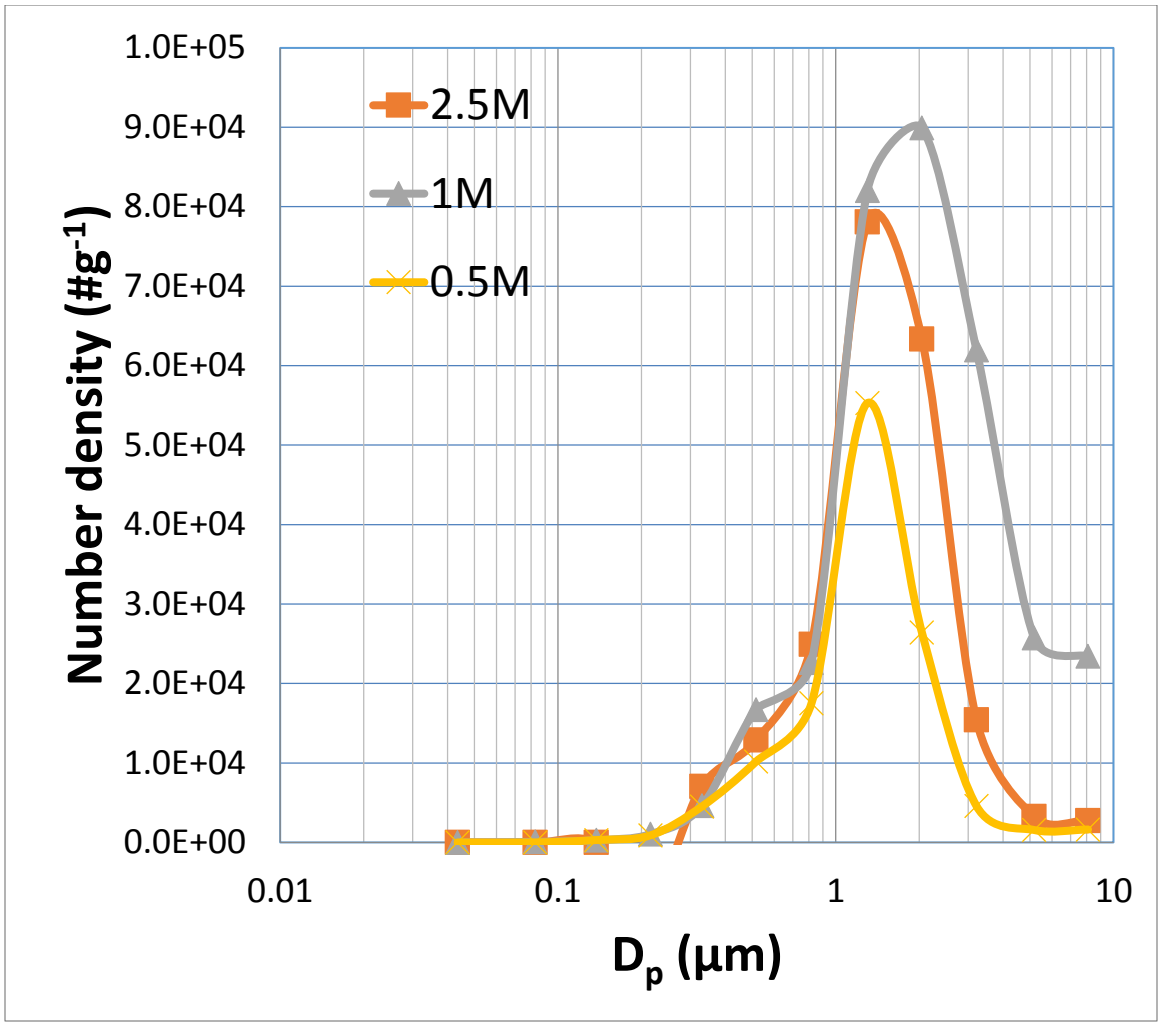

Figure 26 Particle size distribution of the powder synthesized from 0.5 M, 1 M and 2.5 M precursor solutions.

Changing the concentration of the precursor solution provides us with an additional method to control the primary particle size of the product without impacting phase purity. XRD results indicated no significant difference between the different samples and therefore are not displayed. For the range of concentrations considered here, concentration has a minor effect on secondary particle size. The secondary particle size is essentially determined by the nebulizer used in the synthesis process. Significant reduction in the concentration would be necessary to provide accurate control over the particle size of the product, which would limit the practical application of spray pyrolysis.

4.3.4. Effects of flow rate

The aerosol flow rate and the residence time in the aerosol flow reactor are synonymous parameters in a spray pyrolysis process. Residence time in the reactor will define the time available for decomposition and coarsening at a given reactor temperature, both of which can affect the electrochemical performance of the material. Therefore it is essential to evaluate the effect of residence time on the electrochemical properties at a given reactor temperature. Two flow rates were studied: 6.6 lpm and l0.4 lpm corresponding to 6 s and 4 s residence time.

Figure 27 shows the particle size distribution of the powders synthesized at these flow rates. The median particle sizes are around 1.5 μm. Increasing the flow rate leads to a drop in the number density, which is speculated to be the result of impaction [171, 297].

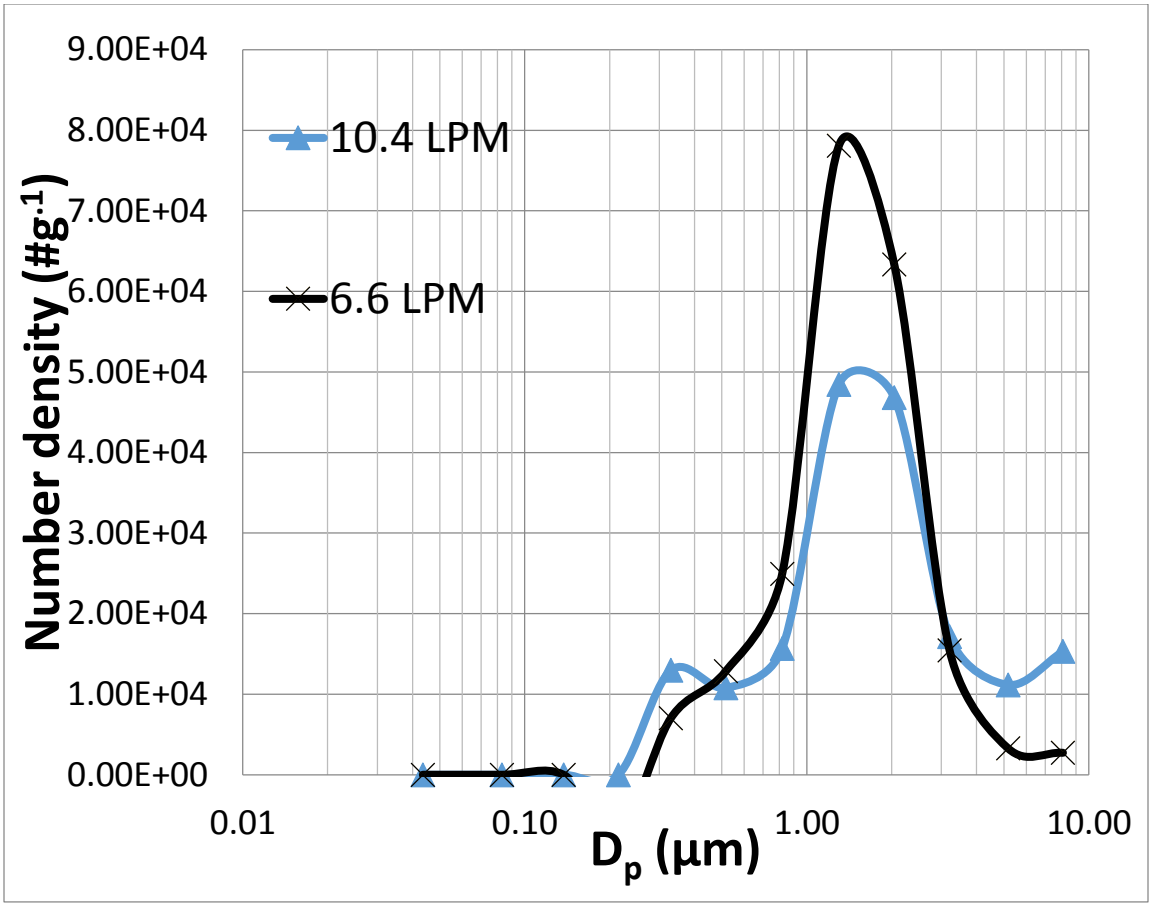

Figure 27 Particle size distribution of the powder synthesized at 6.6 lpm and 10.4 lpm flow rates.

The morphologies of the as-synthesized and annealed powders prepared at a flow rate of 10.4 lpm are displayed in Fig. 28. The as-synthesized powders form interconnected structures and display similar morphologies to those observed for powders synthesized at 350 °C as displayed in 28a. The interconnected structures are indicative of unreacted nitrates. The reduction in residence time shows that at this temperature the amount of heat transported into the droplets is insufficient to ensure complete decomposition. It is clear that a certain minimum temperature must be determined and maintained for a given residence time to ensure complete decomposition. Following the annealing heat treatment at 900 °C for 2 hours the particles separate into spheres and no obvious necking is observed. The primary particle size due to the incomplete decomposition increases to 325±10 nm.

Figures 26 and 27 indicate that the secondary particle size is primarily determined by the droplet generation method, with reactor and flow parameters having only a secondary effect. The oscillation frequency of the ultrasonic nebulizer determines the mean droplet size through the Lang equation [169, 208]. The resulting particle size (d_p) can be empirically estimated based on the droplet size (d_h). The former is dependent on the densities of the precursor solution and the synthesized oxide, and the latter is dependent on the concentration of the precursor solution, which affects the surface tension and viscosity [208, 209, 298]. In order to change the secondary particle size, either a different ultrasonic crystal or a different atomization technique (such as air-assisted atomizers or two-fluid nozzles) must be used [176, 178, 242, 299].

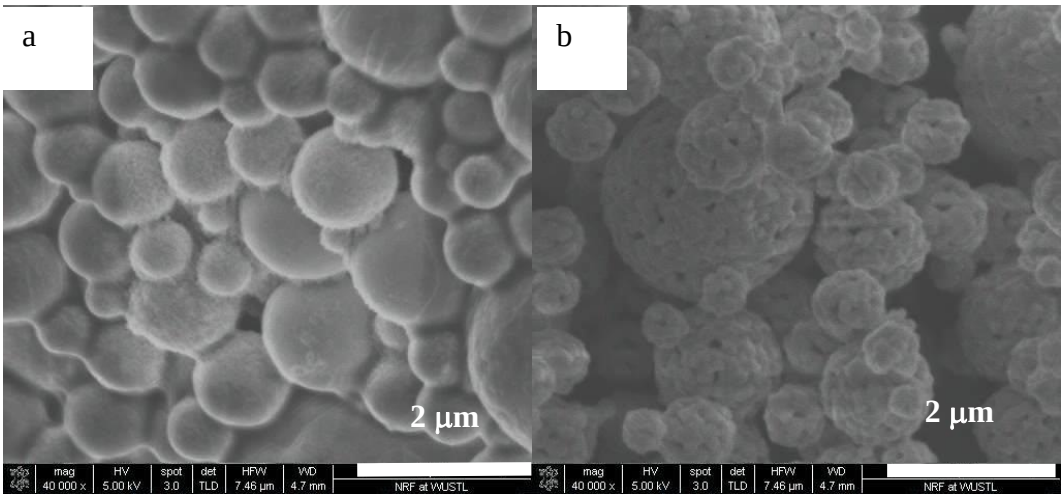

Figure 28 - Morphology of the powder synthesized at 10.4 lpm. (a) as-synthesized; (b) annealed.

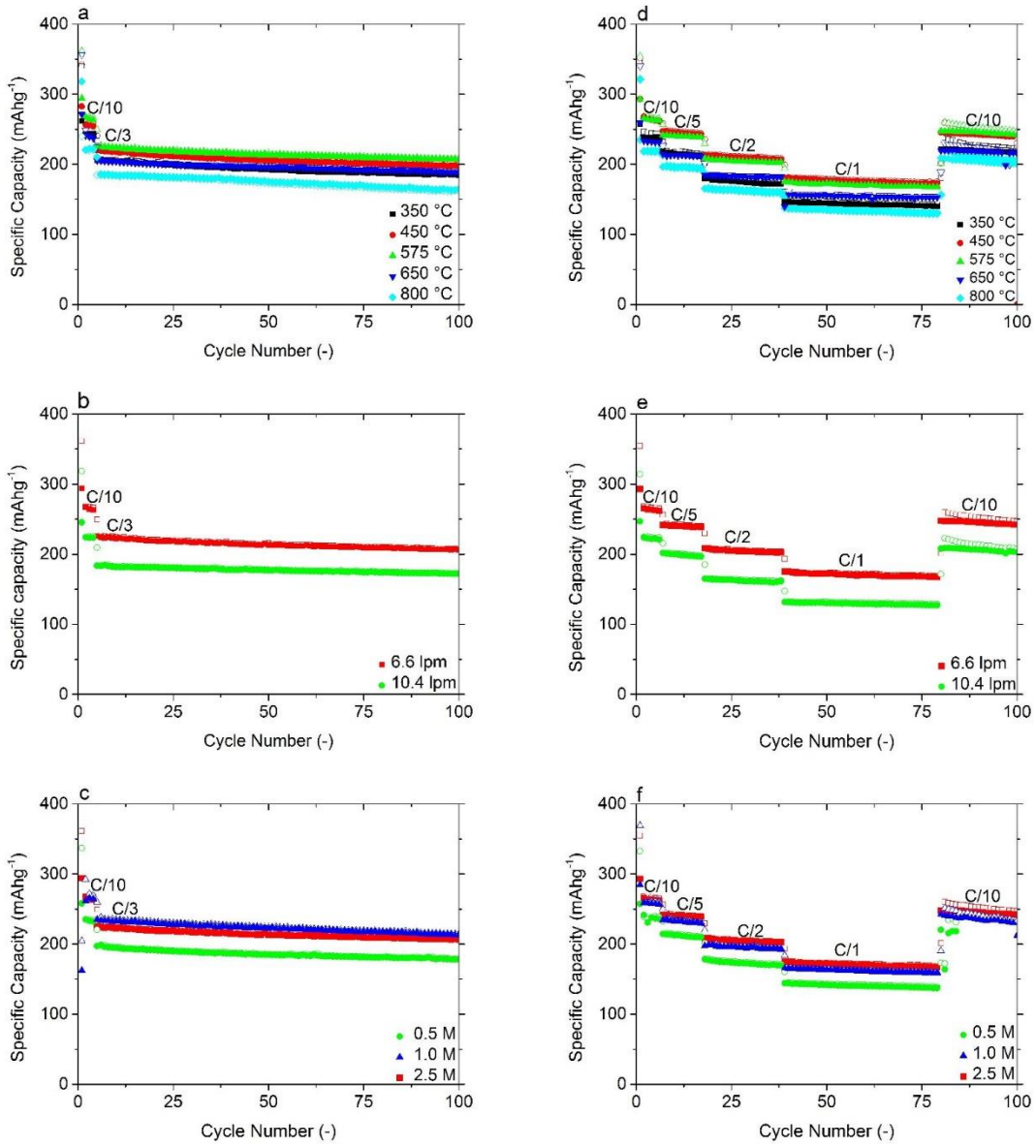

Figure 29 - Cycling performance of cells synthesized at (a) 350 °C, 450 °C, 575 °C, 650 °C and 800 °C; (b) 6.6 lpm and 10.4 lpm; (c) 0.5 M, 1 M and 2.5 M precursor solution; Rate capability tests of cells synthesized at (d) 350 °C, 450 °C, 575 °C, 650 °C, and 800 °C; (e) 6.6 lpm and 10.4 lpm; (f) 0.5 M, 1 M and 2.5 M precursor solution. The open/solid symbols show charge/discharge capacities, respectively.

4.4.1. Cycling and rate capability tests

To evaluate the effects of synthesis conditions on cycle and rate capability, 8 samples were tested. Half cells were assembled from the materials synthesized at the different temperatures, flow rates and concentrations. The reproducibility of the process was evaluated using charge and discharge tests performed on the material synthesized at 575 °C. The standard deviation for cycling tests was 4 $mAhg^{-1}$ at C/3 rate during cycle tests based on 4 batches produced under identical conditions on different dates. This indicates excellent batch-to-batch reproducibility. Figures 29 a, b, and c compare the cycling performance of the materials synthesized at different temperatures, flow rates and concentrations, respectively. Increasing the testing rate from C/10 to C/3 (20 mAg^{-1} to 66.67 mAg^{-1}) leads to a drop of 35±3 $mAhg^{-1}$ for the studied chemistries. The average values were obtained by averaging the differences between the respective discharge capacities for the eight materials studied. Among the different synthesis temperatures the powder synthesized at 575 °C displays the highest absolute capacity, showing a 206 $mAhg^{-1}$ discharge capacity after 100 cycles at C/3 rate. The powder synthesized at 800 °C displays the lowest capacity: after 100 cycles it retains 162 $mAhg^{-1}$ at C/3 rate. The cycling test results can be correlated to the average primary particle size of the materials (Fig. 30).

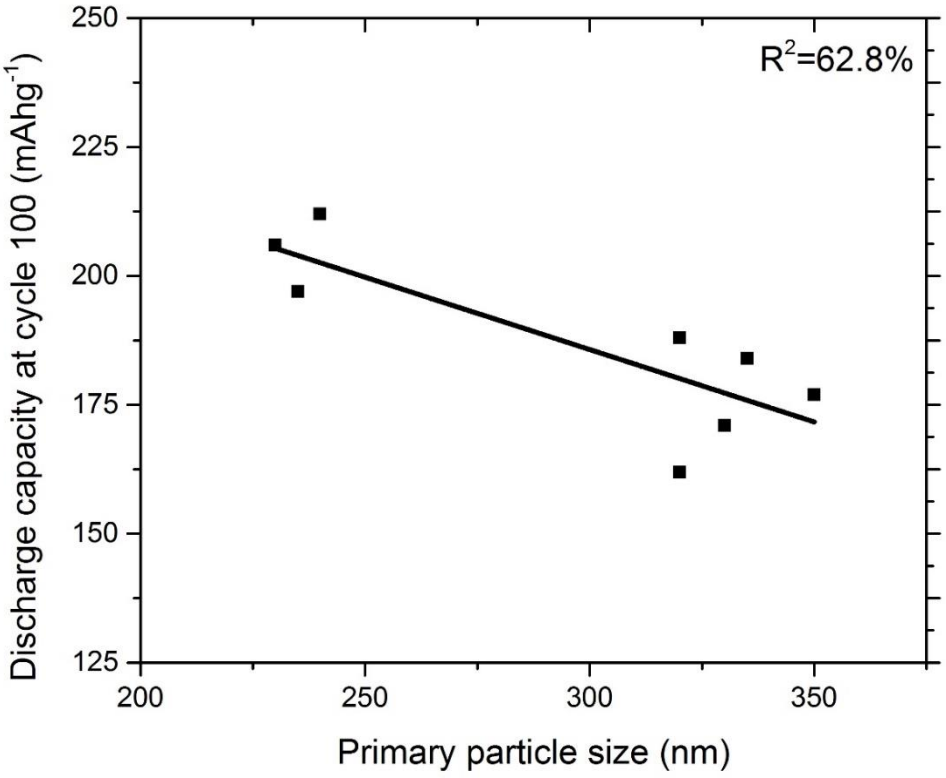

Figure 30 - Particle size vs. discharge capacity after 100 cycles at C/3.

The smaller primary particle size apparently allows the materials to be fully activated at 22 °C. It is speculated that at a primary particle size of around 320-340 nm the core of the primary particles can no longer be fully activated, leading to a reduction in charge and discharge capacity. The sample synthesized at 350 °C has an estimated primary particle size of 335±10 nm, which is larger than that of the samples synthesized at 800 °C (320±10 nm). Nonetheless, the capacity is slightly higher.

The powder synthesized at a flow rate of 6.6 lpm, displays 206 $mAhg^{-1}$ at cycle 100 at C/3 rate, while the powder synthesized at 10.4 lpm only displays 172 $mAhg^{-1}$. This is consistent with our

observation that the primary particle size of the material synthesized at 10.4 lpm increased to 325±10 nm and that the larger size leads to lower capacity.

The effect of precursor concentration on the cycling performance shows a strong correlation with the primary particle size of the material. The cell prepared from the 0.5 M precursor displays only 177 $mAhg^{-1}$ capacity at cycle 100. The electrochemical performances of the materials prepared from the 1 M and 2.5 M precursor solutions are comparable, as the cells display 206 $mAhg^{-1}$ and 212 $mAhg^{-1}$ capacities, respectively. Thus increasing the precursor concentration enhances the electrochemical performance of the material.

Similar trends can be observed for the rate capability tests of the materials (Fig. 29 d, e ,f). For the rate capability tests the increase in testing current from C/10 to C/5, C/2, and C/1 (which corresponds to current densities of 20 mAg^{-1}, 40 mAg^{-1}, 100 mAg^{-1} and 200 mAg^{-1}, respectively) leads to an average drop of 20 ± 3, 30 ± 3 and 26 ± 3 $mAhg^{-1}$ for each step, respectively. The cells fabricated from the materials synthesized at 450 °C and 575 °C display the highest reversible capacity values. At cycle 79, during the last cycle at 1 C the materials retain 174 $mAhg^{-1}$ and 169 $mAhg^{-1}$ capacities respectively, which is comparable to materials synthesized via co-precipitation [100, 258]. No irreversible capacity loss is observed. The material synthesized at 10.4 lpm displays lower capacities. While the powder synthesized at 6.6 lpm shows 169 $mAhg^{-1}$ capacity at cycle 79 at 1C, rate the 10.4 lpm powder only displays 128 $mAhg^{-1}$. The change in the particle size with the precursor concentration has the same effect, and the powder synthesized from the 1 M and 2.5 M precursor solution retains 160 $mAhg^{-1}$ and 169 $mAhg^{-1}$, respectively, at cycle 79 at 1C rate, while the powder synthesized from the 0.5 M solution only shows 138 $mAhg^{-1}$.

According to Fig. 29, for the synthesis temperatures, residence times and precursor concentrations considered, the capacity fade rate or the capacity retention of the material is similar for the conditions studied.

Although some differences can be observed in the morphology of the powder due to differences in the synthesis temperature, no correlation can be identified between the morphology and the electrochemical performance. While studies have revealed that particle shape can be varied with synthesis method [300, 301], the spherical morphology is expected to be the most desirable for packing density, provided that hollow spheres can be avoided.

4.4.2. Voltage Fade

Layered materials are known to experience a structural change occurring during cycling that is speculated to be a layered-spinel phase transition [113, 116, 257, 260, 289]. This leads to voltage fade, which has been discussed by recent studies [113, 116]. Over cycling, the shapes of the charge and discharge curves change significantly with a shift towards lower voltages, which causes a fade in the battery's energy density.

Figure 31 compares the dQ/dV curves for cycles 1 and 100 for the materials synthesized at 350 °C, 450 °C, 575 °C, 650 °C and 800 °C. The first cycle curves all display two activation peaks, where the peak above 4.5 V can be associated with the activation of the Li_2MnO_3 component in the structure. The curves at cycle 100 show that reactor temperature has some effect on the voltage fade but the differences are minor, indicating that this structural change cannot be overcome by changes in the synthesis conditions alone.

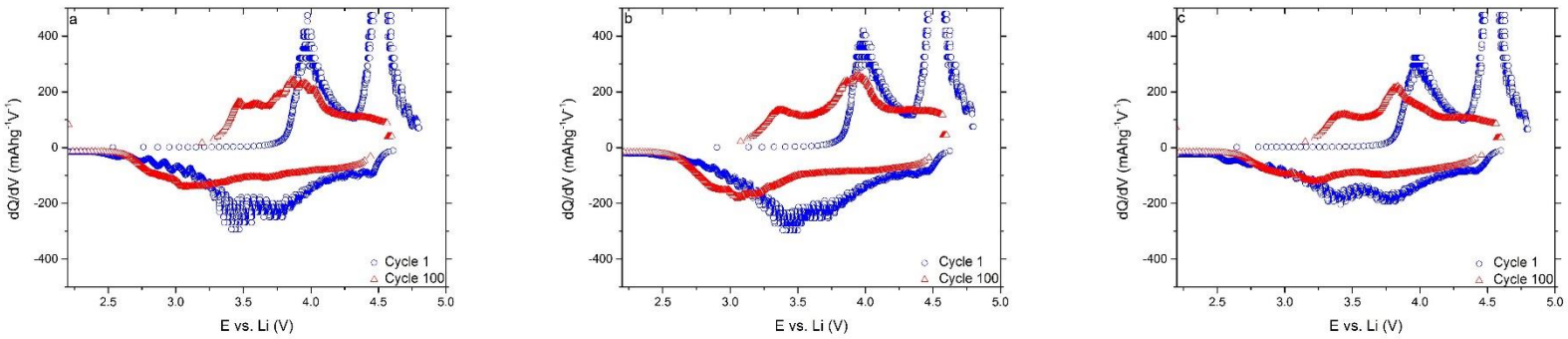

Figure 31 - dQ/dV curves of cycle 1 and cycle 100 of powders synthesized at (a) 350 °C, (b) 575 °C and (c) 800 °C.

4.5 Conclusions

Layered cathode materials were synthesized via spray pyrolysis. The primary and secondary particle sizes of the powders are affected by reactor synthesis temperature, concentration of the precursor and residence time in the reactor. These parameters need to be controlled to achieve optimal electrochemical performance but the spray pyrolysis process is rather robust in that major changes were not observed and the batch-to-batch reproducibility was excellent. Variations in these parameters provide limited control over the morphology of the particles in terms of size, hollowness and shape.

The three analyzed synthesis parameters (synthesis temperature, concentration and flow rate) allow us to improve the rate capability by changing the primary particle size. Minor differences can be observed in the charge and discharge curves of the materials synthesized at different temperatures. The results clearly show that variations in the synthesis conditions are not capable of preventing the structural change that leads to the voltage fade of these materials.

Compared to other synthesis techniques, our study did not reveal any challenges with batch-to-batch reproducibility, compositional non-uniformities or contaminations in the material. The materials produced in the spray pyrolysis process are phase pure and their contamination meets or exceeds that of the precursor salts. Results indicate that a wide range of process variables exist, wherein spray pyrolysis consistently yields cathode materials with excellent electrochemical performance. Nonetheless, improvements to the tap density are necessary. This study demonstrates that spray pyrolysis is a promising alternative synthesis method for the production of layered cathode materials.

Chapter 5

Effects of surface area and lithium content on the electrochemical performance of $Li_{1.2}Mn_{0.54}Ni_{0.13}Co_{0.13}O_2$

5.1 Introduction

Layered composites of Li_2MnO_3 and $LiMO_2$ (where M = Mn, Ni, Co, etc.) have received extensive attention in recent years as candidates for cathode materials for PHEV and EV applications due to their attractive qualities, including high capacity, low cost and safety [67, 84, 87, 109, 112, 212, 258]. Various synthesis methods have been studied for the production of these materials, such as solid-state synthesis, co-precipitation and combustion synthesis [100, 102, 143]. Among these co-precipitation is the conventional method being studied for commercial scale production. The materials synthesized via co-precipitation generally demonstrate good electrochemical performance [101, 103, 302]. In the typical co-precipitation process first the transitional metal oxides are precipitated, followed by a post-lithiation step. As such, to obtain uniformity the as-synthesized powders typically require an extensive (> 10-20 hours) annealing heat treatment at high temperatures (800-1000 °C). Several studies have indicated that lithium in excess of stoichiometry is required to counter the evaporative lithium loss or to obtain good performance [91, 229, 303]. Only a few studies have discussed the effect of lithium content on the electrochemical performance of materials to any extent. Xiao *et al*. found that for co-precipitation the addition of 5% excess lithium is necessary to compensate for evaporative losses and obtain the desired layered composition [304]. Choi et al obtained good results with the application of 7% excess

lithium for layered $LiNi_{1/3}Mn_{1/3}Co_{1/3}O_2$ for a synthesis that combines co-precipitation and solid state synthesis [305]. Ryu *et al.* used a Couette-Taylor reactor to co-precipitate $0.3Li_2MnO_3 \cdot 0.7LiMn_{0.60}Ni_{0.25}Co_{0.15}O_2$ and found that 15 mol % excess lithium was necessary to form the desired layered compound [306]. Deng *et al.* found that co-precipitated materials are very sensitive to lithium concentration and lithium deficiency in the precursor solution can lead to the formation of spinel $LiNi_{0.5}Mn_{1.5}O_4$ upon lithiation, which was found to improve the rate capability of the materials upon cycling [100, 101].

Since many synthesis methods are used to prepare the layered cathodes, different annealing conditions are applied to the as-synthesized powders, and this is sometimes combined with a post-lithiation reaction [100, 112, 306]. Generally, as the annealing time and temperature increase, the primary particles undergo coarsening [307, 308, 309]. However, it has also been observed that increasing the lithium content of the material promotes coarsening and thus, reduces surface area [239]. Several studies have discussed this effect for various materials and have suggested that the reduction in surface area is coupled to internal structural changes of the material, such as transitional metal migration, which typically occurs at the surface [310, 311, 312]. Xia *et al*. found that for Mn-based spinels a reduction in surface area improves the stability of the material, but they did not investigate the mechanism behind this [313].

Spray pyrolysis is a versatile synthesis technique for the production of various oxide materials (ceramic oxides, supercapacitors) and lithium ion battery materials [169, 170, 171, 172, 201, 228, 232, 282]. It is widely applicable for the synthesis of both anode (e.g. $Li_4Ti_5O_{12}$) and cathode materials (including $LiMn_{0.5}Ni_{0.5}O_2$, $Li_{1.2}Mn_{0.54}Ni_{0.13}Co_{0.13}O_2$ and $LiFePO_4$). Spray pyrolysis consists of the following steps. First, a precursor solution is prepared by dissolving the desired precursor salts in a solvent (typically water). The solution is aerosolized into fine droplets which

are dried, and the resulting aerosol particles are decomposed, typically in a hot furnace reactor, and then collected downstream of the reactor [171]. Spray pyrolysis has several distinguishing features over other synthesis methods: each sprayed droplet acts as a microreactor, allowing stoichiometry to be accurately maintained; no precipitating agents are required, ensuring that impurities can be controlled to trace levels; and finally, the short residence times allows for large throughput, which makes the process commercially attractive [200, 314]. As a result, spray pyrolysis has been studied by several groups for mass production of lithium ion battery cathode materials [201, 203, 228, 282]. Recently, Cabot Corp. in a comparative study demonstrated excellent electrochemical performance of $LiNi_{1/3}Mn_{1/3}Co_{1/3}O_2$ compared to materials synthesized via co-precipitation and demonstrated the viability of spray pyrolysis at different production scales [203]. Nonetheless, a challenge associated with spray pyrolysis is the difficulty avoiding interior hollowness in the product particles[169, 172]. While this lowers powder tap density, the electrochemical performance of the material is not affected by the interior morphology.

This group has been developing spray pyrolysis for the production of layered cathode materials [242, 289]. Various layered composites of Li_2MnO_3 and $LiMO_2$ (where M = Mn, Ni and/or Co) have been synthesized using this process, yielding excellent electrochemical performance. The process has also demonstrated excellent reproducibility and robustness for producing layered cathode materials [203, 315]. These and earlier studies with co-precipitation have indicated that the $Li_{1.2}Mn_{0.54}Ni_{0.13}Co_{0.13}O_2$ chemistry shows excellent electrochemical properties for PHEV applications [84, 88, 89, 90, 102, 103]. However, there have not been extensive studies to understand the effect of surface area on the electrochemical performance of materials synthesized by spray pyrolysis.

Due to the high potential of the layered $Li_{1.2}Mn_{0.54}Ni_{0.13}Co_{0.13}O_2$ chemistry, the goal of the current study is to use spray pyrolysis to synthesize $Li_{1.2}Mn_{0.54}Ni_{0.13}Co_{0.13}O_2$ materials with a controlled amount of excess and deficient lithium content to evaluate the effect on morphological and electrochemistry. The annealing conditions were extensively varied for these samples to understand the effect of surface area on the electrochemical properties and to see if the structural changes can be reduced by changes in the lithium content of the material.

5.2. Experimental

The precursor solution was prepared by dissolving $LiNO_3$, $Mn(NO_3)_2 \cdot 4H_2O$, $Ni(NO_3)_2 \cdot 6H_2O$ and $Co(NO_3)_2 \cdot 6H_2O$ at the desired ratios in deionized water corresponding to the compositions listed in Table 12. The excess and deficient lithium content indicated in the text (e.g. 3.3% excess) corresponds to the weight % differences compared to the stoichiometric composition ($Li_{1.2}Mn_{0.54}Ni_{0.13}Co_{0.13}O_2$) and both notations are provided in Table 12. The compositions were calculated according to the following procedure. Adding all the chemical components of $0.5Li_2MnO_3$ $0.5LiMn_{0.33}Ni_{0.33}Co_{0.33}O_2$ leads to the following composition: $Li_{1.5}Mn_{0.67}Ni_{0.17}Co_{0.17}O_{2.5}$. Increasing the lithium content by 0.1 from the previous composition to $Li_{1.6}Mn_{0.67}Ni_{0.17}Co_{0.17}O_{2.5}$ leads to 6.7 wt% excess Li. To preserve the electroneutrality using the +1 oxidation state of lithium the proportion of transitional metal ions (Mn^{+4}, Co^{+3} and Ni^{+2}) is reduced accordingly to have a total oxidation state of +3.4, leading to a composition of $Li_{1.6}Mn_{0.6}Ni_{0.15}Co_{0.15}O_{2.5}$. The previous theoretical composition is then multiplied by 2/2.5 to result in the compositions listed in Table 12. The Li excess or deficiency is defined by dividing the lithium content by the stoichiometric lithium content. Seven compositions including the stoichiometric composition were studied. Prior research has indicated that composition can be accurately controlled with spray pyrolysis at these low dopant levels [203, 289]. Elemental analysis

of the annealed powders were obtained by inductively-coupled-plasma mass spectrometry (Perkin Elmer Elan DRC II ICP-MS) according to the procedure reported earlier [289]. The precursor salts were obtained from Alfa Aesar. The total dissolved salt concentration was fixed at 2.5 $molL^{-1}$ (M).

Target Composition	Composition	Composition measured by ICP-MS	
		900 °C 2 hours	900 °C 20 hours
$Li_{1.28}Mn_{0.52}Ni_{0.13}Co_{0.13}O_2$	+6.7 wt% Li	$Li_{1.29}Mn_{0.52}Ni_{0.14}Co_{0.11}O_2$	$Li_{1.18}Mn_{0.55}Ni_{0.14}Co_{0.11}O_2$
$Li_{1.24}Mn_{0.54}Ni_{0.13}Co_{0.13}O_2$	+ 3.3 wt% Li	$Li_{1.26}Mn_{0.55}Ni_{0.14}Co_{0.11}O_2$	$Li_{1.25}Mn_{0.55}Ni_{0.14}Co_{0.11}O_2$
$Li_{1.22}Mn_{0.54}Ni_{0.13}Co_{0.13}O_2$	+ 1.3 wt% Li	$Li_{1.22}Mn_{0.52}Ni_{0.14}Co_{0.15}O_2$	$Li_{1.22}Mn_{0.52}Ni_{0.14}Co_{0.15}O_2$
$Li_{1.21}Mn_{0.54}Ni_{0.13}Co_{0.13}O_2$	+ 0.7 wt% Li	$Li_{1.21}Mn_{0.53}Ni_{0.14}Co_{0.15}O_2$	$Li_{1.21}Mn_{0.53}Ni_{0.14}Co_{0.15}O_2$
$Li_{1.20}Mn_{0.54}Ni_{0.13}Co_{0.13}O_2$	Stoich. composition	$Li_{1.20}Mn_{0.54}Ni_{0.13}Co_{0.13}O_2$	$Li_{1.24}Mn_{0.55}Ni_{0.13}Co_{0.12}O_2$
$Li_{1.19}Mn_{0.54}Ni_{0.13}Co_{0.13}O_2$	- 0.7 wt% Li	$Li_{1.20}Mn_{0.55}Ni_{0.13}Co_{0.12}O_2$	$Li_{1.20}Mn_{0.55}Ni_{0.14}Co_{0.11}O_2$
$Li_{1.18}Mn_{0.54}Ni_{0.13}Co_{0.13}O_2$	- 1.3 wt% Li	$Li_{1.19}Mn_{0.56}Ni_{0.13}Co_{0.12}O_2$	$Li_{1.19}Mn_{0.56}Ni_{0.13}Co_{0.12}O_2$
$Li_{1.16}Mn_{0.54}Ni_{0.14}Co_{0.14}O_2$	- 3.3 wt% Li	$Li_{1.16}Mn_{0.55}Ni_{0.14}Co_{0.11}O_2$	$Li_{1.16}Mn_{0.55}Ni_{0.14}Co_{0.11}O_2$

Table 12 - Target stoichiometry for the lithium excess and deficient materials. Composition of the materials as identified by ICP-MS.

The precursor solution was aerosolized using a 2.4 MHz ultrasonic nebulizer (Sonaer Inc.). Water-saturated air at 50 °C was used as the carrier gas at a constant flow rate of 6.6 liters per minute (lpm). Details of the experimental setup were reported earlier [315]. Residence time in the system was fixed at 6 seconds. The aerosol gas stream was carried into a 22 inch long preheater, which was kept at 200 °C, followed by a vertical furnace reactor that was kept at 575 °C. All indicated temperatures are wall temperatures. The as-synthesized powders were collected

downstream of the reactor using porous polycarbonate membrane filters (Whatman, GE). The as-synthesized powders were subject to annealing heat treatment at 900 °C for various durations as indicated in the text.

The annealed powders were characterized by XRD using a Rigaku Diffractometer (Geigerflex D-MAX/A) at a scan rate of 0.04 $°s^{-1}$ between 10° and 80° 2 θ . Structural refinement was done using the whole pattern fitting (WPF) method in the Jade software. The formula card of $LiNi_{1/3}Mn_{1/3}Co_{1/3}O_2$ was used as the reference structure for the refinement. Rietveld-refinement was performed using the EXPGUI software package to guide the discussion.

The particle morphology was examined with an FEI Nova 2300 Field Emission Scanning Electron Microscope (SEM). Brunauer-Emmett-Teller (BET) surface area measurements were conducted to characterize the specific surface area of the samples (Autosorb-1, Quantachrome Instruments).

Cathode film fabrication was done according to the procedure reported earlier [239]. The cathode slurry was prepared using polyvinylidene fluoride (PVdF) binder solution (Kureha Corp. Japan) and C45 conductive carbon black (Timcal) suspended in 1-methyl-2-pyrrolidinone (NMP). Half-cells were assembled for the electrochemical tests using pure lithium anodes and 2500 Celgard membranes (Celgard LLC). The electrolyte solution was 1.2 M $LiPF_6$ in ethylene carbonate/ethyl-methyl-carbonate solution (EC:EMC = 3:7 by weight, Tomiyama High Purity Chemicals).

The powders were tested in 2032-type coin cells (Hohsen Corporation) assembled in an argon-filled glove box. Cycling tests and rate capability tests were performed according to the procedures reported earlier [315]. Both cycling and rate capability tests were performed using an

MTI-BST8-WA-type battery tester. All the electrochemical tests were performed at room temperature, 22 °C.

5.3 Results and Discussion

5.3.1 Physical Properties

In order to identify the annealing conditions for the current study and to understand, which annealing times lead to significant coarsening, we synthesized a 6.7% excess lithium-containing sample ($Li_{1.28}Mn_{0.52}Ni_{0.13}Co_{0.13}O_2$). The as-synthesized material was annealed at 900 °C for 2, 5, 10, 20 and 40 hours and the surface area of the powder was measured using BET. According to Fig. 32 the BET surface area of the sample is reduced from approximately 9.1 m^2g^{-1} to 3.0 m^2g^{-1}, when the annealing time is increased from 2 hours to 20 hours. When the annealing time is increased from 2 hours to 5 hours the surface area is reduced from 9.1 m^2g^{-1} to 5.3 m^2g^{-1}. Increasing the annealing time to 10 hours reduced the surface area to 4.7 m^2g^{-1}. Similarly, when the annealing time is increased to 20 hours, the surface area is reduced to 3.0 m^2g^{-1} and a further increase to 40 hours yields only a minor reduction to 2.7 m^2g^{-1} (data not displayed). The change in BET surface area with annealing condition is shown in Fig. 32 for the seven materials. The surface area is continuously reduced with time for all seven samples and the increased lithium content promotes coarsening for the materials [249, 289].

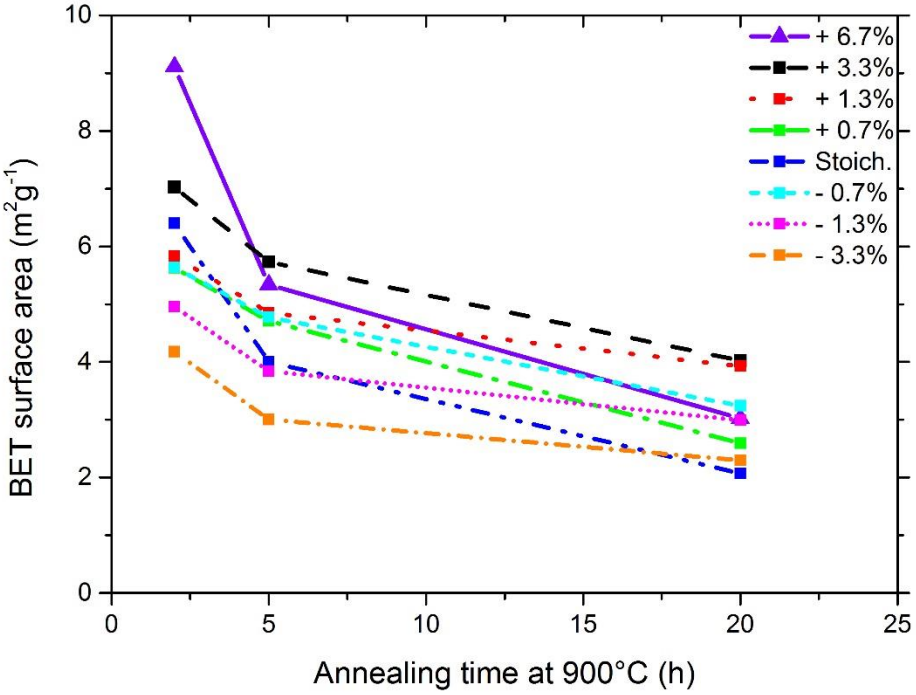

Figure 32 - BET surface area for 6.7 %, 3.3 %, 1.3 % and 0.7% excess Li, stoichiometric Li and, 0.7 %, 1.3 % and 3.3 % deficient Li materials annealed at 900 °C for 2, 5 and 20 hours.

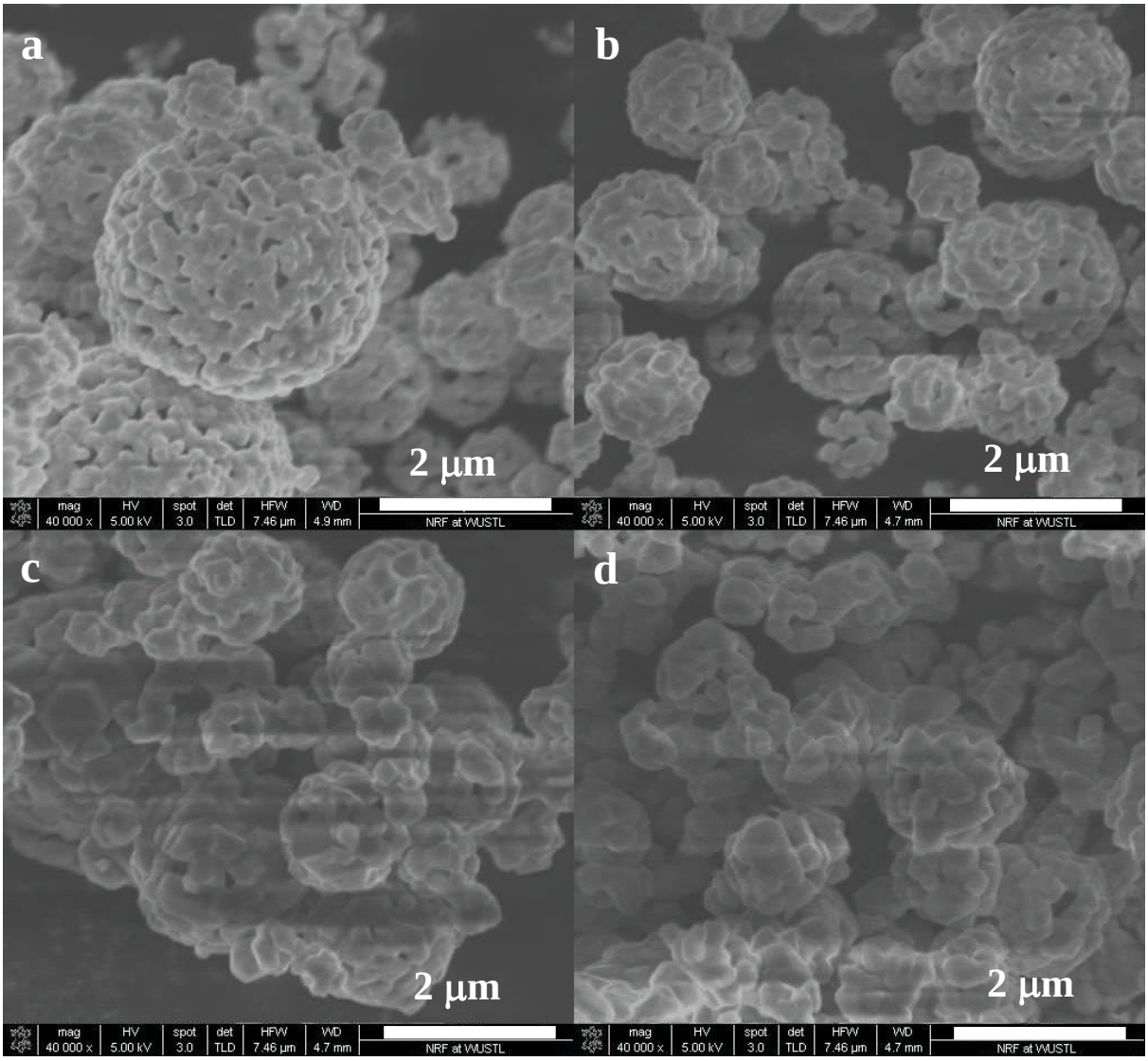

Figure 33 - SEM micrographs of $Li_{1.28}Mn_{0.54}Ni_{0.13}Co_{0.13}O_2$ powders after annealing at 900 °C for (a) 2 hours, (b) 10 hours, (c) 20 hours, (d) 40 hours.

The SEM images for the 6.7 wt% excess Li samples (Fig. 33 a-d) clearly display this trend. The samples annealed for 5 hours (image not shown) and 10 hours maintain an open porous structure without significant visual differences from the sample annealed for 2 hours, while the samples annealed for 20 hours and 40 hours display very large primary particles and do not display open porosity due to the extensive coarsening. A significant change occurred for the sampled annealed for 5 hours, and then again to for the sample annealed for 20 hours. Therefore, in the current

study annealing times of 2, 5 and 20 hours at 900 °C were further evaluated. According to the results of the ICP-MS study listed in Table 13, the 20 hour annealing resulted in measureable evaporative lithium loss for the 6.7% excess lithium sample. Therefore, this sample was omitted from the following studies as evaporative lithium losses would significantly complicate the interpretation of results. Other samples did not display evaporative lithium loss even after annealing for 20 hours.

Figure 34 compares the SEM micrographs of $Li_{1.24}Mn_{0.54}Ni_{0.13}Co_{0.13}O_2$, $Li_{1.2}Mn_{0.54}Ni_{0.13}Co_{0.13}O_2$ and $Li_{1.16}Mn_{0.54}Ni_{0.14}Co_{0.14}O_2$ annealed at 900 °C for 2 and 20 hours. Significant coarsening can be observed when the annealing time is increased to 20 hours, which is in good agreement with the BET results. Primary particle size was estimated by averaging the longest diameter of 100 primary particles based on SEM images. As the lithium content of the samples is reduced the materials gradually lose their open pore structure.

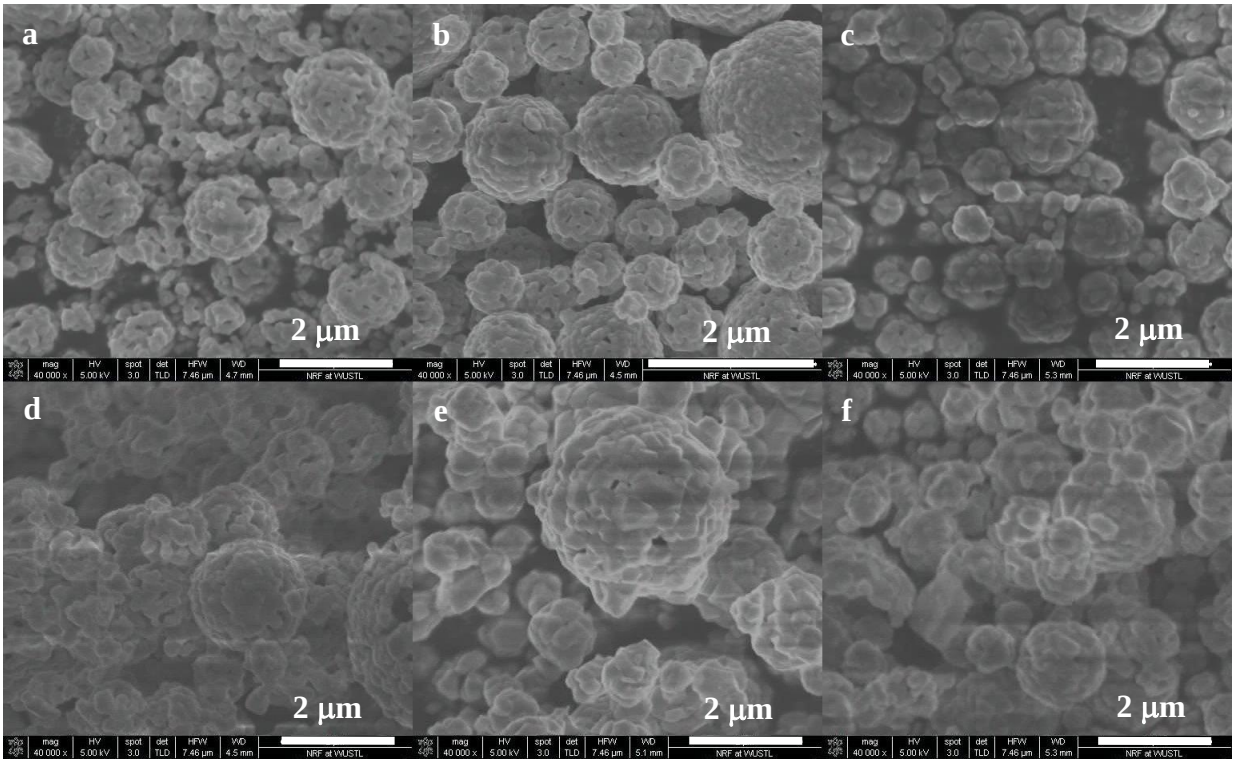

Figure 34 - SEM micrographs of (a) $Li_{1.24}Mn_{0.50}Ni_{0.13}Co_{0.13}O_2$, (b) $Li_{1.2}Mn_{0.54}Ni_{0.13}Co_{0.13}O_2$, and (c) $Li_{1.16}Mn_{0.56}Ni_{0.14}Co_{0.14}O_2$ annealed at 900 °C for 2 hours; and 900 °C for 20 hours (d) $Li_{1.24}Mn_{0.50}Ni_{0.13}Co_{0.13}O_2$, (e) $Li_{1.2}Mn_{0.54}Ni_{0.13}Co_{0.13}O_2$, (f) $Li_{1.16}Mn_{0.56}Ni_{0.14}Co_{0.14}O_2$.

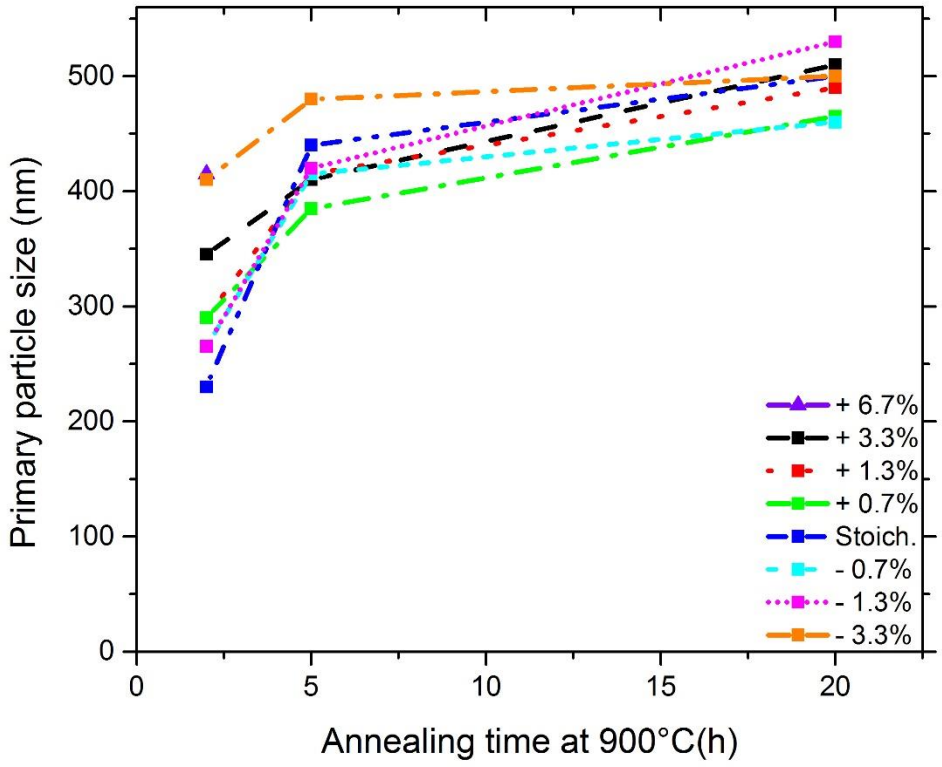

Figure 35 - Estimated primary particle size of the samples based upon SEM-images.

As indicated in Fig. 35 all the materials display a primary particle size close to 500 nm after annealing for 20 hours.

Figure 36 compares the XRD profiles of the 3.3 % excess lithium, stoichiometric and the 3.3 % deficient materials after annealing at 900 °C for 2 hours. No impurity phases can be observed in the spectra of the material and all the materials display a broad peak between 20-25° 2θ corresponding to the superlattice ordering of the structure or a composite structure [92, 94, 103, 105]. The clear splitting of the (006), (012) and (018), (110) peaks indicate layered structures [113]. Two important features can be observed. As the lithium content of the material is decreased, the relative intensities of the two major peaks at (003) and (104) become inverted: the (003) peak is

more intense for the excess lithium containing materials, whereas when the lithium content is reduced to below stoichiometric amounts, the (104) peak becomes more intense. The XRD spectra of $Li_{1.2}Mn_{0.54}Ni_{0.13}Co_{0.13}O_2$ synthesized via co-precipitation or solid-state synthesis displays similar trends: due to the excess lithium content applied during the synthesis the I_{003} is more intense than the I_{104} [84, 94].

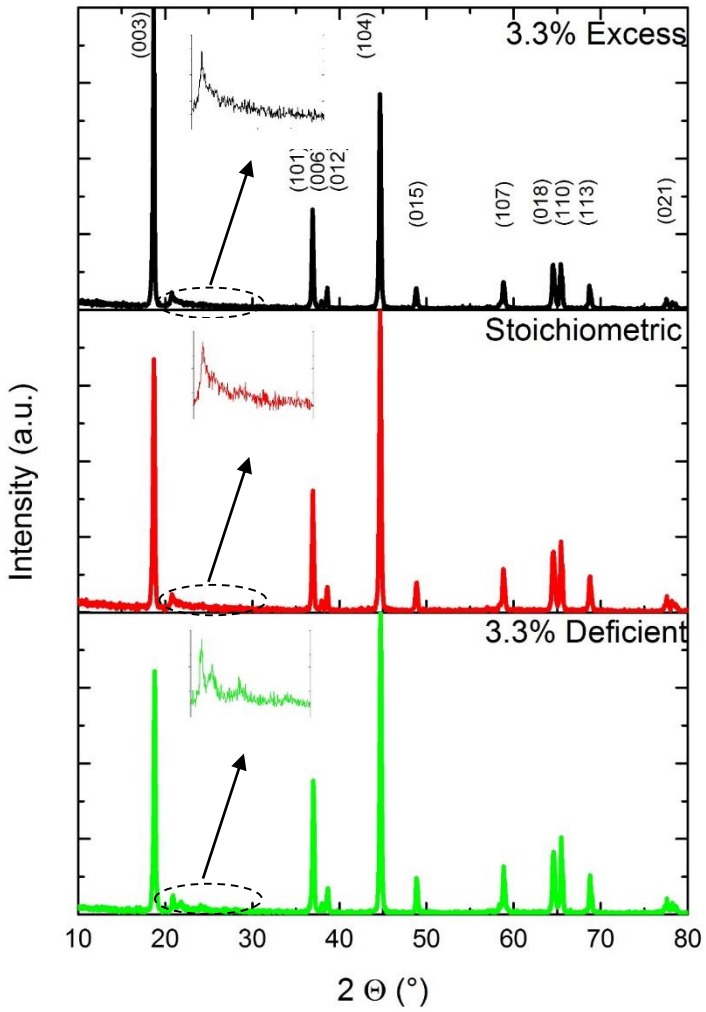

Figure 36 - XRD patterns of $Li_{1.24}Mn_{0.50}Ni_{0.13}Co_{0.13}O_2$, $Li_{1.2}Mn_{0.54}Ni_{0.13}Co_{0.13}O_2$ and $Li_{1.16}Mn_{0.56}Ni_{0.14}Co_{0.14}O_2$ annealed at 900 °C for 2 hours. The insets magnify the broad peak between 20- 25° 2Θ due to the superlattice ordering between the structural components.

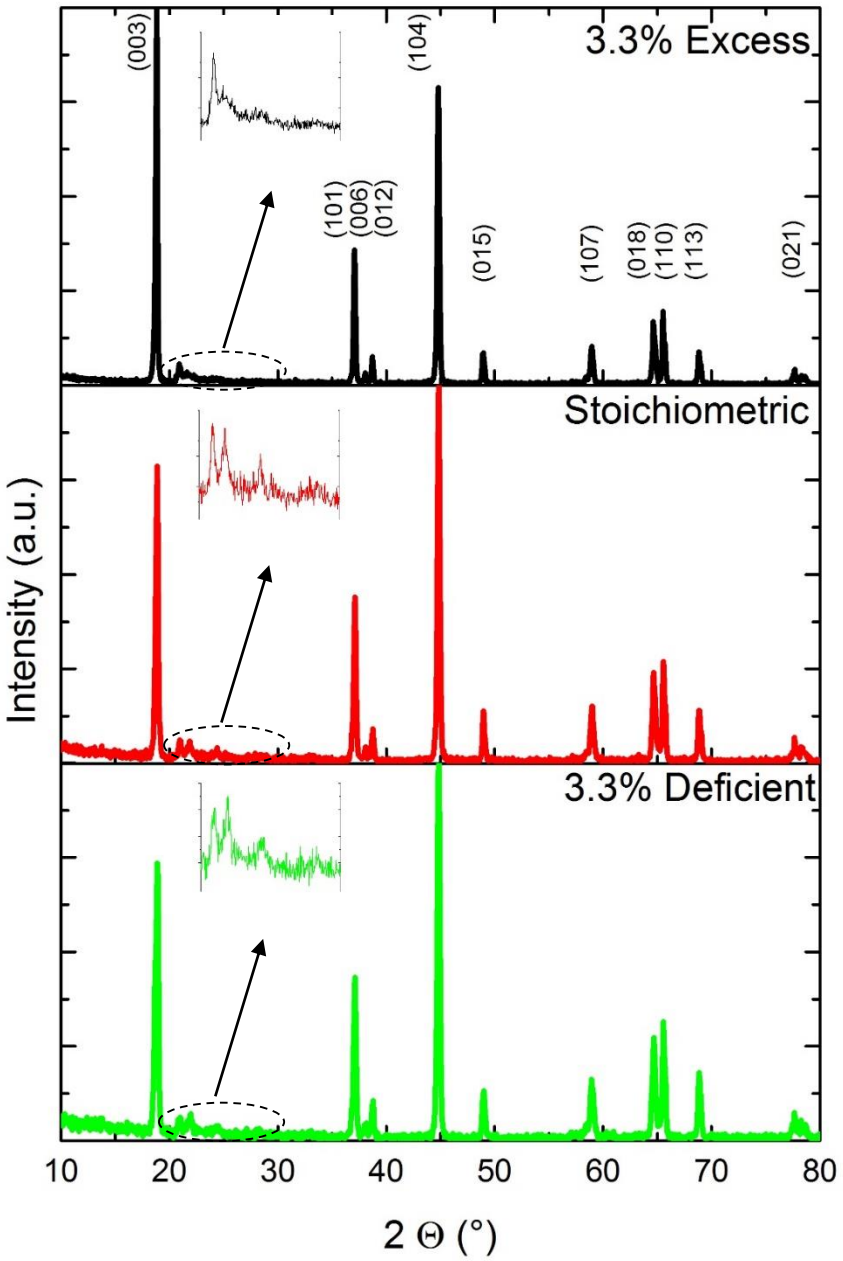

Figure 37 - XRD patterns of $Li_{1.24}Mn_{0.50}Ni_{0.13}Co_{0.13}O_2$, $Li_{1.2}Mn_{0.54}Ni_{0.13}Co_{0.13}O_2$ and $Li_{1.16}Mn_{0.56}Ni_{0.14}Co_{0.14}O_2$ annealed at 900 °C for 20 hours. The insets magnify the broad peak between 20- 25° 2Θ due to the superlattice ordering between the structural components.

The reduction of the lithium content results in the preferential growth of the Li_2MnO_3 (*C2/m*) phase component. This can be observed by the increased intensity of the reflections between 20-25° 2θ corresponding to the *C2/m* phase, which become more intense with the reduction of the lithium content and can be clearly observed in the insets of Fig. 36. This effect is less pronounced for the stoichiometric powder annealed for 2 hours. When the annealing time is increased to 20 hours similar trends can be observed as indicated by the insets in Fig. 37. The results indicate no new phase formation. The relative intensities of the (003) and (104) peaks are inverted for the stoichiometric and deficient powders, but are preserved for the lithium excess sample. The preferential growth of the Li_2MnO_3 phase and the corresponding peaks become even more pronounced, as indicated by the insets of Fig. 37 and these peaks start to emerge in the XRD spectrum of the 3.3 % excess lithium containing material as well. Intermediate compositions display similar trends and therefore are omitted from both Figs. 36 and 37 for clarity. Interestingly, the (018) and (110) peaks increase in relative intensity compared to the (003) and (104) peaks for the stoichiometric and deficient samples as the annealing time is increased from 2 hours to 20 hours. Yi and coworkers recently studied the aging of $Li_{1.2}Mn_{0.54}Ni_{0.13}Co_{0.13}O_2$ using a synchrothron XRD at the Advanced Photon Source [113]. Their results indicated that as the material is extensively cycled the lithium is extracted from their interstitial positions, and the transitional metal (TM) planes undergo structural reorganization, which leads to an expansion along the c axis and an increase in the intensity of the (110) plane. Overall, these changes lead to reduced capacities due to the loss of electrochemically active component from the structure. As discussed below, a similar transition may occur for these materials, which may lead to the reorganization of the structure and a Li-TM exchange between the two respective layers.

Composition	Annealing time at 900 °C (h)	Li_2MnO_3 (*C2/m*)				$LiNi_{1/3}Mn_{1/3}Co_{1/3}O_2$			
		a	b	c	□	a	c	Rp	Chi^2
	2	4.941	8.541	5.024	109.14	2.850	14.213	0.145	1.848
+ 3.3 wt% Li	20	4.944	8.542	5.030	109.10	2.851	14.219	0.134	1.689
	2	4.947	8.529	5.009	108.95	2.850	14.216	0.148	1.833
Stoich.	20	4.940	8.562	5.031	109.44	2.853	14.249	0.174	1.643
	2	4.936	8.552	5.015	109.16	2.850	14.229	0.159	1.906
- 3.3 wt% Li	20	4.943	8.566	5.036	109.34	2.855	14.253	0.173	1.544

Table 13 - Cell parameter and reliability factor results for two phase Rietveld-refinement assuming a phase ratio of 5:5 and between Li_2MnO_3 and $LiNi_{1/3}Mn_{1/3}Co_{1/3}O_2$ for $Li_{1.24}Mn_{0.50}Ni_{0.13}Co_{0.13}O_2$, $Li_{1.20}Mn_{0.54}Ni_{0.13}Co_{0.13}O_2$ and $Li_{1.16}Mn_{0.56}Ni_{0.14}Co_{0.14}O_2$ annealed at 900 °C for 2 hours and 20 hours.

Two-phase Rietveld refinement was performed on $Li_{1.24}Mn_{0.54}Ni_{0.13}Co_{0.13}O_2$, $Li_{1.2}Mn_{0.54}Ni_{0.13}Co_{0.13}O_2$ and $Li_{1.16}Mn_{0.54}Ni_{0.14}Co_{0.14}O_2$ annealed at 900 °C for 2 and 20 hours. The structures were modeled as a mixture of Li_2MnO_3 and $LiNi_{1/3}Mn_{1/3}Co_{1/3}O_2$, with a 5:5 molar ratio [245, 247, 305]. Table 13 shows the cell parameters and the reliability factors for the materials after refinement. It is clear that the cell parameters of the Li_2MnO_3 structural component display changes, which agrees well with the above results. The 3.3 % excess materials ($Li_{1.24}Mn_{0.54}Ni_{0.13}Co_{0.13}O_2$) have almost identical cell parameters at both annealing conditions. The increased annealing time leads to larger *b* and *c* parameters for both the stoichiometric and the 3.3 % deficient material. Similarly, the $LiNi_{1/3}Mn_{1/3}Co_{1/3}O_2$ component shows a minor

increase along the *c* axis for the stoichiometric and the 3.3 % deficient materials, but is essentially intact for the 3.3 % excess material.

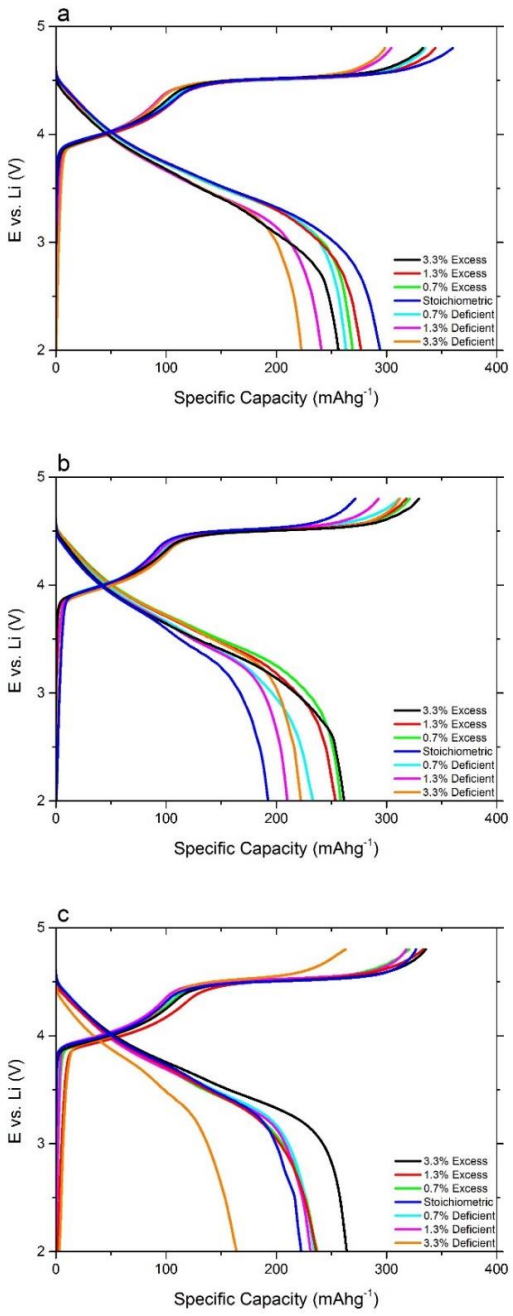

Figure 38 - Initial charge and discharge profiles at a constant current density of 20 mAg^{-1} between 2.0 and 4.8 V: 3.3 %, 1.3 %, and 0.7 excess Li, stoichiometric Li, 0.7 %, 1.3 % and 3.3 % deficient Li materials after annealing at (a) 900 °C for 2 hours, (b) 900 °C for 5 hours, (c) 900 °C for 20 hours.

5.3.4 Electrochemical testing results

Figure 38 shows the initial charge and discharge profiles of the materials annealed for 2, 5 and 20 hours, when charged at a constant current density of 20 mAg^{-1} between 2.0-4.8 V (1C=200 mAg^{-1}). A constant-current, constant-voltage cycling protocol was applied for all the electrochemical tests [239]. All the materials display a two-staged charge profile: the first plateau between 3.5 V and 4.4 V is associated with the Ni^{2+}/Ni^{4+} and the Co^{3+}/Co^{4+} redox couples, while the second plateau above is associated with the activation of the Li_2MnO_3-domains in the material [94]. As can be observed in Fig. 38 (a),

when the materials are annealed for 2 hours the 1.3% and 3.3% deficient materials display lower capacities compared to the stoichiometric and excess lithium containing materials. A possible explanation is that below stoichiometry a rock-salt type Ni_xO_{1-x} phase may exist or form in the materials due to the reorganization of the TM layers. This leads to the elongation of the *c* axis, and the phases remain undetectable by the XRD used in the current study [316]. The formation of the Ni_xO_{1-x} phase may cause the Li_2MnO_3 domains in the material to be partially deactivated. This could potentially reduce the amount of electrochemically-available Li, which can cause the observed loss in capacity.

Similar trends are present for the stoichiometric and Li-deficient materials annealed for 5 hours, and further for the 0.7% excess and 1.3% excess materials annealed for 20 hours. The originally stoichiometric powders may undergo an internal structural reorganization causing a loss of electrochemically active Li in the structure, which can be the reason behind the observed capacity drop. This is speculated to be the main mechanism behind the observed loss of capacity observed in Table 12 since no significant Li-loss can be observed by ICP-MS with increased annealing time. The capacity drop is most severe when the annealing time is increased to 20

hours. Only the 3.3% excess Li containing powder is able to compensate for the loss in electrochemically active Li and the associated structural reorganization at these long hold times.

Figure 38 b shows that after annealing for 5 hours the materials containing excess lithium become fully active and display initial discharge capacities > 250 $mAhg^{-1}$. Interestingly the stoichiometric composition displays an unexpected drop in electrochemical performance, causing it to behave similar to the 1.3% deficient and 3.3% Li deficient samples. The excess lithium content of the samples seem to offset the drop in the electrochemical performance of the samples compared to the ones annealed for 2 hours. When the annealing time is further increased to 20 hours, the 3.3 % deficient material displays a significant reduction in performance, while the 3.3% excess material maintains a discharge capacity > 250 $mAhg^{-1}$. All of the intermediate compositions behave similar to each other, displaying initial discharge capacities close to 220 $mAhg^{-1}$. Although the discharge capacities clearly drop with increasing annealing time, the charge capacities remain close to 300 $mAhg^{-1}$ for most of the materials for all three annealing conditions. Besides the structural reorganization the reduction in discharge capacities can be partially explained by the increased primary particle size, which has a more pronounced effect on the integrated Li_2MnO_3 component of the material [76, 317].

The cycle performance of the materials was tested under a constant current density of 20 mAg^{-1} between 2.0-4.6 V at C/10 and C/3 rate. Details of the cycle and rate test protocol were reported earlier [315].

Figure 39 compares the cycle performance of the materials after annealing for 2, 5 and 20 hours at 900 °C. No significant differences can be observed in the capacity retention of the materials annealed for these three durations, and the materials show very stable cycle performance. The 3.3% deficient material displays the most rapid fade after annealing for 2 hours, probably due to

the least amount of residual lithium in the structure, or more precisely Li_2MnO_3 nano domains, which could help with structure stabilization. When the duration of the annealing heat treatment is further increased leading to a structural reorganization and partial deactivation of Li_2MnO_3 for electrochemical cycling, the capacity fade of this sample shows similar trends to other materials. When the materials are annealed for 2 hours the stoichiometric, excess lithium containing and 0.7% lithium deficient materials display excellent electrochemical performance with discharge capacities, between 195 – 205 $mAhg^{-1}$ after 100 cycles at C/3 rate. When the annealing time is increased to 5 hours only the excess lithium containing materials retain this performance with a discharge capacities after 100 cycles of 195 $mAhg^{-1}$. These capacities indicate essentially identical electrochemical performance, with the difference in the electrochemical performance of the materials being less than the standard deviation of the process [315]. A further increase to 20 hours only allows the sample with 3.3% excess lithium to retain discharge capacities close to 200 $mAhg^{-1}$ after 100 cycles. The originally 1.3% and 0.7% excess lithium samples drop to close to 170 $mAhg^{-1}$ and display a slow activation of the nano domains of Li_2MnO_3, which may have a stabilizing effect on the materials as proposed earlier [84, 318].

Rate capability tests for these materials show similar trends to those observed for the cycle tests. Materials with stoichiometric or deficient lithium content show slightly faster capacity fade in the samples annealed for 2 hours. However, when the annealing time is increased all the materials become more stable. The results indicate that adding 3.3% excess lithium is sufficient to offset structural changes occurring during the increased annealing times and yield good capacity without significant lithium loss from evaporation. Fell *et al*. concluded similarly for cobalt-free layered materials [316].

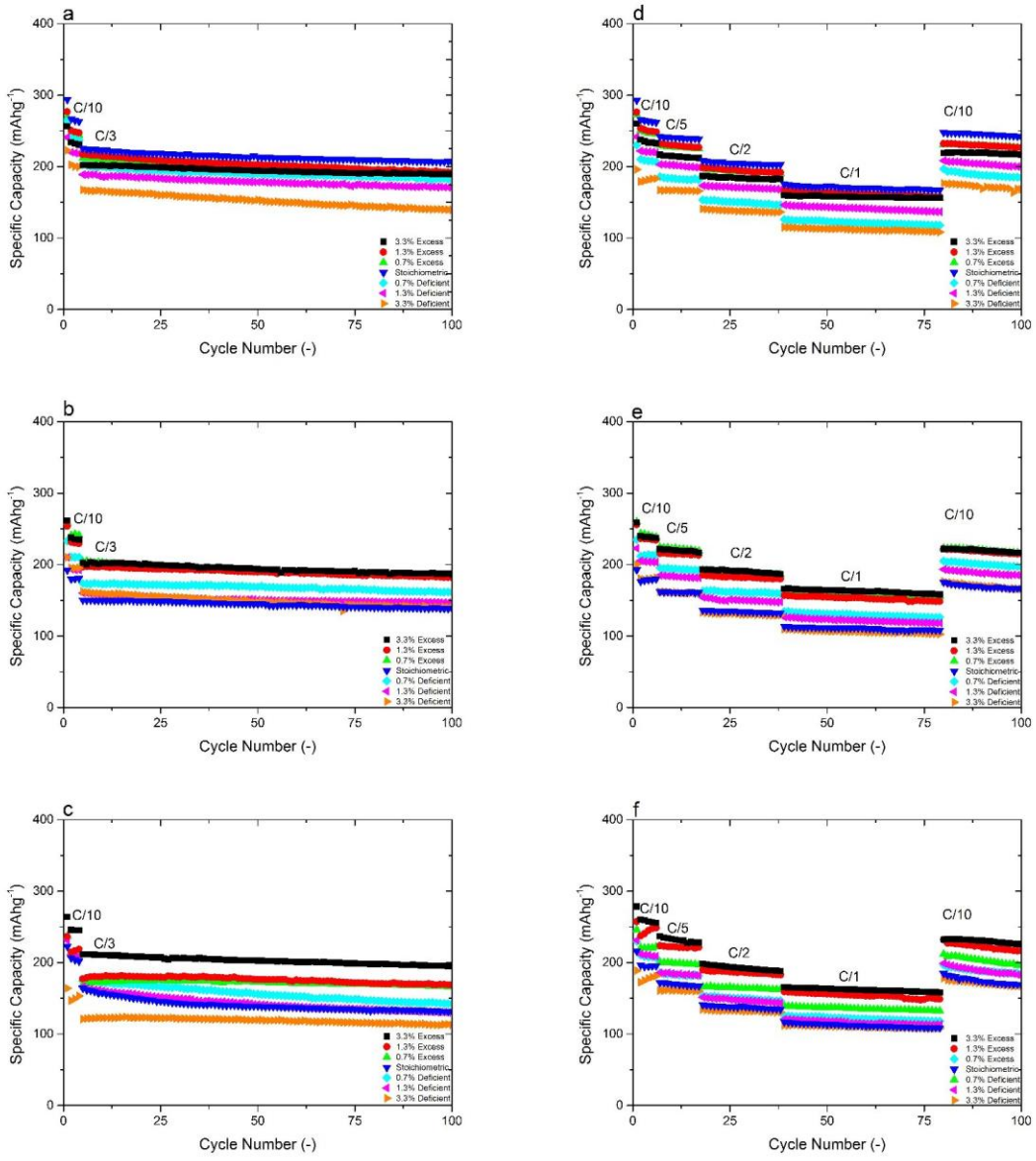

Figure 39 - Cycling performance of 3.3 %, 1.3 %, and 0.7 excess Li, stoichiometric Li, 0.7 %, 1.3 % and 3.3 % deficient Li materials after annealing at (a) 900 °C for 2 hours, (b) 900 °C for 5 hours, (c) 900 °C for 20 hours; Rate capability tests of 3.3 %, 1.3 %, and 0.7 excess Li, stoichiometric Li, 0.7 %, 1.3 % and 3.3 % deficient Li materials after annealing at (d) 900 °C for 2 hours, (e) 900 °C for 5 hours, (f) 900 °C for 20 hours. The solid symbols show discharge capacities.

5.3.2 Voltage Fade

Recently several studies have discussed the voltage fade of layered materials, which is a critical issue that needs to be addressed for these materials before application in PHEVs and EVs [113, 114,

[115, 116, 289]. Due to an internal phase change, which is typically observed as a layered-spinel transition, the voltage profile of the materials continuously decays.

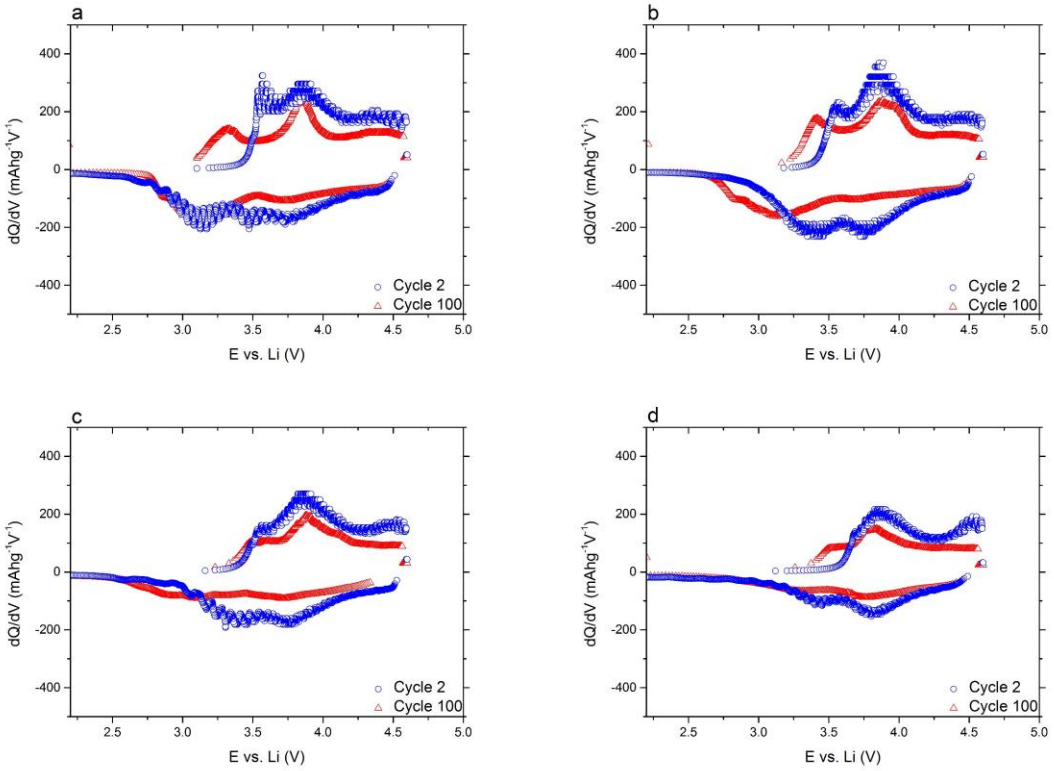

Figure 40 - dQ/dV curves of cycle 1 and cycle 100 of 3.3 % excess Li (a) annealed at 900 °C for 2 hours, (b) 900 °C for 20 hours; and 3.3 % deficient Li annealed at (c) 900 °C for 2 hours, and (d) 900 °C for 20 hours.

According to the results discussed above, the 3.3% excess lithium leads to additional stability with higher overall charge and discharge capacities, while the 3.3% deficient material and/or the long annealing times results in preferential growth of Li_2MnO_3 phase in the material. To determine if these conditions also affect voltage fade, dQ/dV curves are compared for cycles 2 and 100 in Fig. 40 for the 3.3% excess and deficient materials annealed for 2 hours and 20 hours. All the materials display two peaks during cycle 2. Typically these two peaks are associated with the electrochemical activation of the two structural components. The existence of the second

minor peak above 4.5 V indicates that the Li_2MnO_3 structural component undergoes extended activation, which is more pronounced in the lithium deficient samples compared with the excess lithium containing materials. No significant difference can be observed for cycle 100 for the 3.3% excess material annealed at 2 hours and 20 hours. Apparently the excess lithium does not affect the voltage fade of the structure. The 3.3% deficient material annealed for 2 hours already displays significantly smaller new peaks compared to the excess lithium containing materials, especially during the discharge curve around 3.1 V, which indicates a reduction in the layered-spinel conversion of the sample. When the annealing time is increased to 20 hours, the intensity of the new peaks is further reduced, which implies less voltage fade. The electrochemical performance of these materials demonstrates a prolonged activation or partial deactivation of the Li_2MnO_3 phase due to the reorganization occurring in the TM layers, as discussed above, leading to lower capacities. These results imply that the Li_2MnO_3 component has a key role in the voltage fade of the materials, and in order to overcome it, the Li_2MnO_3 structural component needs to be stabilized.

5.4. Conclusions

Lithium excess and deficient $Li_{1.2}Mn_{0.54}Ni_{0.13}Co_{0.13}O_2$ materials were synthesized via spray pyrolysis and annealed between 2 to 20 hours at 900 °C. XRD results indicate that a reduction in the lithium content or an increase in the annealing time leads to a preferential growth of the Li_2MnO_3 phase, coupled to a reorganization of the internal structure in the TM layers in the material in addition to a reduction in the surface area of the samples. Minor compositional variations are sufficient to induce significant changes in the electrochemical performance of the materials. Reduction of the BET surface area is coupled to an internal structural change.

Although the electrochemical performance of the material can be maintained by the addition of excess lithium, which allows some control over surface area, these are likely coupled to minor changes in the internal composition of the material. These changes do not affect the capacity fade and do not provide us with a method to further stabilize the structure. Compared to earlier reports with other synthesis methods our results indicate that 3.3 % excess lithium is sufficient to maintain high discharge capacities over cycling even after 20 hours of annealing at 900 °C for materials synthesized via spray pyrolysis.

With a reduction in lithium content and extended annealing, the Li_2MnO_3 domains phase out, which is coupled to an internal structural reorganization. This results in lower discharge capacities, which is speculated to be due to the reorganization of the transitional metal layers occurring inside the material. The smaller extent of activation of this structural component however leads to a reduction in the voltage fade of these materials, as observed in the dQ/dV plots. These results imply that in order to overcome voltage fade the Li_2MnO_3 structural component needs to be further stabilized.

Chapter 6

Trace level doping to improve capacity retention and prevent voltage fade

6.1. Introduction

Lithium rich layered NMC cathode materials following the composition $x Li_2MnO_3 \cdot (1-x) Li(Ni_{1/3}Mn_{1/3}Co_{1/3})O_2$ have received significant attention as cathode materials for PHEV and EV applications [89, 91, 103, 318]. The materials can deliver capacities in excess of 200 $mAhg^{-1}$ when charged above 4.6 V vs. Li/Li^+ by activating the Li_2MnO_3 structural component. Numerous papers have analyzed the activation process and the large irreversible first cycle capacity loss to understand the simultaneous structural reorganization [10, 85, 92, 94, 114, 153, 217, 316, 319, 320]. Most studies agree that the activation is coupled to a virtual loss of "Li_2O" from the structure, which progresses via a complex mechanism that leads to an irreversible structural transformation. Several studies have discussed the activation process [94, 321, 322, 323]. A study by Simonin and coworkers is of particular importance to the current study as it suggests that during the initial cycle, a new cubic spinel phase forms that is very similar in nature to the original structure and is carried over throughout subsequent cycles influencing the capacity fade of the material [323].

Despite their high capacities, it has been recently determined that these materials display voltage fade due to an internal layered-spinel phase transition, which leads to an overall loss of power from the cathode material throughout cycling [115, 116, 117, 324, 325]. Gu and coworkers found that for cobalt free materials the voltage fade is related to a continuous migration of Ni to the surface coupled to a layered-spinel phase transition [262]. Mohanty *et al.* found a similar transformation of

the materials during high voltage hold and cycling and their in situ XRD studies indicated a layered-spinel phase transformation coupled to formation of a new phase due to migration of transitional metal (TM) ions between the lithium and TM layers [116, 117]. The same authors found that when the upper cutoff voltage is 4.8 V, the cation ordering of the structure diminishes after the activation process; however the cation ordering is retained if the upper cutoff voltage is 4.2 V [324]. Li and coworkers used synchrotron XRD techniques to understand the structural evolution of these materials [113]. Their results suggest a migration of cations between the TM layers similar to other reports. Other studies discussing the gradual activation of the Li_2MnO_3 component, electrolyte additives, surface effects and analogous materials offer further insights to structural causes behind voltage fade [326] [327] [119]. Lee and Manthiram synthesized Ti doped and layered composites of Li, Ni, Mn and Co [328]. Their results indicated that the length of the second plateau during the first cycle, which is typically associated to the activation of the Li_2MnO_3 structural component, governs the voltage fade of the material and thus appropriate design of the cathode chemistry may reduce voltage fade. Earlier several studies (including those from our laboratory) found that compositions with a lower Li_2MnO_3 content display better structural stability and less voltage fade [103, 201, 242, 244, 289, 329]. Significant progress has been made to understand voltage fade, however at this point no solution for stabilizing the materials and overcoming voltage fade has been advanced.

Trace elemental doping is a widely reported technique for stabilizing cathode materials. Of the possible dopants, Mo, Ti, Ag, Mg, Tb, Al and Ru have been reported to improve electrochemical performance, safety characteristics and stability of spinel and layered derivatives of $LiMO_2$ (where M = Mn, Ni, etc.) [330, 331, 332, 333, 334, 335, 336, 337, 338, 339]. Improvements were demonstrated with the addition of Al, Ti, Zr, Cr, Ru, Ga and Na specifically for the layered $xLi_2MnO_3 \cdot (1-$

x)$LiMO_2$ chemistry in terms of rate capability, cycling stability, first cycle Coulombic efficiency and first cycle charge and discharge capacities [318, 340, 341, 342, 343, 344, 345, 346, 347]. Most studies reported that dopants primarily affected the electrochemical properties of the Li_2MnO_3 structural component. While these studies demonstrated improvements of the electrochemical performance with the addition of dopants, none of them discussed their effect on voltage fade. The addition of rare and expensive dopants (e.g., Ru) may improve the cycleability significantly, however, they may not offer cost-competitive solutions for EVs.

Various synthesis methods exist for producing layered cathode materials including co-precipitation, solid-state synthesis, polymer-assisted synthesis, ball milling, combustion synthesis and spray pyrolysis [84, 102, 143, 155, 202, 228, 242, 282, 330]. Among these methods, spray pyrolysis allows for a level of control of product purity that is unlikely to be reproduced by any other synthesis method. In the spray pyrolysis process each droplet acts as a microreactor, accurately preserving the composition of the precursor solution. The main particle formation mechanism is understood to be the one-droplet to one-particle (ODOP) mechanism [348]. No additives are required, which allows accurate control of the dopant profile to trace levels in the product. The lack of precipitating aids also leads to an inherent purity of the product and the high temperature of the process yields product purity that meets or exceeds the purity of the precursor salts [315]. In a recent study we demonstrated that the addition of small amounts of Li (<4 wt%) leads to well-preserved stoichiometries after annealing and that evaporative Li loss during synthesis and annealing is negligible, allowing the ultimate particle stoichiometry to be dictated by the precursor chemistry [329].

In the present study our goal is to use inexpensive materials, including alkali (Na, K), alkali earth (Mg, Ca, Sr, Ba) and Al as dopants to improve the voltage fade of layered $xLi_2MnO_3 \cdot (1-$

x)$Li(Ni_{1/3}Mn_{1/3}Co_{1/3})O_2$. Of particular interest is $Li_{1.2}Mn_{0.54}Ni_{0.13}Co_{0.13}O_2$ (*x = 0.5*), but $Li_{1.09}Mn_{0.43}Ni_{0.24}Co_{0.24}O_2$ (x = *0.2*) *and* $Li_{1.14}Mn_{0.46}AlNi_{0.2}Co_{0.2}O_2$ (x= *0.3*) will also be evaluated.

6.2 Experimental

The precursor solution was prepared by dissolving $LiNO_3$, $Ni(NO_3)_2 \cdot 6H_2O$, $Co(NO_3)_2 \cdot 6H_2O$ (Alfa Aesar) and $Mn(NO_3)_2 \cdot 4H_2O$ (Sigma Aldrich) at the ratio corresponding to the doped $Li_{1.2-x}Mn_{0.54-y}Ni_{0.13}Co_{0.13-z}O_2$ chemistries in deionized water. The list of chemistries used for in the current study is displayed in Table 1 and includes the multidoped samples that will be discussed. Alkali metals are substitutes for Li, alkali earth metals for Co, and Al is a substitute for Mn. The total dissolved salt concentration was fixed at 2.5 $molL^{-1}$ (M). The as-synthesized powders were heat treated at either 850 °C or 900 °C for 2 hours, as indicated in the text.

	Chemical formula	Dopant levels
Alkali	$Li_{1.2-x}Na_xMn_{0.54}Ni_{0.13}Co_{0.13}O_2$	0.01, 0.025, 0.05, 0.1
	$Li_{1.2-x}K_xMn_{0.54}Ni_{0.13}Co_{0.13}O_2$	0.01
Alkali earth	$Li_{1.2}Mn_{0.54}Ni_{0.13}Co_{0.13-z}Mg_zO_2$	0.01, 0.02
	$Li_{1.2}Mn_{0.54}Ni_{0.13}Co_{0.13-z}Ca_zO_2$	0.01
	$Li_{1.2}Mn_{0.54}Ni_{0.13}Co_{0.13-z}Sr_zO_2$	0.01
	$Li_{1.2}Mn_{0.54}Ni_{0.13}Co_{0.13-z}Ba_zO_2$	0.01
Al	$Li_{1.2}Mn_{0.54-y}Al_yNi_{0.13}Co_{0.13}O_2$	0.01
Multi-doped samples	$Li_{1.13}Na_{0.01}Mn_{0.45}Al_{0.01}Ni_{0.2}Co_{0.19}Ba_{0.01}O_2$	0.01
	$Li_{1.13}Na_{0.01}Mn_{0.45}Al_{0.01}Ni_{0.2}Co_{0.2}O_2$	0.01
	$Li_{1.08}Na_{0.01}Mn_{0.42}Al_{0.01}Ni_{0.24}Co_{0.23}Ba_{0.01}O_2$	0.01
	$Li_{1.08}Na_{0.01}Mn_{0.42}Al_{0.01}Ni_{0.24}Co_{0.24}O_2$	0.01

Table 14 - List of doped samples and dopants synthesized in the current study

The annealed powders were characterized by XRD using a Rigaku Diffractometer (Geigerflex D-MAX/A) at a scan rate of 0.04 $°s^{-1}$ between 10° and 80° 2θ. Particle morphology was examined with an FEI Nova 2300 Field Emission SEM.

The cathode film was fabricated according to the procedure reported earlier [239]. A slurry was prepared using 10 wt % polyvinylidene fluoride (PVdF) binder solution (Kureha Corp. Japan), 10 wt % Super-C45 conductive carbon black (Timcal) suspended in 1-Methyl-2-pyrrolidinone (NMP – Sigma Aldrich) and 80 wt% active material. The active material loading density was between 3.0-5.0 $mgcm^{-2}$. Half-cells were assembled for the electrochemical tests using pure lithium anodes and 2500 Celgard membranes (Celgard, LLC). The electrolyte was 1.0 M $LiPF_6$ in a solution of ethylene carbonate/diethyl-carbonate/dimethyl-carbonate (EC: DEC: DMC= 1:1:1 by volume - MTI Corp.). The cells were activated between 2.0 – 4.8 V at 20 mAg^{-1} (C/10) and then cycled between 2.0 – 4.6 V at 20 mAg^{-1} for 4 cycles and then at 66.67 mAg^{-1} (C/3) for

95 cycles. Rate capability tests ranged between 20 mAg^{-1} (C/10) to 200 mAg^{-1} (C/1) according to the testing protocols reported earlier [315].

Electrochemical impedance spectra (EIS) were recorded with a Gamry Reference 600 potentiostat. The AC amplitude was 10 mV and the scan frequency was in the range of 5.0×10^{-4}-1.0×10^{6} Hz. The data were analyzed with the Gamry EChem Analyst.

Electrochemical performance of the powders was evaluated in 2032-type coin cells (Hohsen Corporation) that were assembled in an argon-filled glove box. Cycling tests were performed using an MTI-BST8-WA-type battery tester. All electrochemical tests were performed at 22 °C.

6.3 Results and Discussion

MATERIAL CHARACTERIZATION – The goal of this study was to synthesize doped samples of NMCs, at dopant levels small enough that they do not lead to detectable phase separation or major reductions in electrochemical performance compared to dopant-free samples, with the goal of reducing voltage fade. To this end, Na doped samples were prepared at four different concentrations to experimentally identify the maximum levels of Na that can be introduced without causing phase separation. Figure 41 shows the XRD profiles for $Li_{1.2-x}Na_xMn_{0.54}Ni_{0.13}Co_{0.13}O_2$, where x= 0, 0.025 and 0.05.

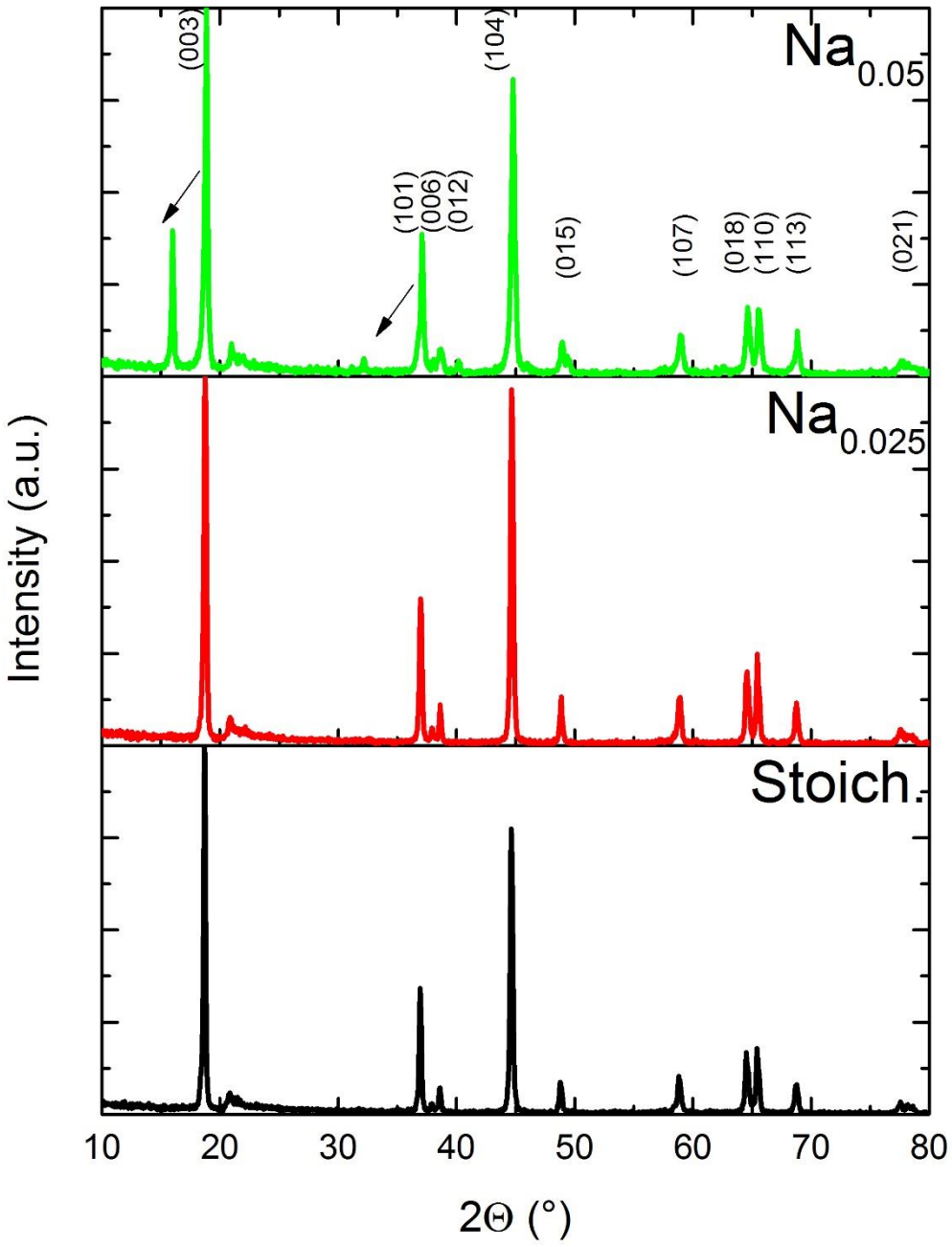

Figure 41 - XRD patterns of $Li_{1.2-x}Na_xMn_{0.54}Ni_{0.13}Co_{0.13}O_2$ for x= 0, 0.025 and 0.05 (x=0.01 and 0.1 are omitted for clarity). The arrows indicate the new phase formation in the sample.

Most peaks are characteristic of the layered-layered chemistry having a rock salt pattern α-$NaFeO_2$ $R\bar{3}m$ structure, with the superlattice reflections between 20-25° 2θ, corresponding to the ordering of the Li_2MnO_3 and $LiMO_2$ components in the TM layers. The clear splitting of the (006), (012) and (018), (110) peaks indicate the layered structure of the material [113].When Na levels reach or exceed 0.05 new peaks in the structure's XRD pattern are found, as indicated by the arrows. These peaks are similar to those reported by Qiu *et al*. and the additional phase is speculated to be a spinel $NaMn_xO_y$, [344] No phase separation can be observed for substituent concentrations up to x = 0.025.

The critical dopant concentration for phase separation is likely dependent on the dopant. Nonetheless, as most of the substituents considered have a smaller ionic radii than Na^+, and phase separation does not occur for Na concentrations below x = 0.025, substituent levels were typically kept at 0.01 for most dopants and were not optimized further. At these low dopant levels no phase separation was observed by XRD for any of the samples, so these spectra are omitted for clarity.

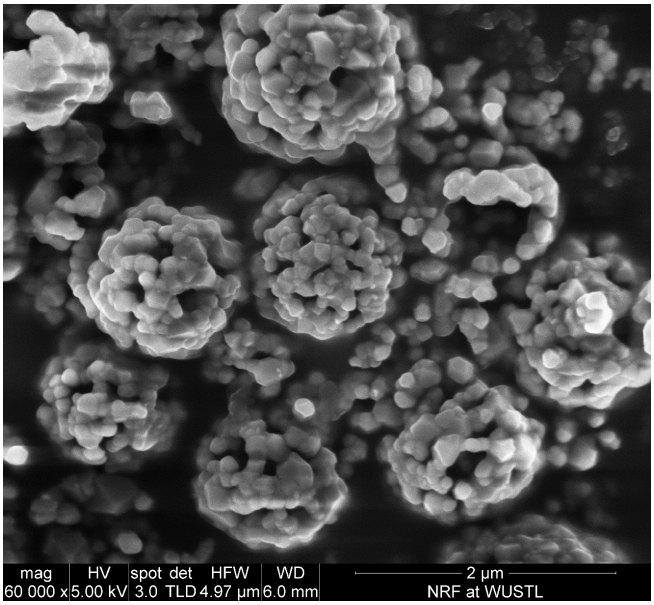

Figure 42 - SEM micrograph displaying a typical morphology for powders synthesized in the current paper. The SEM shows $Li_{1.2}Mn_{0.54}Ni_{0.13}Co_{0.12}Sr_{0.01}O_2$ after annealing at 900 °C for 2 hours.

The low dopant levels did not induce noticeable changes in the particle morphology compared to our earlier reports [289]. Figure 42 shows the typical morphology of the particles synthesized via ultrasonic spray pyrolysis. The secondary particles are porous and primarily spherical in shape, and have a mean particle size around 1.7 µm [289]. Primary particles are between 150-300 nm and are randomly oriented within the secondary particles.

ELECTROCHEMICAL TESTING RESULTS – The electrochemical properties of the cathode materials were tested in 2032 type coin cells vs. Li anodes. A constant-current, constant-voltage cycling protocol was applied for the cells. Details of the cycling and rate capability test protocols were reported earlier [315]. Figure 43 shows the initial charge and discharge curves for $Li_{1.2-x}Na_xMn_{0.54}Ni_{0.13}Co_{0.13}O_2$, where x= 0.01, 0.025, 0.05 and 0.1.

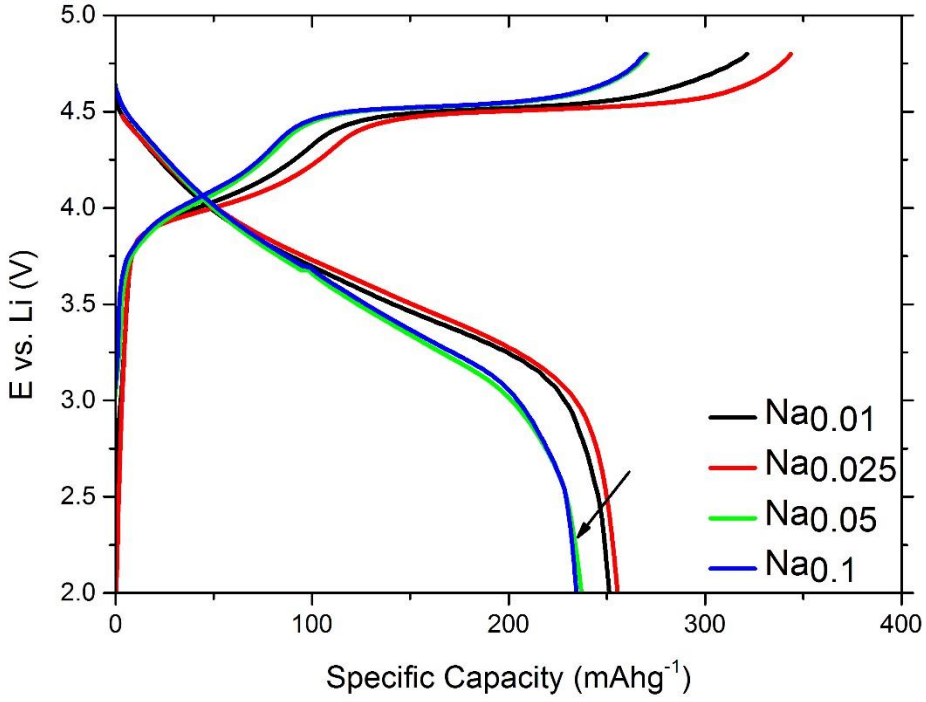

Figure 43 - Initial charge and discharge profiles at a constant current density of 20 mAg^{-1} between 2.0 and 4.8 V for $Li_{1.2-x}Na_xMn_{0.54}Ni_{0.13}Co_{0.13}O_2$, where x= 0.01, 0.025, 0.05 and 0.1.

All of the samples display two plateaus associated with the activation of the two structural components [84]. It can be clearly observed that for x = 0.05 and 0.1 the appearance of the additional spinel phase (as seen in Fig. 41) reduces the charge and discharge capacity of the materials by ~ 20 $mAhg^{-1}$, as indicated by the arrow. These results indicate that phase separation detectable by XRD suggests significant impact on the electrochemical performance of the material. Figure 44 further confirms these observations: comparing the dopant-free (a) sample to the 0.01 Na level the additional peak in the charge profile is reduced. Additional substitution of Na to 0.05 (c) and 0.1 (d) levels leads to the appearance of new and more pronounced peaks in the charge and discharge peaks compared to the 0.01 Na. Therefore, as mentioned earlier, dopant levels of samples were typically maintained at 0.01 to ensure that they would have minimal effect on the charge and discharge capacities of the materials.

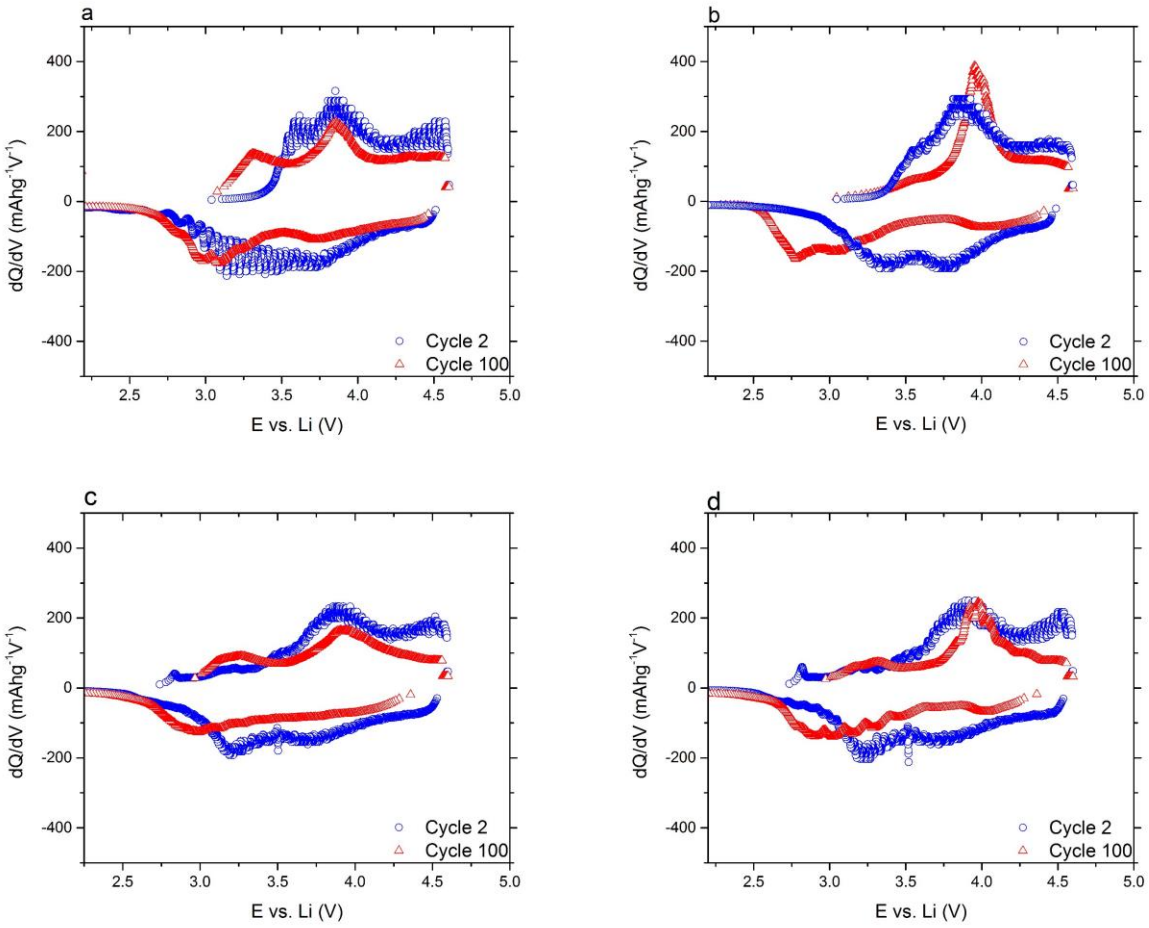

Figure 44 -- dQ/dV curves of cycle 2 and cycle 100 of cells doped with (a) Dopant-free; (b) Na 0.01; (c) Na 0.05; and (d) Na 0.1.

Figure 45 a-c show the initial charge and discharge profiles of the $Li_{1.2}Mn_{0.54}Ni_{0.13}Co_{0.13}O_2$ samples doped with Na, K, Mg, Ca, Sr, Ba and Al after annealing at 900 °C for 2 hours. All of the materials display the two-stage activation corresponding to the two-layered compounds. The initial charge and discharge capacities drop slightly due to the dopants, however, no significant drop can be observed, which confirms that at these dopant levels the capacities of the samples are not affected. Furthermore, the charge and discharge curves do not display additional peaks or shape changes that would imply internal structural changes.

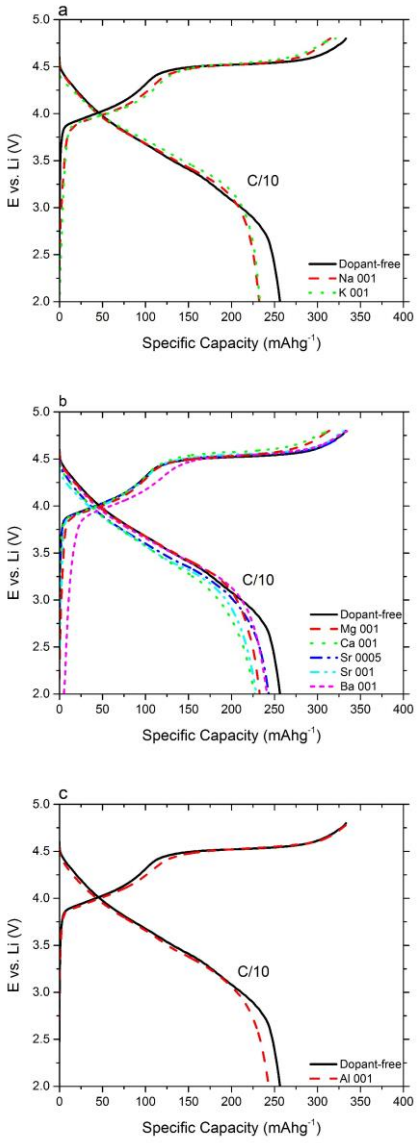

Figure 45 - Initial charge and discharge profiles at a constant current density of 20 mAg^{-1} between 2.0 and 4.8 V for $Li_{1.2}Mn_{0.54}Ni_{0.13}Co_{0.13}O_2$ samples doped with (a) Na and K; (b) Mg, Ca, Sr and Ba; (c) Al.

Figure 46 compares the cycle and rate capability test results for the doped samples. The dopants clearly affect the capacity retention of the materials, as observed by the different slopes for the respective cycle and rate tests. The larger alkali and alkali earth dopants typically cause an extended activation in the Li_2MnO_3 component of the samples, which can be seen by the increasing slope of the cycle tests [326]. Doping with Al clearly leads to an improved capacity retention of the samples, which can be observed both in the cycle and rate capability tests.

Figure 47 compares the charge and discharge curves of cycle 6 and 100 for the Na, Al and Ba doped $Li_{1.2}Mn_{0.54}Ni_{0.13}Co_{0.13}O_2$ samples. The addition of Al leads to a significant improvement in the discharge voltage profiles. While, as shown in Table 15, the dopant-free sample retains 91.5% of its capacity between cycles 6-100 at C/3 rate this is improved to 99.5% by Al doping. This is among the best results for these materials reported in the literature [102, 103, 201]. Other alkali and alkali earth dopants do not lead to similar improvements. Several samples, which are indicated with a * symbol, display an extended activation, probably of the Li_2MnO_3 component, and thus show increasing capacities, which lead to higher observed capacity retention but the discharge capacity of these samples is fading by 100 cycles.

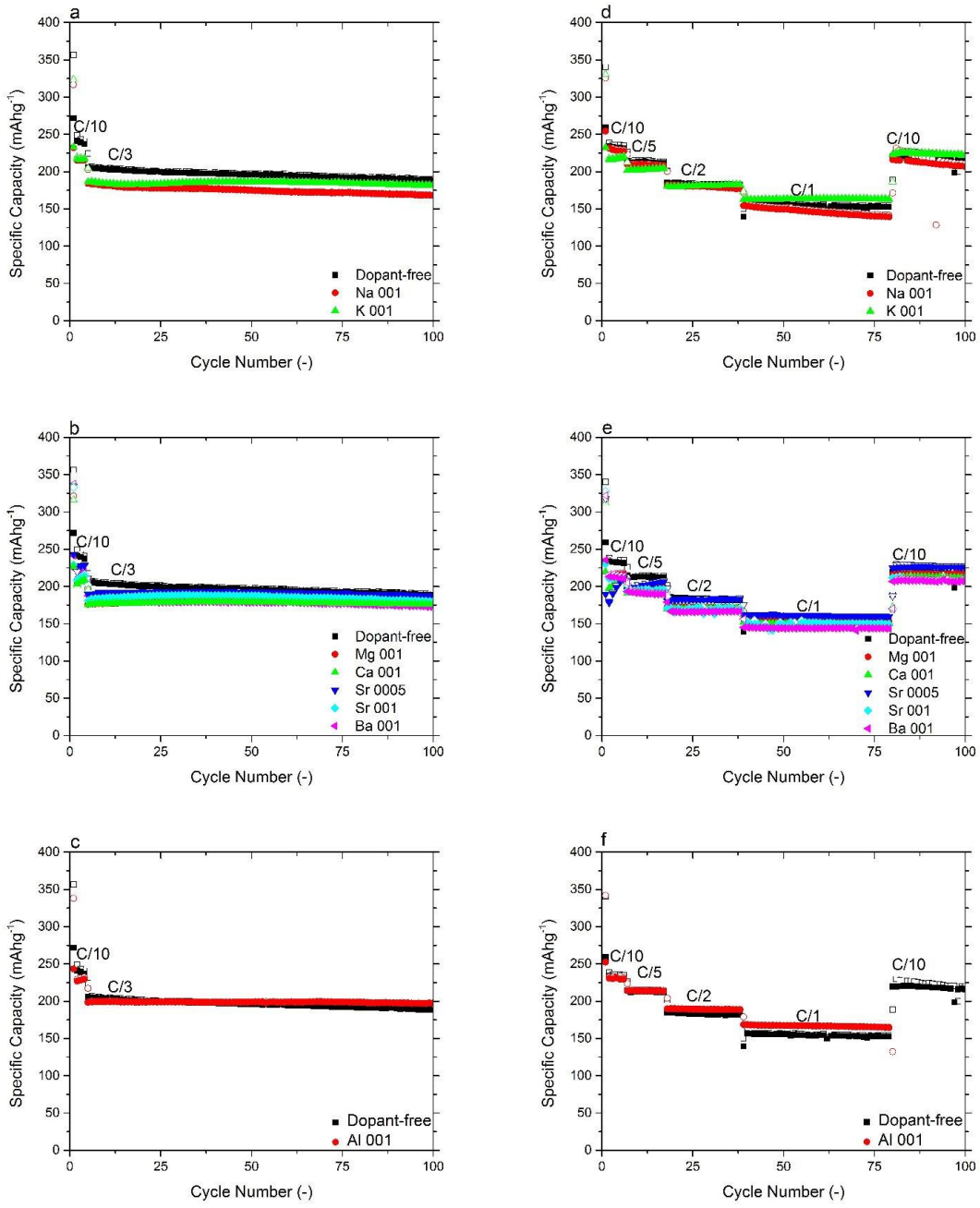

Figure 46 - Cycling performance of cells doped with (a) Na and K; (b) Mg, Ca, Sr and Ba; (c) Al. Rate capability tests of cells synthesized at cells doped with (d) Na and K; (e) Mg, Ca, Sr and Ba; (f) Al. The open/solid symbols show charge/discharge capacities, respectively.

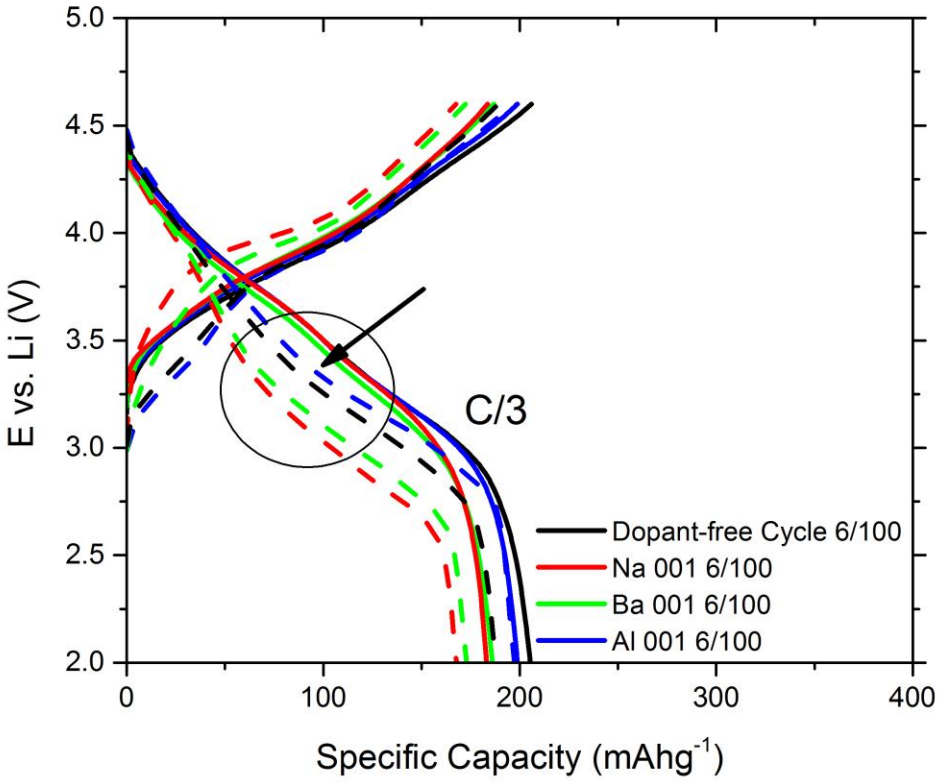

Figure 47 - Comparison of charge and discharge profile of cycle 6 and 100 for the dopant-free, Na, Al and Ba doped samples. The circled area indicates the voltage fade occurring during the discharge cycles.

Dopant	% Capacity Retained between Cycles 5-100 (%)
$Li_{1.2}Mn_{0.54}Ni_{0.13}Co_{0.13}O_2$	91.5
$Li_{1.19}Na_{0.01}Mn_{0.54}Ni_{0.13}Co_{0.13}O_2$	91.1
$Li_{1.19}K_{0.01}Mn_{0.54}Ni_{0.13}Co_{0.13}O_2$*	97.3
$Li_{1.2}Mn_{0.54}Ni_{0.13}Co_{0.12}Mg_{0.01}O_2$*	104.7
$Li_{1.2}Mn_{0.54}Ni_{0.13}Co_{0.12}Ca_{0.01}O_2$*	100.1
$Li_{1.2}Mn_{0.54}Ni_{0.13}Co_{0.12}Sr_{0.01}O_2$*	99.4
$Li_{1.2}Mn_{0.54}Ni_{0.13}Co_{0.13-z}Ba_zO_2$	92.2
$Li_{1.2}Mn_{0.53}Al_{0.01}Ni_{0.13}Co_{0.13}O_2$	99.4

Table 15 - The effect of dopants on the capacity retention of the samples. * indicates samples where due to the slow activation of the electrochemically active structures the capacities increased over time.

The dQ/dV curves of the samples are compared for cycle 2 and 100 in Figure 48. The alkali and alkali earth metals are seen to display reduced spinel phase peaks, primarily during the charge, while showing worse performance in the discharge curves at 100 cycles. Ca and Sr doping seems to improve the phase transition during discharge as well, while having a smaller effect on the charge performance. Interestingly, despite the ability to improve capacity retention, Al does not appear to reduce the growth of the spinel charge peak that indicates voltage fade. This implies that Al doping improves capacity retention via a different mechanism, for example by reducing the strains along the *c* axis during cycling, as reported for several $LiMn_xO_y$ based spinel materials [349, 350].

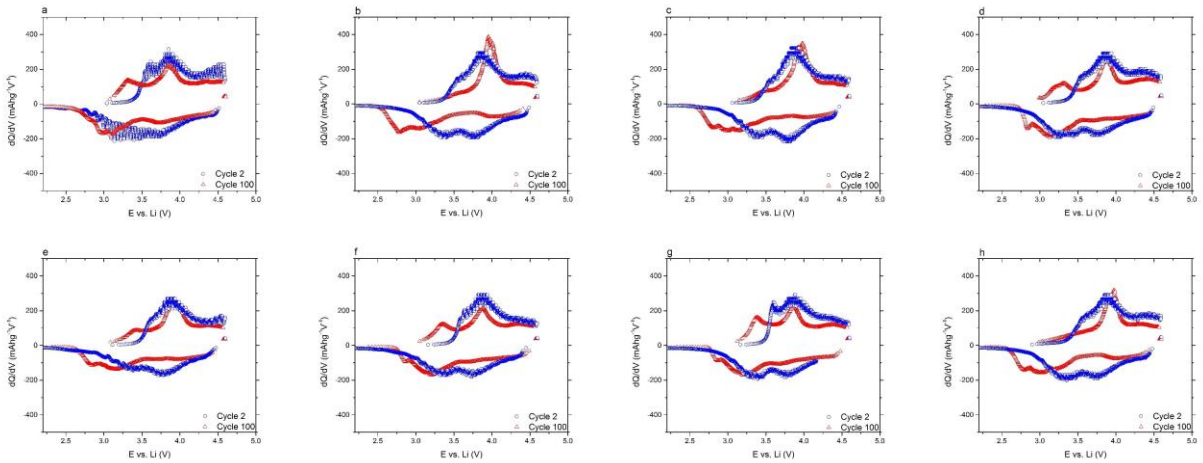

Figure 48- dQ/dV curves of cycle 1 and cycle 100 of cells doped with (a) Dopant-free; (b) Na 0.01; (c) K 0.01; (d) Al 0.01; (e) Mg 0.01; (f) Ca 0.01; (g) Sr 0.01; and (h) Ba 0.01.

DOPANT CHEMISTRY – In the current study three dopant categories were studied: alkali metals, alkali earth metals and Al. As indicated in the Introduction, the dopants are primarily expected to affect the stability of the Li_2MnO_3 structural unit of the materials. The average anticipated oxidation states of the transitional metals are assumed to be Ni^{+2}, Co^{+3} and Mn^{+4} in the parent structures [103]. At the same time it is understood that the situation is clearly more complex as MAS-NMR results indicate multiple oxidation states are present in the materials concurrently [92]. Therefore these assumptions will only provide guidance to our discussion. The ionic radii in the discussion are based on those defined by Shannon [351].

Substituting Li^+ with an alkali metal primarily improves the stability of the structure due to steric effects caused by the larger size of the dopant, as they also carry a single positive charge. Replacing Li^+ ions in the interstitial sites with larger alkali metals leads to an increase in the residual ions in the interstitial sites after charging because often the dopants do not participate in the intercalation reaction, as reported for Na doping [346, 352]. Kim *et al.* found that Li_xMO_2 based structures have strong driving forces and low energy kinetic paths to transform into spinel structures and that these driving forces do not exist for Na-based counterparts of the materials [353].

These spinel-transformation reactions are speculated to proceed via transitional metal hopping. The migration of the TM (e.g., Mn) ions has to be coupled to the migration of Li^+ ions, which becomes hindered due to the larger size of the Na^+ ions. This effect is expected to be even more pronounced for the larger K ions. Other alkali metals, Rb and Cs, were omitted from the present study due to their high cost compared to Na and K, but it is anticipated that Rb and Cs doping would lead to similar observations. Alkali metal substitutions are expected to lead to a minor loss of capacity due to a small reduction in the amount of intercalatable lithium ions.

Substituting Mn with Al leads to a slight reduction in the electrochemically active cathode material content of the sample with aluminum having only a single $^{+3}$ oxidation state. Al is similar to Mn in size and therefore the similar size allowing substitution and the single oxidation state may be the reasons behind the stability of Al doped compounds. Several studies have demonstrated the beneficial effect of Al on stabilizing the cathode material primarily by creating an Al-coated surface to prevent surface dissolution of the Mn-based active cathode material [111, 112, 354]. Additionally, replacing Mn^{+4} with Al^{+3} ions should lead to an increase in the average oxidation state of the Mn ions. To maintain charge neutrality this beneficial effect can mitigate the potentially arising Jahn-Teller distortion effects [93].

Alkali earth metals (Mg, Ca, Sr, Ba) have larger ionic radii than Co^{3+} atoms. Their introduction to the structure has been shown to improve the stability similar to Al and may reduce the capacity to a minor extent by reducing the available intercalation sites due to their single +2 oxidation state [278, 331, 333, 335, 355]. We have observed by comparing the electrochemical performance of $Li_{1.2}Mn_{0.54}Ni_{0.13}Co_{0.13}O_2$ synthesized from cobalt nitrates supplied by different vendors, that samples synthesized from cobalt nitrate having a significant amount of Ba contaminant displayed enhanced cycling stability compared to their Ba-free counterparts. The

alkali earth metals (e.g., Mg) have larger ionic radii and smaller electronegativity than cobalt, demonstrated that by initiating a short range ordering in $LiNi_{0.80}Co_{0.15}Al_{0.05}O_2$ enhance cycle stability can result due to the stronger bonding [335, 351]. Substituting Co^{+3} for M^{+2} ions is also expected to increase the average oxidation state of the transitional metal ions originally residing in the structure thereby improving the stability of the materials. Therefore, we expect a stabilizing effect of these dopants on the apparent layered-spinel transformation, especially when replacing Co with the larger alkali earth metals (Sr, Ba), due to a combination of steric and charge effects.

Several earlier reports experimentally observed that a reduction in the Li_2MnO_3 content of the materials leads to reduced voltage fade and these studies identified this structural component as a major contributor leading to the voltage fade of the layered chemistry [242, 328]. With this in mind, we next evaluate the effect of these dopants on $x Li_2MnO_3 \cdot (1-x)\ Li(Ni_{1/3}Mn_{1/3}Co_{1/3})O_2$ chemistries, where $x \leq 0.5$, with the understanding that these samples are expected to be more easily stabilized and therefore are of higher practical importance. Since, as noted above, for both alkali and alkali earth doping reduces the new peaks arising in the dQ/dV curves throughout the charge cycling, and for Al doping there was a significant improvement in capacity retention, we next chose to synthesize Na, Al and Ba triple-doped samples.

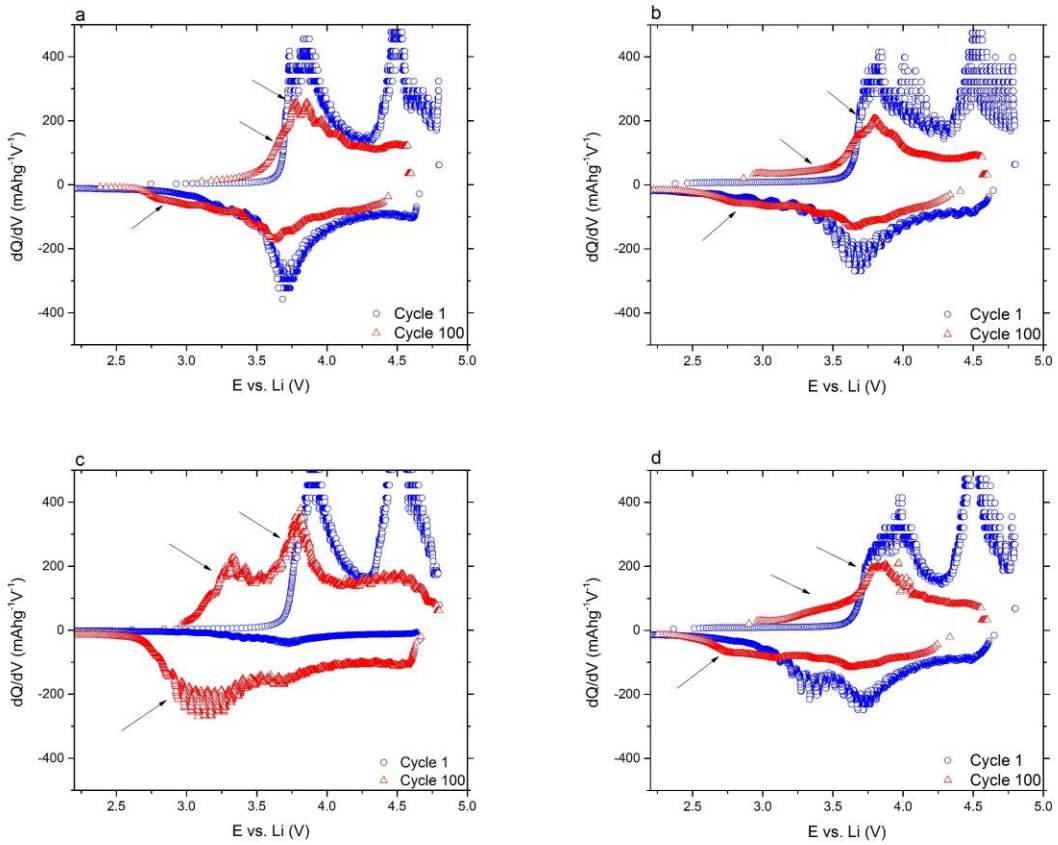

Figure 49 - dQ/dV curves of cycle 1 and cycle 100 of (a) $Li_{1.09}Mn_{0.43}Ni_{0.24}Co_{0.24}O_2$ (850 °C); (b) $Li_{1.08}Na_{0.01}Mn_{0.42}Al_{0.01}Ni_{0.24}Co_{0.23}Ba_{0.01}O_2$ (800 °C); (c) $Li_{1.14}Mn_{0.46}AlNi_{0.2}Co_{0.2}O_2$ (850 °C); and (d) $Li_{1.13}Na_{0.01}Mn_{0.45}Al_{0.01}Ni_{0.2}Co_{0.19}Ba_{0.01}O_2$ (800 °C). The temperatures after the compositions indicate the annealing temperature of the samples.

Figure 49 compares the dQ/dV curves of the dopant-free and triple-doped $Li_{1.09}Mn_{0.43}Ni_{0.24}Co_{0.24}O_2$ and $Li_{1.14}Mn_{0.46}Ni_{0.2}Co_{0.2}O_2$ samples for cycles 1 and 100. Both materials display significant improvement compared to the dopant-free materials and less spinel phase evolution both in their charge and discharge profiles as indicated by the arrows. To the best of the author's knowledge these results demonstrate for the first time experimental improvements to the voltage fade of the layered chemistries.

For the $Li_{1.09}Mn_{0.43}Ni_{0.24}Co_{0.24}O_2$ and $Li_{1.14}Mn_{0.46}Ni_{0.2}Co_{0.2}O_2$ samples the improvements in voltage fade compared to $Li_{1.2}Mn_{0.54}Ni_{0.13}Co_{0.13}O_2$ can be summarized as follows. Lowering the Li_2MnO_3 content of the material reduces the structural component that is prone to exhibit a phase

change. The residual Li_2MnO_3 component is electrochemically activated when charged above 4.6 V as indicated by the peak around 4.5 V in Fig. 48 in all the samples. The addition of Al and Ba is expected to increase the average oxidation state of manganese and thus improve the stability of the material. Na doping causes some of the lithium sites to have residual interstitial Na^+ present even at a completely charged state. These dopants apparently reduce the rate of transitional ion migration between the TM and Li layers, thereby improving the stability of the material. Similar improvements are expected for the $Li_{1.2}Mn_{0.54}Ni_{0.13}Co_{0.13}O_2$ chemistry and these studies are currently under way.

ELECTROCHEMICAL IMPEDANCE TESTING RESULTS – EIS spectra of single-doped $Li_{1.2}Mn_{0.54}Ni_{0.13}Co_{0.13}O_2$ cells were recorded after 30 cycles with the Abraham voltage fade protocol [327]. Examples of Na, K, Al, Mg, Sr and Ba doped results are displayed in Figure 50 and the insets show the amplified first semi-circle. Figure 50 (d) shows the equivalent circuit model that was applied to analyze the data. The equivalent circuit model contained the following circuit elements: (*i*) resistance from the electrolyte, R_s; (*ii*) solid electrolyte interface resistance, R_{SEI}; (*iii*) the capacitance of the SEI layer, C_{SEI} with a non-ideality factor α_{SEI}; (*iv*) charge transfer R_{ct} at the surface film – particle bulk interface; (*v)* double-layer capacitance, C_{DL} with a non-ideality factor α_{DL}; and (*vi*) a resistance coefficient and its characteristic frequency for diffusion/Warburg impedance R_D and ω_D. Each Nyquist plot displays two semicircles and a diffusion tail. The first semicircle in the high frequency region is primarily related to the migration of Li^+ ions through the surface film and the conductivity of the material [356, 357, 358]. The second lower frequency semicircle can mainly be related to contributions from the surface kinetics of the sample and are overlapping with the diffusion occurring in the Warburg region of the spectra. The Warburg region is mainly due to the solid-state diffusivity of the Li ion in the cathode material. The large charge transfer resistance of the samples suggests that this may have a more dominant rate limiting effect compared to the diffusivity of Li in the material. Nevertheless, all of the samples show that doping significantly improves the conductivity of these cells by lowering the impedance of the cells. The high impedance of the dopant-free samples is speculated to be the

result of the high purity of the samples, which is due to the intrinsic purity of the spray pyrolysis method of synthesis, and additional surface effects, such as SEI layer formation during decomposition and voltage interruptions during cycling.

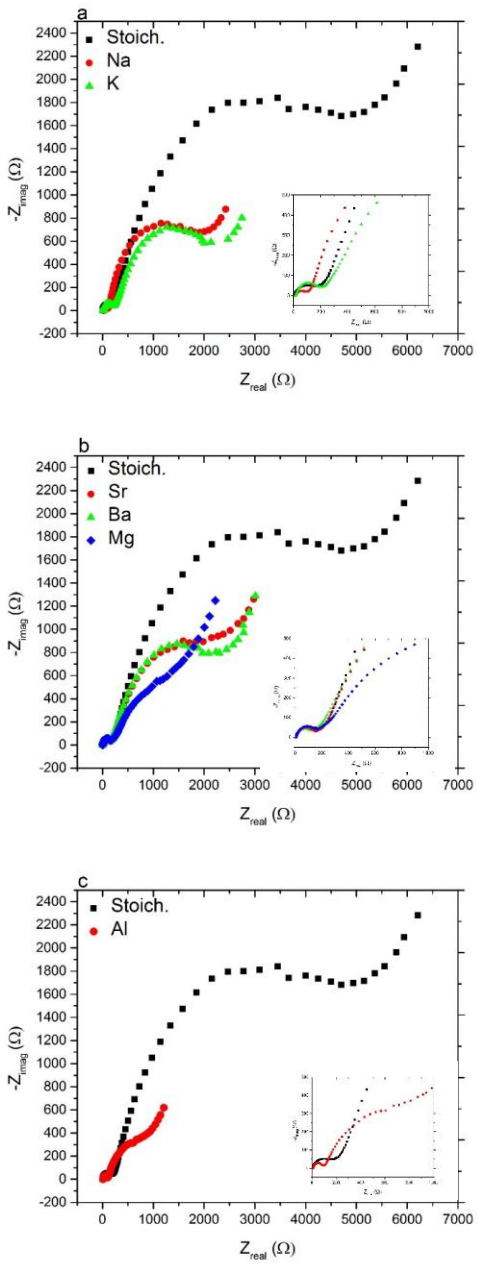

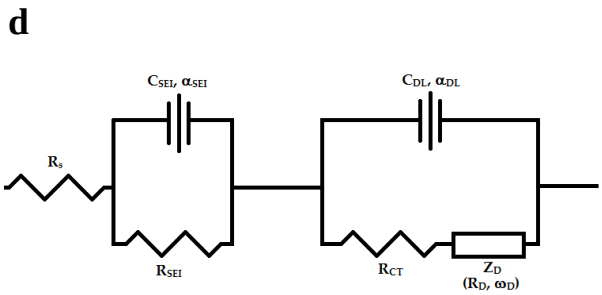

Figure 50 - Nyquist plots of doped $Li/Li_{1.2}Ni_{0.13}Co_{0.13}Mn_{0.54}O_2$ cells measured between 2.0 V and 4.6 V of cells after 30 cycles in a discharged state for (a) Na 0.01 and K 0.01; (b) Mg 0.01, Sr 0.01 and Ba 0.01; and (c) Al. The insets show the shape of the first semi-circles. The AC amplitude was 10 mV and scan frequency was in the range of 5.0×10^{-4}-1.0×10^{6} Hz. (d) The equivalent circuit model used for the interpretation of the EIS spectra.

6.4 Conclusions

Layered lithium battery cathode materials were synthesized via spray pyrolysis. By taking advantage of the unique ability of spray pyrolysis to control impurities to small levels, inexpensive alkali, alkali earth and aluminum doping were tested to improve the capacity retention and voltage fade of the layered materials. Alkali and alkali earth metals were found to reduce the new phase formation either during the charge or the discharge profiles while on some occasions leading to additional phase formation and thus affect voltage fade, while aluminum doping improves capacity fade. Alkali dopants are speculated to improve the voltage fade primarily via steric effects as these dopants are unlikely to be intercalated during charge discharge testing. Alkali earth metals are speculated to increase the average oxidation state of transitional metal ions in the sample and thus improve voltage fade. Samples triple-doped with Na, Ba and Al displayed less voltage fade character in their charge and discharge voltage curves after 100 cycles compared to pristine materials and the multidoping prevented the unwanted structural changes in the sample. Although voltage fade was not completely overcome in the current study, it is anticipated that further improvements can be obtained by adjusting individual dopant levels.

Chapter 7

Development of a Spray Pyrolysis Process for the Production of Non-hollow Battery Materials

7.1 Introduction

To attain high quality low-cost batteries, inexpensive, scalable and highly reproducible processes are needed for synthesizing electrochemically active materials. Conventional synthesis methods for battery materials include sol-gel processes, solid-state synthesis and co-precipitation [13, 86, 88, 94]. Co-precipitation can deliver materials with excellent electrochemical performance and high tap density (> 1.0 gcm^{-3}) at a laboratory scale. Yet, the process presents challenges in terms of scale up, including long processing times during precipitation (up to 24 hours), extended annealing conditions because of post-lithiation (> 5-20 hours at 900-1000 °C), excessive waste products due to several purification steps, and issues related to product uniformity and reproducibility.

Recently, spray pyrolysis has been developed for the production of layered cathode materials and the materials have shown excellent electrochemical performance, comparable to or exceeding that of materials produced by co-precipitation [239, 242]. Spray pyrolysis is a fast and inexpensive method of producing multicomponent oxides, including lithium ion battery cathode materials [169, 201, 223]. The process is robust and delivers uniform materials due to the one droplet - one particle conversion mechanism. The main process variables can also be controlled accurately [315]. Typical process times in the reactor are on the order of a few seconds, and a post heat treatment

at 800-900 °C for 2 hours is typically sufficient to obtain the desired crystallinity and electrochemical performance. This offers significant cost advantages compared to other synthesis methods, and the materials display excellent reproducibility. A recent study by Oljaca and coworkers from Cabot Corp. offered a comprehensive comparison of materials synthesized via spray pyrolysis and co-precipitation, demonstrating distinct advantages for spray pyrolysis [203]. Despite the advantages of spray pyrolysis, hollow and deformed spheres are typically produced when the secondary particles are larger than approximately 2 μm. These particles form from the larger droplets and are hollow due to the rapid surface precipitation and melt formation encountered in the process [169, 170, 226]. If hollow spheres can be eliminated, spray pyrolysis offers significant advantages over other synthesis processes in terms of process and equipment costs.

This paper presents an approach to avoid hollow sphere formation in a scalable process via a flame-assisted slurry spray pyrolysis process. The process is termed Flame Assisted Spray Technology - Slurry Spray Pyrolysis (FAST - SSP) [359]. Herein we report on the process and the electrochemical properties of $Li_{1.2}Mn_{0.54}Ni_{0.13}Co_{0.13}O_2$ synthesized via FAST - SSP.

7.2. Experimental

Figure 51a shows the steps of the FAST - SSP process. First, the precursor solution is employed in conventional spray pyrolysis to form particles of the desired material. These materials are then milled to break-up hollow spheres and the powder is converted into a slurry with a precursor solution that has the same composition as the original precursor solution. This slurry becomes the precursor for subsequent spray pyrolysis.

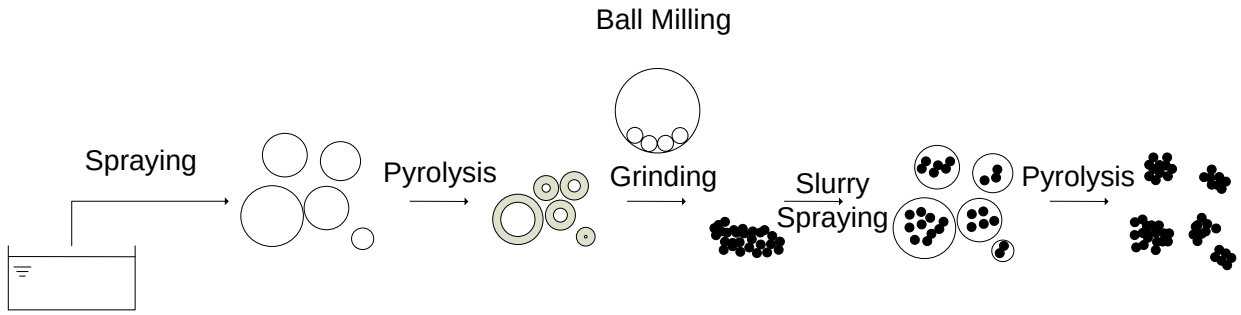

Figure 51a - Block flow diagram of the FAST - SSP process.

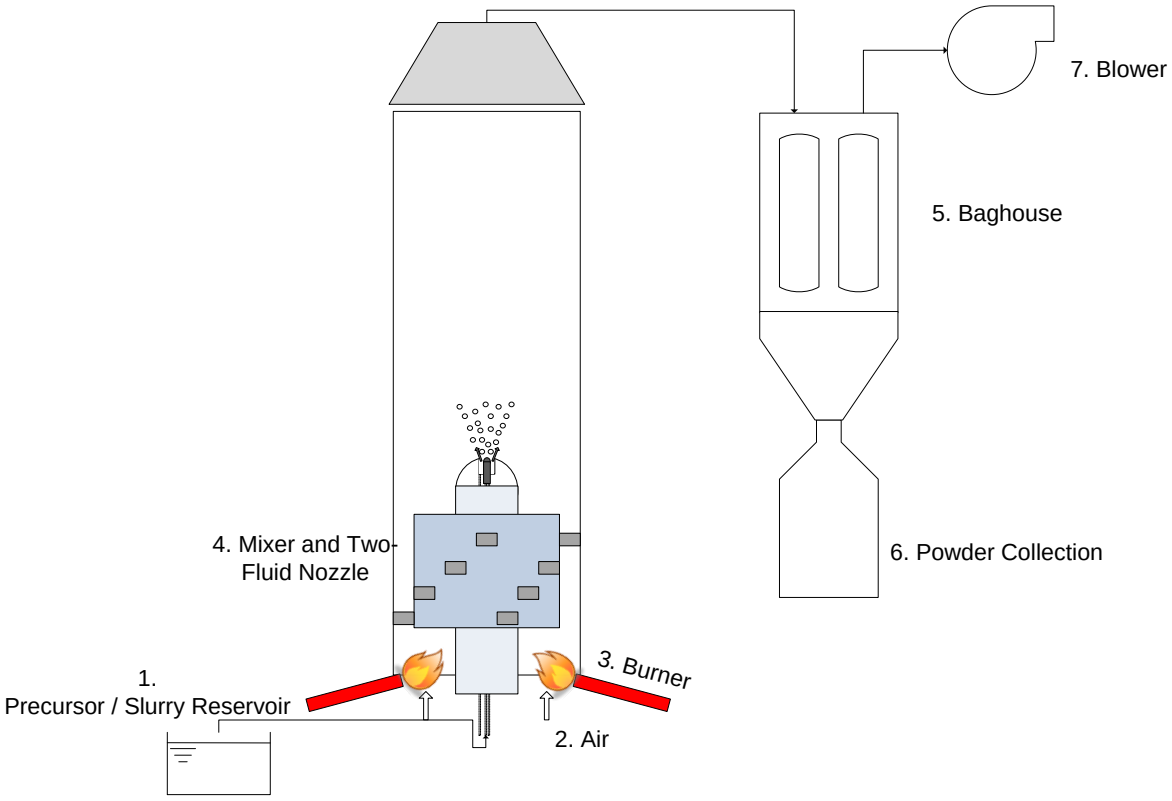

Figure 51b – Schematic diagram of the FAST-SSP setup. (1) Precursor/Slurry reservoir; (2) excess air supply; (3) burners; (4) mixer and two-fluid nozzle; (5) baghouse filter; (6) powder collection; and (7) blower.

The spray pyrolysis experimental setup is displayed in Fig. 1b [239, 240]. The system, termed Flame Assisted Spray Technology (FAST), incorporates a back flame for heating and a two-fluid nozzle (Delavan Inc.) to generate the spray. The feed rate of the nozzle is adjusted to produce materials at 50 gh^{-1}. The typical residence time in the system is about 1s and the temperature at the exit of the reactor is approximately 500-600 °C.

The precursor solution was prepared by dissolving $LiNO_3$, $Mn(NO_3)_2 \cdot 4H_2O$, $Ni(NO_3)_2 \cdot 6H_2O$ and $Co(NO_3)_2 \cdot 6H_2O$ (Alfa Aesar) in deionized water at the precursor ratio corresponding to the chemistry for $Li_{1.2}Mn_{0.54}Ni_{0.13}Co_{0.13}O_2$. The total dissolved salt concentration was fixed at 2.5 $molL^{-1}$ (M).

The as-synthesized samples after FAST-SSP were subject to an annealing heat treatment at 900 °C for 2 hours. The annealed powders were characterized by XRD using a Rigaku Diffractometer (Geigerflex D-MAX/A) at a scan rate of 0.04 $°s^{-1}$ between 10° and 80° 2θ. The tapped powder density of the material was measured by a Quantachrome Autotap tapped density analyzer. Particle morphology was examined with an FEI Nova 2300 Field Emission SEM. The interior morphology of the product powder was observed by embedding the powder in an epoxy-based resin. Two μm thick sections were cut by a Leica Ultramicrotome and the sections were examined by SEM microscopy.

Cathode film fabrication was performed according to the procedure reported earlier [239]. The cathode slurry was prepared using 10 wt% polyvinylidene fluoride (PVdF) binder solution (Kureha Corp. Japan), 10 wt% Super-C45 conductive carbon black (Timcal) suspended in 1-Methyl-2-pyrrolidinone (NMP – Sigma Aldrich) and 80 wt% active material. The active material loading density was between 2.5 - 4.0 $mgcm^{-2}$. Half-cells were assembled for the electrochemical tests using pure lithium anodes and 2500 Celgard membranes (Celgard, LLC). The electrolyte

solution was 1.2 M $LiPF_6$ in ethylene carbonate/ethyl-methyl-carbonate solution (EC: EMC = 3:7 by weight) (Tomiyama High Purity Chemicals). The cells were activated between 2.0 – 4.8 V at 20 mAg^{-1} (C/10) and then cycled between 2.0 – 4.6 V at 20 mAg^{-1} and then 66.7 mAg^{-1} (C/3). Rate capability tests ranged between 20 mAg^{-1} (C/10) and 200 mAg^{-1} (C/1) according to the protocols reported earlier [315].

The electrochemical performance of the powders was evaluated in 2032-type coin cells (Hohsen Corporation) assembled in an argon-filled glove box. Cycling tests were performed using an MTI-BST8-WA-type battery tester. The electrochemical tests were performed at 22 °C.

7.3 Results and Discussion - Material characterization

In Fig. 52 the XRD patterns for the $Li_{1.2}Mn_{0.54}Ni_{0.13}Co_{0.13}O_2$ cathode materials synthesized using the FAST-SSP are compared with the same material synthesized using a standard Aerosol Flow Reactor (AFR) [289]. Most of the diffraction peaks can be indexed according to the α-$NaFeO_2$ (R-3m) structure. The splitting of the (006), (012) and (018), (110) peaks indicate a layered structure. The broad peak between 20-25° 2θ is characteristic of the superlattice ordering between the $LiMn_{0.33}Ni_{0.33}Co_{0.33}O_2$ and the Li_2MnO_3 components that form the layered composite cathodes. [113]. Clearly, no significant difference can be observed in the XRD pattern of the materials synthesized by the two methods, despite the fact that the production rates of the FAST-SSP system are 50 times greater than that of the AFR system.

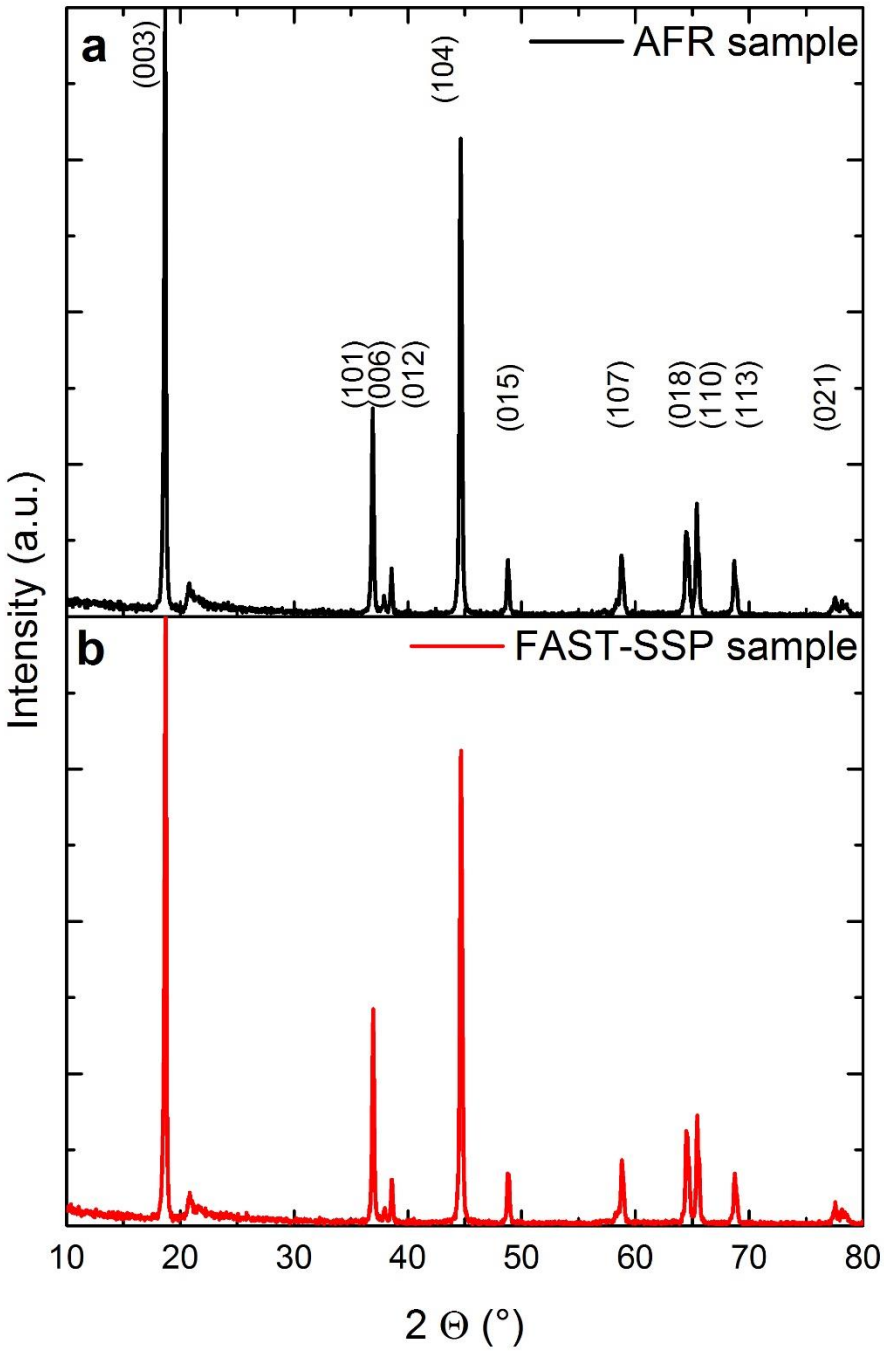

Figure 52 - Comparison of the XRD patterns of $Li_{1.2}Mn_{0.54}Ni_{0.13}Co_{0.13}O_2$ synthesized via (a) AFR and (b) FAST-SSP.

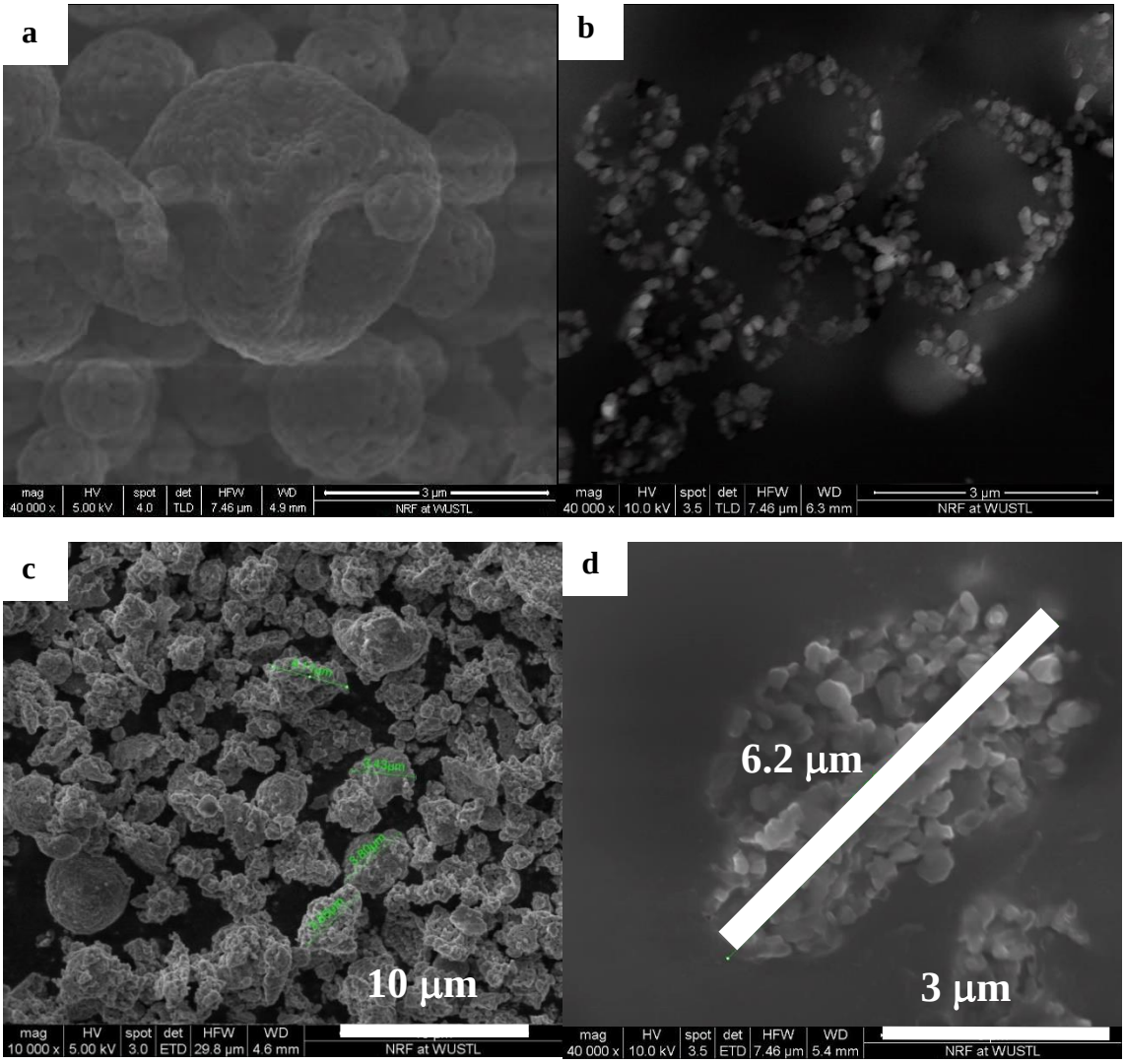

Figure 53 - Morphology of $Li_{1.2}Mn_{0.54}Ni_{0.13}Co_{0.13}O_2$ synthesized via (a) AFR; (b) interior structure after AFR synthesis; (c) FAST–SSP; (d) interior structure after FAST-SSP, as observed by SEM.

The typical morphology of particles produced from the AFR is spherical provided that the particles are less than 2 microns [239]. Larger particles can be deformed due to their hollow interior, as shown in Fig. 53a. Figure 53b shows the microtome of the particles produced by spray pyrolysis and the hollow interior is clearly visible.

Figure 53c shows the morphology of the particles synthesized via FAST-SSP. The secondary particles are non-spherical and display a relatively wide size distribution ranging from 1 – 10 μm, with a mean particle size between 4-5 μm. The primary particle size is between 200 – 400

nm. The interior morphology of the particles is shown in Figure 53d. These results show significant improvements in morphology compared to materials synthesized via ultrasonic spray pyrolysis [315]. Due to the slurry spraying step the interior morphology of larger particles is either solid (and porous) or the interior hollowness is significantly reduced. Particles above 6 μm in size with a solid (non-hollow) interior morphology can be clearly observed. To the best knowledge of the authors these are the largest non-hollow particles synthesized via spray pyrolysis. The tapped powder density of the material after FAST-SSP was found to be 1.05 gcm^{-3} compared to 0.4-0.6 gcm^{-3} obtained by ultrasonic spray pyrolysis [315]. The non-hollow morphology is clearly responsible for the improvement in the tapped density of the material.

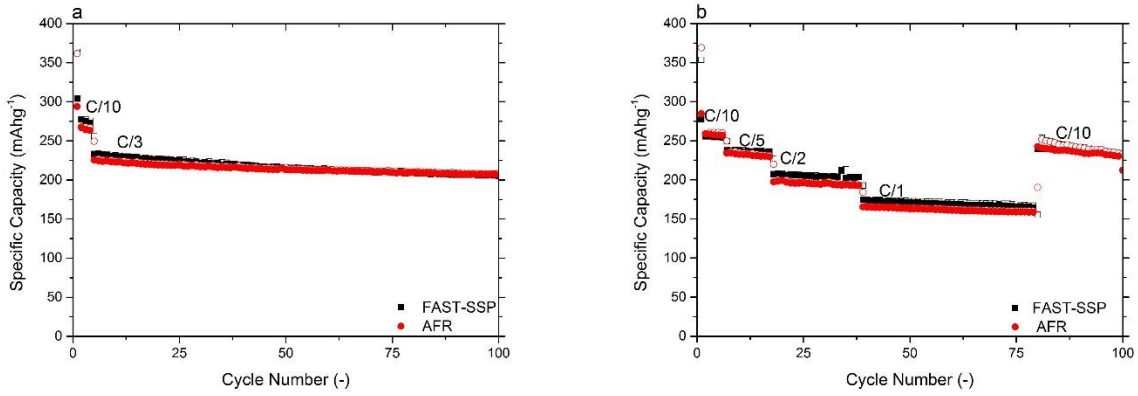

Figure 54 - Comparison of (a) cycling and (b) rate capability of $Li_{1.2}Mn_{0.54}Ni_{0.13}Co_{0.13}O_2$ synthesized via FAST-SSP and AFR.

Figure 54 compares the cycle and rate capability test results for materials synthesized via FAST-SSP with those via the AFR. These results indicate that the electrochemical performance of the materials synthesized via FAST-SSP are excellent, similar to those obtained when synthesized via the AFR or co-precipitation [100]. The reproducibility of the process was evaluated by synthesizing five batches of $Li_{1.2}Mn_{0.54}Ni_{0.13}Co_{0.13}O_2$ under identical synthesis conditions on five different days. The electrochemical performance was evaluated for each batch in cycle tests and the standard deviation of the discharge capacities at C/3 rate was ~11 $mAhg^{-1}$. Figure 4a shows that after 100 cycles at C/3 rate the discharge capacity exceeds 200 $mAhg^{-1}$. Rate capability tests indicate discharge capacities > 170 $mAhg^{-1}$ at 1C rate. No irreversible capacity loss was observed during the rate capability tests. It is clear that improvements in production rate, morphology and tapped density can be achieved without compromising the electrochemical performance of the material.

7.4 Conclusions

A novel slurry spray pyrolysis process (FAST-SSP) was demonstrated by synthesizing powders of the layered $Li_{1.2}Mn_{0.54}Ni_{0.13}Co_{0.13}O_2$ material. The process shows high potential for large

scale synthesis of cathode materials and yields improved tapped density compared to traditional spray pyrolysis. For the layered materials the tapped density increased from 0.5 gcm^{-3} to greater than 1.0 gcm^{-3}. FAST-SSP is the only known solution for addressing the hollow spheres during spray pyrolysis.

The electrochemical results for $Li_{1.2}Mn_{0.54}Ni_{0.13}Co_{0.13}O_2$ powders indicate that performance comparable to that obtained either via traditional spray pyrolysis or co-precipitation can be obtained via FAST-SSP. FAST-SSP is a simple, scalable, rapid process that yields excellent reproducibility and offers significant potential for reducing processing and production costs of cathode materials, suggesting high potential for commercial scale production.

Chapter 8

Summary and recommendations for future work

7.1 Summary of Results

The work presented in this dissertation studied the optimization of layered composite cathode materials synthesized via spray pyrolysis. In particular cathode materials with various composition, trace elemental dopants were studied and their optimal composition was identified. Improvements of the voltage fade were demonstrated for the first time as of writing this thesis. Parallel to this work a novel flame-assisted spray pyrolysis was designed, which represents an intermediate step towards the scale up of spray pyrolysis as well as the only known solution to the hollow sphere problem. Spray pyrolysis requires external heating and the process is less resource and capital intensive than similar methods. The process delivers excellent uniformity and reproducibility in terms of electrochemical properties, due to the high purity synthesis technique and lack of additives. A brief summary of the key results in this dissertation is presented.

Layered composite materials of $xLi_2MnO_3 \cdot (1-x)LiNi_{0.33}Mn_{0.33}Co_{0.33}O_2$ have shown attractive properties including high capacity, good cycle life and are relatively inexpensive cathode materials. Their synthesis is often challenging with co-precipitation, due to non-stoichiometry that is the result of the lack of accurate control on synthesis parameters (temperature, stirring speed, etc.). The advantages of an aerosol based synthesis process were discussed extensively in the previous chapters. The layered composites of $xLi_2MnO_3 \cdot (1-x)\ LiNi_{0.33}Mn_{0.33}Co_{0.33}O_2$ display

highly reproducible, excellent electrochemical properties when synthesized via spray pyrolysis. When cycled between 2.0-4.6 V at C/3 rate the materials display capacities greater than 200 $mAhg^{-1}$ after 100 cycles at room temperature, which places them among the best known cathode materials in the field. The annealing heat treatment allows us to control surface area and primary particle size accurately, without causing any evaporative lithium loss in the samples. The addition of 3.3 wt% excess Li offsets structural changes occurring during the annealing. Voltage fade of the layered composites, which is speculated to be caused by a layered-spinel phase transition can be affected by the surface area, the composition and trace elemental doping. Results to date indicate that by reducing the Li_2MnO_3 content of the composites and by adding trace level dopants of Al, alkali and alkali earth metals the voltage fade can be reduced or mitigated.

Parallel to this research the scale-up efforts lead to the development of a novel slurry spray pyrolysis process, which as of writing is the only known solution to the hollow sphere problem. By developing this flame-assisted spray pyrolysis process materials having high density, good reproducibility and excellent electrochemical properties were successfully produced at greater than 50 gh^{-1} scale.

In summary slurry spray pyrolysis paves the way for the scale up of spray pyrolysis to commercial production levels. Trace level doping of NMC cathode materials shows that by additional stabilization this intensely researched chemistry may find applications in commercial batteries.

7.2 Recommendations for Future Work

As of writing, some new challenges are identified and could further improve the spray pyrolysis process and novel cathode material design.

1. Cobalt incorporation and trace level doping showed that the process is capable of delivering materials with improved performance and reduced / eliminated voltage fade. Based upon these results and the results of the study of Tarascon et al. a novel class of cathode materials can be designed and synthesized without voltage fade [119]. Additional dopants may further improve the stability of the material or additional properties, such as the cycleability or rate capability.
2. Preliminary results on the effect of doping on voltage fade were obtained. Dopants were not evaluated in terms of their effect on the safety characteristics of the materials. Therefore the stability of the materials should be evaluated both at high (55 °C) and low (0/-10 °C) temperatures.
3. Development of larger cells is recommended, to better characterize the fade properties of these materials in a more industrially applicable setting.
4. Recently, layered Na-ion based battery cathode materials were reported in the literature as analogs of the layered Li-ion based chemistries. Although the materials will provide lower energy due to their lower working potential compared to their Li-based counterparts, however they may display significant advantages in terms of safety and stability. Therefore a preliminary evaluation of the Na-analogs of the Li-based layered materials is suggested.

5. Slurry spray pyrolysis demonstrated that non-hollow particles greater than 3 μm can be produced via spray pyrolysis. The reproducibility of the process is lower than that of the original spray pyrolysis process both in terms of electrochemical properties and in terms of tap density results. A detailed study unveiling the important process parameters (residence time, flow rate, flow patterns, effect of heating rates, used materials, potential binders) will help improve consistency as well as drive the discovery of future improvements.
6. An alternative way of future improvements lies with the better understanding of hollow sphere formation. Several theories and potential explanations were discussed earlier ultimately indicating that improved understanding of local liquid phase structures by a combination of modelling and experimental methods may allow us to control and eliminate hollow sphere formation. The following studies include the suggested literature to start studying additives for potentially overcoming hollow spheres during droplet formation: [360, 361, 362].
7. The current thesis primarily focused on the development of the layered chemistries for commercial implementation. During this process many synthesis parameters demonstrated the level of control that can easily be exercised with this spray pyrolysis process. Other applications have not been explored due to time constraints. Therefore exploring the application of the current spray pyrolysis process for producing supercapacitor materials, lithium-air battery cathode catalysts are recommended with taking advantage of the ability to tune the surface area of the materials accurately.
8. In wet chemistry processes complexation allows the tuning of surface properties. After analyzing the surface of the powders tuning its properties could allow better macroscopic

adhesion, which could further improve the bulk density due to the reduction of van der Waals forces.

9. The slurry spray pyrolysis process demonstrated production capability greater than 50 gh^{-1}. Further scale up could be achieved with different spray sources (rotary atomizer, high pressure nozzles), which could lead to a novel system design and pave the way to commercial scale production as well as a better understanding of process parameters.

References

1. Mizushima K, Jones PC, Wiseman PJ, Goodenough JB. Li_xCoO_2 ($0<x\leqslant 1$): a new cathode material for batteries of high energy density. *Materials Research Bulletin* 1980, 15(6): 783-789

2. Nagaura T, Ozawa K. *Prog Batteries Solar Cells* 1990, 9: 209.

3. Goodenough JB, Kim Y. Challenges for rechargeable batteries. *Journal of Power Sources* 2011, 196: 6688-6694.

4. He P, Yu H, Li D, Zhou H. Layered lithium transition metal oxide cathodes towards high energy lithium ion batteries. *J Mater Chem* 2012, 22: 3680.

5. Dunn B, Kamath H, Tarascon J-M. Electrical Energy Storage for the Grid: A Battery of Choices. *Science* 2011, 334: 928.

6. Ohzuku T, Brodd RJ. An overview of positive-electrode materials for advanced lithium-ion batteries. *Journal of Power Sources* 2007, 174: 449-456.

7. Yang H, Amiruddin S, Bang HJ, Sun Y-K, Prakash J. A Review of Li-Ion Cell Chemistries and their Potential use in Hybrid Electric Vehicles. *J Ind Eng Chem* 2006, 12(1): 12-38.

8. Cheng F, Liang J, Tao Z, Chen J. Functional Materials for Rechargeable Batteries. *Adv Mater* 2011, 23: 1695-1715.

9. Ellis BL, Lee KT, Nazar LF. Positive Electrode Materials for Li-Ion and Li-Batteries. *Chem Mater* 2010, 22: 691-714.

10. Manthiram A. Materials Challenges and Opportunities of Lithium Ion Batteries. *J Phys Chem Lett* 2011, 2: 176-184.

11. Song H-K, Lee KT, Kim MG, Nazar LF, Cho J. Recent Progress in Nanostructured Cathode Materials for Lithium Secondary Batteries. *Adv Funct Mater* 2010, 20(22): 3818-3834.

12. Tarascon JM, Armand M. Issues and Challenges Facing Rechargeable Lithium Batteries. *Nature* 2001, 414(6861): 359-367.

13. Fergus JW. Recent developments in cathode materials for lithium ion batteries. *J Power Sources* 2010, 195(4): 939-954.

14. Scrosati B, Garche J. Lithium Batteries: Status, prospects and future. *J Power Sources* 2010, 195: 2419-2430.

15. Ohzuku T, Ueda A. Why transition metal (di)oxides are the most attractive materials for batteries. *Solid State Ionics* 1994, 69: 201-211.

16. Marom R, Amalraj SF, Leifer N, Jacob D, Aurbach D. A review of advanced and practical lithium battery materials. *Journal of Materials Chemistry* 2011, 21: 9938-9954.

17. Lu X, Lemmon JP, Sprenkle V, Yang Z. Sodium-beta Alumina Batteries: Status and Challenges. *Energy Storage Technologies* 2010, 62(9): 31.

18. Lu X, Xia G, Lemmon JP, Yang Z. Advanced Materials for sodium-beta alumina batteries: status, challenges and perspectives. *J Power Sources* 2010, 195: 2431-2442.

19. Shin S-H, Yun S-H, Moon S-H. A review of current developments in non-aqueous redox flow batteries: characterization of their membranes for design perspective *RSC Advances* 2013, 3: 9095.

20. Szczech JR, Jin S. Nanostructured silicon for high capacity lithium battery anodes. *Energy Environ Sci* 2011, 4: 56-72.

21. Terranova ML, Orlanducci S, Tamburri E, Guglielmotti V, Rossi M. Si/C hybrid nanostructures for Li-ion anodes: An overview. *J Power Sources* 2014, 246: 167-177.

22. Eom K, Joshi T, Bordes A, Do I, Fuller TF. The design of a Li-ion full cell battery using a nano silicon and nano multi-layer graphene composite anode. *J Power Sources* 2014, 249: 118-124.

23. Fan X, Zheng WT, Kuo J-L, Singh DJ. Adsorption of Single Li and the Formation of Small Li Clusters on Graphene for the Anode of Lithium-Ion Batteries. *ACS Appl Mater Interfaces* 2013, 5: 7793-7797.

24. Chiu H-c, Brodusch N, Gauvin R, Guerfi A, Zaghib K, Demopoulos GP. Aqueous Synthesized Nanostructured $Li_4Ti_5O_{12}$ for High-Performance Lithium Ion Battery Anodes. *J Electrochem Soc* 2013, 160(5): A3041-A3047.

25. McCloskey BD, Bethune DS, Shelby RM, Mori T, Scheffler R, Speidel A, *et al.* Limitations in Rechargeability of Li-O_2 Batteries and Possible Origins. *J Phys Chem Lett* 2012, 3: 3043-3047.

26. Hovington P, Dontigny M, Guerfi A, Trottier J, Lagacé M, Mauger A, *et al.* In situ Scanning electron microscope study and microstructural evolution of nano silicon anode for high energy Li-ion batteries. *J Power Sources* 2014, 248: 457-464.

27. Zaghib K, Dontigny M, Perret P, Guerfi A, Ramanathan M, Prakash J, *et al.* Electrochemical and thermal characterization of lithium titanate spinel anode in $CeLiFePO_4$//$CeLi_4Ti_5O_{12}$ cells at sub-zero temperatures. *J Power Sources* 2014, 248: 1050-1057.

28. Guyomard D, Tarascon JM. Li metal-free rechargeable $LiMn_2O_4$/carbon cells: Their understanding and optimization. *J Electrochem Soc* 1992, 139(4): 937-948.

29. Whittingham MS. Lithium batteries and cathode materials. *Chem Rev* 2004, 104(10): 4271-4301.

30. Whittingham MS. Electrical energy storage and intercalation chemistry *Science* 1976, 192: 1126-1127.

31. Garcia-Araez N, Novák P. Critical aspects in the development of lithium–air batteries. *J Solid State Electrochem* 2013, 17: 1793-1807.

32. Christensen J, Albertus P, Sanchez-Carrera RS, Lohmann T, Kozinsky B, Liedtke R, *et al.* A Critical Review of Li/Air Batteries. *J Electrochem Soc* 2012, 159(2): R1-R30.

33. Bhattacharyya R, Key B, Chen H, Best AS, Hollenkamp AF, Grey CP. In Situ NMR Observation of the formation of metallic lithium microstructures in lithium batteries. *Nat Mater* 2010, 9: 504.

34. Kanevskii LS, Dubasova VS. Degradation of lithium-ion batteries and how to fight it: A review. *Russ J Electrochem* 2005, 41(1): 1-16.

35. Broussely M, Biensan P, Bonhomme F, Blanchard P, Herreyre S, Nechev K, *et al.* Main aging mechanisms in Li ion batteries. *J Power Sources* 2005, 146(1-2): 90-96.

36. Park M, Zhang X, Chung M, Less GB, Sastry AM. A review of conduction phenomena in Li-ion Batteries. *J Power Sources* 2010, 195: 7904-7929.

37. Kostecki R, McLarnon F. Power and capacity fade mechanism of $LiNi_{0.8}Co_{0.15}Al_{0.05}O_2$ composite cathodes in high power lithium-ion batteries. *204th Meeting of the Electrochemical Society*. Orlando, FL; 2003. p. 114.

38. Bloom I, Jones SA, Battaglia VS, Henriksen GL, Christophersen JP, Wright RB, *et al.* Effect of cathode composition on capacity fade, impedance rise and power fade in high-power lithium-ion cells. *J Power Sources* 2003, 124: 538-550.

39. Arora P, White RE, Doyle M. Capacity fade mechanisms and side reactions in lithium-ion batteries. *J Electrochem Soc* 1998, 145(10): 3647.

40. Aurbach D, Markovsky B, Rodkin A, Cojocaru M, Levi E, Kim H-J. An analysis of rechargeable lithium-ion batteries after prolonged cycling. *Electrochim Acta* 2002, 0: 1-13.

41. Choi W, Manthiram A. Comparison of metal ion dissolutions from lithium ion battery cathodes. *J Electrochem Soc* 2006, 153(9): A1760-A1764.

42. Imanishi N, Ohashi S, Ichikawa T, Takeda Y, Yamamoto O, Kanno R. Carbon-lithium anodes for lithium secondary batteries. *J Power Sources* 1992, 39(2): 185-191

43. Yazami R, Zaghib K, Deschamps M. Carbon fibers and natural graphite as negative electrodes for lithium ion-type batteries. *J Power Sources* 1994, 52: 55-59.

44. Shimoda H, Gao B, Tang XP, Kleinhammes A, Fleming L, Wu Y, *et al.* Lithium intercalation into opened single-wall carbon nanotubes: Storage capacity and electronic properties. *Physical review letters* 2002, 88: 015502.015501-015502.015504.

45. Hsoeh HM, Tai NH, Lee CY, Chen JM, Wang FT. Electrochemical properties of the multi-walled carbon nanotube electrode for secondary lithium-ion battery. *Rev Adv Mater Sci* 2003, 5: 67-71.

46. Yamaura J, Ozaki Y, Morita A, Ohta A. High voltage, rechargeable lithium batteries using newly developed carbon for negative electrode material. *J Power Sources* 1993, 43: 233-239.

47. Mabuchi A, Fujimoto H, Tokumitsu K, Kasuh T. Charge-discharge mechanism of graphitized mesocarbon microbeads. *J Electrochem Soc* 1995, 142: 3049-3051.

48. Chang YC, Sohn HJ, Ku CH, Wang YG, Korai Y, Mochida I. Anodic performances of mesocarbon microbeads (MCMB) prepared from synthetic naphthalene isotropic pitch. *Carbon* 1999, 37: 1285-1297.

49. Chan CK, Peng H, Liu G, McIlwrath K, Zhang XF, Huggins RA, *et al.* High-performance lithium battery anodes using silicon nanowires. *Nature Nanotechnology* 2008, 3: 31-35.

50. Park M-H, Kim MG, Joo J, Kim K, Kim J, Ahn S, *et al.* Silicon nanotube battery anodes. *Nano Lett* 2009, 9(11): 3844-3847.

51. Jung DS, Hwang TH, Park SB, Choi JW. Spray Drying Method for Large-Scale and High-Performance Silicon Negative Electrodes in Li-Ion Batteries. *Nano Lett* 2013, 13(5): 2092-2097.

52. Green M, Fielder E, Scrosati B, Wachtler M, Morenob JS. Structured silicon anodes for lithium battery applications. *Electrochem Solid-State Lett* 2003, 6(5): A75-A79.

53. Cui Y, Lauhon LJ, Gudiksen MS, Wang J, Lieber CM. Diameter-controlled synthesis of single-crystal silicon nanowires. *Applied Physics Letters* 2001, 78(15): 2214-2216.

54. Padhi AK, Nanjundaswamy KS, Goodenough JB. Phospho‐olivines as Positive‐Electrode Materials for Rechargeable Lithium Batteries. *J Electrochem Soc* 1997, 144(4): 1188-1194.

55. Zhang Y, Wang C-Y, Tang X. Cycling degradation of an automotive $LiFePO_4$ lithium-ion battery. *J Power Sources* 2011, 196: 1513-1520.

56. Tang M, Carter WC, Chiang Y-M. Electrochemically Driven Phase Transitions in Insertion Electrodes for Lithium-Ion Batteries: Examples in Lithium Metal Phosphate Olivines. *Annu Rev Mater Res* 2010, 40: 501-529.

57. Xu Y-N, Chung S-Y, Bloking JT, Chiang Y-M, Ching WY. Electronic Structure and Electrical Conductivity of Undoped LiFePO4. *J Electrochem Soc* 2004, 7(6): A131-A134.

58. Yang M-R, Teng T-H, Wu S-H. $LiFePO_4$/carbon cathode materials prepared by ultrasonic spray pyrolysis. *J Power Sources* 2006, 159: 307-311.

59. Meligrana G, Gerbaldi C, Tuel A, Bodoardo S, Penazzi N. Hydrothermal synthesis of high surface $LiFePO_4$ powders as cathode for Li-ion cells. *J Power Sources* 2006, 160: 516-522.

60. Amine K, Liu J, Belharouak I. High-temperature storage and cycling of LiFePO4/graphite Li-ion cells. *Electrochem Comm* 2005, 7: 669-673.

61. Hamid NA, Wennig S, Hardt S, Heinzel A, Schulz C, Wiggers H. High-capacity cathodes for lithium-ion batteries from nanostructured $LiFePO_4$ synthesized by highly-flexible and scalable flame spray pyrolysis. *J Power Sources* 2012, 216: 76-83.

62. Winter M, Besenhard JO, Spahr ME, Novak P. Insertion electrode materials for rechargeable lithium batteries. *Advanced Materials* 1998, 10(10): 725-763.

63. Whittingham MS. Lithium Batteries and Cathode Materials. *Chem Rev* 2004, 104(10): 4271-4302.

64. Kim G-H, Pesaran A, Spotnitz R. A three-dimensional thermal abuse model for lithium-ion cells. *J Power Sources* 2007, 170: 476-489.

65. Cras FL, Anne M, Bloch D, Strobel P. Structural in-situ study of Li intercalation in Li1+aMn2-aO4 spinel-type oxides. *Solid State Ionics* 1998, 106: 1-10.

66. Chi LH, Dinh NN, Brutti S, Scrosati B. Synthesis, characterization and electrochemical properties of 4.8 V $LiNi_{0.5}Mn_{1.5}O_4$ cathode material in lithium-ion batteries. *Electrochim Acta* 2010, 55: 5110-5116.

67. McCalla E, Dahn JR. The spinel and cubic rocksalt solid-solutions in the Li–Mn–Ni oxide pseudo-ternary system. *Solid State Ionics* 2013, 242: 1-9.

68. Thackeray MM, David WIF, Bruce PG, Goodenough JB. Lithium insertion into manganese spinels. *Materials Research Bulletin* 1983, 18: 461-472.

69. Goodenough JB, Thackeray MM, David WIF, Bruce PG. Lithium insertion / extraction reactions with manganese. *Rev Chim Minér* 1984, 21: 435.

70. Thackeray MM, Picciotto LAD, Kock AD, Johnson PJ, Nicholas VA, Adendorff KT. Spinel Electrodes for lithium batteries - a review. *J Power Sources* 1987, 21: 1-8.

71. Thackeray MM, Johnson PJ, Picciotto LAd, Bruce PG, Goodenough JB. ELectrochemical extraction of Lithium from LiMn2O4. *Mat Res Bull* 1984, 19: 179-187.

72. Sahan H, Göktepe H, Patat S. Cycling behavior of barium doped LiMn2O4 cathode materials for Li ion secondary batteries. *Mater Sci - Poland* 2010, 28(4): 773.

73. Liu D, Zhu W, Trottier J, Gagnon C, Barray F, Guerfi A, *et al.* Spinel materials for high-voltage cathodes in Li-ion batteries. *RSC Advances* 2014, 4: 154.

74. Paik Y, Grey CP, Johnson CS, Kim JS, Thackeray MM. Lithium and deuterium NMR studies of acid-leached layered lithium manganese oxides. *Chem Mater* 2002, 14(12): 5109-5115.

75. Jain GR, Yang JS, Balasubramanian M, Xu JJ. Synthesis, electrochemistry, and structural studies of lithium intercalation of a nanocrystalline Li_2MnO_3-like compound. *Chem Mater* 2005, 17(15): 3850-3860.

76. Yu DYW, Yanagida K, Kato Y, Nakamura H. Electrochemical Activities in Li2MnO3. *J Electrochem Soc* 2009, 156(6): A417-A424.

77. Yu DYW, Yanagida K. Structural Analysis of Li_2MnO_3 and Related Li-Mn-O Materials. *J Electrochem Soc* 2011, 158(9): A1015-A1022.

78. Rossouw MH, Thackeray MM. Lithium manganese oxides from Li_2MnO_3 for rechargeable lithium battery applications. *Mater Res Bull* 1991, 26(6): 463-473.

79. Johnson CS, Korte SD, Vaughey JT, Thackeray MM, Bofinger TE, Shao-Horn Y, *et al.* Structural and electrochemical analysis of layered compounds from Li_2MnO_3. *J Power Sources* 1999, 82: 491-495.

80. Johnson CS, Kim JS, Lefief C, Li N, Vaughey JT, Thackeray MM. The significance of the Li_2MnO_3 component in 'composite' $xLi_2MnO_3 \cdot (1-x)LiMn_{0.5}Ni_{0.5}O_2$ electrodes. *Electrochem Commun* 2004, 6(10): 1085-1091.

81. Kim JS, Johnson CS, Vaughey JT, Thackeray MM, Hackney SA. Electrochemical and structural properties of $xLi_2M'O_3 \bullet (1-x)LiMn_{0.5}Ni_{0.5}O_2$ eIectrodes for lithium batteries (M' = Ti, Mn, Zr; $0 \leqslant x \leqslant 0.3$). *Chem Mater* 2004, 16(10): 1996-2006.

82. Amalraj F, Kovacheva D, Talianker M, Zeiri L, Grinblat J, Leifer N, *et al.* Synthesis of Integrated Cathode Materials $xLi_2MnO_3 \cdot (1 - x)LiMn_{1/3}Ni_{1/3}Co_{1/3}O_2$ (x = 0.3, 0.5, 0.7) and Studies of Their Electrochemical Behavior. *J Electrochem Soc* 2010, 157(10): A1121-A1130.

83. Deng HX, Belharouak I, Cook RE, Wu HM, Sun YK, Amine K. Nanostructured lithium nickel manganese oxides for lithium-ion batteries. *J Electrochem Soc* 2010, 157(4): A447-A452.

84. Thackeray MM, Kang S-H, Johnson CS, Vaughey JT, Benedek R, Hackney SA. Li_2MnO_3-stabilized $LiMO_2$ (M=Mn, Ni, Co) electrodes for lithium-ion batteries. *J Mater Chem* 2007, 17: 3112-3125.

85. Wu Y, Manthiram A. High Capacity, Surface-Modified Layered $(Li[Li_{(1-x)/3}Mn_{(2-x)/3}Ni_{x/3}Co_{x/3}]O_2$ cathodes with Low Irreversible Capacity Loss. *J Electrochem Soc* 2006, 9(5): A221-A224.

86. Lu Z, MacNeil DD, Dahn JR. Layered Cathode Materials $Li[Ni_xLi_{(1/3-2x/3)}Mn_{(2/3-x/3)}]O_2$ for Lithium-Ion Batteries. *Electrochem Solid St* 2001, 4(11): A191-A194.

87. Thackeray MM, Johnson CS, Vaughey JT, Li N, Hackney SA. Advances in manganese-oxide 'composite' electrodes for lithium-ion batteries. *J Mater Chem* 2005, 15: 2257-2267.

88. Johnson CS, Kim J-S, C.Lefief, N.Li, J.T.Vaughey, Thackeray MM. The significance of the Li_2MnO_3 component in 'composite' xLi_2MnO_3 . $(1 - x)LiMn_{0.5}Ni_{0.5}O_2$ electrodes. *Electrochem Comm* 2004, 6: 1085.

89. Johnson CS, Li N, Lefief C, Thackeray MM. Anomalous capacity and cycling stability of $xLi_2MnO_3*(1-x)LiMO_2$ electrodes (M=Mn, Ni, Co) in lithium batteries at 50°C. *Electrochem Comm* 2007, 9: 787-795.

90. Thackeray MM, Kang S-H, Johnson CS, Vaughey JT, Hackney SA. Comments on the structural complexity of lithium-rich $Li_{1+x}M_{1-x}O_2$ electrodes (M=Mn, Ni, Co) for lithium batteries. *Electrochem Comm* 2006, 8: 1531-1538.

91. McCalla E, Rowe AW, Camardese J, Dahn JR. The Role of Metal Site Vacancies in Promoting Li-Mn-Ni-O Layered Solid Solutions. *Chem Mater* 2013, 25: 2716-2721.

92. Cabana J, Johnson CS, Yang X-Q, Chung K-Y, Yoon W-S, Kang S-H, *et al.* Structural complexity of layered-spinel composite electrodes for Li-ion batteries. *J Mater Res* 2010, 25(8): 1601.

93. Cabana J, Kang S-H, Johnson CS, Thackeray MM, Grey CP. Structural and Electrochemical Characterization of Composite Layered-Spinel Electrodes Containing Ni and Mn for Li-Ion Batteries. *J Electrochem Soc* 2009, 156(9): A730-A736.

94. Yabuuchi N, Yoshii K, Myung S-T, Nakai I, Komaba S. Detailed Studies of a High-Capacity Electrode Material for Rechargeable Batteries, Li_2MnO_3-$LiCo_{1/3}Ni_{1/3}Mn_{1/3}O_2$. *J Am Chem Soc* 2011, 133: 4404-4419.

95. Chernova NA, Ma M, Xiao J, Whittingham MS, Breger J, Grey CP. Layered $Li_xNi_yMn_yCo_{1-2y}O_2$ Cathodes for Lithium Ion Batteries: Understanding Local Structure via Magnetic Properties. *Chem Mater* 2007, 19: 4682-4693.

96. Shin D, Wolverton C, Croy JR, Balasubramanian M, Kang S-H, Rivera CML, *et al.* First-Principles Calculations, Electrochemical and X-Ray Absorption Studies of LiNi-PO4 Surface-Treated xLi_2MnO_3 $(1-x)LiMO_2$ (M = Mn, Ni, Co) Electrodes for Li-Ion Batteries. *J Electrochem Soc* 2011, 159(2): A121-A127.

97. Xiao P, Deng ZQ, Manthiram A, Henkelman G. Calculations of Oxygen Stability in Lithium-Rich Layered Cathodes. *J Phys Chem C* 2012, 116: 23201-23204.

98. Shang S, Wang Y, Wang WY, Fang H, Liu Z-K. Low energy structures of lithium-ion battery materials $Li(Mn_xNi_xCo_{1-2x})O_2$ revealed by first-principles calculations. *Appl Phys Lett* 2013, 103: 053903.

99. McCalla E, Lowartz CM, Brown CR, Dahn JR. Formation of Layered–Layered Composites in the Li–Co–Mn Oxide Pseudoternary System during Slow Cooling. *Chem Mater* 2013, 25(6): 912-918.

100. Deng H, Belharouak I, Wu H, Dambournet D, Amine K. Effect of Cobalt Incorporation and Lithium Enrichment in Lithium Nickel Manganese Oxides. *J Electrochem Soc* 2010, 157(7): A776-A781.

101. Deng H, Belharouak I, Cook RE, Wu H, Sun Y-K, Amine K. Nanostructured Lithium Nickel Manganese Oxides for Lithium-Ion Batteries. *J Electrochem Soc* 2010, 157(4): A447-A452.

102. Amalraj F, Kovacheva D, Talianker M, Zeiri L, Grinblat J, Leifer N, *et al.* Synthesis of Integrated Cathode Materials $xLi_2MnO_3*(1-x)LiMn_{1/3}Ni_{1/3}Co_{1/3}O_2$ (x=0.3, 0.5, 0.7) and Studies of Their Electrochemical Behavior. *J Electrochem Soc* 2010, 157(10): A1121-A1130.

103. Johnson CS, Li N, Lefief C, Vaughey JT, Thackeray MM. Synthesis, Characterization and Electrochemistry of Lithium Battery Electrodes: $xLi_2MnO_3*(1-x)LiMn_{0.333}Ni_{0.333}Co_{0.333}O_2$ ($0 \leqslant x \leqslant 0.7$). *Chem Mater* 2008, 20: 6095-6106.

104. Park B-C, Bang HJ, Amine K, Jung E, Sun Y-K. Electrochemical Stability of core-shell structure electrode for high voltage cycling as positive electrode for lithium ion batteries. *J Power Sources* 2007, 174: 658-662.

105. Jr. GMK, Belharouak I, Wu HM, Amine K. Hollow Lithiated metal oxide particles as lithium-ion battery cathode materials. *Electrochim Acta* 2011, 56: 1426-1431.

106. Sun Y-K, Myung S-T, Park B-C, Prakash J, Belharouak I, Amine K. High-energy cathode material for long-life and safe lithium batteries. *Nat Mater* 2009, 8: 320-324.

107. Sun Y-K, Kim D-H, Yoon CS, Myung S-T, Prakash J, Amine K. A Novel Cathode Material with a Concentration-gradient for High-Energy and Safe Lithium-Ion Batteries. *Adv Funct Mater* 2010, 20: 485-491.

108. Sun Y-K, Myung S-T, Shin H-S, Bae YC, Yoon CS. Novel Core-Shell-Structured $Li[(Ni_{0.8}Co_{0.2})0.8(Ni0.5Mn_{0.5})_{0.2}]O_2$ via Coprecipitation as Positive Electrode Material for Lithium Secondary Batteries. *J Phys Chem B* 2006, 110: 6810-6815.

109. Liu J, Wang Q, Reeja-Jayan B, Manthiram A. Carbon-coated high capacity layered $Li[Li_{0.2}Mn_{0.54}Ni_{0.13}Co_{0.13}]O_2$ cathodes. *Electrochem Comm* 2010, 12: 750-753.

110. Liu J, Reeja-Jayan B, Manthiram A. Conductive Surface Modification with Aluminum of High Capacity Layered $Li[Li_{0.2}Mn_{0.54}Ni_{0.13}Co_{0.13}]O_2$ Cathodes. *J Phys Chem C* 2010, 114: 9528-9533.

111. Sun Y-K, Cho S-W, Lee S-W, Yoon CS, Amine K. AlF_3-Coating To Improve High Voltage Cycling Performance of $Li[Ni_{1/3}Co_{1/3}Mn_{1/3}]O_2$ Cathode Materials for Lithium Seconday Batteries. *J Electrochem Soc* 2007, 154(3): A168-A172.

112. West WC, Soler J, Smart MC, Ratnakumar BV, Firdosy S, Ravi V, *et al.* Electrochemical Behavior of Layered Solid Solution $Li_2MnO_3{-}LiMO_2$ (M = Ni, Mn, Co) Li-Ion Cathodes with and without Alumina Coatings *J Electrochem Soc* 2011, 158(8): A883-A889.

113. Li Y, Bettge M, Polzin B, Zhu Y, Balasubramanian M, Abraham DP. Understanding Long-Term Cycling Performance of $Li_{1.2}Ni_{0.15}Mn_{0.55}Co_{0.1}O_2$–Graphite Lithium-Ion Cells. *J Electrochem Soc* 2013, 160(5): A3006-A3019.

114. Gu M, Belharouak I, Zheng J, Wu H, Xiao J, Genc A, *et al.* Formation of the Spinel Phase in the Layered Composite Cathode Used in Li-Ion Batteries. *ACS Nano* 2012, 7(1): 760-767.

115. Croy JR, Gallagher KG, Balasubramanian M, Chen Z, Ren Y, Kim D, *et al.* Examining Hysteresis in Composite xLi_2MnO_3 $(1-x)LiMO_2$ Cathode Structures. *J Phys Chem C* 2013, 117: 6525-6536.

116. Mohanty D, Kalnaus S, Meisner RA, Rhodes KJ, Li J, Payzant EA, *et al.* Structural transformation of a lithium-rich $Li_{1.2}Co_{0.1}Mn_{0.55}Ni_{0.15}O_2$ cathode during high voltage cycling resolved by in situ X-ray diffraction. *J Power Sources* 2013, 229(1): 239-248.

117. Mohanty D, Kalnaus S, Meisner RA, Safat AS, Li J, Payzant EA, *et al.* Structural transformation in a $Li_{1.2}Co_{0.1}Mn_{0.55}Ni_{0.15}O_2$ lithium-ion battery cathode during high-voltage hold. *RSC Advances* 2013, 3: 7479.

118. Bareno J, Balasubramanian M, Kang SH, Wen JG, Lei CH, Pol SV, *et al.* Long-Range and Local Structure in the Layered Oxide $Li_{1.2}Co_{0.4}Mn_{0.4}O_2$. *Chem Mater* 2011, 23: 2039-2050.

119. Sathiya M, Rousse G, Ramesha K, Laisa CP, Vezin H, Sougrati MT, *et al.* Reversible anionic redox chemistry in high-capacity layered-oxide electrodes. *Nat Mater* 2013, 12.

120. Lengyel M, Atlas G, Shen K-Y, Axelbaum RL. Effects of Na Doping On $Li_{1.2}Mn_{0.53}Ni_{0.13}Co_{0.13}O_2$ Prepared Via Spray Pyrolysis. *224th meeting of the Electrochemical Society*. San Francisco; 2013.

121. Levi E, Levi MD, Chasid O, Aurbach D. A review on the problems of the solid state ions diffusion in cathodes for rechargeable Mg batteries. *J Electroceram* 2009, 22: 13-19.

122. Levi E, Gofer Y, Aurbach D. On The Way to Rechargeable Mg Batteries: The challenge of new cathode materials. *Chem Mater* 2010, 22: 860-868.

123. Aurbach D, Suresh GS, Levi E, Mitelman A, Mizrahi O, Chusid O, *et al.* Progress in Rechargeable Magnesium Battery Technology. *Adv Mater* 2007, 19: 4260-4267.

124. Rauh RD, Abraham KM, Pearson GF, Surprenant JK, Brummer SB. A Lithium/Dissolved Sulfur Battery with an Organic Electrolyte. *J Electrochem Soc* 1979, 126(4): 523-527.

125. Song M-K, Zhang Y, Cairns EJ. A Long-Life, High-Rate Lithium/Sulfur Cell: A Multifaceted Approach to Enhancing Cell Performance. *Nano Lett* 2013, 13(12): 5891-5899.

126. Song M-K, Cairns EJ, Zhang Y. Lithium/sulfur batteries with high specific energy: old challenges and new opportunities. *Nanoscale* 2013, 5: 2186.

127. Ji X, Lee KT, Nazar LF. A highly ordered nanostructured carbon-sulphur cathode for lithium-sulphur batteries. *Nat Mater* 2009, 8: 500.

128. Shim J, Cairns KASEJ. The Lithium/Sulfur Rechargeable Cell. *J Electrochem Soc* 2002, 149(10): A1321-A1325.

129. Wang Y-X, Huang L, Sun L-C, Xie S-Y, Xu G-L, Chen S-R, *et al.* Facile synthesis of a interleaved expanded graphite-embedded sulfphur nanocomposite as cathode of Li-S batteries with excellent lithium storage performance. *J Mater Chem* 2012, 22: 4744.

130. Hassoun J, Scrosati B. Moving to a Solid-State Configuration: A Valid Approach to Making Lithium-Sulfur batteries viable for practical applicationsn. *Adv Mater* 2010, 22: 5198-5201.

131. Jin L, Xu L, Morein C, Chen C-h, Lai M, Dharmarathna S, *et al.* Titanium containg gamma-MnO2 (TM) Hollow Spheres: One-step synthesis and catalytic activities in Li/Air Batteries and oxidative chemical reactions. *Adv Funct Mater* 2010, 22: 3373-3382.

132. Zheng JP, Liang RY, Hendrickson M, Plichta EJ. Theoretical Energy Density of Li-Air Batteries. *J Electrochem Soc* 2008, 155(6): A432-A437.

133. Chen J, Hummelshoj JS, Thygesen KS, Myrdal JSG, Norskov JK, Vegge T. The role of transitional metal interfaces on the electronic transport in lithium-air batteries. *Catal Today* 2011, 165: 2-9.

134. Andrei P, Zheng JP, Hendrickson M, Plichta EJ. Some Possible Approaches for Improving the Energy Density of Li-Air Batteries. *J Electrochem Soc* 2010, 157(12): A1287-A1295.

135. Padhi AK, Nanjundaswamy KS, Goodenough JB. Phospho-olivines as positive-electrode materials for rechargeable lithium batteries. *Journal of the Electrochemical Society* 1997, 144(4): 1188-1194.

136. Tarascon JM, McKinnon WR, Coowar F, Bowmer TN, Amatucci G, Guyomard D. Synthesis conditions and oxygen stoichiometry effects on Li insertion into the spinel $LiMn_2O_4$. *J Electrochem Soc* 1994, 141(6): 1421-1431.

137. Manev V, Momchilov A, Nassalevska A, Sato A. Rechargeable lithium battery with spinel-related λ-MnO_2. III: Scaling-up problems associated with $LiMn_2O_4$ synthesis. *J Power Sources* 1995, 54: 323-328.

138. Tarascon JM, Coowar F, Amatuci G, Shokoohi FK, Guyomard DG. The $Li_{1+x}Mn_2O_4$/C system materials and electrochemical aspects. *J Power Sources* 1995, 54: 103-108.

139. Lanz M, Kormann C, Steininger H, Heil G, Haas O, Novak P. Large-agglomerate-size lithium manganese oxide spinel with high rate capability for Lithium-ion batteries. *J Electrochem Soc* 2000, 147(11): 3997-4000.

140. Guo ZP, Ahn JH, Liu HK, Dou SX. Characterization of nanoparticles of $LiMn_2O_4$ synthesized by a one-step intermediate-temperature solid-state reaction. *J Nanosci Nanotechnol* 2004, 4(1-2): 162-166.

141. Wang DY, Hong L, Wang ZX, Wu XD, Sun YC, Huang XJ, *et al.* New solid-state synthesis routine and mechanism for $LiFePO_4$ using LiF as lithium precursor. *J Solid State Chem* 2004, 177(12): 4582-4587.

142. Belharouak I, Johnson C, Amine K. Synthesis and electrochemical analysis of vapor-deposited carbon-coated $LiFePO_4$. *Electrochem Commun* 2005, 7(10): 983-988.

143. West WC, Soler J, Ratnakumar BV. Preparation of high quality layered-layered composite Li_2MnO_3-$LiMO_2$ (M = Ni, Mn, Co) Li-ion cathodes by a ball milling-annealing process. *J Power Sources* 2012, 204: 200-204.

144. Shi SJ, Tu JP, Tang YY, Yu YX, Zhang YQ, Wang XL. Synthesis and electrochemical performance of $Li_{1.131}Mn_{0.504}Ni_{0.243}Co_{0.122}O_2$ cathode materials for lithium ion batteries via freeze drying. *J Power Sources* 2013, 221: 300-307.

145. G. Meligrana G, Gerbaldi C, Tuel A, Bodoardo S, Penazzi N. Hydrothermal synthesis of high surface $LiFePO_4$ powders as cathode for Li-ion cells. *J Power Sources* 2005, 160(1): 516-522.

146. Li N, Martin CR. A High-Rate, High-Capacity, Nanostructured Sn-Based Anode Prepared Using Sol-Gel Template Synthesis. *J Electrochem Soc* 2001, 148(2): A164-A170.

147. Huang X, Zhang Q, Gan J, Chang H, Yang Y. Hydrothermal Synthesis of a Nanosized $LiNi_{0.5}Mn_{1.5}O_4$ Cathode Material for High Power Lithium-Ion Batteries. *J Electrochem Soc* 2011, 158(2): A139-A145.

148. Chang C-C, Kumta PN. Particulate sol-gel synthesis and electrochemical characterization of LiMO2 (M=Ni, $Ni_{0.75}Co_{0.25}$) powders. *J Power Sources* 1998, 75: 44-45.

149. Deng HX, Belharouak I, Sun YK, Amine K. $Li_xNi_{0.25}Mn_{0.75}O_y$ ($0.5 \leqslant x \leqslant 2$, $2 \leqslant y \leqslant 2.75$) compounds for high-energy lithium-ion batteries. *Journal of Materials Chemistry* 2009, 19(26): 4510-4516.

150. Cho S, Jang J-W, Jung S-H, Lee BR, Oh E, Lee K-H. Precursor Effects of Citric Acid and Citrates on ZnO Crystal Formation. *Langmuir* 2009, 25: 3825-3831.

151. Lee SB, Cho SH, Cho SJ, Park GJ, Park SH, Lee YS. Synthesis of $LiFePO_4$ material with improved cycling performance under harsh conditions. *Electrochem Comm* 2008, 10: 1219-1221.

152. Carey GH, Dahn JR. Combinatorial Synthesis of Mixed Transition Metal Oxides for Lithium-Ion Batteries. *ACS Comb Sci* 2011, 13: 186-189.

153. Liu J, Chen L, Hou M, Wang F, Che R, Xia Y. General synthesis of $xLi_2MnO_3(1-x)LiMn_{1/3}Ni_{1/3}Co_{1/3}O_2$ nanomaterials by a molten-salt method: towards a high capacity and high power cathode for rechargeable lithium batteries. *J Mater Chem* 2012, 22: 25380-25387.

154. Johnson CS, Li N, Vaughey JT, Hackney SA, Thackeray MM. Lithium-manganese oxide electrodes with layered-spinel composite structures $xLi_2MnO_3 \cdot (1-x)Li_{1+y}Mn_{2-y}O_4$ ($0<x<1$, $0 \leqslant y \leqslant 0.33$) for lithium batteries. *Electrochemistry Communications* 2005, 7(5): 528-536.

155. Wang D, Belharouak I, Zhou G, Amine K. Synthesis of Lithium and Manganese-Rich Cathode Materials via an Oxalate Co-Precipitation Method. *J Electrochem Soc* 2013, 160(5): A3108-A3112.

156. Zhang X. Aerosol Synthesis of Cathode Materials for Li-Ion Batteries. PhD thesis, Washington University in St. Louis, St. Louis, 2011.

157. Jang H, Seong C, Suh Y, Kim H, Lee C. Synthesis of lithium-cobalt oxide nanoparticles by flame spray pyrolysis. *Aerosol Sci Technol* 2004, 38: 1027-1032.

158. Ng SH, Patey TJ, Buechel R, Krumeich F, Wang JZ, Liu HK, *et al.* Flame spray-pyrolyzed vanadium oxide nanoparticles for lithium battery cathodes. *Phys Chem Chem Phys* 2009, 11(19): 3748-3755.

159. Patey TJ, Büchel R, Nakayama M, Novák P. Electrochemistry of $LiMn_2O_4$ nanoparticles made by flame spray pyrolysis. *Phys Chem Chem Phys* 2009, 11(19): 3756 -3756

160. Patey TJ, Buchel R, Ng SH, Krumeich F, Pratsinis SE, Novak P. Flame co-synthesis of $LiMn_2O_4$ and carbon nanocomposites for high power batteries. *J Power Sources* 2009, 189(1): 149-154.

161. Zhang X, Zheng H, Battaglia V, Axelbaum RL. Electrochemical performance of spinel $LiMn_2O_4$ cathode materials made by flame-assisted spray technology. *J Power Sources* 2011, 196(7): 3640-3645

162. Zhang X, Zheng H, Battaglia VS, Axelbaum RL. Flame synthesis of 5 V spinel-$LiNi_{0.5}Mn_{1.5}O_4$ cathode-materials for lithium-ion rechargeable-batteries. *Proc Combust Inst* 2011, 33(2): 1867-1874

163. Yi JH, Kim JH, Koo HY, Ko YN, Kang YC, Lee J-H. Nanosized $LiMn_2O_4$ powders prepared by flame spray pyrolysis from aqueous solution. *J Power Sources* 2011, 196(5): 2858-2862.

164. Guo ZP, Liu H, Liu HK, Dou SX. Characterization of layered $Li[Ni_{1/3}Mn_{1/3}Co_{1/3}]O_{-2}$ cathode materials prepared by spray-drying method. *Journal of New Materials for Electrochemical Systems* 2003, 6(4): 263-266.

165. Li DC, Ito A, Kobayakawa K, Noguchi H, Sato Y. Electrochemical characteristics of $LiNi_{0.5}Mn_{1.5}O_4$ prepared by spray drying and post-annealing. *Electrochim Acta* 2007, 52(5): 1919-1924.

166. Ito A, Li D, Lee Y, Kobayakawa K, Sato Y. Influence of Co substitution for Ni and Mn on the structural and electrochemical characteristics of $LiNi_{0.5}Mn_{1.5}O_4$. *J Power Sources* 2008, 185(2): 1429-1433.

167. Myoujin K, Kojima M, Ogihara T, Nakane K, Ogata N. Synthesis and characterization of $LiNi_{0.5}Mn_{1.5}O_4$ particle by internal combustion type spray pyrolysis and spray drying. *Transactions of the Materials Research Society of Japan* 2008, 33(4): 985-988.

168. Taniguchi I, Fukuda N, Konarova M. Synthesis of spherical $LiMn_2O_4$ microparticles by a combination of spray pyrolysis and drying method. *Powder Technol* 2008, 181: 228-236.

169. Messing GL, Zhang SC, Jayanthi GV. Ceramic Powder Synthesis by Spray-Pyrolysis. *J Am Ceram Soc* 1993., 76: 2707-2726.

170. Jain S, Skamser DJ, T. T. Kodas. Morphology of Single-Component Particles Produced by Spray Pyrolysis. *Aerosol Sci Technol* 1997, 27(5): 575-590.

171. Kodas TT, Hampden-Smith MJ. *Aerosol Processing of Materials*. Wiley-VCH publication, 1999.

172. Gurav A, Kodas T, Pluym T, Y. Xiong. Aerosol processing of materials. *Aerosol Sci Technol* 1993, 19: 411.

173. Xiong Y, Kodas TT. Droplet evaporation and solute precipitation during spray pyrolysis. *J Aerosol Sci* 1993, 24(7): 893-908.

174. Wang W-W, Widiyastuti W, Ogi T, Lenggoro IW, Okuyama K. Correlations between Crystallite/Particle Size and Photoluminescence Properties of Submicrometer Phosphors. *Chem Mater* 2007, 19(7): 1723-1730.

175. Gao L, Xu H. Preparation of spherical, solid barium titanate particles with uniform composition at high precursor concentration by spray pyrolysis. *J Am Ceram Soc* 2004, 87(5): 830-833.

176. Zhang S-C, Messing GL. Synthesis of solid, spherical zirconia particles by spray pyrolysis. *J Am Ceram Soc* 1990, 73(1): 61-67.

177. Xu H, Gao L, Gu H, Guo J, Yan D. Synthesis of solid, spherical CeO_2 particles prepared by the spray hydrolysis reaction method. *J Am Ceram Soc* 2002, 85(1): 139-144.

178. Kieda N, Messing GL. Preparation of silver particles by spray pyrolysis of silver-diammine complex solutions. *J Mater Res* 1998, 13(6): 1660.

179. Taniguchi I, Fukuda N, Konarova M. Synthesis of spherical LiMn2O4 microparticles by a combination of spray pyrolysis and drying method. *Powder Technol* 2008, 181(3): 228-236.

180. Lyons SW, Wang LM, Kodas TT. Nanophase oxide formation by intraparticle reaction. *Nanostruct Mater* 1992, 1: 283-291.

181. Ogihara T, Saito Y, Yanagawa T, Ogata N, Yoshida K, Takashima M, *et al.* Preparation of spherical $LiCoO_2$ powders by the ultrasonic spray decomposition and its application to cathode active material in lithium secondary battery. *J Ceram Soc Jpn* 1993, 101(10): 1159-1163.

182. Chen CH, Buysman AAJ, Kelder EM, Schoonman J. Fabrication of $LiCoO_2$ Thin-Film Cathodes for Rechargeable Lithium Battery by Electrostatic Spray-Pyrolysis. *Solid State Ionics* 1995, 80(1-2): 1-4.

183. Ogihara T, Ogata N, Yonezawa S, Takashima M, Mizutani N. Synthesis of porous $LiNiO_2$ powders by ultrasonic spray pyrolysis and their cathode property. *Denki Kagaku* 1998, 66(12): 1202-1205.

184. Ogihara H, Aikiyo H, Ogata N, Katayama K, Azuma Y. Particle morphology and battery property of lithium manganate synthesized by ultrasonic spray pyrolysis. *J Soc Powder Technol* 2001, 38: 396-400.

185. Taniguchi I, Lim CK, Song D, Wakihara M. Particle morphology and electrochemical performances of spinel $LiMn_2O_4$ powders synthesized using ultrasonic spray pyrolysis method. *Solid State Ionics* 2002, 146: 239-247.

186. Jugovic D, Milosevic O, Cvjeticanin N, Mitric M, Miljkovic M, Jokanovic V, *et al.* Aerosol synthesis of $LiMn_2O_4$ and its electrochemical performances. *Science of Sintering: Current Problems and New Trends* 2003: 197-202.

187. Matsuda K, Taniguchi I. Relationship between the electrochemical and particle properties of $LiMn_2O_4$ prepared by ultrasonic spray pyrolysis *J Power Sources* 2004, 132(1-2): 156-160

188. Mukoyama I, Kodera T, Ogata N, Ogihara T. Synthesis and lithium battery properties of $LiM(M=Fe,Al,Mg)_xMn_{2-x}O_4$ powders by spray pyrolysis. *Key Eng Mater* 2006, 301: 167-170.

189. Park SB, Eom WS, Cho WI, Jang H. Electrochemical properties of LiNi0.5Mn1.5O4 cathode after Cr doping. *J Power Sources* 2006, 159(1): 679-684.

190. Ju SH, Kim DY, Jo EB, Kang YC. $LiMn_2O_4$ particles prepared by spray pyrolysis from spray solution with citric acid and ethylene glycol. *J Mater Sci* 2007, 42: 5369-5374.

191. Park SH, Sun YK. Synthesis and electrochemical properties of 5 V spinel $LiNi_{0.5}Mn_{1.5}O_4$ cathode materials prepared by ultrasonic spray pyrolysis method. *Electrochim Acta* 2004, 50(2-3): 431-434.

192. Park SH, Oh SW, Myung ST, Kang YC, Sun YK. Effects of synthesis condition on $LiNi_{1/2}Mn_{3/2}O_4$ cathode material for prepared by ultrasonic spray pyrolysis method. *Solid State Ionics* 2005, 176(5-6): 481-486

193. Oh SW, Park SH, Kim JH, Bae YC, Sun YK. Improvement of electrochemical properties of $LiNi_{0.5}Mn_{1.5}O_4$ spinel material by fluorine substitution. *J Power Sources* 2006, 157(1): 464-470.

194. Park SH, Oh SW, Kang SH, Belharouak I, Amine K, Sun YK. Comparative study of different crystallographic structure of $LiNi_{0.5}Mn_{1.5}O_{4-delta}$ cathodes with wide operation voltage (2.0-5.0 V). *Electrochim Acta* 2007, 52(25): 7226-7230.

195. Kojima M, Mukoyama I, Myoujin K, Kodera T, Ogihara T. Mass production and battery properties of $LiNi_{0.5}Mn_{1.5}O_4$ powders prepared by internal combustion type spray pyrolysis. *Key Eng Mater* 2009, 388: 85-88.

196. Yang MR, Teng TH, Wu SH. $LiFePO_4$/carbon cathode materials prepared by ultrasonic spray pyrolysis. *J Power Sources* 2006, 159(1): 307-311.

197. Bewley SL, Konstantinov K, Wang GX, Dou SX, Liu HK. Conductivity improvements to spray-produced $LiFePO_4$ by addition of a carbon source. *Mater Lett* 2004, 58: 1788-1791.

198. Ju SH, Kang YC. $LiFePO_4$/C cathode powders prepared by spray pyrolysis from the colloidal spray solution containing nano-sized carbon black. *Mater Chem Phys* 2008, 107(2-3): 328-333.

199. Konarova M, Taniguchi I. Preparation of $LiFePO_4$/C composite powders by ultrasonic spray pyrolysis followed by heat treatment and their electrochemical properties. *Mater Res Bull* 2008, 43(12): 3305-3317.

200. J. H. Kim SHC, M. Y. Son, M. H. Kim, J.-K. Lee, Y. C. Kang. Electrochemical properties of nanometer-sized $0.6Li_2MnO_3$- $0.4LiNi_{0.5}Mn_{0.5}O_2$ composite powders prepared by flame spray pyrolysis. *Ceram Int* 2013, 39: 331.

201. Son MY, Hong YJ, Choi SH, Kang YC. Effects of ratios of $Li_2MnO_3$and $Li(Ni_{13}Mn_{13}Co_{13})O_2$ phases on the properties of composite cathode powders in spray pyrolysis. *Electrochim Acta* 2013, 103: 110.

202. Axelbaum RL, Zhang X, inventors; Spray Pyrolysis Synthesis of Mesoporous Positive Electrode Materials for High Energy Lithium-Ion Batteries 2012.

203. Oljaca M, Blizanac B, Pasquier AD, Sun Y, Bontchev R, Suszko A, *et al.* Novel $Li(Ni_{1/3}Co_{1/3}Mn_{1/3})O_2$ cathode morphologies for high power Li-ion batteries. *J Power Sources* 2014, 248: 729-738.

204. Ogihara T, Kodera T, Myoujin K, Motohira S. Preparation and electrochemical properties of cathode materials for lithium ion battery by aerosol process. *Mater Sci Eng B* 2009, 161: 109-114.

205. Zhang S-C, Messing GL, Huebner W. $YBa_2Cu_3O_{7-x}$ Superconductor powder synthesis by spray pyrolysis of organic acid solutions. *J Aerosol Sci* 1991, 22(5): 585-599.

206. Hinds WC. *Aerosol Technology*. John Wiley & Sons, Inc, 1999.

207. Eslamian M, Ahmed M, Ashgriz N. Modeling of Solution Droplet Evaporation and Particle Evolution in Droplet-to-Particle Spray Methods. *Drying Technol* 2009, 27: 3-13.

208. Lang RJ. Ultrasonic Atomization of Liquids. *J Acoust Soc Am* 1962, 34(1): 6.

209. Mwakikunga BW. Progress in Ultrasonic Spray Pyrolysis for Condensed Matter Sciences Developed From Ultrasonic Nebulization Theories Since Michael Faraday. *Crit Rev Solid State Mater Sci* 2014, 39: 46-80.

210. Tussupbayev R, Shokanbay T, Bakenov Z, Taniguchi I. Preparation of $LiNi_{0.5}Mn_{1.5}O_4$ Cathode Materials of Lithium-Ion Batteries by Drip Pyrolysis in Fluidized Bed Reactor

Followed by Heat Treatment and Their Electrochemical Properties. *J Chem Eng Jpn* 2011, 44(3): 179-186.

211. Taniguchi I, Nakajima S, Bakenov Z. Synthesis of Nanostructured $LiM_{0.15}Mn_{1.85}O_4$ (M ¼ Mn, Co, Al, and Fe) Particles by Spray Pyrolysis in a Fluidized Bed Reactor. *Chem Eng Comm* 2008, 195: 1292-1301.

212. Tarascon J-M, Armand M. Issues and challenges facing rechargeable lithium batteries. *Nature* 2001, 414: 359-367.

213. Zhang L, Takada K, Ohta N, Fukuda K, Sasaki T. Synthesis of $(1-2x)LiNi_{1/2}Mn_{1/2}O_2*xLi[Li_{1/3}Mn_{2/3}]O_2*xLiCoO_2$ ($0 \leqslant x \leqslant 0.5$) electrode materials and comparative study on cooling rate. *J Power Sources* 2005, 146: 598-601.

214. Lu Z, MacNeil DD, Dahn JR. Layered $Li[Ni_xCo_{1-2x}Mn_x]O_2$ Cathode Materials for Lithium-Ion Batteries. *Electrochem Solid St* 2001, 4(11): A200-A203.

215. Venkatraman S, Subramanian V, Kumar SG, Renganathan NG, Muniyandi N. Capacity of layered cathode materials for lithium-ion batteries - a theoretical study and experimental evaluation *Electrochem Comm* 2000, 2(1): 18-22.

216. Labrini M, Saadoune I, Almaggoussi A, Elhaskouri J, Amoros P. The $Li_yNi_{0.2}Mn_{0.2}Co_{0.6}O_2$ electrode materials: a structural and magnetic study. *Mat Res Bull* 2012, 47: 1004.

217. Gao J, Manthiram A. Eliminating the irreversible capacity loss of high capacity layered $Li[Li_{0.2}Mn_{0.54}Ni_{0.13}Co_{0.13}]O_2$ cathode by blending with other lithium insertion hosts. *J Power Sources* 2009, 191: 644-647.

218. Arico AS, Bruce P, Scrosati B, Tarascon J-M, Schalkwijk WV. Nanostructured materials for advanced energy conversion and storage devices. *Nat Mater* 2005, 4(5): 366-377.

219. Bruce PG, Scrosati B, Tarascon J-M. Nanomaterials for rechargeable lithium batteries. *Angew Chem Int Ed* 2008, 47(16): 2930-2946.

220. Hartley PA, Parfitt GD, Pollack LB. The role of the van der Waals force in the agglomeration of powders containing submicron particles. *Powder Technol* 1985, 42(1): 35-46.

221. Visser J. Van der Waals and other cohesive forces affecting powder fluidization. *Powder Technol* 1989, 58(1): 1-10.

222. Kang YC, Park SB, Lenggoro IW, Okuyama K. Preparation of nonaggregated $Y2O_3$:Eu phosphor particles by spray pyrolysis method. *J Mater Res* 1999, 14(6): 2611.

223. Park SH, Yoon CS, Kang SG, Kim H-S, Moon S-I, Sun Y-K. Synthesis and structural characterization of layered $Li[Ni_{1/3}Co_{1/3}Mn_{1/3}]O_2$ cathode materials by ultrasonic spray pyrolysis method. *Electrochim Acta* 2004, 49: 557-563.

224. Park S-H, Oh SW, Sun Y-K. Synthesis and structural characterization of layered $Li[Ni_{1/3+x}Co_{1/3}Mn_{1/3-2x}Mo_x]O_2$ cathode materials by ultrasonic spray pyrolysis. *J Power Sources* 2005, 146: 622-625.

225. Jung KY, Lee JH, Koo HY, Kang YC, Park SB. Preparation of solid nickel nanoparticles by large-scale spray pyrolysis of $Ni(NO_3)_2 \cdot 6H_2O$ precursor: Effect of temperature and nickel acetate on the particle morphology. *Mater Sci Eng B* 2007, 137: 10-19.

226. Yamada M, Dongying B, Kodera T, Myoujin K, Ogihara T. Mass Production of cathode materials for lithium ion battery by flame type spray pyrolysis. *J Ceram Soc Japan* 2009, 117(9): 1017-1020.

227. Shelke PN, Khollam YB, Hawaldar RR, Gunjal SD, Udawant RR, Sarode MT, *et al.* Synthesis, characterization and optical properties of selective Co_3O_4 films 1-D interlinked nanowires prepared by spray pyrolysis technique. *Fuel* 2013, 112: 542-549.

228. Waser O, Büchel R, Hintennach A, Novák P, Pratsinis SE. Continuous flame aerosol synthesis of carbon-coated nano-LiFePO4 for Li-ion batteries. *J Aerosol Sci* 2011, 42(10): 657-667.

229. Kim JH, Yi JH, Ko YN, Kang YC. Electrochemical properties of nano-sized $LiNi_{1/3}Co_{1/3}Mn_{1/3}O_2$ powders in the range from 56 to 101 nm prepared by flame spray pyrolysis. *Mater Chem Phys* 2012, 134(1): 254-259.

230. Chen Y, Xu G, Li J, Zhang Y, Chen Z, Kang F. High capacity $0.5Li_2MnO_3 \cdot 0.5LiNi_{0.33}Co_{0.33}Mn_{0.33}O_2$ cathode material via a fast co-precipitation method. *Electrochim Acta* 2013, 87: 686-692.

231. Jeon H-J, Monim SA, Kang C-S, Son J-T. Synthesis of $Li_x[Ni_{0.225}Co_{0.125}Mn_{0.65}]O_2$ as a positive electrode for lithium-ion batteries by optimizing its synthesis conditions via a hydroxide co-precipitation method. *J Power Sources* 2013, 74(9): 1185-1195.

232. Yang KM, Kang YC, Jeong SM, Choi YJ, Kim YS. Electrochemical properties of spherical hollow composite powders with various $Li_4Ti_5O_{12}/SnO_2$ ratios prepared by spray pyrolysis. *Int J Electrochem Sci* 2013, 8(10): 11972-11983.

233. Kim MH, Hong YJ, Kang YC. Electrochemical properties of yolk-shell and hollow $CoMn_2O_4$ powders directly prepared by continuous spray pyrolysis as negative electrode materials for lithium ion batteries. *RSC Advances* 2013, 3(32): 13110-13114.

234. Son MY, Hong YJ, Choi HS, Kang YC. Effects of ratios of Li_2MnO_3 and $Li(N_{1/3}Mn_{1/3}Co_{1/3})O_2$ phases on the properties of composite cathode powders in spray pyrolysis. *Electrochim Acta* 2013, 103: 110-118.

235. Sim CM, Kim JH, Hong YJ, Lee J-K, Kang YC. Electrochemical characteristics of layered-spinel $0.7Li_2MnO_3$ $0.3Li_4Mn_5O_{12}$ composite powders with spherical shape and porous nanostructure. *Int J Electrochem Sci* 2013, 8(4): 4850-4863.

236. Kim JH, Kang YC. Electrochemical properties of nanosized Li_2MnO_3 $Li(Ni_{0.8}Co_{0.15}Al_{0.05})O_2$ composite cathode powders. *Int J Electrochem Sci* 2013, 8(3): 3664-3675.

237. Son MY, Kim JH, Kang YC. Study of Co_3O_4 mesoporous nanosheets prepared by a simple spray-drying process and their electrochemical properties as anode material for lithium secondary batteries. *Electrochim Acta* 2014.

238. Son MY, Kim JH, Kang YC. Electrochemical Properties of $0.6Li_2MnO_3$-$0.4Li(Ni_{1/3}Mn_{1/3}Co_{1/3})O_2$ Composite Cathode Powders with Spherical Shape and Fine Size. *Int J Electrochem Sci* 2013, 8: 2417-2429.

239. Zhang X, Axelbaum RL. Spray Pyrolysis Synthesis of Mesoporous Lithium-Nickel-Manganese-Oxides for High Energy Li-Ion Batteries. *J Electrochem Soc* 2012, 159(6): A834-A842.

240. Zhang X, Zheng H, Battaglia V, Axelbaum RL. Electrochemical performance of spinel $LiMn_2O_4$ cathode materials made by flame-assisted spray technology. *J Power Sources* 2011, 196(7): 3640-3645.

241. Zhang X, Zheng H, Battaglia V, Axelbaum RL. Flame synthesis of 5 V spinel-LiNi0.5Mn1.5O4 cathode-materials for lithium-ion rechargeable-batteries. *Proc Comb Instit* 2011, 33(2): 1867-1874.

242. Zhang X, Lengyel M, Axelbaum RL. Nanostructured High-Energy $xLi_2MnO_3 \cdot (1-x)LiNi_{0.5}Mn_{0.5}O_2$ ($0.3 \leqslant x \leqslant 0.6$) Cathode Materials. *AIChE J* 2014, 60(2): 443-450.

243. Zhang X, Lengyel M, Belharouak I, Axelbaum RL. Optimization of the Electrochemical Properties of $xLi_2MnO_3 \cdot (1-x)LiMO_2$ Electrodes (M= Mn, Ni, Co) Prepared via Spray Pyrolysis Process *221St meeting of the Electrochemical Society*. Seattle; 2012.

244. Liu J, Liu J, Wang R, Xia Y. Degradation and Structural Evolution of $xLi_2MnO_3 \cdot (1–x)LiMn_{1/3}Ni_{1/3}Co_{1/3}O_2$ during Cycling. *J Electrochem Soc* 2014, 161(1): A160-A167.

245. Yin S-C, Rho Y-H, Swainson I, Nazar LF. X-ray/Neutron Diffraction and Electrochemical Studies of Lithium De/Re-Intercalation in $Li_{1-x}Co_{1/3}Ni_{1/3}Mn_{1/3}O_2$ (x) 0 f 1). *Chem Mater* 2006, 18: 1901-1910.

246. Choi J, Manthiram A. Factors influencing the crystal chemistry of chemically delithiated layered $H_xNi_{1-y-z}Mn_yCo_zO_2$. *J Mater Chem* 2006, 16: 1726-1733.

247. Boulineau A, Croguennec L, Delmas C, Weill F. Reinvestigation of Li_2MnO_3 Structure: Electron Diffraction and High Resolution TEM. *Chem Mater* 2009, 21: 4216-4222.

248. Buesser B, Pratsinis SE. Design of Nanomaterial Synthesis by Aerosol Processes. *Annu Rev Chem Biomol Eng* 2012, 3: 103-127.

249. Chun-Fa Y, Cai-Fu L, Zhi-Quan L, Jian-Ku S. Structural Ordering and Magnetic Property of Complex Perovskite Solid Solution $(1-x)Pb(Fe_{2/3}W_{1/3})O_3$-$xPb(Mg_{1/2}W_{1/2})O_3$. *J Inorg Mater* 2011, 26(6): 649-654.

250. Singhal A, Dhamne A, Bisso S, Skandan G, Pereira N, Badway F, *et al.* High Power and Fast Charge Rate Li-Ion Batteries. *Proc Power Sources* 2006.

251. Liu J, Wang Z, Zhang G, Liu Y, Yu A. Size-controlled synthesis of $LiFePO_4$/C composites as cathode materials for lithium ion batteries. *Int J Electrochem Sci* 2013, 8: 2378.

252. Fujii Y, Miura H, Suzuki N, Shoji T, Nakayma N. Structural and electrochemical properties of $LiNi_{1/3}Co_{1/3}Mn_{1/3}O_2$: Calcination temperature dependence. *J Power Sources* 2007, 171(2): 894-903.

253. Bang H, Kim D-H, Bae YC, Prakash J, Soon Y-K. Effects of Metal Ions on the Structural and Thermal Stabilities of $Li[Ni_{1-x-y}Co_xMn_y]O_2$ $(x+y \leqslant 0.5)$ Studied by In Situ High Temperature XRD. *J Electrochem Soc* 2008, 155(12): A952-A958.

254. Yabuuchi N, Kumar S, Li HH, Kim Y-T, Shao-Horn Y. Changes in the Crystal Structure and Electrochemical Properties of $Li_xNi_{0.5}Mn_{0.5}O_2$ during Electrochemical Cycling to High Voltages *J Electrochem Soc* 2007, 154(6): A566-A578.

255. Jiang M, Key B, Meng YS, Grey CP. Electrochemical and Structural Study of the Layered, "Li-Excess" Lithium-Ion Battery Electrode Material Li[Li1/9Ni1/3Mn5/9]O2. *Chem Mater* 2009, 21(13): 2733-2745.

256. Xu B, Fell CR, Chi M, Y. S. Ming. Identifying surface structural changes in layered Li-excess nickel manganese oxides in high voltage lithium ion batteries: A joint experimental and theoretical study *Energy Environ Sci* 2011, 4: 2223-2233.

257. Song B, Liu Z, Lai MO, Lu L. Structural evolution and the capacity fade mechanism upon long-term cycling in Li-rich cathode material. *Phys Chem Chem Phys* 2012, 14(37): 12875-12883.

258. Kang S-H, Thackeray MM. Enhancing the rate capability of high capacity $xLi_2MnO_3*(1-x)LiMO_2$ (M=Mn, Ni, Co) electrodes by Li-Ni-PO_4 treatment. *Electrochem Comm* 2009, 11: 748-751.

259. Zheng H, Tan L, Liu G, Song X, V. S. Battaglia. Calendering effects on the physical and electrochemical properties of $Li[Ni_{1/3}Mn_{1/3}Co_{1/3}]O_2$ cathode. *J Power Sources* 2012, 208: 52-57.

260. Yu X, Nam K, Hu E, Abraham DP, X.Yang. *222nd meeting of the Electrochemical Society*. Oahu, Hawaii; 2012.

261. Nukuda T, Inamasu T, A. Fujii DE, Nakagawa H, Kozono S, Iguchi T, *et al.* Development of a lithium ion battery using a new cathode material. *Journal of Power Sources* 2005, 146: 611-616.

262. Gu M, Genc A, Belharouak I, Wang D, Amine K, Thevuthasan S, *et al.* Nanoscale Phase Separation, Cation Ordering, and Surface Chemistry in Pristine $Li_{1.2}Ni_{0.2}Mn_{0.6}O_2$ for Li-Ion Batteries. *Chem Mater* 2013, 25: 2319-2326.

263. Kang KS, Choi S, Song J, Woo S-G, Jo YN, Choi J, *et al.* Effect of additives on electrochemical performance of lithium nickel cobalt manganese oxide at high temperature. *J Power Sources* 2014, 253: 48-54.

264. Yoshida H, Fukunaga T, Hazama T, Terasaki M, Mizutani M, M. Yamachi. Degradation mechanism of alkyl carbonate solvents used in lithium-ion cells during initial charging. *J Power Sources* 1997, 68(2): 311-315.

265. Tasaki K. Solvent decompositions and physical properties of decomposition compounds in Li-ion battery electrolytes studied by DFT calculations and molecular dynamics simulations. *J Phys Chem B* 2005, 109(7): 2920-2933.

266. Yang L, Lucht BL. Inhibition of Electrolyte Oxidation in Lithium Ion Batteries with Electrolyte Additives. *Electrochem Solid-State Lett* 2009, 12(12): A229-A231.

267. Leung K. First-Principles Modeling of the Initial Stages of Organic Solvent Decomposition on $Li_xMn_2O_4$(100) Surfaces. *J Phys Chem C* 2012, 116(18): 9852-9861.

268. J. Hong D-HS, S.-W. Kim, H. Gwon, S.-T. Oh, K. Kang. Structural evolution of layered $Li_{1.2}Ni_{0.2}Mn_{0.6}O_2$ upon electrochemical cycling in a Li rechargeable battery. *J Mater Chem* 2010, 20: 10179-10186.

269. Singh G, Thomas R, Kumar A, Katiyar RS. Electrochemical Behavior of Cr- Doped Composite Li_2MnO_3-$LiMn_{0.5}Ni_{0.5}O_2$ Cathode Materials *J Electrochem Soc* 2012, 159(4): A410-A420.

270. Shin S-S, Sun Y-K, Amine K. Synthesis and electrochemical properties of $Li[Li_{(1-2x)/3}Ni_xMn_{(2-x)/3}]O_2$ as cathode materials for lithium secondary batteries. *J Power Sources* 2002, 112(2): 634-638.

271. Xu Y, Chen G, Fu E, Zhou M, Dunwell M, Fei L, *et al.* Nickel substituted $LiMn_2O_4$ cathode with durable high-rate capability for Li-ion batteries. *RSC Advances* 2013, 3: 18441.

272. Liu Q, Wang S, Tan H, Yang Z, Zeng J. Preparation and Doping Mode of Doped $LiMn_2O_4$ for Li-Ion Batteries. *Energies* 2013, 6(3): 1718-1730.

273. Yabuuchi N, Yano M, Yoshida H, Kuze S, Komaba S. Synthesis and Electrode Performance of O3-Type $NaFeO_2$-$NaNi_{1/2}Mn_{1/2}O_2$ Solid Solution for Rechargeable Sodium Batteries *J Electrochem Soc* 2013, 160(5): A3131-A3137.

274. Xiang Y, Yin Z, Zhang Y, Li X. Effects of synthesis conditions on the structural and electrochemical properties of the Li-rich material $Li[Li_{0.2}Ni_{0.17}Co_{0.16}Mn_{0.47}]O_2$ via the solid-state method. *Electrochim Acta* 2013, 91: 214-218.

275. Mahmoud A, Amarilla JM, Lasri K, Saadoune I. Influence of the synthesis method on the electrochemical properties of the $Li_4Ti_5O_{12}$ spinel in Li-half and Li-ion full-cells. A systematic comparison. *Electrochim Acta* 2013, 93: 163-172.

276. Nythia C, Thirunakaran R, Sivashanmugam A, Kiruthika GVM, Gopukumar S. High-Capacity Sol−Gel Synthesis of $LiNi_xCo_yMn_{1-x-y}O_2$ ($0 \leqslant x, y \leqslant 0.5$) Cathode Material for Use in Lithium Rechargeable Batteries. *J Phys Chem C* 2009, 113(41): 17936-17944.

277. Shojan J, Rao CV, Torres L, Singh G, Katiyar RS. Lithium-ion battery performance of layered $0.3Li_2MnO_3–0.7LiNi_{0.5}Mn_{0.5}O_2$ composite cathode prepared by co-precipitation and sol–gel methods. *Mater Lett* 2013, 104: 57-60.

278. Pelosato R, Cristiani C, Dotelli G, Latorrata S, Ruffo R, Zampori L. Co-precipitation in aqueous medium of $La_{0.8}Sr_{0.2}Ga_{0.8}Mg_{0.2}O_{3-\delta}$ via inorganic precursors. *J Power Sources* 2010, 195: 8116-8123.

279. Noh M, Cho J. Optimized Synthetic Conditions of $LiNi_{0.5}Co_{0.2}Mn_{0.3}O_2$ Cathode Materials for High Rate Lithium Batteries via Co-Precipitation Method *J Electrochem Soc* 2013, 160(1): A105-A111.

280. Liu D, Han J, Goodenough JB. Structure, morphology, and cathode performance of $Li_{1-x}[Ni_{0.5}Mn_{1.5}]O_4$ prepared by coprecipitation with oxalic acid. *J Power Sources* 2010, 195(9): 2918-2923.

281. Fang X, Ding N, Feng XY, Lu Y, Chen CH. Study of $LiNi_{0.5}Mn_{1.5}O_4$ synthesized via a chloride-ammonia co-precipitation method: Electrochemical performance, diffusion coefficient and capacity loss mechanism. *Electrochim Acta* 2009, 54: 7471-7475.

282. Hong YJ, Kim JH, Kim MH, Kang YC. Electrochemical properties of $0.3Li_2MnO_3 \cdot 0.7LiNi_{0.5}Mn_{0.5}O_2$ composite cathode powders prepared by large-scale spray pyrolysis. *Mat Res Bull* 2012, 47: 2022-2026.

283. Fu LJ, Liu H, Li C, Wu YP, Rahm E, Holze R, *et al.* Electrode materials for lithium secondary batteries prepared by sol-gel methods. *Prog Mat Sci* 2005, 50.

284. Htay MT, Hashimoto Y, Momose N, Ito K. Position-selective growth of ZnO nanowires by ultrasonic spray pyrolysis. *J Crystal Growth* 2009, 311(20): 4499-4504.

285. Schimmoeller B, Hoxha F, Mallat T, Krumeich F, Pratsinis SE, Baiker A. Fine tuning the surface acid/base properties of single step flame-made Pt/alumina. *Appl Catal, A* 2010, 374(1-2): 48-57.

286. Konstantinov K, Ng SH, Wang JZ, Wang GX, Wexler D, Liu HK. Nanostructured PbO materials obtained in situ by spray solution technique for Li-ion batteries. *J Power Sources* 2006, 159(1): 241-244.

287. Qu Q, Fu L, Zhan X, Samuelis D, Maier J, Li L, *et al.* Porous LiMn2O4 as cathode material with high power and excellent cycling for aqueous rechargeable lithium batteries. *Energy Environ Sci* 2011, 4: 3985-3990.

288. Balaya P, Saravanan K, Ramar V, Lee HS, Kuezma M, Devaraj S, *et al.* Nanostructured mesoporous materials for lithium-ion battery applications Proc. SPIE; 2011; Orlando, Florida; 2011.

289. Lengyel M, Zhang X, Atlas G, Bretscher HL, Belharouak I, Axelbaum RL. Composition Optimization of Layered Lithium Nickel Manganese Cobalt Oxide Materials Synthesized Via Ultrasonic Spray Pyrolysis. *J Electrochem Soc* 2014.

290. Stern KH. *High Temperature Properties and Thermal Decomposition of Inorganic Salts with Oxyanions* CRC Press, 2000.

291. Brockner W, Ehrhardt C, Gjikaj M. Thermal decomposition of nickel nitrate hexahydrate, $Ni(NO_3)_2 \cdot 6H_2O$, in comparison to $Co(NO_3)_2 \cdot 6H_2O$ and $Ca(NO_3)_2 \cdot 4H_2O$. *Thermochim Acta* 2007, 456(1): 64-68.

292. Nissinen T, Leskelä M, Gasik M, Lamminen J. Decomposition of mixed Mn and Co nitrates supported on carbon. *Thermochim Acta* 2005, 427(1-2): 155-161.

293. Minami T, Wang W-N, Iskandar F, Okuyama K. Photoluminescence Properties of Submicrometer Phosphors with Different Crystallite/Particle Sizes. *Jpn J Appl Phys* 2008, 47(9): 7220-7223.

294. Leong KH. Morphological Control of Particles Generated from the Evaporation of Solution Droplets: Experiment. *J Aerosol Sci* 1987, 18(5): 525-552.

295. Leong KH. Morphological Control of Particles Generated from the Evaporation of Solution Droplets: Theoretical Considerations. *J Aerosol Sci* 1987, 18: 511-524.

296. Arkenbout GF. *Melt crystallization technology*, 1 edn. Technomic: Basel, 1995.

297. Cramer C, Fischer P, Windhab EJ. Drop formation in a co-flowing ambient fluid. *Chem Eng Sci* 2004, 59(15): 3045-3058.

298. Mokkelbost T, Kaus I, Haugsrud R, Norby T, Grande T, Einarsrud M-A. High-Temperature Proton-Conducting Lanthanum Ortho-Niobate-Based Materials. Part II: Sintering Properties and Solubility of Alkaline Earth Oxides. *J Am Ceram Soc* 2008, 91(3): 879-886.

299. Thybo P, Hovgaard L, Lindeløv JS, Brask A, Andersen SK. Scaling Up the Spray Drying Process from Pilot to Production Scale Using an Atomized Droplet Size Criterion. *Pharmaceut Res* 2008, 25(7): 1610.

300. Luo X, Wang X, Liao L, Gamboa S, Sebastian PJ. Synthesis and characterization of high tap-density layered $Li[Ni_{1/3}Co_{1/3}Mn_{1/3}]O_2$ cathode material via hydroxide co-precipitation. *J Power Sources* 2006, 158(1): 654-658.

301. Cao A, Manthiram A. Shape-controlled synthesis of high tap density cathode oxides for lithium ion batteries. *Phys Chem Chem Phys* 2012, 14: 6724-6728.

302. Amine K, Liu J, Belharouak I, Kang S-H, Bloom I, Vissers D, *et al.* Advanced cathode materials for high-power applications. *J Power Sources* 2005, 146: 111-115.

303. Kang S-H, Park S-H, Johnson CS, Amine K. Effects of Li Content on Structure and Electrochemical Properties of $Li_{1+x}(Ni_{0.5}Mn_{0.5})_{1-x}O_2$ ($0<x<0.15$) Electrodes in Lithiucm Cells (1.0-4.8 V). *J Electrochem Soc* 2007, 154(4): A268-A274.

304. Xiao J, Chernova NA, Whittingham MS. Influence of lithium content on performance of layered $Li_{1\ z}[Ni_{0.45}Mn_{0.45}Co_{0.1}]_{1-z}O_2$ in lithium ion batteries. *MRS Proceedings* 2007, 972.

305. Choi J, Manthiram A. Role of Chemical and Structural Stabilities on the Electrochemical Properties of Layered $LiNi_{1/3}Mn_{1/3}Co_{1/3}O_2$ Cathodes. *J Electrochem Soc* 2005, 152(9): A1714-A1718.

306. Ryu S-H, Jin B-S, Kim J-S, Park S-J, Lee CW, Kim H-S. Synthesis and Electrochemical Performance of $0.3Li_2MnO_3 \cdot 0.7LiMO_2$ (M = Mn, Co, Ni) Cathode Materials for Li-Ion Batteries. *J Nanosci Nanotechnol* 2013, 13: 3679-3684.

307. Cheng F, Chen J, Zhou H, Manthiram A. Structural and Electrochemical Characterization of $(NH_4)_2HPO_4$-Treated Lithium-Rich Layered $Li_{1.2}Ni_{0.2}Mn_{0.6}O_2$ Cathodes for Lithium-Ion Batteries. *J Electrochem Soc* 2013, 160(10): A1661-A1667.

308. Taniguchi I, Tussupbayev R. Synthesis of $LiFePO_4$/C nanocomposites by a novel process and their electrochemical properties. *CHem Eng J* 2012, 192: 334-342.

309. Chen Y, Zeng D, Peng J, Hu S, Li Z, Lei G. Synthesis and Electrochemical Properties of Li_2FeSiO_4/C as Cathode Materials for Lithium-ion Batteries. *Funct Mater Lett* 2013, 6(3): 1-6.

310. Pereira N, Matthias C, Bell K, Badway F, Plitz I, Al-Sharab J, *et al.* Stoichiometric, Morphological, and Electrochemical Impact of the Phase Stability of LixCoO2. *J Electrochem Soc* 2005, 152(1): A114-A125.

311. Yabuuchi N, Lu Y-C, Mansour AN, Kawaguchi T, Shao-Horn Y. The Influence of Surface Chemistry on the Rate Capability of $LiNi_{0.5}Mn_{0.5}O_2$ for Lithium Rechargeable Batteries. *Electrochem Solid-State Lett* 2010, 13(11): A158-A161.

312. Pickup DM, Simon D, Fooken M, Krampitz H, Eck ERHv, Kelder EM. 6 Li MAS NMR study of stoichiometric and chemically delithiated LixMn2O4 spinels. *J Mater Chem* 2003, 13: 963-968.

313. Xia Y, Kumada N, Yoshio M. Enhancing the elevated temperature performance of $Li/LiMn_2O_4$ cells by reducing LiMn2O4 surface area. *J Power Sources* 2000, 90: 135-138.

314. Rudin T, Wegner K, Pratsinis SE. Uniform nanoparticles by flame-assisted spray pyrolysis (FASP) of low cost precursors. *J Nanopart Res* 2011, 13: 2715-2725.

315. Lengyel M, Atlas G, Elhassid D, Luo PY, Zhang X, Belharouak I, *et al.* Effects of synthesis conditions on the physical and electrochemical properties of $Li_{1.2}Mn_{0.54}Ni_{0.13}Co_{0.13}O_2$ prepared by spray pyrolysis. *J Power Sources* 2014, 262: 286-296.

316. Fell CR, Caroll KJ, Chi M, Meng YS. Synthesis–Structure–Property Relations in Layered, "Li-excess" Oxides Electrode Materials $Li[Li_{1/3-2x/3}Ni_xMn_{2/3-x/3}]O_2$ (x = 1/3, 1/4, and 1/5). *J Electrochem Soc* 2010, 157(11): A1202-A1211.

317. Park S-H, Sato Y, Kim J-K, Lee Y-S. Powder property and electrochemical characterization of Li_2MnO_3 material. *Mater Chem Phys* 2007, 102: 225-230.

318. Kim J-S, Johnson CS, Vaughey JT, Thackeray MM, Hackney SA, Yoon W, *et al.* Electrochemical and Structural Properties of $xLi_2M'O_3$ (1-x) $LiMn_{0.5}Ni_{0.5}O_2$ Electrodes for Lithium Batteries (M' =Ti, Mn, Zr $0<x<0.3$). *Chem Mater* 2004, 16: 1996-2006.

319. Yu H, Kim H, Wang Y, He P, Asakura D, Nakamura Y, *et al.* High-energy 'composite' layered manganese-rich cathode materials via controlling Li_2MnO_3 phase activation for lithium-ion batteries. *Phys Chem Chem Phys* 2012, 14: 6584-6595.

320. Hong J, Lim H-D, Lee M, Kim S-W, Kim H, Oh S-T, *et al.* Critical Role of Oxygen Evolved from Layered Li−Excess Metal Oxides in Lithium Rechargeable Batteries. *Chem Mater* 2012, 24: 2692-2697.

321. Ghanty C, Basu RN, Majumder SB. Electrochemical performances of $0.9Li_2MnO_3$–$0.1Li(Mn_{0.375}Ni_{0.375}Co_{0.25})O_2$ cathodes Role of the cycling induced layered to spinel phase transformation. *Solid State Ionics* 2014, 256: 19-28.

322. Wang Y, Bie X, Nikolowski K, Ehrenberg H, Du F, Hinterstein M, *et al.* Relationships between Structural Changes and Electrochemical Kinetics of Li-Excess $Li_{1.13}Ni_{0.3}Mn_{0.57}O_2$ during the First Charge. *J Phys Chem C* 2013, 117: 3279-3286.

323. Simonin L, Colin J-F, Ranieri V, Canévet E, Martin J-F, Bourbon C, *et al.* In situ investigations of a Li-rich Mn–Ni layered oxide for Li-ion batteries. *J Mater Chem* 2012, 22: 11316.

324. Mohanty D, Sefat AS, Ku J, Meisner RA, Rondidone AJ, Payzant EA, *et al.* Correlating cation ordering and voltage fade in a lithium–manganese-rich lithium-ion battery cathode oxide: a joint magnetic susceptibility and TEM study. *Phys Chem Chem Phys* 2013, 15: 19496.

325. Mohanty D, Huq A, Payzant EA, Sefat AS, Li J, Abraham DP, *et al.* Neutron Diffraction and Magnetic Susceptibility Studies on a High- Voltage $Li_{1.2}Mn_{0.55}Ni_{0.15}Co_{0.10}O_2$ Lithium Ion Battery Cathode: Insight into the Crystal Structure. *Chem Mater* 2013, 25: 4064-4070.

326. Yu S-H, Yoon T, Mun J, Park S, Kang Y-S, Park J-H, *et al.* Continuous activation of Li_2MnO_3 component upon cycling in $Li_{1.167}Ni_{0.233}Co_{0.100}Mn_{0.467}Mo_{0.033}O_2$ cathode material for lithium ion batteries. *J Mater Chem A* 2013, 1: 2833.

327. Bloom I, Trahey L, Abouimrane A, Belharouak I, Zhang X, Wu Q, *et al.* Effect of interface modifications on voltage fade in $0.5Li_2MnO_3$ $0.5LiNi_{0.375}Mn_{0.375}Co_{0.25}O_2$ cathode materials. *J Power Sources* 2014, 249: 509-514.

328. Lee E-S, Manthiram A. Smart design of lithium-rich layered oxide cathode compositions with suppressed voltage decay. *J Mater Chem A* 2014, 2: 3932.

329. Lengyel M, Atlas G, Elhassid D, Zhang X, Belharouak I, Axelbaum RL. Effects of surface area and lithium content on the electrochemical performance of $Li_{1.2}Mn_{0.54}Ni_{0.13}Co_{0.13}O_2$ 2014.

330. Wang H, Tan TA, Yang P, Lai MO, Lu L. High-Rate Performances of the Ru-Doped Spinel $LiNi_{0.5}Mn_{1.5}O_4$:Effects of Doping and Particle Size. *J Phys Chem C* 2011, 115: 6102-6110.

331. Luo W, Zhou F, Zhao X, Lu Z, Li X, Dahn JR. Synthesis, Characterization and Thermal Stability of $LiNi_{1/3}Mn_{1/3}Co_{1/3-z}Mg_zO_2$, $LiNi_{1/3-z}Mn_{1/3}Co_{1/3}Mg_zO_2$ and $LiNi_{1/3}Mn_{1/3-z}Co_{1/3}Mg_zO_2$. *Chem Mater* 2010, 22: 1164-1172.

332. Pouillerie C, Perton F, Biensan P, Péres JP, Broussely M, Delmas C. Effect of Magnesium substitution on the cycling behavior of lithium nickel cobalt oxide. *J Power Sources* 2001, 96: 293-302.

333. Chowdari BVR, Rao GVS, Chow SY. Cathodic behavior of (Co, Ti, Mg)- doped $LiNiO_2$. *Solid State Ionics* 2001, 140: 55-62.

334. Lee DK, Han SC, Ahn D, Singh SP, Sohn K-S, Pyo M. Suppression of Phase Transition in $LiTb_{0.01}Mn_{1.99}O_4$ Cathodes with Fast Li+Diffusion. *ACS Appl Mater Interfaces* 2012, 4: 6842-6848.

335. Tavakoli AH, Kondo H, Ukyo Y, Navrotsky A. Stabilizing Effect of Mg on the Energetics of the $Li(Ni,Co,Al)O_2$ Cathode Material for Lithium Ion Batteries. *J Electrochem Soc* 2013, 160(2): A302-A305.

336. Zhou W-J, He B-L, Li H-L. Synthesis, structure and electrochemistry of Ag-modified $LiMn_2O_4$ cathode materials for lithium-ion batteries. *Mat Res Bull* 2008, 43: 2285-2294.

337. Johnson CS, Kim J-S, Kropf AJ, Kahaian AJ, Vaughey JT, Thackeray MM. The role of Li_2MO_2 structures (M = metal ion) in the electrochemistry of (x)$LiMn_{0.5}Ni_{0.5}O_2$ (1-x) Li_2TiO_3 electrodes for lithium-ion batteries. *Electrochem Comm* 2002, 4: 492-498.

338. Park SH, Oh SW, Kang SG, Myung S-T, Sun Y-K. Effects of Molybdenum Doping on the Layered $Li[Ni_{0.5+x}Mn_{0.5-2x}Mo_x]O_2$ Cathode Materials for Lithium Secondary Batteries. *Chem Lett* 2004, 33(1): 2.

339. Idemoto Y, Horiko K, Ito Y, Koura N, Ui K. Li content dependence of the thermodynamic stability, crystal structure and electrode performance of $Li_xMn_{2-y}M_yO_4$ as a cathode active material for the lithium secondary battery. *Electrochemistry* 2005, 72(11): 755-762.

340. Yabuuchi N, Yamamoto K, Yoshii K, Nakai I, Nishizawa T, Omaru A, *et al.* Structural and Electrochemical Characterizations on Li_2MnO_3-$LiCoO_2$-$LiCrO_2$ System as Positive Electrode Materials for Rechargeable Lithium Batteries. *J Electrochem Soc* 2013, 160(1): A39-A45.

341. Song B, Lai MO, Lu L. Influence of Ru subtitution on Li-rich $0.55Li_2MnO_3$ $0.45LiNi_{1/3}Co_{1/3}Mn_{1/3}O_2$ cathode for Li-ion batteries. *Electrochim Acta* 2012, 80: 187-195.

342. Wang C-C, Manthiram A. Influence of cationic substitutions on the first charge and reversible capacities of lithium-rich layered oxide cathodes. *J Mater Chem A* 2013, 1: 10209.

343. Yu H, Zhou H. Initial Coulombic efficiency improvement of the $Li_{1.2}Mn_{0.567}Ni_{0.166}Co_{0.067}O_2$ lithium-rich material by ruthenium substitution for manganese. *J Mater Chem* 2012, 22: 15507.

344. Qiu B, Wang J, Xia Y, Liu Y, Qin L, Yao X, *et al.* Effects of Na+ contents on electrochemical properties of $Li_{1.2}Ni_{0.13}Co_{0.13}Mn_{0.54}O_2$ cathode materials. *J Power Sources* 2013, 240: 530-535.

345. Tang Z, Li X, Wang Z. Effects of Al doping for $Li[Li_{0.09}Mn_{0.65}*0.91Ni_{0.35}*_{0.91}]O_2$ cathode material. *Ionics* 2013, 19: 1495-1501.

346. He W, Yuan D, Qian J, Ai X, Yang H, Cao Y. Enhanced high-rate capability and cycling stability of Na-stabilized layered $Li_{1.2}[Co_{0.13}Ni_{0.13}Mn_{0.54}]O_2$ cathode material. *J Mater Chem A* 2013, 1: 11397.

347. Dong X, Xu Y, Xiong L, Sun X, Zhang Z. Sodium substitution for partial lithium to significantly enhance the cycling stability of Li_2MnO_3 cathode material. *J Power Sources* 2013, 243: 78-87.

348. Widiyastuti W, Balgis R, Iskandar F, Okuyama K. Nanoparticle formation in spray pyrolysis under low-pressure conditions. *Chem Eng Sci* 2010, 65(5): 1846-1854.

349. Conry TE, Mehta A, Cabana J, Doeff MM. Structural Underpinnings of the Enhanced Cycling Stability upon Al Substitution in $LiNi_{0.45}Mn_{0.45}Co_{0.1-y}Al_yO_2$ Positive Electrode Materials for Li-ion Batteries. *Chem Mater* 2012, 24: 3307-3317.

350. Conry TE, Mehta A, Cabana J, Doeff MM. XAFS Investigations of $LiNi_{0.45}Mn_{0.45}Co_{0.1-y}Al_yO_2$ Positive Electrode Materials. *J Electrochem Soc* 2012, 159(9): A1562-A1571.

351. Shannon RD. Revised Effective Ionic Radii and Systematic Studies of Interatomie Distances in Halides and Chaleogenides. *Acta Cryst* 1976, A 32: 751.

352. Gao J, Huang Z, Li J, He X, Jiang C. Enhanced high-rate capability and cycling stability of Na-stabilized layered $Li_{1.2}[Co_{0.13}Ni_{0.13}Mn_{0.54}]O_2$ cathode material. *Ionics* 2013.

353. Kim S, Ma X, Ong SP, Ceder G. A comparison of destabilization mechanisms of the layered Na_xMO_2 and

LixMO2 compounds upon alkali de-intercalation. *Phys Chem Chem Phys* 2012, 14: 15571-15578.

354. Amalraj F, Talianker M, Markovsky B, Burlaka L, Leifer N, Goobes G, *et al.* Studies of Li and Mn-Rich $Li_x[MnNiCo]O_2$ Electrodes: Electrochemical Performance, Structure, and the Effect of the Aluminum Fluoride Coating *J Electrochem Soc* 2013, 160(11): A2220-A2233.

355. Chung W, Jung H, Lee CH, Kim SH. Characteristics of MgO-coated alkaline Earth selenide phosphor prepared by spray pyrolysis. *Thin Solid Films* 2013, 546: 98-103.

356. Aurbach D, Levi MD, Levi E, Teller H, Markovsky B, Salitra G, *et al.* Common electroanalytical behavior of Li intercalation processes into graphite and transition metal oxides. *J Electrochem Soc* 1998, 145(9): 3024-3034.

357. Levi MD, Salitra G, Markovsky B, Teller H, Aurbach D, Heider U, *et al.* Solid-state electrochemical kinetics of Li-ion intercalation into $Li_{1-x}CoO_2$: Simultaneous application of electroanalytical techniques SSCV, PITT, and EIS. *J Electrochem Soc* 1999, 146(4): 1279-1289.

358. Zhuang QC, Wei T, Du LL, Cui YL, Fang L, Sun SG. An Electrochemical Impedance Spectroscopic Study of the Electronic and Ionic Transport Properties of Spinet LiMn2O4. *J Phys Chem C* 2010, 114(18): 8614-8621.

359. Elhassid D, Axelbaum RL, Lengyel M, Moller W, Atlas G, inventors; Method for the Use of Slurries in Spray Pyrolysis for the Production of Non-hollow, Porous Particles. 2014.

360. Molinari R, Argurio P, Poerio T. Membrane Processes Based on Complexation Reactions of Pollutants as Sustainable Wastewater Treatments. *Sustainability* 2009, 1: 978-993.

361. Cremades E, Echeverria J, Alvarez S. The Trigonal Prism in Coordination Chemistry. *Chem Eur J* 2010, 16: 10380-10396.

362. Geckeler KE. Water-Soluble Polymer-Metal Complexes for Liquid-Phase Retention Separation. *Macromol Symp* 2000, 156: 29-35.

Appendix A

Example recipes

The following recipes are provided as an example. Detailed recipes of the used precursor solutions, binder solutions and for cathode films can be found in the laboratory notebooks.

Doped samples							
0.2 NMC	nominal stoich.	red. Stoich.	Mass of nitrate salt	0.3 NMC	nominal stoich.	red. Stoich.	Mass of nitrate salt
$LiNO_3$	1.188	1.080	14.887	$LiNO_3$	1.288	1.120	15.439
$Mn(NO_3)_2$.$4H_2O$	0.454	0.413	20.727	$Mn(NO_3)_2$.$4H_2O$	0.521	0.453	22.736
$Ni(NO_3)_2$· $6H_2O$	0.267	0.242	14.099	$Ni(NO_3)_2$· $6H_2O$	0.233	0.203	11.800
$Co(NO_3)_2$· $6H_2O$	0.254	0.231	13.449	$Co(NO_3)_2$· $6H_2O$	0.221	0.192	11.177
$Al(NO_3)_3$* $9H_2O$	0.013	0.011	0.853	$Al(NO_3)_3$* $9H_2O$	0.013	0.011	0.816
$Na(NO_3)$	0.013	0.011	0.193	$Na(NO_3)$	0.013	0.011	0.185
$Ba(NO_3)_2$	0.013	0.011	0.594	$Ba(NO_3)_2$	0.013	0.011	0.568
O_2	2.200	2.000		O_2	2.300	2.000	
0.2 NMC	nominal stoich.	red. Stoich.		0.3 NMC	0.2 NMC	red. Stoich.	
$LiNO_3$	1.188	1.080	14.887	$LiNO_3$	1.288	1.120	15.439
$Mn(NO_3)_2$.$4H_2O$	0.454	0.413	20.727	$Mn(NO_3)_2$.$4H_2O$	0.521	0.453	22.736
$Ni(NO_3)_2$· $6H_2O$	0.267	0.242	14.099	$Ni(NO_3)_2$· $6H_2O$	0.233	0.203	11.800
$Co(NO_3)_2$· $6H_2O$	0.267	0.242	14.111	$Co(NO_3)_2$· $6H_2O$	0.233	0.203	11.810
$Al(NO_3)_3$* $9H_2O$	0.013	0.011	0.853	$Al(NO_3)_3$* $9H_2O$	0.013	0.011	0.816
$Na(NO_3)$	0.013	0.011	0.193	$Na(NO_3)$	0.013	0.011	0.185
O_2	2.200	2.000		O_2	2.300	2.000	

Nominal stoichiometry stands for adding up the nominal composition from the formula. I.e. for $0.5Li_2MnO_3$ $0.5LiNi_{0.33}Mn_{0.33}Co_{0.33}O_2$ = $Li_{1.5}Mn_{0.67}Ni_{0.17}Co_{0.17}O_{2.5}$, which can be converted to the reduced stoichiometry, by recalculating it using the O content. If we convert the

$Li_{1.5}Mn_{0.67}Ni_{0.17}Co_{0.17}O_{2.5}$ by multiplying 2/2.5, we get the reduced stoichiometry $Li_{1.2}Mn_{0.54}Ni_{0.13}Co_{0.13}O_2$.

Cathode film making

m_{act} = 1.01 g

m_{binder} = 1.01/0.0693*20/80=3.64 g

Details are discussed in the SOP section.

The target binder amount should be between 3.5-4.5 gram to ensure good uniformity and flow properties. Smaller amounts will make the film too viscous.

Binder solution making (target: 8%)

$m_{C\text{-}black}$ = 10.00 g

m_{PVdF} 12% = 83.33 g

m_{NMP} = 156.67g

Once the solution has been mixed together and sonicated for 2 hours weigh out 3* 5-6 gram samples, vacuum dry them overnight and calculate actual concentrations.

ICP-MS sample preparation

Dilute the precursor solution by taking 0.1 ml, diluting it to 10 ml-s with ultrapure water. Repeat this for a second time and then take 1 ml out from the twice diluted sample and dilute it to 10 ml with 1% HNO_3 solution.

Microtome sample preparation

The following section provides a general overview of the process and the NNIN staff has the accurate recipe for preparation of the sample.

1. Suspend 50-100 mg of powder in HPLC grade acetone and let it sit overnight until the acetone evaporates.
2. Add pure NMA + Eponate 12 resin + DDSA + DMP-30 EPco (Ted Pella) – mix them with sample until air bubbles are removed
3. Shake the solution for 1 hour with acetone : Epon 1:1 – after an hour switch to pure Epon
4. Replace the Epon twice by centrifuging the samples at 8000-13000 rpm after 1-1 hour
5. Put the samples to the oven for polymerizing at 60 °C overnight
6. Remarks: Epon alone does not penetrate the particles. While embedding use Epon + acetone overnight followed by 1 day Epon, then exchanged for embedding Epon to polymerize.

Appendix B

Standard Operating Procedures (SOPs)

The following SOPs are provided as an example of the standard protocols related to this research and are updated as of March 2014.

Microburner setup

Tasks to perform before the first operation of the system:

- Create a closed system for leak checking so that there is one open inlet for air but no outlet is left open.
- Perform a leak check on the system. Attach an air inlet to the system analyzed using the appropriate inlets for the setup (bolts, needle valves, etc).
- Slowly apply 60 psi pressure with opening the air supply gradually to each closed individual system after one another without any flow. After the pressure has been applied to the closed system, put "Snoop" liquid behind each piping attachment and observe whether or not growing bubbles are present (growing bubbles indicate a leak). If no growing bubbles can be observed and the system holds the pressure for at least 20 minutes, then turn off the gas going in and slowly release pressure with slowly untying a bolt on the back of the panel. Make sure no person is in the direction of the bolt being released.
- If no alteration or damage is observed in the system, repeat the leak check every 3 months.
- Calibrate the rotameters and measure their response performance to certain gases and inlet pressures. The measurement can be performed according to the following: Gilibrator Tube Cube Calibration.

Operation of the microflame reactor

Before the first use

- Connect the inlets of the honeycomb burner to the oxidizer (air; this goes to the inlet that is on the top part of the burner) and the fuel to the inlet on the bottom of the burner. Attach the atomizer gas inlet to the fuel line. If any other combination of fuel/ oxidizer (diluted gases) is needed, mount the system with the appropriate joints, such as a T-joint or a cross.
- Check if all the valves on the control panel are turned off.
- Purge the H_2 line with either N_2 or Ar, depending on availability.
- Identify the temperature under the heating tape coiled up around the bubbler containing methanol before the first use. Try to identify a setting between 45-55 °C and record that setting.

Daily operation

- Check the methanol level in the viewing tube attached to the bubbler. Refill with detaching the bolt using a funnel if necessary. Recap the system after refilling.
- Empty the methanol collected inside the bubbler located before the atomizer and pour it back into the methanol bubbler column. If the methanol would appear to be contaminated dispose of it according to the safety procedures.
- Turn on the bubbler heating variac. Check if it is at the preset adjustment. It is safe to start the experiment if the temperature is above 40 °C, but the temperature should never exceed 60 °C, where methanol starts to boil.
- Turn on the H_2 and then the air flow with opening the gas tank for the H_2 flow and the gas inlet on the fume hood for the air. Turn on the adequate switch valves on the flow panel (each switch valve is labeled), and increase the pressure with the regulators to the desired operating pressure (generally 40 psi). Open the valve for the H_2 flow before the

burner and increase the flow rate to approximately 0.5 lpm. Open the valve for the air flow before the burner, and increase the air flow rate to above 1-2 lpm. Ignite the mixture with an igniter above the glass tube.

- After ignition increase the air and H_2 flow rates to the desired values. Adjust the regulators appropriately.
- Make sure to maintain complete combustion in order to avoid migration of the flame to the top of the glass vial. If the flame migrates to the top of the glass vial, turn off fuel supply and reignite the burner. During the operation, make sure to regularly check if the flow pressures are preserved.
- Turn on the N_2 source and the switch valve on the panel. Turn on the valve before the bubbler.
- Plug in the vacuum pump and check if enough vacuum is in the filter holder inlet above the glass tube.
- Place the filter holder above the glass tube and start collecting the sample. Sample collection can be controlled with monitoring the gas temperature flowing into the filter support (powder collection is achieved when the flow temperature is around 160-225 °C). Make sure not to exceed 250 °C, as both the filter and the filter support can melt. Once a sufficient amount has been collected (or after one hour after startup) unplug the vacuum pump, turn off the switch valve for the atomizing gas and remove the sample collected. Once finished, resume sampling with restarting the atomization and the vacuum.
- To shut down the system close the needle valves on the gas cylinders first. Turn off the N_2 source. When the pressure on the external pressure gauge drops to nearly 0, close the H_2 switch valve (make sure that the N2 pressure reaches 0 earlier) and allow the system

to burn the remaining fuel in the tubing. After the burning seizes, close the valves on the rotameter and close the air tap (or oxidizer valve). Once the pressure gauge monitoring the oxidizer flow rate starts dropping, close the switch valve and then the valve on the rotameter. Make sure to close all the pressure regulators.

Emergency shutdown instructions

- **Turn off the H_2 switch valve (labeled above the valve "H2") on the bottom of the flow panel.**
- **Turn off the N_2 switch valve (labeled above the valve "N2") on the bottom of the flow panel.**
- **Unplug the vacuum pump to turn it off (labeled "Vacuum pump").**
- **Turn off the heating of the bubbler (labeled "Bubbler heating").**
- **Turn off the air switch valve (labeled above the valve "Air") on the bottom of the flow panel.**
- **Close the valve on the H_2 cylinder.**
- **Close the brown valve labeled "N_2" on the side of the fume hood.**

Rietveld SOP

Instructions can be found at:
http://www.aps.anl.gov/Xray_Science_Division/Powder_Diffraction_Crystallography/EXPGUItricks.html

and at

http://www.ccp14.ac.uk/tutorial/cmpr/manindex.htm

https://subversion.xor.aps.anl.gov/trac/CMPR

https://subversion.xor.aps.anl.gov/trac/CMPR/wiki/InstallWindows

http://www.aps.anl.gov/Xray_Science_Division/Powder_Diffraction_Crystallography/

1. Rename .txt to .dat
2. select dataset
3. Select peak list
4. select a region to fit
5. select peaks
6. Refine FWHM
7. refine peak areas (last boxes)
8. refine backgrounds
9. refine eta
10. refine other peak widths (middle column)
11. refine asymmetry
12. Increment range by 5 degree (depending on spectrum)
13. select new peaks
14. Repeat steps 6-11
15. Repeat step 12 until spectrum is covered
16. Go to fitwidths
17. load peaklist (> 13 peaks)
18. Fit profile
19. These will provide initial estimates for u, v, w values

Appendix C

Microburner design plans

Earlier a small microburner was constructed to allow low temperature material synthesis. Due to the small capillary tubes the burner was capable of producing low temperature, uniform flames. To increase the productivity scale up of the burner was initiated, but the setup was never assembled. Appendix C contains the assembly instructions and the design plans for future reference.

Figure 55 – Flame structure of the small scale microburner while producing cathode materials.

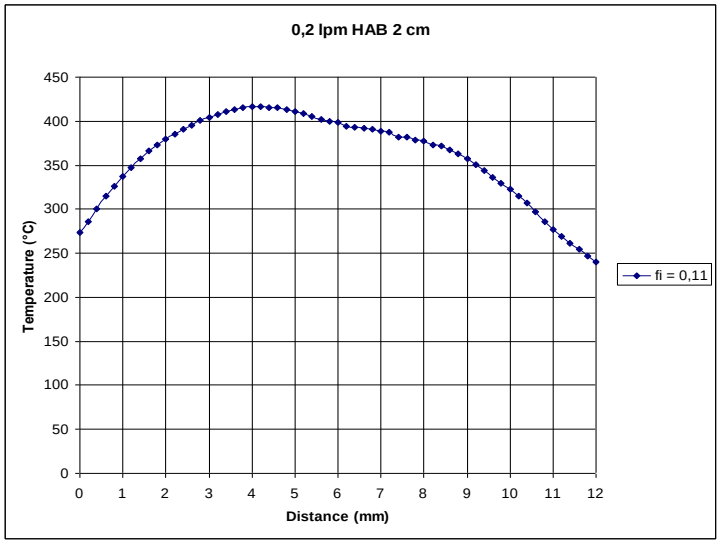

Figure 56 – Example of a temperature profile above the burner.

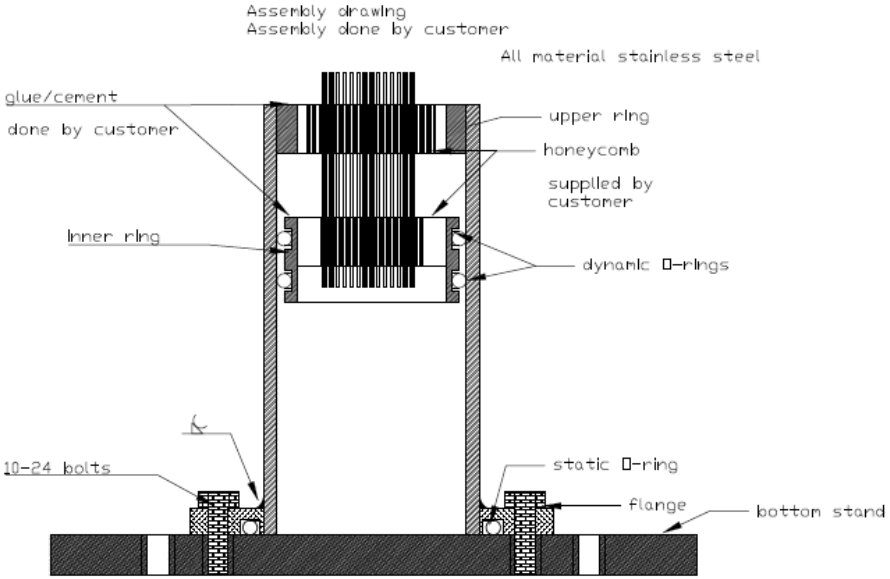

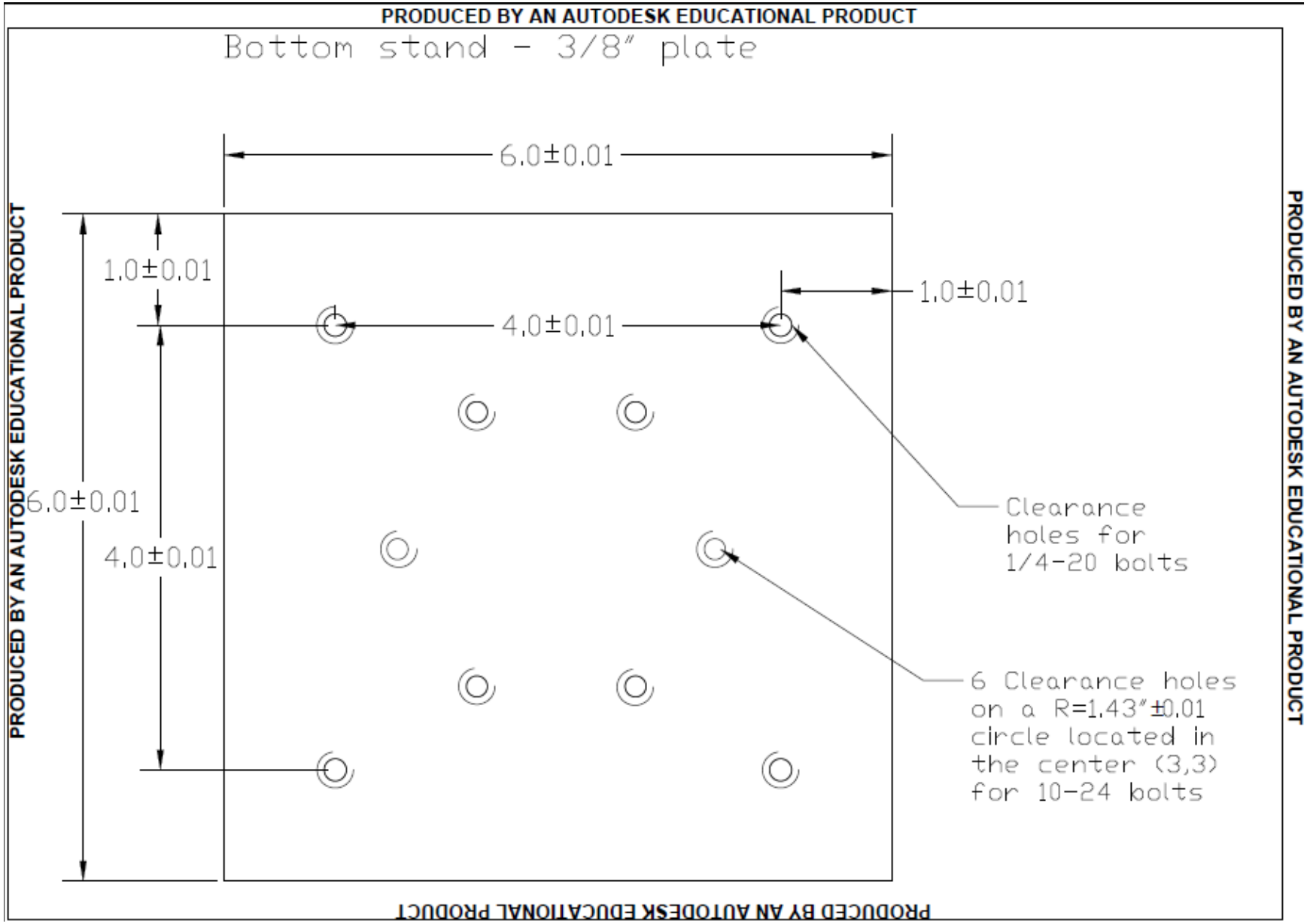
PRODUCED BY AN AUTODESK EDUCATIONAL PRODUCT
Bottom stand - 3/8" plate
6.0±0.01
1.0±0.01
1.0±0.01
4.0±0.01
6.0±0.01
4.0±0.01
Clearance holes for 1/4-20 bolts
6 Clearance holes on a R=1.43"±0.01 circle located in the center (3,3) for 10-24 bolts
PRODUCED BY AN AUTODESK EDUCATIONAL PRODUCT
PRODUCED BY AN AUTODESK EDUCATIONAL PRODUCT
PRODUCED BY AN AUTODESK EDUCATIONAL PRODUCT

Fitting locations

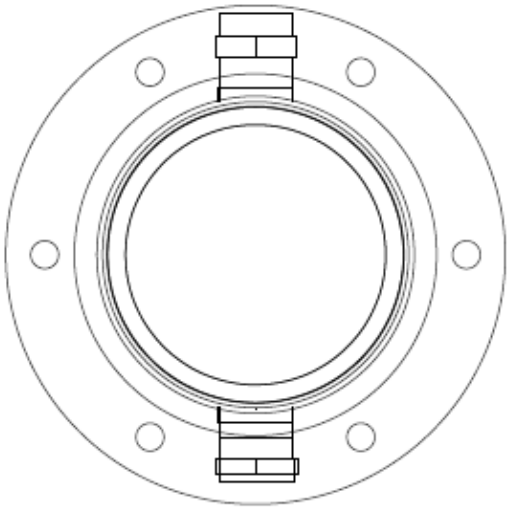

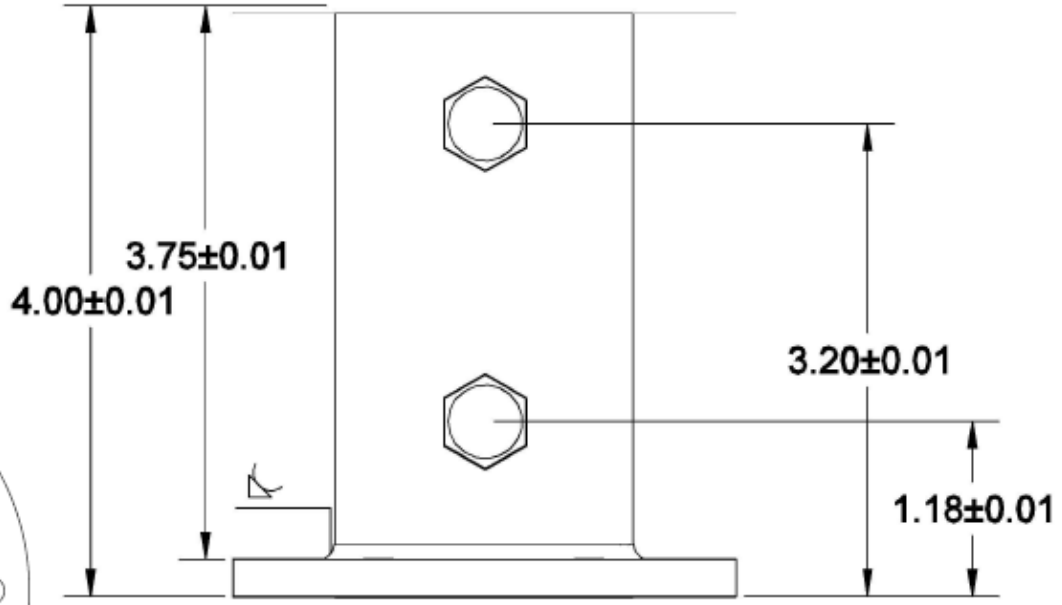

1/4" Swagelok tube fittings (4 - two for the top part, 1 for the bottom + 1 replacement) are supplied by the customer
4" tall 2" OD stainless steel tube supplied by the customer
honed interior surface

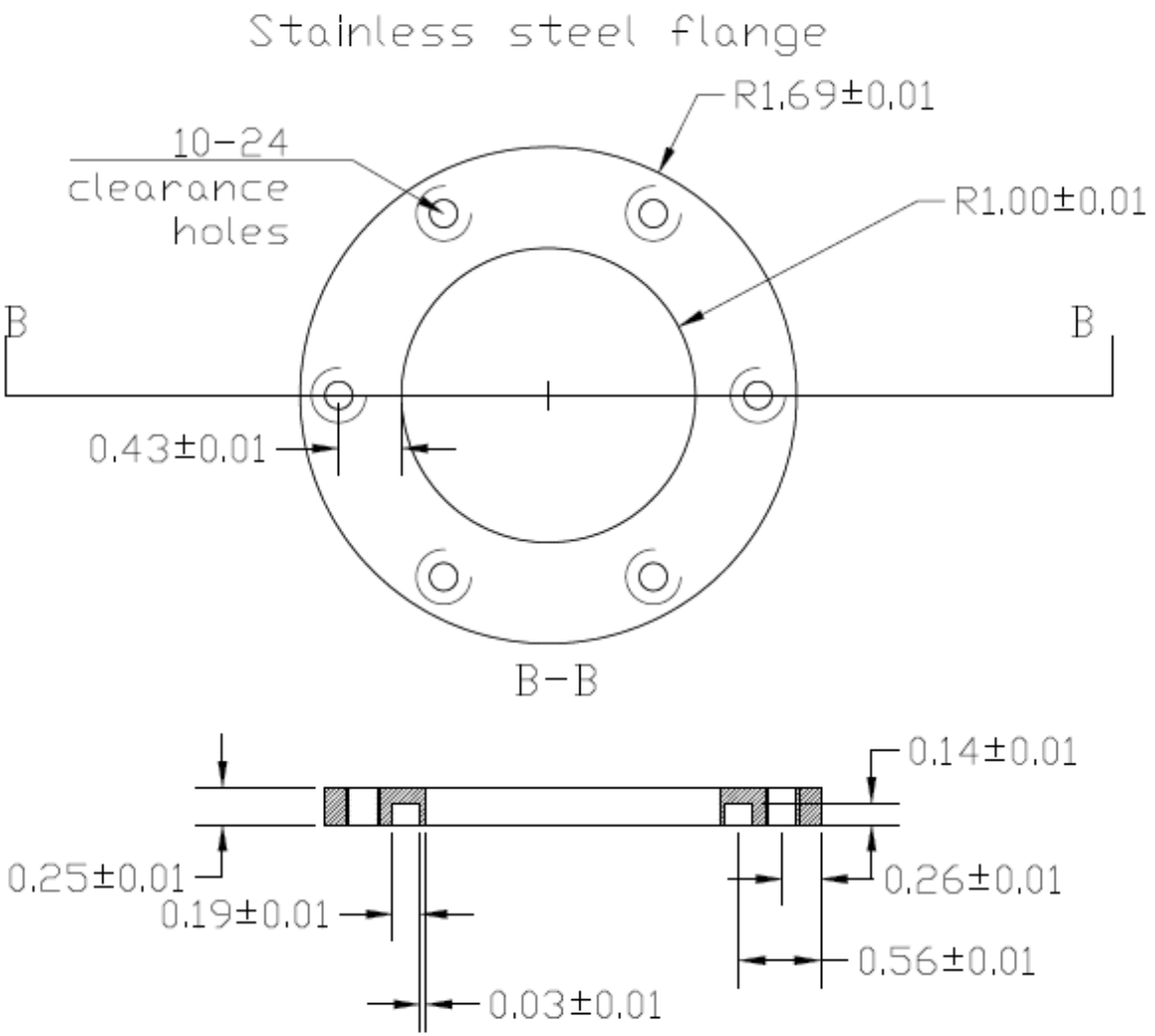

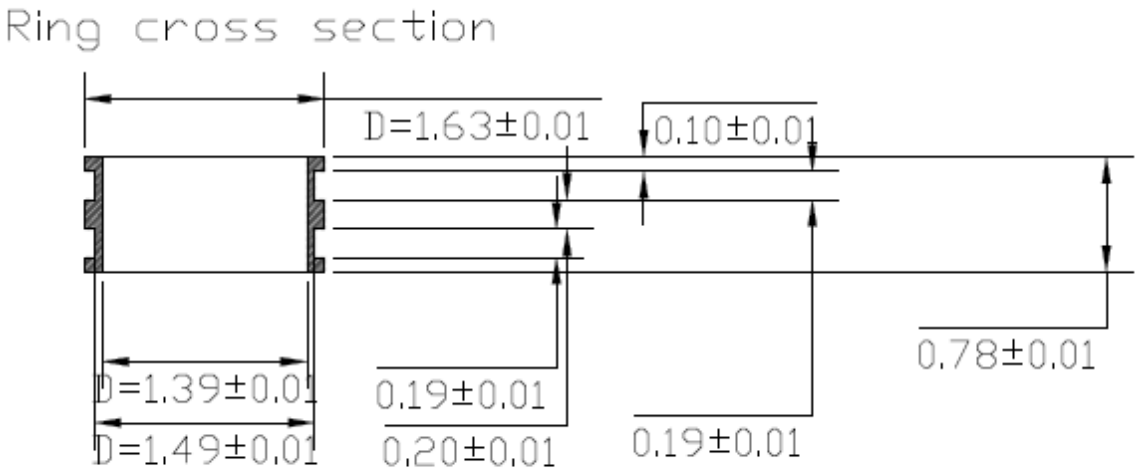

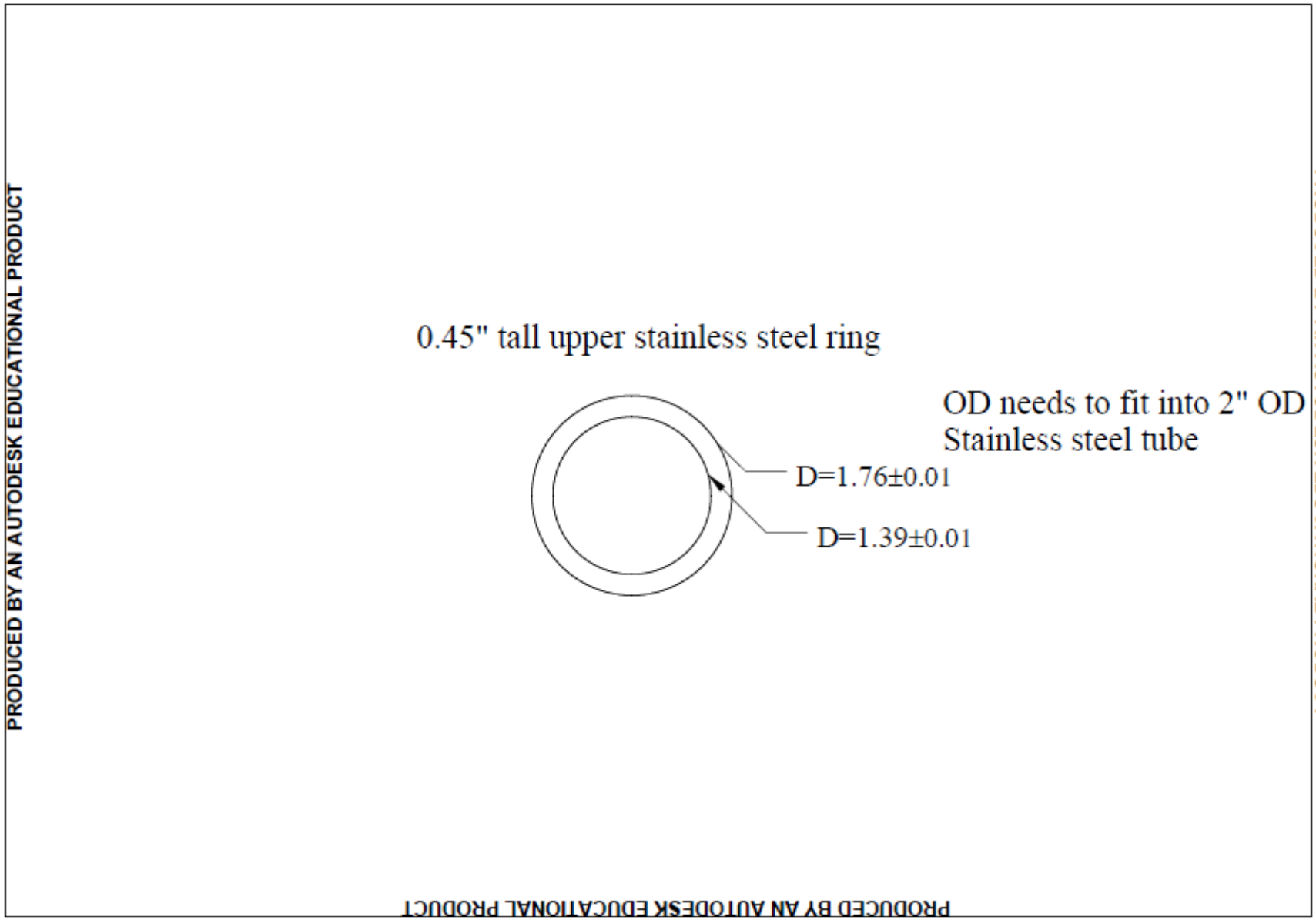

PRODUCED BY AN AUTODESK EDUCATIONAL PRODUCT

PRODUCED BY AN AUTODESK EDUCATIONAL PRODUCT

PRODUCED BY AN AUTODESK EDUCATIONAL PRODUCT

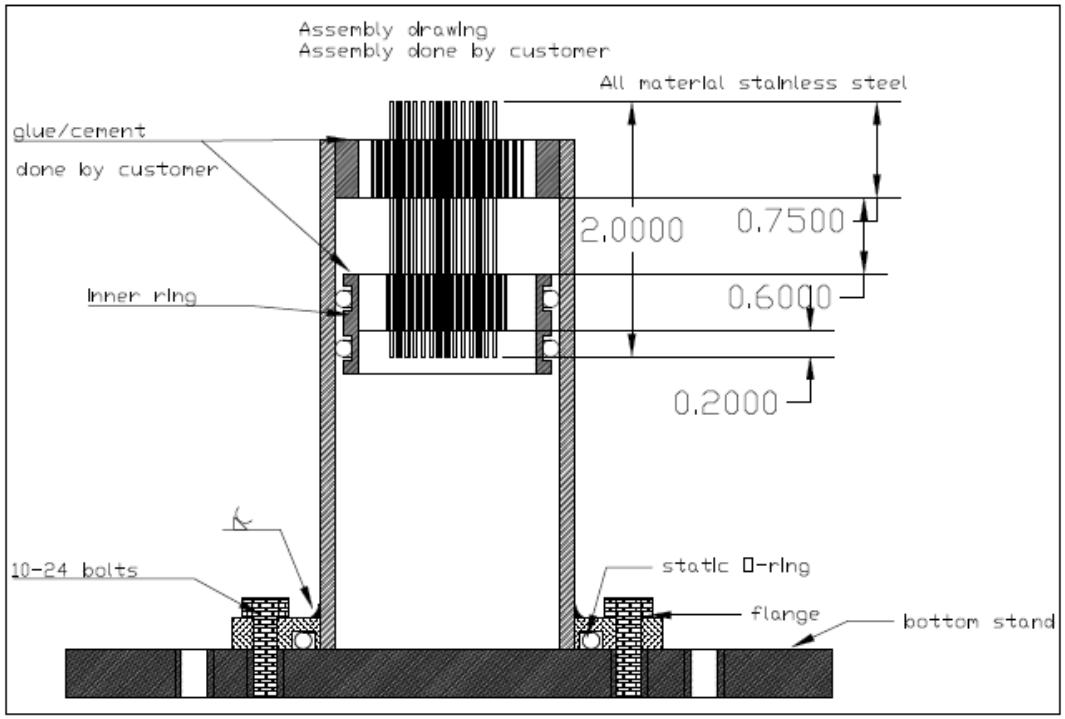

Resume

MIKLOS LENGYEL

6648 Oakland Ave. Apt. 3S, St. Louis, MO 63139, USA

+1-314-571-0901

mlengyel@wustl.edu

SUMMARY

PhD graduate May 2014 in Energy, Environmental and Chemical Engineering with over 8 years of laboratory experience. Extensive experience with material characterization related analytical methods (XRD, SEM, EDX, TEM, BET, ICP-MS). Strong experience (> 3 years) in the development and testing of NMC based lithium ion battery oxide cathode materials. Diverse experience with the application and scale up of aerosol based and wet chemistry processes at various production scales and the development of novel intellectual property. Familiar with Design of Experiments (DOE). Diverse academic and experimental background in organic and inorganic chemistry, analytical chemistry, process development and material science. Experience with training and supervising groups.

RESEARCH HIGHLIGHTS

- High level of proficiency in the testing of electrochemically active materials in thin films and coin cells.
- Studied the relationship between structural properties and electrochemical performance.
- Scaled-up a process for the production of cathode materials at > 50 gram/hour scale.
- Patent application in progress for NMC materials with reduced voltage fade.
- Patented a process for the production of solid and core-shell morphology particles by spray pyrolysis.
- Participated in a collaborative research with Dr. Ilias Belharouak at Argonne National Laboratory and X-Tend Energy to study the scale up of spray pyrolysis from laboratory scale.

ACADEMIC BACKGROUND

Washington University in St. Louis August 2009- May 2014
Department of Energy, Environmental and Chemical Engineering
PhD in Energy, Environmental and Chemical Engineering
Advisor: Dr. Richard L. Axelbaum
Research topic: Optimization of lithium-ion battery cathode materials synthesized via spray pyrolysis

Washington University in St. Louis
Teaching Center
Partial completion of teaching citation

Washington University in St. Louis – Office of Technology Management February 2012
Technology transfer workshop (2012)

Budapest University of Technology and Economics September 2004- June 2009
(Hungary)
Faculty of Chemical Technology and Biotechnology
MSc. in Chemical Engineering*, *Pharmaceutical major
Advisor: Dr. Laszlo Hazai, Dr. Csaba Szantay
Research topic: Synthesis of biologically active vindoline derivatives

WORK EXPERIENCES

PhD student researcher at X-Tend Energy, LLC March 2011-May 2014

- Scaled-up a process for the production of cathode materials at > 50 gram/hour scale.
- Patented a process for the production of solid and core-shell morphology particles by spray pyrolysis.
- Participated in a collaborative research with Dr. Ilias Belharouak at Argonne National Laboratory and X-Tend Energy to study the scale up of spray pyrolysis from laboratory scale.

Research in the Laboratory for Advanced Combustion and Energy Research (LACER - Washington University in St. Louis) May 2010- May 2014
Synthesized and optimized layered cathode materials prepared via aerosol synthesis method

- Identified optimal chemistry with variations in the cobalt content;
- Tested the relationship between surface area and electrochemical performance;
- Demonstrated the robustness of spray pyrolysis for the synthesis of lithium ion battery cathode materials.
- Optimized synthesis conditions and chemistry of cathode materials for optimal electrochemical performance in coin cells.
- Studied the effect of dopants on the electrochemistry and surface area of cathode materials.
- Working knowledge on the design of research level aerosol-based synthesis reactors (spray pyrolysis, flame spray pyrolysis, flame-assisted spray pyrolysis reactors).

Safety manager at LACER (Washington University in St.Louis) June 2012- May 2014

- Responsible for monthly and annual laboratory inspections, supervising SOPs and the laboratory safety protocols;

Teaching assistant (Washington University in St.Louis, graduate and undergraduate courses) — Fall 2010- Fall 2011 (3 semesters)
Chemical Reaction Engineering Laboratory, Environmental Engineering Laboratory, Transport Phenomena

Research in the Biomolecules laboratory (Budapest University of Technology and Economics) — 2006-2009 Jun (3 years)

- Demonstrated rearrangement occurring on the aromatic ring of vindoline;
- Prepared a new vindoline derivative with moderate biological activity for anti-cancer therapy applications;
- Designed and performed various organic synthesis reactions;

Teaching assistant (Budapest University of Technology and Economics, Hungary) — Fall 2007-Spring 2008 (2 semesters)
Synthesis of biologically active molecules laboratory

Procter & Gamble – Gillette R&D. (Egham near London, UK) — Summer 2008 (12 weeks)
Scientist intern

- Received a hire recommendation upon conclusion of the internship.
- Synthesized shaving gels using a 3 liter laboratory reactor.
- Studied scale up of shaving gels at bench scale (1 liter), laboratory reactor scale (3 liter) and pilot plant scale (200 liter).
- Analyzed, prepared and evaluated consumer studies.
- Various cGMP and manufacturing related trainings.

Private coaching. (Budapest, Hungary) — 2004-2009 (5 years)
Tutoring of high school students for college entry exams.

SKILLS

Laboratory instrument skills: FEI Nova 2300 Field Emission SEM, JEOL JSM-7001FLV, FEI Spirit Lab6 TEM, Perkin Elmer Elan DRC II ICP-MS, Perkin Elmer Optima 7300 DV-ICP-OES, Quantachrome Autosorb-1 BET, Leica Ultramicrotome, Dekati - ELPI, Welas – Pallas Instruments, TSI-OPS, Quantachrome Tapped Density analyzer, glove box, coin cell cathode film making, design of battery testing protocols, battery testing on Arbin, Gamry reference 600 Potentiostat/Galvanostat/ZRA, MTI BST8-WA, Sonaer 241PG, BGI Inc. Collison nebulizer, Rigaku XRD operation with Jade optimization, EDAX spectroscopy, miniMOUDI impactor, Union Process 01-HD attritor, TGA (TA instruments), SOP design and implementation, analysis of simple FT-IR, UV-VIS and NMR spectra, synthesis of materials using flame and spray pyrolysis techniques, aerosol reactor design, organic chemistry synthesis.

Computer skills: AutoCAD, Cadkey, Maple, MS Excel, MS Word, MS Power Point

LANGUAGES

Hungarian: native speaker
English: fluent
French: conversational level
German: basic level

PUBLICATIONS:

1. **M. Lengyel**, K.-Y. Shen[a], G. Atlas, H. L. Bretscher, D. M. Lanigan, J. M. Martin, M. D. Tracey, X. Zhang, R. L. Axelbaum , Trace Level Doping of NMC Cathode Materials to Reduce Voltage Fade (in preparation)

2. X. Zhang, I. Belharouak, **M. Lengyel**, R. Xu, G. Atlas, R. L. Axelbaum, Ultrahigh Capacity Nanostructured Li-Mn-Rich Cathode Materials from Spray Drying (in preparation)

3. **M. Lengyel,** D. Elhassid, G. Atlas, W. Moller, R. L. Axelbaum: Development of a Novel Spray Pyrolysis Process for the Large Scale Production of Battery Materials (submitted)

4. **M. Lengyel,** G. Atlas, D. Elhassid, X. Zhang, I. Belharouak, R. L. Axelbaum: Effects of lithium content and surface area on the electrochemical performance of $Li_{1.2}Mn_{0.54}Ni_{0.13}Co_{0.13}O_2$ (submitted)

5. **M. Lengyel**, X. Zhang, G. Atlas, H. L. Bretscher, R. L. Axelbaum: Composition Optimization of Layered Lithium Nickel Manganese Cobalt Oxide Materials Synthesized Via Ultrasonic Spray Pyrolysis (submitted)

6. **M. Lengyel**, G. Atlas, D. Elhassid, P. Y. Luo, X. Zhang, I. Belharouak, R. L. Axelbaum: Effects of synthesis conditions on the physical and electrochemical properties of $Li_{1.2}Mn_{0.54}Ni_{0.13}Co_{0.13}O_2$ prepared by spray pyrolysis (Accepted)

7. X. Zhang, **M. Lengyel**, R. L. Axelbaum: Nanostructured High-Energy $xLi_2MnO_3 \cdot (1-x)$ $LiNi_{0.5}Mn_{0.5}O_2$ ($0.3 \leq x \leq 0.6$) Cathode Materials Synthesized From Spray Pyrolysis: AIChE J., 60 (2), 2014, 443-450.

8. **M. Lengyel**, L. Hazai, Cs. Szantay (abstract): Synthesis of new biologically active vindoline derivatives, Periodica Polytechnica, 53 (1), 2009, 19-27.

9. A. Gorka-Kereskenyi, L. Szabo, L. Hazai, **M. Lengyel**, Cs. Jr. Szantay, Zs. Santa, Gy. Kalaus, Cs. Szantay: Aromatic electrophilic substitutions on vindoline, Heterocycles, 71 (7), 2007, 1553-1563

PATENTS:

1. R. L. Axelbaum, **M. Lengyel**: Doped Lithium-rich Layered Composite Cathode Materials (2014).

2. D. Elhassid, R. L. Axelbaum, **M. Lengyel**, G. Atlas, W. Moller: A Method for the Use of Slurries in Spray Pyrolysis for the Production of Non-hollow, Porous Particles (patent application with X-Tend Energy LLC., 2013).

CONFERENCE PRESENTATIONS:

1. **M. Lengyel**, G. Atlas, K.-Y. Shen, R. L. Axelbaum: Effects of Na Doping On $Li_{1.2}Mn_{0.53}Ni_{0.13}Co_{0.13}O_2$ Prepared *Via* Spray Pyrolysis, in: 224th ECS Meeting, San Francisco, 2013

2. K.-Y. Shen, **M. Lengyel**, G. Atlas, D. Elhassid, W. Moller, R. L. Axelbaum: Electrochemical Performance of Materials Synthesized By Flame-Assisted Spray Pyrolysis, in: 224th ECS Meeting, San Francisco, 2013

3. **M. Lengyel**, G. Atlas, W. Wu, X. Zhang, D. Elhassid, I. Belharouak, R. L. Axelbaum: Study of the effect of annealing conditions and lithium content on the electrochemical performance of $Li_{1.2}Mn_{0.53}Ni_{0.13}Co_{0.13}O_2$ prepared *via* spray pyrolysis process, in: 223rd ECS Meeting, Toronto, 2013

4. **M. Lengyel,** G. Atlas, D. Elhassid, P. Y. Luo, H. L. Bretscher, A. D. Ariel, X. Zhang, I. Belharouak: The Effect of Synthesis Temperature On The Electrochemical performance of $Li_{1.2}Mn_{0.53}Ni_{0.13}Co_{0.13}O_2$ Prepared via Spray Pyrolysis, in: MRS Fall Meeting, Boston, 2012

5. **M. Lengyel**, Xiaofeng Zhang, Gal Atlas, Dror Elhassid, Ilias Belharouak, Richard L. Axelbaum: Composition optimization of $xLi_2MnO_3 \cdot (1-x)LiMO_2$ electrodes (M= Mn, Ni, Co) prepared *via* spray pyrolysis process, in: 222nd ECS Meeting, Oahu, 2012

6. X.Zhang, **M. Lengyel**, I. Belharouak, R. L. Axelbaum: Optimization of the electrochemical properties of $xLi_2MnO_3 \cdot (1-x)LiMO_2$ electrodes (M= Mn, Ni, Co) prepared *via* spray pyrolysis process, in: 221st ECS Meeting, Seattle, 2012.

7. X. Zhang, **M. Lengyel**, R. Axelbaum: Advances in Aerosol Synthesis of Li-rich Composite Materials for Li-ion Positive Electrodes in: 220th ECS Meeting, Boston, 2011.

8. **M. Lengyel**, X. Zhang, R. Axelbaum, Electrochemical Performance of $LiMn_2O_4$ Powders Prepared with a Novel Honeycomb Burner, in: 219th ECS Meeting, Montréal, 2011.

Awards and honors

Energy & Technology Division Travel grant for attending the 2013 ECS Fall meeting

IEEE Travel grant for attending 2013 ECS Spring meeting

Battery Division travel grant for attending 2012 ECS Fall meeting

Poster presentation at the 17th Annual Graduate Student Symposium 2012.

3rd place at the conference of MSc. Students National round at Debrecen University, Hungary 2009

Best Chemical Engineering Diploma thesis work award at Budapest University of Technology and Economics, Hungary 2009.

McDonnell International Scholars Academy Scholarship at Washington University in St. Louis in 2009.

James & Cora Miller Fellowship at Washington University in St. Louis in 2009.

Presentation at Procter & Gamble in Egham near London, United Kingdom 2008.

Conference of MSc. Students University round at Budapest University of Technology and Economics, Hungary 2008. Special 1st place provided by Richter Gedeon Ltd.

3rd place in regional and national International Latin dance competition in 2007.